ISBN 978-82-326-7234-9 (printed ver.)
ISBN 978-82-326-7233-2 (electronic ver.)
ISSN 1503-8181 (printed ver.)
ISSN 2703-8084 (electronic ver.)

NTNU
Norwegian University of
Science and Technology

Doctoral theses at NTNU, 2023:267

Håvard Snefjellå Løvås

Optical Techniques for Hyperspectral Imaging of the Seafloor

NTNU
Norwegian University of
Science and Technology
Thesis for the degree of
Philosophiae Doctor
Faculty of Engineering
Department of Marine Technology

NTNU
Norwegian University of
Science and Technology

Doctoral theses at NTNU, 2023:267

NTNU

Håvard Snefjellå Løvås

Doctoral thesis

Håvard Snefjellå Løvås

Optical Techniques for Hyperspectral Imaging of the Seafloor

Thesis for the degree of Philosophiae Doctor

Trondheim, September 2023

Norwegian University of Science and Technology
Faculty of Engineering
Department of Marine Technology

NTNU
Norwegian University of
Science and Technology

NTNU
Norwegian University of Science and Technology

Thesis for the degree of Philosophiae Doctor

Faculty of Engineering
Department of Marine Technology

ISBN 978-82-326-7234-9 (printed ver.)
ISBN 978-82-326-7233-2 (electronic ver.)
ISSN 1503-8181 (printed ver.)
ISSN 2703-8084 (electronic ver.)

Doctoral theses at NTNU, 2023:267

Printed by Skipnes Kommunikasjon AS

Summary

In this thesis, optical techniques for hyperspectral mapping of the seafloor have been developed with an emphasis on geometric and radiometric processing. One of the overarching ideas researched is how a concurrent conventional camera and a hyperspectral line scanner can be used in tandem. This is motivated by recent developments in digital camera hardware and software that has boosted the capability and availability to accurately map geometry and texture. The thesis has specifically considered techniques for transferring some of this accuracy to hyperspectral images of the seabed. The underlying principle is that the line scanner measures the same color texture as the camera, just in a different form. This allows to optimize geometric parameters for the hyperspectral scan lines with the objective of aligning the lines to the texture and geometry of the camera images. When such a calibration has been carried out, the lines' equivalent light beam paths can be simulated backwards to find beam collisions with a 3D model of the seabed. The collision points define the seafloor-origin of the scan line. This provides a global reference to each individual spectrum within the scan line. The technique was first demonstrated for concurrent hyperspectral and conventional imaging from a remotely operated underwater vehicle. The test site was a geometrically complex deep-water coral reef, and the work demonstrated contiguous hyperspectral mapping with high geometric accuracy. By geometrical accuracy it is referred to how well the final hyperspectral map was aligned to the conventional camera map. The resulting hyperspectral map was further used in a larger context for multi-scale mapping of the coral reef.

A similar technique was further adapted for shallow water mapping from an unmanned aerial vehicle. This required, among other things, adaptation when it came to navigation estimation, and perhaps most of all the refraction effect at the water surface. The alignment gave hyperspectral scan lines that were well-aligned to the photo maps. For the aligned data, we demonstrated how to simultaneously estimate water depths through two measuring principles; multi-view stereo with subsequent refraction compensation and hyperspectral inversion. The former used the photos, while the latter used individual spectra.

One of the advantages of the geometric alignment technique above is that we get an accurate understanding of the light beam paths associated to individual spectra. In water, light at different wavelengths is absorbed and strongly scattered along a beam as a function of distance. In the dissertation's final work, a semi-analytical model was proposed that described the relation between the seabed's

reflectance and measured spectra. Such a model basically had unknown 1) geometric parameters and 2) unknown optical properties for the water column. We could derive the former from the previously mentioned alignment procedure. We could break down the latter by using known physical and empirical relationships from radiative transfer theory and the remote sensing community. This allowed for representing the spectral properties of the water column with a low number of latent parameters. To demonstrate the semi-analytical model on deep-water field data, we proposed using overlapping scanned areas so that two different perspectives of the same seabed substrates were obtained. This allowed finding the last unknown latent parameters so that the semi-analytical model was complete.

Sammendrag

I denne avhandlingen har optiske teknikker for hyperspektral kartlegging av havbunnen blitt utviklet med spesielt fokus på geometrisk og radiometrisk prosessering. En av de gjennomsyrende ideene som har blitt studert er hvordan et samtidig konvensjonelt kamera og en hyperspektral linjeskanner kan brukes i tandem. Nylig utvikling i digitale kameraer og påfølgende prosessering har gjort sensoren til et kraftig verktøy for nøyaktig kartlegging av høyoppløselig geometri og tekstur. Avhandlingen har spesielt tatt for seg teknikker for å overføre noe av denne nøyaktigheten til hyperspektrale bilder av havbunnen. Det underliggende prinsippet er at linjeskanneren måler den samme fargeteksturen som kameraet, bare i en annen form. Dette tillater å optimalisere geometriske parametere for de hyperspektrale skannelinjene med målsetning om å innrette linjene til kamerabildenes tekstur. Når en slik kalibrering er utført, kan linjenes ekvivalente lysstråle-baner simuleres baklengs for å finne stråle-kollisjon med en 3D modell av havbunnen. Kollisjonspunktene definerer opphavet til skannelinjen, og det gir en global referanse som hvert enkelt spektrum kan knyttes til. Teknikken ble først demonstrert for samtidig hyperspektral og konvensjonell avbildning fra en undervannsrobot. Teknikken ble demonstrert for et geometrisk komplekst dypvannskorallrev, og det var første gang kontinuerlig, overlappende hyperspektral kartlegging ble demonstrert for en undervannsplatform. Det resulterende kartet ble videre brukt i en større sammenheng for multi-skala kartlegging av korallrevet.
En liknende teknikk ble videre tilpasset for gruntvannskartlegging fra en ubemannet luftfartøy. Dette krevde blant annet tilpasning når det kom til navigasjonsestimering, og kanskje aller mest refraksjonseffekten ved vannflaten. For den sammenstilte kartdataen demonstrerte vi hvordan man samtidig kunne estimere vanndybder gjennom to måleprinsipper; multi-synspunkt stereo med påfølgende refraksjonskompensasjon og hyperspektral inversjon.
En av fordelene med den geometriske innrettingsteknikken over er at vi får en nøyaktig forståelse av skanne-linjenes lysstråle-baner. I vann er det nemlig slik at lys ved forskjellige bølgelengder absorberes og spres kraftig langs en stråle som en funksjon av avstand. I avhandlingens siste arbeid beskrives en semi-analytisk modell som beskriver relasjonen mellom havbunnens reflektans og målte hyperspektrale spektra. En slik modell har i utgangspunktet ukjente 1) geometriske parametere og 2) ukjente optiske egenskaper for vannkolonnen. Den førstnevnte kan vi med stor konfidens uthente fra konvensjonelle bilder. Den sistnevnte kan vi bryte ned ved å bruke kjente fysiske og empiriske sammenhenger fra strålingsteori og fjern-

målingsmiljøet. Dette tillater å representere vannkolonnens spektrale egenskaper ved et lavt antall latente parametere. For å demonstrere den semi-analytiske modellen på dypvanns feltdata foreslo vi å bruke overlappende skannede områder slik at man fikk to forskjellige perspektiver av samme havbunn. Dette tillot å finne de siste ukjente latente paremetrene slik at den semi-analytiske modellen var komplett.

Preface

This thesis is submitted in partial fulfillment of the requirements for the degree of Philosophiae Doctor (PhD) at the Norwegian University of Science and Technology (NTNU), Trondheim. The work presented has been conducted at the Department of Marine Technology supported by the Research Council of Norway through the Centre of Excellence funding scheme, NTNU AMOS, project number 223254.

Acknowledgements

Sir Isaac Newton wrote in 1675 in a letter to his peer Robert Hooke that "If I have seen further it is by standing on the shoulders of Giants". Science is cumulative and collaborative, and I am thankful for the incredible efforts of predecessors and peers. The idea that science is built by a handful of genius people with radially protruding hair is best suited for Hollywood.
Firstly, I could like to thank my main supervisor Asgeir. You have given me the freedom to pursue my curiosities, and supported me throughout this journey. You are undoubtedly one of the most motivating people I met, and I appreciate that immensely. You also pushed me to face my worst fear, writing. Thanks to you, I can now say that I enjoy it. I would also like to thank my co-supervisor and the head of Applied Underwater Robotics Laboratory (AURlab) Martin Ludvigsen. My time in the AURlab was highly varied and interesting. During my time in the lab, I got the opportunity to work with underwater robotic vehicles and operative experience in incredible locations. I would like to thank my co-supervisor, Geir Johnsen. A biologist thriving in the field, even in subzero temperature Arctic waters in the middle of the night. I am thankful for our great conversations. I would also like to thank Paul Gader who was a visiting professor at NTNU. He was truly a joy to be around, always positive and making jokes. Sadly, Paul passed away during the time of writing. He will be missed. I would like to thank Oscar Pizarro for many great conversations and interesting ideas. He has a rare ability to reflect on and communicate complex topics in an understandable language. A thank is also due to Øyvind Ødegård who shared many interesting ideas about underwater hyperspectral imaging.
I would like to thank my dear and incredibly skilled colleagues from the AURlab office for a great time in the office, in the field and during our spare time. Firstly, I must thank Jens, my colleague and co-adventurer, for our four years together on the PhD. Whether it was kayaking amongst beluga whales in Svalbard or 24 hours

of looking for a lost Autonomous Underwater Vehicle (AUV) with a hydrophone. Through good and bad times you are the definition of stamina, and the face of optimism. Secondly, I would like to thank Tore for three years together during the PhD. Tore, you are arguably the perfect combination of engineer and scientist who can make just about anything work. Thirdly, I would like to thank Martin K. for our multiple great conversations about computer vision and sensor fusion. You are incredibly knowledgeable and I learned a lot from you. Fourthly, I would like to thank Markus for being a patient sparring partner both when it comes to anything. Lastly, I could like to thank Alexandre, Ambjørn, Gabriele, Karoline, Ole, and Fredrik who I got the pleasure of sharing office with. Thank you for the sharing of ideas, sparring and knowledge transfer.
I would like to thank co-author and friend Aksel. It was inspiring to work with a biologist like Aksel, and I think we made a great team. He is a man with an exceptional sense of humor and a very talented researcher. I would also like to thank my collaborator Oliver from the Unmanned Aerial Vehicles Laboratory (UAVlab). He tough me about navigation and aerial drones, and it was fun to be in the field with together in Ny-Ålesund. I would also like to thank collaborators Dennis Langer, Joseph Garrett, Natalie Summers, Eleni Diamanti, and Hongbo Liu.
I would like to thank my parents Randi and Gunnar for bringing me to this world and for supporting me through all these years. I would also like so thank my siblings and my step-families. Lastly, and most importantly I want to thank my love and fiancee, Rikke. She makes my life better in every way possible. She has supported me through the entire process, and I am eternally thankful. As I am writing this, she is carrying our first child, a little boy. Although he is not born yet, I would like to dedicate this thesis to him.

Contents

Abbreviations

ALB Airborne Laser Bathymetry
APOS Acoustic Positioning System
AURlab Applied Underwater Robotics Laboratory
AUV Autonomous Underwater Vehicle
BRDF Bi-Directional Reflectance Distribution Function
CCD Charged Coupled Device
CDOM Colored Dissolved Organic Matter
CPU Central Processing Unit
CRS Coordinate Reference System
CV Computer Vision
DEM Digital Elevation Model
DSM Digital Surface Model
DVL Doppler Velocity Log
ECEF Earth-Centered Earth Fixed
EMR Electromagnetic Radiation
ESKF Error-state Kalman Filter
FF Fournier-Forand
FoV Field-of-View
GCP Ground Control Point
GIS Geographic Information Systems
GNSS global navigation satellite system
GPS Global Positioning system
HOPE Hyperspectral Optimization Processing Exemplar
HSI Hyperspectral Imager
IMU Inertial Measurement Unit
INS Inertial Navigation System
IOP Inherent Optical Properties
LUT Look-Up-table

MBES Multibeam Echosounder
MiDAR Multispectral Imaging Detection and Active Reflectance
MPA Marine Protected Area
MVS Multi-View Stereo
NN Nearest Neighbor
NTNU Norwegian University of Science and Technology
OECD The Organization for Economic Cooperation and Development
PhD Philosophiae Doctor
PPK Post-Process Kinematic
PSF Point Spread Function
QSSA Quasi-Single-Scattering-Approximation
RGB Red-Green-Blue
ROV Remotely Operated Vehicle
RS Remote Sensing
RTE Radiative Transfer Equation
RTK Real-Time Kinematic
SA Semi-Analytic
SBES Singlebeam Echosounder
SD Secchi Depth
SfM Structure-from-Motion
SIFT Scale-Invariant Feature Transform
SLAM Simultaneous Localization and Mapping
SLERP Spherical Linear Interpolation
SNR Signal-to-Noise Ratio
SVM Support Vector Machine
ToF Time-of-Flight
UAV Unmanned Aerial Vehicle
UAVlab Unmanned Aerial Vehicles Laboratory
UHI Underwater Hyperspectral Imager
USV Unmanned Surface Vehicle
UTM Universal Transverse Mercator
UUV Unmanned Underwater Vehicle

Chapter 1

Introduction

1.1 Background and motivation

> *"Nowhere is more powerful and unforgiving, yet more beautiful and endlessly fascinating than the ocean."*
>
> — Sir David Frederick Attenborough

The ocean covers 71 percent of the earth surface [1] and is sometimes referred to as the blue planet. The average depth of the ocean is an astonishing 3800 meters, constituting an immense volume of water which is commonly described as the water column. The surface below the water column is called the seabed, seafloor or benthic zone. A benthic habitat can be defined by both abiotic factors such as the bathymetry and geology, and by the biological composition, or flora and fauna [2]. The benthic zone holds many impressive habitats ranging from shallow-water tropical coral reefs to deep-water communities around hydro-thermal vents. Unfortunately, all these habitats are under increasing pressure from human activities, and scientific mapping and monitoring over time is the only way in which we can properly understand these impacts.
The ocean has historically been important for humans and they have used the ocean for transportation, energy, food etc. Population and consumption grew drastically after the onset of the industrial revolution, and our technological ability to exploit nature was revolutionized. By some definitions, this marked the beginning of the Anthropocene, a pronounced increase in humanity's impact on the natural world. An illustrative example is the hunting (almost to extinction) of the largest animal to ever exist, the blue whale for the production of whale oil. In [3] the author describes how it was the technological novelties of the steam propulsion and modern weaponry that enabled humans in the 1870s to take down the gigantic whale in Arctic and Antarctic areas. According to [4] there has been a disconnect between humans' history of transforming marine ecosystems and the recognition of the effects due to lacking scientific monitoring. The result has been that humanity has been unable to understand the magnitude of human impact on ecosystems during the Anthropocene. To monitor these impacts, time series of data over temporal and

spatial scales are needed. Such surveys could emphasize spatial coverage to map and monitor large-scale ecosystems, or spatial resolution to monitor smaller scale details. The surveying methods also need to consider the temporal resolution or re-visitation frequency and be feasible in terms of cost.
According to [5], the Challenger expedition (1872-1876) arguably represented the beginning of the ocean sciences. The HMS Challenger took samples of the bottom sediment, a depth sounding with a lead line, and conducted dredging and trawling on the seafloor to get biological samples. A revolution in bathymetry mapping later came in the 1900s with the Singlebeam Echosounder (SBES) [6]. The early beams were broad, meaning that the achievable resolution would be 0.5-1 times the measured depth. Today, the use of the area-scanning Multibeam Echosounder (MBES) has provided humanity with the opportunity to contiguously map the entire seafloor. However, according to [7] only a small fraction fraction of the bathymetry has been measured directly, while the main fraction has been estimated from satellite altimetry. The word estimate is used because satellite altimetry measures the height of the sea surface and tries to infer bathymetric features of horizontal sizes larger than 6-9 km in deep ocean [8]. High-resolution bathymetric maps are key to predicting the location and extent of various benthic habitats and global coverage of visual observation of the seafloor are unrealistic [7].
Recently, the The Organization for Economic Cooperation and Development (OECD) described an area-based ambition to conserve 10 percent of coastal and marine areas in so-called Marine Protected Area (MPA)s as stated below. Note the term "the best available scientific information".

> *"Sustainable Development Goal Target 14.5 states: By 2020, conserve at least 10% of coastal and marine areas, consistent with national and international law and based on the best available scientific information."*
>
> — OECD Marine Protected Areas Policy Highlights [9]

Acoustic MBES and even low-resolution satellite altimetry undoubtedly plays a huge role in defining MPAs of such scales through mapping abiotic factors such as bathymetry. There are also examples where high-resolution acoustic backscatter images from AUV [10] and ships [11][12] has been used for identifying deep water coral reef structures. However, these methods are less suited for monitoring habitats over time and acquiring detailed biological information. The methods are also less suited for bathymetry mapping in shallow waters, because of collision risk, small MBES swath, economic feasibility, etc [13]. In shallow waters, it might be more feasible with above-water optical methods such as Airborne Laser Bathymetry (ALB)[14], spectral inversion methods (e.g. [15]) or photogrammetry [16], [17] from a satellite, an aircraft or a Unmanned Aerial Vehicle (UAV).
For all optical systems transmitting and/or receiving signals through oceanic water column, there are inherent limits to range because of how seawater and its constituents absorbs and scatter Electromagnetic Radiation (EMR). For example, the optical technique with the highest depth penetration is ALB with a green, 532 nm laser. State-of-the-art ALB systems can measure depth up to 3 times the Secchi Depth (SD), which can be upt to 60 m for clear coastal water

[14]. Moreover, it is common to say that optical sensing from air or space is limited to optically shallow water depths (i.e. 1-3 SD). An important application of airborne/spaceborne sensors is monitoring of shallow tropical coral reefs as thoroughly reviewed in [18]. The largest reef in the world, the Great barrier Reef, is 340 thousand km^2. It has had the most extensive time-series data on reef degradation, the Australian Institute of Marine Science Long-Term Monitoring Program [19]. Although the program has surveyed across the reef over time, the sampling is sparse both temporally and spatially. According to [18], long-range remote sensing from satellite and aircrafts would highly benefit such monitoring programs, because of their ability for inferring large scale patterns, cost efficiency and frequent re-visitation. As such, long-range remote sensing for shallow water habitats plays a similar role to MBES in deep water. They are both essential for inferring the large-scale patterns, but need to be combined with more detailed sensing or physical sampling.

In terms of large-scale habitat monitoring programs from underwater vehicles it is worth mentioning the AUV-based program in [20]. One of their monitoring strategies are revisits to reference sites where they perform contiguous mow-the-lawn imaging every visit for 25m $\times$ 25 m grids. This is challenging because accurate global positioning solutions underwater are expensive, and capabilities decrease with increasing depth. The particular advantage of revisiting reference sites is that quantitative comparisons of time-dependent effects can be studied with minimal ambiguity, e.g. in-situ growth rates of individual coral colonies. The downside of dense mow-the-lawn monitoring is that it is ill-suited for spatially heterogeneous impacts [18], e.g. bottom trawling. In such cases, it might be more powerful to record non-overlapping long transects or broad-scale sparse grids emphasizing spatial variability [20].

Closer-range optical systems above water refers to copter and fixed-wing UAVs which have become available platforms for detailed small-scale monitoring [13]. While cheap small-scale copter drones typically only carry an Red-Green-Blue (RGB) camera, medium sized drones have been used to for active sensing (e.g. ALB [21] and Multispectral Imaging Detection and Active Reflectance (MiDAR) [22]), and passive multispectral imaging [23] and hyperspectral imaging [24]. Arguably, these developments have also been facilitated by sensor miniaturization in recent years. The active and passive systems described can be used for studying various geometric and radiometric properties of the seafloor in shallow-water habitats. These tools are most suited for near-shore small-scale monitoring, and are by far the most feasible tool for monitoring of reference sites with frequent re-visitation. Also, it is important to note that the resolution of close-range aerial systems allows for incredible detail and decent coverage at the same time. Long-range remote sensing will suffer from a higher degree of mixing (for example kelp and sand in one pixel). Notably, an underwater robot gives the highest resolution images in shallow water, but has an extremely limited swath width compared to the UAV.

Underwater close-range optical systems underwater are typically separated into tethered Remotely Operated Vehicle (ROV)s and non-tethered AUVs, and their design ranges from several tons box-like structures to lightweight hydrodynamic bodies. As opposed to above the surface, optical communication and global

navigation satellite system (GNSS) is practically impossible, and therefore use acoustics are used for navigation and communication (ROV use tether for communication). When it comes to optical sensing of the seafloor, the range of systems are equally limited by the Inherent Optical Properties (IOP) of the water. However, any optical system deployed below the sunlit zone must bring their own sources of light, making them active sensing systems. This constitutes an additional limitation because a regular light source (non-laser) diverges with $1/r^2$ where r is the range. A field study of a state-of-the art imaging system [25] from an advanced large AUV concluded with a maximal imaging distance of 4-7 m for colour texture and 10 m for mere geometry in optimal conditions. They mapped 0.09 km^2 in 3.5 hours at an altitude of $\approx$ 5 m, meaning it would take roughly 40 hours to map one km^2, and 1.5 million years to map the entire seafloor. Moreover, [25] states an important point, that their AUV is unsuited for rugged seabed imaging due to lack of maneuverability and risk of collision. This is because many AUVs are dynamically actuated by fins and a stern thruster where the AUV needs a certain speed for maintaining and changing it's depth/altitude. In such cases, for example coral reefs, it is more suited with a slower-moving hovering AUV, e.g. AUV Sirius in [20], or an ROV [26].

Generally, most benthic-mapping underwater vehicles carry RGB cameras, either as a single camera or as two cameras in a stereo configuration, e.g. [20]. Given sufficient detectable texture across multiple photos, methods from Computer Vision (CV) and photogrammetry can are employed to build 3D models of the seabed. Synchronized, calibrated stereo images have the advantage that 1) the scale of objects can be directly inferred and 2) 2.5 dimensional structure of dynamic objects can be inferred. Another optical sensing method is structured light, typically through the use of a laser/camera where some known laser pattern is projected, and distances to the pattern can be derived, e.g. two laser lines in [27]. Both structured light and stereo benefit from having a certain displacement, or baseline, between cameras or camera/transmitter as this increases the ability to resolve distances using triangulation. Multi-spectral imaging has not been used for seabed mapping on underwater vehicles to the author's knowledge, but there has been some laboratory trials towards this goal [28]. Underwater hyperspectral imaging has been demonstrated for mow-the-lawn coral reef mapping from ROV, e.g. [29] and from AUV in [30]. It is also worth mentioning the mapping of a shoal on the Great Barrier Reef [31] where they used a hyperspectral point spectrometer from a hovering AUV.

As emphasized above, there are a variety of sensor-platform observation systems for mapping and monitoring of the seafloor with different capabilities in terms of area coverage, resolution and degree of detail. The systems must also be evaluated in terms of cost-of-survey including availability of systems and feasibility of re-visitation. Close-range optical sensing serves a crucial role in above-air sensing, and it is the only form of optical sensing from underwater vehicles. The sensors have different capabilities in terms of the geometric, textural and radiometric information they record. This thesis will focus on hyperspectral imaging from unmanned aerial and underwater vehicles, aided by RGB imaging and photogrammetric processing of such images. Hyperspectral imaging is the compromise between spectroscopy and imaging, recording light in contiguous,

narrow spectral bands, i.e. spectra, and in spatial pixels. When imaging through water column, hyperspectral imaging as all other forms of imaging is roughly limited to visible light, 400 nm-700 nm, by the water's IOPs.
The principle of hyperspectral imaging is that seabed materials, or substrates, interact with EMR in unique ways. The most studied interaction in remote sensing of the seafloor is reflectance spectroscopy which identifies substrates based on a unique spectral response. Notably, it is also possible to study several pixels' reflectances, or texture, which is how regular images are typically classified, but this is out of the scope here. Inferring a material's reflective properties from an in-situ spectrum is by no means trivial. It requires a proper solution to the Radiative Transfer Equation (RTE) and constitutes a simultaneous estimation of reflectance, water body IOPs and the light's path length, or water depth. Moreover, a well-known approach are the physics-based Semi-Analytic (SA) inversion models originating from the Hyperspectral Optimization Processing Exemplar (HOPE) approach in [15]. Another approach to the inverse problem are Look-Up-table (LUT) methods, e.g. CRISTAL [32], based on matching a recorded observation against synthetic spectra in a LUT for different depths, IOPs and bottom reflectances.
According to [33], hyperspectral imagery minimizes the non-uniqueness of inversion and the retrieved IOP, water depth and bottom reflectance. The main downside is that a hyperspectral sensor sacrifices spatial resolution and typically the 2D frame imaging mode to prioritize spectral resolution. Lastly, it seems fit to include the more empirical classification modes, e.g. machine learning, that uses human-labeled spectral fingerprints from the site and trains a model to classify spectra. This is for example done using Support Vector Machine (SVM) classifier from UAV in [24], ROV in [29], and AUV in [31]. A set of approaches not rigorously studied in the shallow-water/underwater hyperspectral domain are classification methods that exploit textural information, or group structures of adjacent spectral pixels.

1.2 Research questions

The overarching aim of this thesis is to develop geometric and radiometric processing methods for facilitating underwater and shallow-water hyperspectral mapping of benthic habitats. In comparison to shallow-water hyperspectral methods, underwater hyperspectral methods are severely less researched. There are differences in environmental conditions, vehicles, illumination and RTE boundary conditions, sensor-terrain geometry, and navigation solutions. However, there are many similarities, and certainly many methodologies that can be adapted between domains. For an anecdotal illustration of some differences, consider Figure 1.1. Figure 1.1(a) e.g. shows bathymetry-induced variations in swath width from 1-3 m causing large variations in illumination. This is because the ROV's altitude control (above seafloor) is unable to keep the swath constant. In contrast, the gimbal-stabilized UAV hyperspectral imagery in Figure 1.1(b) has a relatively constant swath width and illumination from sunlight.

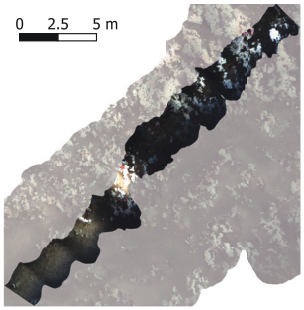

(a) ROV-based hyperspectral of rugged reef structures, strong currents, mean altitude 2 m, ≈80 m depth from [34].

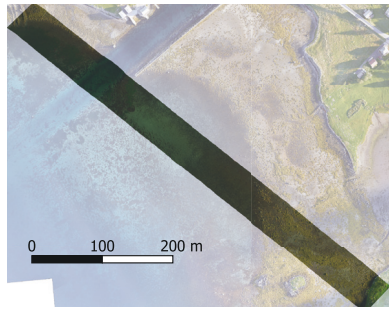

(b) UAV-based hyperspectral of inter-tidal zone, kelp forest and seagrass meadows. The altitude was ≈80 m above mean sea level with the a gimbal stabilization. Data was acquired by the UAVlab on behalf of the SeaBee project [35]. Courtesy to SpectroFly for building the photogrammetry model.

Figure 1.1: RGB representations of georeferenced hyperspectral imagery (raw radiance) from an ROV and UAV. Both illustrations are shown with corresponding photogrammetry-based mosaics. Geometric processing was done by the author.

Within the overarching aim, the following research questions are raised:

- **RQ1**: How can we make geometrically accurate maps in underwater hyperspectral imagery?
- **RQ2**: How can a semi-analytical model be designed for hyperspectral imaging from an underwater vehicle with active light sources? And how can the unknown parameters of that model be determined?
- **RQ3**: How can we achieve consistent georeferencing for concurrent RGB and Hyperspectral Imager (HSI) imagery in airborne shallow-water hyperspectral imagery? Can we utilize this to perform concurrent bimodal bathymetry estimation from spectral inversion and photogrammetry?

1.3 Research methodologies

The research methodologies used for answering the research questions are mainly theoretical studies and experimental work in addition to several field campaigns in the Trondheimsfjord and around Svalbard. Admittedly, the research questions themselves were more found through data exploration and attempts to solve specific problems rather than by exhaustive literature studies. I have been fortunate to be part of an applied underwater robotics lab, AURlab, and had a close collaboration with the unmanned aerial vehicles lab, UAVlab, at the university. This has enabled access to experimental data and knowledge across domains. In addition, the collaborations with end users such as marine biologists at NTNU or SeaBee in mapping/monitoring contexts has been important for understanding the bigger picture.

In the beginning of the PhD, 2019, I stepped into the unknown world of underwater robotics and the world of spectroscopy. Firstly, I worked on putting together a remotely operated underwater vehicle system for carrying an underwater hyperspectral imager. It was realized when working with data from a field experiment with this system that radiometric and geometric "distortions" of the spectral images posed challenges to classification and mapping. Through suggestions and experiments by colleagues, it seemed that photogrammetry could be a useful tool for achieving geometrically accurate hyperspectral maps. In 2020, I was fortunate to get access to a large hyperspectral data set of the rugged deep-water coral reef where the spectral images were highly distorted. This started an exiting journey on trying to build geometrically accurate maps, including laboratory experiments for method development. This sprung into the first and second Journal papers J.1, J.2. Furthermore, after these works, I got the opportunity to work with hyperspectral imaging from UAVs with the ambition of helping out a master's student with georeferencing and radiometric processing. This led me into the shallow-water Remote Sensing (RS) field where I learned about two-media photogrammetry and hyperspectral inversion. This work became the third journal paper J.2. The experience in shallow-water mapping from UAV also allowed me to work with coregistration of hyperspectral imagery in the SeaBee project. The exposure to the shallow-water field along with a literature study on radiative transfer in water made me realize that there was a large potential in transferring and adapting semi-analytical methods to the underwater hyperspectral domain. This concluded and was the last journal paper, J.4, that was conducted as a part of this thesis.

1.4 List of publications and contributions

Journal papers:

J.1 **H. S. Løvås**, A. A. Mogstad, A. J. Sørensen, and G. Johnsen, "A Methodology for Consistent Georegistration in Underwater Hyperspectral Imaging," *IEEE Journal of Oceanic Engineering*, vol. 47, no. 2, pp. 331–349, 2021
Contribution: We proposed a methodology for geometrically accurate georeferencing in underwater hyperspectral imaging. The method used Structure-from-Motion (SfM)-photogrammetry with a concurrent RGB camera for achieving self-consistent camera trajectories and seabed geometry. A laboratory and in-situ co-calibration approach was developed for determining the HSI camera model and relative offset in rotation and lever arm between the RGB and HSI. Georeferencing was conducted by ray tracing the HSI rays onto the mesh model. Based on the HSI distances to seafloor points, an attenuation and light source correction was conducted that was calibrated using some known bright substrates at varying distances. This resulted in overlapping transects of spectral reflectance that were mosaicked using the HSI-seabed distances.

J.2 A. A. Mogstad, **H. S. Løvås**, Ø. Sture, G. Johnsen, and M. Ludvigsen, "Remote Sensing of the Tautra Ridge: An Overview of the World's Shallowest Cold-Water Coral Reefs," *Frontiers in Marine Science*, vol. 9, p. 848 888, 2022

Co-author contribution: I supplied the main author with the georeferenced and radiometric corrected reflectance as described in the previous paper. The data was then used for classifying key species coverage on the reef as well as live coverage using SVM.

J.3 **H. S. Løvås**, O. Hasler, D. D. Langer, and A. J. Sørensen, "Coregistration of Hyperspectral Imagery With Photogrammetry for Shallow-Water Mapping," *IEEE Transactions on Geoscience and Remote Sensing*, vol. 61, pp. 1–24, 2023
Contribution: We proposed a method for co-registration of concurrent hyperspectral and RGB imagery in shallow-water mapping from UAV. The method was conceptually similar to the J.1, but accounted for refraction in a different way, and integrated SfM-derived trajectories in a Kalman Smoother for consistency and high-frequency motion. The co-registration enabled two modes of concurrent bathymetry estimation that were demonstrated and compared. The first was refraction corrected bathymetry from Multi-View Stereo (MVS) and the second was inversion of the hyperspectral images. The hyperspectral inversion method was calibrated using some sparse acoustic data points.

J.4 **H. S. Løvås**, M. K. Larsen, O. Pizarro, and A. J. Sørensen (Submitted 29.06.2023), "A semi-analytical model for deep-water hyperspectral imaging," *Applied optics*, 2023
Contribution: We proposed a SA model for hyperspectral imaging in deep water based on adjacent fields such as shallow-water hyperspectral remote sensing, radiative transfer theory and computer vision. The SA model utilized the high-accuracy geometry obtained through the method proposed in J.1. The remaining unknown parameters of the model were the IOPs. A parameterization for IOPs was suggested, and we conducted spectral optimization to find the parameters based on two-perspective views of the seafloor.

J.5 N. Summers, G. Johnsen, A. Mogstad, **H. Løvås**, G. Fragoso, and J. Berge, "Underwater hyperspectral imaging of Arctic macroalgal habitats during the polar night using a novel mini-ROV-UHI portable system," *Remote sensing*, vol. 14, no. 6, p. 1325, 2022
Co-author contribution: I contributed with the development of dual ROV system including vehicle frame, electronics, sensors and control, and deployment and operation of the vehicle during the experiment. I also conducted geometric and radiometric processing for reflectance estimation.

Conference papers:

C.1 **H. S. Løvås**, A. J. Sørensen, and M. Ludvigsen, "Framework for Combining Multiple Lightweight Underwater Vehicles into Super Underwater Vehicle," in *2020 IEEE/OES Autonomous Underwater Vehicles Symposium (AUV)*, IEEE, 2020, pp. 1–6
Contribution: The paper describes the development of the remotely operated dual ROV system used in J.5, for carrying an underwater hyperspectral

imager. The principle is simply based on using two small ROVs, with a payload/navigation frame in-between with an underwater hyperspectral imager. A simple control algorithm for allowing joystick control of the rig was also developed. The concept was demonstrated first for a field survey in Ny-Ålesund 2020, and later used for under-ice mapping of sea ice in the Barents Sea 2021.

Dissemination not included as attachments in thesis:

- SeaBee project: Multi-modal mapping of intertidal zone and shallow-water habitats from UAVs at Remøy, Norway. A journal paper describing the methods and results is under preparation by Joseph Garrett.
  Co-author contribution: Performed co-registration of hyperspectral imagery to enable consistency in mapping with other modalities. The co-registred data is visualized at [40]. The developed co-registration method aligned push-broom hyperspectral imagery from one UAV to a high-resolution reference orthomosaic and Digital Elevation Model (DEM) from another survey. The principle of the co-registration was to attribute registration errors for transects to slowly varying navigation errors in position and heading of the drone. The method and results will be part of the coming paper, but it was not be finalized in time for this thesis.
- Arctic Frontiers Conference 2022, Tromsø: Poster "Monitoring the Arctic with autonomous underwater vehicles" by David Williamson and Håvard Løvås. Abstract can be found at [41].
  Co-author contribution: Helped with data acquisition and data processing.
- E. Diamanti, **H. S. Løvås**, M. K. Larsen, and Ø. Ødegård, "A multi-camera system for the integrated documentation of Underwater Cultural Heritage of high structural complexity; The case study of M/S Helma wreck," *IFAC-PapersOnLine*, vol. 54, no. 16, pp. 422–429, 2021
  Co-author contribution: Provided colour corrected, geotagged images with camera calibration from one of the RGB cameras in the study. The imagery were then used for georeferencing the multi-camera alignment.
- O. Hasler, **H. Løvås**, T. H. Bryne, and T. A. Johansen, "Direct georeferencing for Hyperspectral Imaging of ocean surface," in *2023 IEEE Aerospace Conference*, IEEE, 2023, pp. 1–19
  Co-author contribution: Collaborative discussions and sharing of methods since we were working with similar navigation sensors and similar hyperspectral imagers.

1.5 Thesis structure and outline

The thesis is structured in the following manner.

- Chapter 2 introduces underwater and shallow-water hyperspectral habitat mapping to give an overview and to put the geometric and radiometric methods of this thesis into the mapping context.
- Chapter 3 describes the geometrical methods applied in this thesis for RGB frame imagery and HSI push-broom imaging. We here mainly describe methods for photogrammetry-aided georeferencing and coregistration of hyperspectral imagery. In doing so, we also give a description of photogrammetry in underwater and shallow-water imaging.
- Chapter 4 describes the radiometric methods applied in this thesis for spectral images.
- Chapter 5 summarizes the results of the publications and attempts to answer the research questions.
- Chapter 6 presents the concluding remarks and gives some recommendations for further work.
- Chapter 7 presents the collection of articles, including the five journal papers and the one conference paper.

Chapter 2

Hyperspectral Habitat Mapping

This chapter will start by introducing push-broom hyperspectral images. Then vehicle-based spatial acquisition of hyperspectral images is described. This includes acquisition from aerial vehicles of shallow-water targets and underwater vehicles in deeper. Lastly, the processing of the acquired imagery into habitat maps will be habitat maps will be presented.

2.1 A hyperspectral image

A push-broom hyperspectral imager spatially records a 1D slit image, or scan line across-track, per exposure and is similar to other line cameras geometrically. By forward motion, along-track, the imager scans the non-planar 2D surface defined by the rays' intersection with the terrain. Within the instrument, the panchromatic light of the slit image is dispersed into monochromatic light (narrow spectral bands) by means of refraction or diffraction using a prism or a diffraction grating. This is possible because refraction and diffraction properties are wavelength dependent. This "division" of light enables the use of common 2D pixel arrays for recording the light.
Each spectral channel/band, k, is typically characterized by a central wavelength λ_k and a band width $\Delta\lambda_k$ often defined by the full-width at half maximum. When the monochromatic light hits the detector, e.g. a 2D Charged Coupled Device (CCD) array, the photoelectric effect generates an electric signal which can be recorded. By exposing the array over an exposure time, t_{exp}, the sensor records a digital count $\hat{N}_m(u, v)$, where u and v are column and row indices of the 2D array. Assume that u is the pixel number along the spatial axis of the imager and $v = k$ is the spectral-axis pixel number. In [44] they describe how to calibrate a hyperspectral camera. In essence, there is two main calibrations:

- A spectral calibration describing the mapping $v \rightarrow \lambda_k$ which utilizes spectrally peaked light sources and curve fitting.
- A radiometric calibration utilizing a non-peaked light source with a known spectral radiance spectrum $[W/(m^2\ sr\ nm)]$ in an integrating sphere.

In total, the conversion from $\hat{N}_m(u, \lambda)$ to in-air radiance $L(u, \lambda_k)$ can then be computed as

$$L(u, \lambda_k) = \frac{\hat{N}_m(u, \lambda_k) - \hat{N}_d(u, \lambda_k)}{C(u, \lambda_k) t_{exp}}. \tag{2.1a}$$

Where $\hat{N}_d(u, \lambda_k)$ is the dark current or dark count, which in e.g. [44] is recorded with a lens cap on. The calibration gain $C(u, \lambda_k)$ describes the proportional relationship between radiance and dark frame-subtracted digital counts. The results in [44] suggested that the dark count was almost constant across the sensor. Radiometrically, they show that the sensor as a whole suffers from spatial vignetting, or reduced quantum efficiency towards the spatial edges of the image. As we will get to later, a submerged HSI must also account for the immersion factor as done for a point radiometer in [45]. For non-slanted observations, this I_f is 1.71-1.77 so that in-water radiance is $L_w(u, \lambda_k) = L(u, \lambda_k) I_f(u, \lambda_k)$. Simply explained, light hitting a pixel area for a submerged HSI is collected in a smaller and different set of directions than in air. This means that a certain measured radiant power implies a higher directional density of power (radiance) in water than in air. Note that an airborne imager implicitly accounts for a similar effect when converting from remote sensing reflectance R_{rs} to subsurface remote-sensing reflectance r_{rs} as shown in [46] including internal reflection effects.

2.2 Acquiring spatial data

This section explains vehicle-based acquisition of hyperspectral images from airborne and underwater platforms. Besides from some geometric and radiometric differences explaining the formation of the hyperspectral images, the vehicle-based acquisition shares many conceptual similarities. Having explained the spatial-spectral radiance measurement or, still frame of a push-broom imager, the next step is the acquisition of several sequential frames. This stacked sequence of still frames is called the 3D radiance-corrected datacube. The datacube's first axis i is the frame number which is associated to a timestamp given proper time synchronization. The second axis $j = u$ is the pixel number, associated with a view angle given proper geometric calibration. The third axis $k = v$ is the band number which is associated with λ_k and a band width $\Delta\lambda_k$ given a proper spectral calibration. A spectral radiance entry in the datacube is $L(i, j, k)$. In itself a datacube gives no substantial spatial information. The optimal form of push-broom scanning a site is through keeping a constant height above ground z, or distance along z-axis, and a constant forward velocity V and no change in the scanner's orientation [47]. If these criteria are satisfied, it is possible to quantify the spatial resolutions $\Delta x, \Delta y$ and swath width SW as follows

$$\Delta x = \frac{z w_s}{f} + V t_{exp} \tag{2.2a}$$

$$\Delta y = \frac{z h_s}{f W} \tag{2.2b}$$

$$SW = W \Delta y. \tag{2.2c}$$

Where w_s, h_s are slit width and height, while W is the number of effective spatial pixels. Although such metrics may be idealized, they are potent for planning missions, and they might be quite accurate for an aircraft with an HSI on a gimbal above flat terrain, see e.g. Figure 1.1(b). In contrast, the swath of the underwater ROV-based mapping in Figure 1.1(a) is far from constant due to highly rugged terrain. The ruggedness is of similar magnitude as the Himalayan mountain range seen from a passenger aircraft. A better term is relative ruggedness, meaning the high-frequent variation in terrain elevation (ruggedness) relative to imaging distance. The ROV is also faced with very strong currents, causing across-track motion and rotations. Without diving into the mathematics of it, the spatial resolutions and SW will inevitably vary according to the relative ruggedness. The variations in swath width can be compensated for by planning increased overlap between contiguous transects. The variations in imaging distance could also be accounted for when mosaicking overlapping transects as was done in J.1.
When selecting a vehicle system for HSI-based mapping, the specifics of the mission are crucial. A couple of things that are worth considering are:

- Range: How long, e.g. in meters, can the vehicle travel during one deployment? For underwater vehicles it can also be relevant to know the depth rating of the vehicle. For UAVs it is also relevant to know feasible flying height.
- Payload capacity: Can the vehicle carry the HSI? Both aerial vehicles and small underwater vehicles have limited payload capacity both in terms of available volume and weight. Can the vehicle carry auxiliary instruments such as illumination and a RGB camera?
- Portability/Flexibility: Can the vehicle be deployed/transported in a feasible manner at/to the relevant site? A fixed-wing UAV requiring a runway or other infrastructure may be infeasible for operation at remote locations. Medium-large ROVs requires deployment and operation from a large ship, which may not be feasible.
- Maneuverability and control: Can the vehicle follow the desired control objective? As previously mentioned, some AUVs need forward speed for fin-based actuation in the vertical direction. When the terrain becomes rugged, these vehicles are infeasible for close-range imaging of the seabed due to the risk of collision. Another aspect is to what extent the vehicle can counteract environmental loads, such as currents for underwater vehicles or wind for UAVs.
- Stability: Stability in roll/pitch/yaw motions are important for limiting motion blur in the hyperspectral imagery. A gimbal system with an integrated Inertial Measurement Unit (IMU) is an effective solution for an aerial vehicle if feasible. For an underwater vehicle where a gimbal is less feasible, the stability is related to hydrodynamic properties (e.g. inertia, damping) of the vehicle, but also the actuation.
- Navigation and payload suite: Is the navigation and payload suite adequate for the mapping requirements? In all cases position/attitude information is vital. Hyperspectral mapping always needs a model of the seafloor elevation,

which may require other payload sensors that can infer this information. In some cases geographic accuracy is important. This could require more expensive Acoustic Positioning System (APOS)-systems for underwater vehicles or Real-Time Kinematic (RTK)/Post-Process Kinematic (PPK) positioning for aerial systems.

- Cost: Is the vehicle within the budget? Is it cost efficient?

Based on the studies of others (e.g. [21] [13]), sensor miniaturization driven by platform miniaturization is a trend in UAV-based mapping. It is possible that the same trend will follow for underwater vehicles, in particular AUVs.
Furthermore, this thesis will here present some hyperspectral push-broom scanners and vehicles as relevant to the conducted work, and then go on to discuss potential developments. Firstly, the underwater vehicles are presented. Figure Section 2.2 illustrate the Underwater Hyperspectral Imager (UHI)-4 and two vehicle platforms that were used for acquiring data.

(a) Front-view of the UHI-4 by Ecotone. The large lens is the HSI, while the smaller lens is an RGB imager.

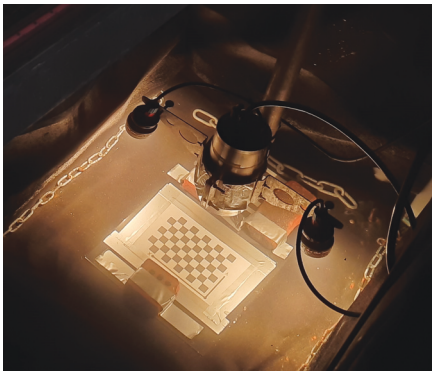

(b) Setup of UHI in a push-broom tank with two halogen light sources.

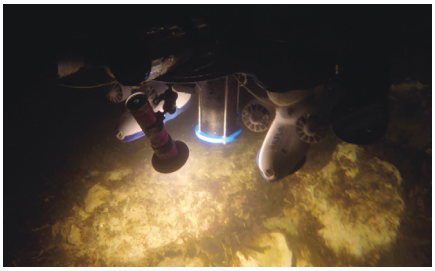

(c) The UHI-4 on a dual mini ROV platform in the polar night in Svalbard. Courtesy to Geir Johnsen for taking the picture. The vehicle is described in C.1 and J.5.

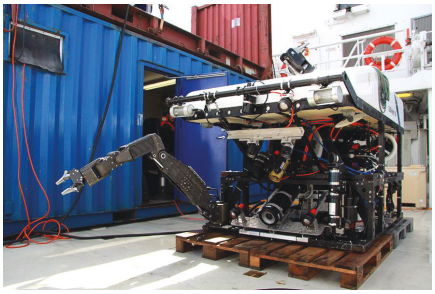

(d) NTNU's light working class ROV 30k onboard RV Gunnerus. Acquired from [48].

Figure 2.1: The UHI-4 by Ecotone and two vehicles used.

The UHI-4 has a total weight of 9 kg (5 kg in water), a cylindrical body with diameter of 135 mm and a length of 355 mm. The imager records light in wavelengths from 380 nm - 750 nm over ≈ 900 spectral channels with a bandwidth of 2.2 nm-5.5 nm. It also records roughly 1920 spatial channels. These are figures from the manufacturer, and they will vary slightly from instrument to instrument. The data is typically binned by a factor 4 spectrally and 2 spatially during data acquisition. Binning effectively means down-sampling. This results in roughly 225 spectral channels and 960 spatial pixels. Increasing binning will increase Signal-to-Noise Ratio (SNR), and the maximal achievable frame rate. The in-water field-of-view is roughly 50° for the UHI.
Relevant aerial vehicles and hyperspectral payloads to this thesis are illustrated in Section 2.2. The HSI-v4 [49] and HSI-v6 [50] are made from commercial-off-the-shelf parts, and they are low-cost and low-weight. This enabled integration of the payload in Figure 2.2(b) from the fixed-wing Minicruiser vehicle in Figure 2.2(d) for mid-range ocean colour mapping in Ny-Ålesund, Svalbard, Norway, 2022. A potential challenge of these instruments for aerial surveys is the small Field-of-View (FoV) (v4: 11° , v6: 8° degrees) when there is no gimbal stabilization. This yields small coverage, and reduced resolution from rotational blur. The Specim AFX 10 solution with a gimbal yields larger and more predictable coverage (FoV≈40) and less rotational motion allowing optimal spatial resolution if frame rate, forward speed and flying height is set suitably. However, the use of a gimbal increases requirements for payload capacity and was not feasible for integration on the Minicruiser.

2.3 Post-processing of data

When the spectral data has been acquired from an area, the overarching goal of hyperspectral imaging in an RS-context is to classify seabed substrates based on their reflective properties. The following list briefly describes this process.

- Establishment of ground truth: It is always beneficial to have ground truth from a surveyed area, particularly for validation of new classification approaches. If the classification approach is sufficiently tested and believed to be robust, the ground truth has less value. In the context of seabed mapping from an underwater vehicle, particularly in deep water, ground truth can be realized through the extraction of physical samples or using high-resolution imagery labeled by a domain expert. By the former approach, we refer to the use/creation of spectral libraries of reflectance in a controlled environment. By the latter we refer to the creation of geographical labels (e.g. shape files), for example using a high resolution orthomosaic or imagery. For underwater hyperspectral imaging, the geographical labeling has been conducted in studies like [29] and the use of high-resolution images for labeling was done in [31] for point spectrometer measurements. The creation of spectral libraries for underwater hyperspectral imaging, was demonstrated with a point spectrometer in [51] and using hyperspectral imagery in a test tank in [52].
- Geometric processing: In order to associate each spectrum in the datacube,

(a) DJI M600 with a Specim AFX10 on a gimbal. Courtesy of Joseph Garrett.

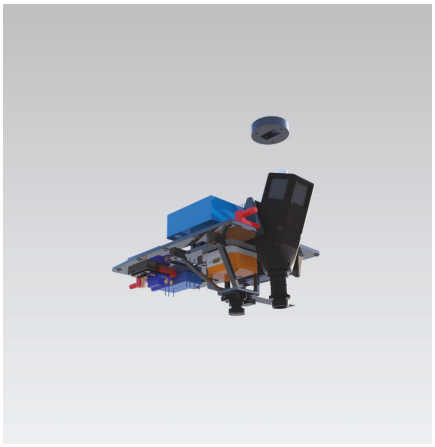

(b) CAD illustration of a micro-payload developed by Oliver Hasler and it integrates an HSI-v4 (160 grams), a downwelling irradiance spectrometer, an IMU, an RGB camera and processing units. Total payload weight is 500 grams. Courtesy of Oliver Hasler.

(c) The UAV is a DJI S1000 equipped with an HSI-v6. Courtesy of Pål Kvaløy.

(d) NTNU UAVlab's Minicruiser. Equipped with the payload in Figure 2.2(b). Courtesy of Oliver Hasler.

Figure 2.2: Hyperspectral sensors and vehicles for UAV-based mapping relevant to this thesis.

$L_{i,j}(k)$ to a geographic point on earth, a process called georeferencing is conducted. When the georeferencing emphasizes consistency against reference data from another sensor, it will in this thesis be referred to as co-registration. These geometric processing operations are key to the thesis and will be described in detail in Chapter 3. Georeferencing yields a spatial coordinate for each spectrum. As such, the full georeference is a 3D point cloud. The point cloud may be used for radiometric processing or it might be rectified and projected onto an orthographic plane to create a raster image. The rectification can be done using some form of re-sampling of the data, such as nearest neighbor interpolation. Lastly, overlapping rasters should be mosaicked to produce a contiguous map. For producing orthomosaics in very rugged terrain, there may be occlusions that should be accounted for. The geometric processing of imagery is fundamentally similar for airborne and underwater acquisition, except how images are effected by refraction, which is a topic discussed in Chapter 3.

- Radiometric processing: For physics-based inversion methods where the RTE is solved properly, the classification, water depth and IOPs are typically estimated simultaneously. In this thesis we used a physics-based empirical inversion model for estimating water depths from UAV imagery in Section J.3. In Section J.4 we developed an SA model for underwater hyperspectral imaging with active light sources and demonstrated estimation of the IOPs using overlapping imagery. Such a SA model in combination with IOPs and accurate close-range geometry from georeferencing allows for low ambiguity in classification, since only the bottom substrate needs to be estimated. The physical principles governing the RTE are the same for airborne imaging and underwater imaging, but the boundary conditions are not. In particular, there is a significant difference between the laterally homogeneous sunlight and an artificial point source as used in airborne and underwater imaging, respectively. On the other hand, airborne imaging is faced with a variety of effects occurring at the air-water boundary due to the change in the refractive index. The changes in boundary conditions means that the approximate solutions to the RTE take different shapes. This is described in Chapter 4, with a particular emphasis on the underwater hyperspectral imaging case.

- Classification: A spectral library could be used for SA or LUT inversion schemes for determining classes of substrates. If an invertible SA forward model f is used, relating bottom reflectance ρ_b, and measured radiance L is possible. Then, $L = f(\rho_b)$, and it is possible to compute $\rho_b = f^{-1}(L_m)$ if IOPs and geometry is known. A more common approach in underwater hyperspectral classification has been supervised SVM [31], [29], [53] using labeled measurements to train a classifier. This has been shown to be a robust classifier that seems robust to some of the variations in spectra due to the water column and illumination. So far, to the author's knowledge, no classification approaches for hyperspectral mapping from underwater imagers has used spectral libraries for physics-based inversion-classification. In the airborne shallow water RS community, several hyperspectral inversion-based classifiers (e.g. [33], [54]) have been developed that simultaneously estimates

IOPs, substrate classes and water depth. For underwater hyperspectral imaging, it seems useful to adapt such methods for classification. An interesting idea is to incorporate known information (e.g. geometry, or measured water properties) to improve the solution to the inversion as done in [54].

For convenience, the whole process is illustrated in Section 2.3 for underwater hyperspectral imaging and is based on materials from the cooperative papers [34] and [29]. One of the main contributions of this thesis lies in the geometric steps leading from Figure 2.3(a) to Figure 2.3(b), called the georeferencing. To do so, the thesis suggests the use of photogrammetry and coregistration with a concurrent RGB frame camera for accurate alignment of the hyperspectral imagery. This was performed in J.1 for UHI and in J.3 for shallow-water hyperspectral imaging. This in turn, yields geometric information that can help solve the RTE. The use of this geometry in solving the RTE in underwater hyperspectral imaging, is another key contribution of the in J.4. In shallow-water, geometry from photogrammetry could also help solving the RTE. However, there seems to also be synergy the other way around for bathymetry estimation. As shown in [55], aerial photogrammetry in shallow-water struggles with bathymetry estimation in texture-less sandy areas where spectral inversion is well suited. As such, another key contribution contribution of the thesis is the demonstration of concurrent and coregistred photogrammetry-based and inversion-based bathymetry estimation in J.3.

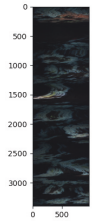

(a) A radiance datacube, visualized as an RGB composite. Row is the frame number i while column is the pixel number j.

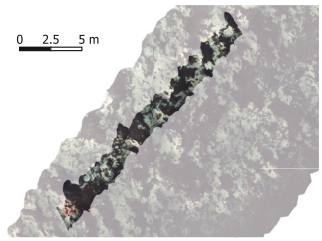

(b) The georeferenced datacube.

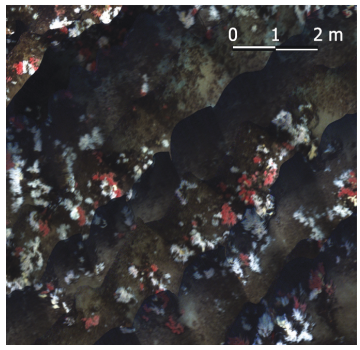

(c) Several overlapping georeferenced datacubes before radiometric correction.

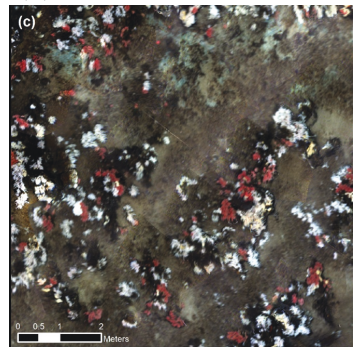

(d) Data after reflectance conversion and overlap handling.

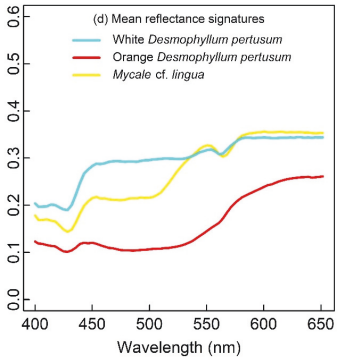

(e) Mean reflectance ρ spectra from three labeled classes. Based on 800 spectral pixel of each species.

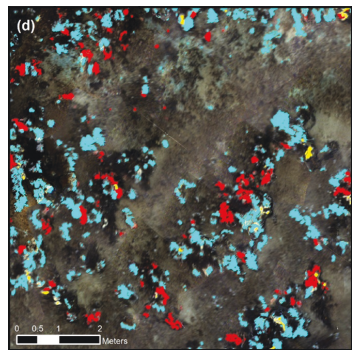

(f) Data classified into the colors corresponding to classes from Figure 2.3(e) using SVM.

Figure 2.3: Processing steps from a radiance datacube to a classified map. Note that cropping was done manually so the geographic windows are slightly approximate. Images here are all 3-channel, or pseudo RGB representations, but each pixel has an associated contiguous spectrum.

Chapter 3

Geometry

The geometry dealt with in this thesis are geometrical aspects as relevant to vehicle-based mapping of the seabed with hyperspectral push-broom imagers and RGB frame cameras. To give a description of relevant methods, we included the following topics:

- Navigation: First give a general description of some typical navigation sensors onboard a UAV and Unmanned Underwater Vehicle (UUV). This section describes how briefly how sensor measurements can be combined.

- Photogrammetry: In this thesis, photogrammetry serves to aid the georeferencing of hyperspectral imagery with self-consistent terrain/camera geometry, but it also has an inherent value in itself, e.g. for bathymetry estimation. The section focuses on geometrical aspects that are specific to through-water and underwater photogrammetry.

- Georeferencing: This section gives a description of how to conduct georeferencing of hyperspectral images when the HSI/seabed geometries are known. The steps explained here are ray tracing, orthorectification and accuracy evaluation.

- Co-registration: This section describes ways of making the georeferencing of hyperspectral imagery consistent with photogrammetry. It describes correlation-based and feature-based co-registration for concurrent RGB/HSI imagers in a fixed configuration. In addition, an example of non-concurrent co-registration is given.

The governing geometrical principles of airborne and underwater hyperspectral imaging are the same. The navigation sensors, vehicle motion characteristics and photogrammetry practices are different, however, the solutions should be different.

3.1 Navigation

3.1.1 Navigation sensors

The following list describes a non-exhaustive overview of common sensors for aerial and underwater navigation.

- IMU (both): We split this into measurements of body-fixed accelerations from an accelerometer and body-fixed rotation rates from a gyroscope. The measurements have slowly varying biases that are typically estimated in an aided Inertial Navigation System (INS). This means that some aiding measurement allows a navigation filter to observe/estimate the slowly varying biases. For a simple case, think of a vehicle only changing its true heading (yaw) by $\delta\psi_t$ during a time δt. Assume that the integral of the IMU yaw-rate gave $\delta\psi_m = \delta\psi_t + \delta_t b_\psi$ if the bias was assumed constant during the motion. This is not exactly how a navigation filter works, but it shows how a heading sensor could "aid" in figuring out the bias of the IMU. For example, pure integration of low-cost IMU measurements was shown in [56] to give a one-minute positional drift of over 150 m, while aiding from a magnetometer bounded it to 5 m. IMUs can be aided by just about any sensor, even frame cameras [57], resulting in dead-reckoning estimates or true global positions if a GNSS is available. IMUs are mounted on all UUVs and UAVs and typically define the body-axes of a vehicle.
- GNSS (airborne): For UAV-based mapping today, vehicle GNSS and GNSS-measured landmarks, i.e. Ground Control Point (GCP)s, is common-practice. It relies on multi-satellite observations of EMR with wavelengths around 20 cm. In a standalone GNSS solution, GNSS satellites send their clock time and orbit information, allowing the on-the-ground receiver to calculate it's position with an accuracy ≈3 m [6]. Other more accurate GNSS solutions are differential GNSS ($\approx 1m$) and PPK and RTK solutions ($cm - dm$) which require a reference station of known exact position nearby. Today, PPK and RTK positioning is becoming more and more available for small UAVs, and software solutions for open-source processing is available, e.g. RTKlib [58]. Studies such as [59] are showing that photogrammetric mapping with position references from PPK can produce equally accurate results as the conventional GCPs. PPK is important in the case of shallow-water photogrammetry as shown in [17], where underwater GCPs are infeasible. All aerial platforms carry a GNSS (or several) today, but this is not the case for UUVs. Proper AUVs have GNSS antennas so that they can record positions in the surface for navigation and safety of operation. However, once a vehicle dives, it relies on either dead-reckoning or an APOS. APOS gives relative positions and is therefore often coupled with GNSS for global position.
- APOS (underwater): Acoustic positioning for underwater navigation are position estimates that use Time-of-Flight (ToF) between acoustic transducers with known global location and a vehicle-fixed transponder for ranging the submerged vehicle. Bearing and elevation angles are derived by having transducers that that are displaced and looking at either the difference in ToF or

phase differences. The polar measurement (range, bearing, elevation) yields a relative position that in conjunction with GNSS gives a global position.

- Barometer/depth sensor (airborne/underwater): A barometer can give heights for an aerial vehicle, while a depth sensor yields orthometric depths below the water surface. It should be noted that water depth can be related to global ellipsoid heights using the water's tide level and the geoid model describing the mean sea level. For surveys over a certain duration, tide contributions are essential for having a consistent vertical reference.
- Magnetometer (both): Magnetometers make use of earth's magnetic field and aids an INS by providing a body-fixed vectorial measurement of the magnetic field. Assuming that a magnetometer is calibrated to give the direction to magnetic north, and the accelerometer can resolve the gravitational vector, the true heading and attitude can be found by using a global magnetic model. It is important for vehicle-based navigation to be aware that the vehicle will cause disturbances in the magnetic field. If these are sufficiently constant, they may be calibrated as biases in the body-frame. The magnetometer plays an important role in providing true heading during dead reckoning for underwater vehicles.
- Doppler Velocity Log (underwater): A Doppler Velocity Log (DVL) is a common sensor for dead-reckoning underwater, particularly close to the seafloor. The sensor records 4 beams, and yields the body-fixed velocity with respect to the seafloor. For dead reckoning underwater, an INS will typically be aided by DVL, a magnetometer and a depth sensor, e.g. [60]. The DVL also measures 4 distances along the beams resulting in measurements of local bathymetry. These are important in underwater imaging because they allow for observing, controlling and planning the vehicle's height above the seafloor, e.g. [61].
- Terrain and feature-based navigation approaches (both): If there is a known georeferenced map, single observations such as a frame image can provide a full pose with $n > 2$ features matched in the map/image. In its simplest form, the special case of $n = 3$ is called the perspective-3-point-problem [62]. Another form of map-based navigation underwater is bathymetry aided, where seafloor elevation observations from one acoustic beam (or multiple) are matched against a reference map to infer position [63]. If there is not a known map, feature-based techniques can still be used on overlapping observations, for example consecutive images [57] or overlapping MBES transects [64]. This is called Simultaneous Localization and Mapping (SLAM) since the 3D map and the poses are adjusted in tandem with new observations. One such image-based approach commonly used in post-processing is SfM photogrammetry where the pose adjustment, i.e. navigation, is the first step. Acoustic localization techniques are used in the underwater domain while camera-based techniques can be used for both. It is important to note that the quality of the navigation estimates from SfM photogrammetry depend on the quality of the reference points. These are either camera poses (particularly position) or GCPs. In aerial photogrammetry of terrestrial scenes, the use of high-accuracy GNSS positions or GCPs enable accuracy in the order of centimeters, which is quite incredible for flying heights of several hundred

meters. From underwater vehicles it is hard to achieve absolute accuracy in photogrammetric models, as illustrated in [65]. The dominating errors are horizontal translations and scale errors in the model.

3.1.2 Combining sensor data

Navigation data is important for accurate georeferencing of frame camera imagery and HSI imagery. Unless ground control points are available, photogrammetry relies on accurate positions. The arguably most used form of combining navigation sensors for inferring position/orientations are Kalman filters. In J.1 we used Kalman-filtered poses from the ROV control system as input for the SfM photogrammetry software. The poses after image-based SfM alignment are shown in Figure 3.2. In this case, the frame camera is running at a sufficiently high frame rate (5 Hz) to capture the vehicle motion fairly well, since the vehicle dynamics are slow. Therefore, constant-velocity interpolation is adequate for computing the poses of the higher frequency hyperspectral images (50 Hz). Linear interpolation for position is equivalent to constant velocity, while Spherical Linear Interpolation (SLERP) for quaternion orientation is equivalent to constant rotational velocity.
When working with aerial hyperspectral images from the UAV in J.3 without a gimbal, we had a frame camera running at 0.5 Hz that was used for SfM-based alignment. However, SfM-based poses were not sufficient for capturing the rotational motion as shown by the middle panel in Figure 3.1. Therefore, we adapted an Error-state Kalman Filter (ESKF) to fuse the SfM-based poses with IMU data and GNSS velocity. Since we were doing post-processing, we ran the filter forwards and backwards and combined the two estimates using Kalman smoothing. This gave poses that could be used for georeferencing of the hyperspectral imagery.

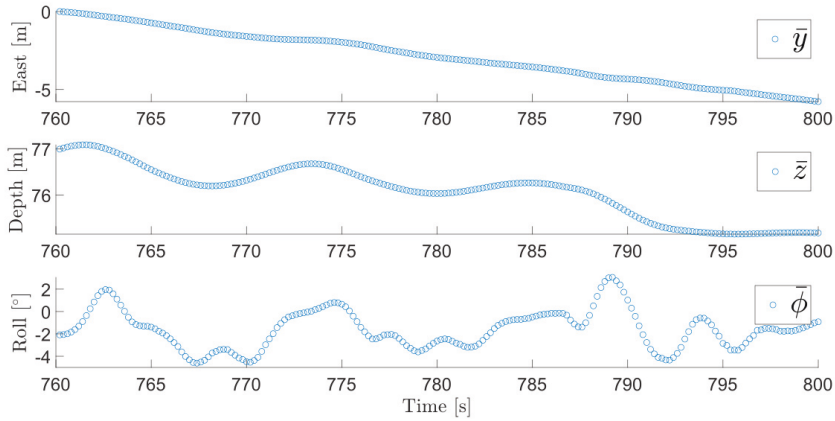

Figure 3.2: Photogrammetry-derived poses from Tautra experiment J.1 over a 40 s period. The frame camera ran at 5 Hz and the figure shows East position, depth and roll angle denoted $\bar{y}, \bar{z}, \bar{\phi}$, respectively. It seems that roll motion is more high-frequent than the linear motions. Our approach in Section J.1 simply performed interpolation to estimate poses for the hyperspectral frames at 50 Hz.

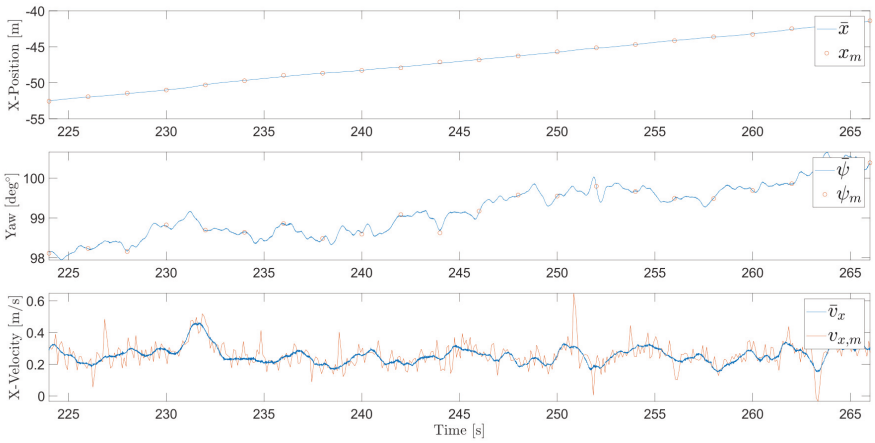

Figure 3.1: The ESKF estimates of X-position, true heading and X-velocity for a copter UAV in blue and measurements in orange. The INS is driven by an ADIS16490 IMU and aided by GNSS-velocity and photogrammetry-poses. Since processing was conducted in post, the filter was run two-ways with uncertainty weighting, so-called Kalman Smoothing [66]. The blue $\bar{x}, \bar{\psi}, \bar{v}_x$ are the 250 Hz Kalman smoothed estimates, while x_m, ψ_m are SfM pose components and $v_{x,m}$ were GNSS-velocities. Note that outliers were rejected prior to sensor fusion.

3.2 Photogrammetry

A frame camera represents something in-between a position/orientation sensor and a dead-reckoning sensor. In this thesis it has the role of providing consistent motion (poses) for the frame camera and 3D modeling of the seafloor. This could have an intrinsic value, for example in the prediction of bathymetry in J.2. The other use of photogrammetry in this thesis is to compute the seafloor model and the motion of the frame camera for georeferencing the hyperspectral imagery, as was done in J.1 and J.2. It is important to note that the photogrammetry is only as good as the navigation, meaning that high quality navigation data should be used as input to the photogrammetry software. In the case of aerial photogrammetry, highly accurate, visual GCPs can also be used.

If sufficient features, meaning patterns in photometric texture, are detected and matched across multiple images, it is possible to simultaneously estimate the 3D location of features (structure) and the relative orientations and translations between images (motion). This step is called SfM and it is integrated in modern photogrammetry software such as Agisoft, Pix4D, OpenDroneMap, etc. SfM does not provide scaled positions or 3D structure, or absolute orientations in itself. However, providing either GCPs or position measurements for the camera, SfM-based alignment results in georeferenced camera poses and 3D structure. In certain cases, self-calibration of the intrinsic camera parameters is included as part of the alignment.

The second step of typical photogrammetry tools is MVS that uses the SfM-aligned

camera geometries for estimating a dense 3D model of the scene. In this thesis we used a software that employed the dense image matching technique by [67]. This semi-global matching algorithm enables efficient pixel-wise matching in MVS. The method performs pixel-wise stereo matching between between a reference image and a match image using the notion of epipolar geometry. The result of the matching, the disparity map (related to depth map) is found by maximizing pixel similarity under a smoothness constraint. Such pairwise matching of the reference image is done against multiple match images, and merged into a total depth map for the reference image whilst accounting for outliers. When this process has been conducted and all images have played the role as the reference image, the depth maps are fused as described in [68] in the software. The result is a dense point cloud which can be further processed to a mesh, a DEM, and an orthomosaics downstream in the photogrammetry pipeline. As will be shown later, the photogrammetric data products and camera geometries can be used in a variety of ways in both georeferencing and co-registration for hyperspectral imagery.

3.2.1 Photogrammetry in/through water

Now that the general steps for photogrammetric processing have been described, it is possible to specify the main challenges of photogrammetry in and through water which is done in the following list.

- Specular reflection (airborne): Airborne imaging is faced with Fresnel reflected, specular sunlight off the sea surface. This may saturate the image sensor and inhibit the pixels to detect seabed signal as illustrated in [55].
- Forward scattered light (both): Oceanic scattering is highly peaked towards small-angle forward scattering [69], causing blur. It can be understood as an increase in the pixel's footprint size on the seafloor. The effect of forward scattering on underwater images is sometimes modeled using a Point Spread Function (PSF) ([70],[71]). The forward scatter problem is similar in nature for deep-water and aerial imagery.
- Backscatter (both): Backscatter is the integral of light that is scattered back into the image without reaching the bottom. This yields additive light to the bottom signal. Backscatter is definitely a challenge for both the underwater and aerial case. For artificially lit underwater imaging, backscatter depends on the placement and beam patterns of light sources relative to the camera as was described in J.4. For aerial imaging, the backscatter will be different for near-nadir rays and slanted rays.
- Attenuation (both): The light that is absorbed and some of the light that is scattered effectively disappears, or attenuates in a diffuse manner. A good SA model for describing this in the shallow-water case is given in [15]. The bottom reflectance signal decays exponentially, while the backscattered signal grows and converges to a deep-water signal. As such, the total signal approaches the deep-water signal, or for us humans, the colour of the deep ocean.
- Light sources (underwater): In underwater imaging, even illumination is challenging due to light's beam patterns, varying heights above the seafloor and

so on. For an underwater vehicle with artificial lighting there is an additional weakening of the bottom signal from the $1/r^2$ law of irradiance.

- Substrates (both): Low-texture substrates like sand or dark kelp forests are poorly suited for image matching [55], [16]. Additionally, the low albedo of e.g. kelp substrates will further weaken matching. Further, moving substrates or transparent/specular substrates will challenge the underlying assumptions in photogrammetry, namely that objects look the same from different angles.
- Refraction (both): For shallow-water aerial imaging refraction occurs at the interface between water and air. A non-planar water surface, often called waves in the sea, make the geometry dynamic and unpredictable which could resulting in phenomena like caustics, blur and distortions. In the underwater imaging case, refraction occurs first at the water-glass interface, then at the glass-air interface of the underwater housing. Unlike the other effects above, refraction yields systematic geometric errors if not properly accounted for. Therefore, this topic is elaborated in more detail in Section 3.2.2.

Some of the listed effects are illustrated in Figure 3.3.

3.2.2 Refraction

Any form of photogrammetry through water can be considered two-media photogrammetry. An underwater camera is often mounted in a depth proof underwater-housing and images are taken through either a flat camera port or a dome. With a perfectly machined and configured dome, for which camera rays are perpendicular to the glass, refraction will not bend camera rays. In this thesis, the flat glass port is considered. For a flat port the rays will be refracted (change direction) both at the water-glass and glass-air interface according to Snell's law. Analogously for air-borne mapping, camera-rays will refract at the water surface. Although refraction is a spectral property, the refraction index is within the range of $n_w = 1.33 - 1.37$ in natural oceanic waters for relevant wavelengths [72]. However, a common bulk value for RGB images in seawater is $n_w = 1.34$ [73].

3.2.3 Underwater photogrammetry

According to [74], the refraction effect can be be compensated for by means of radial distortion in underwater photogrammetry. As a result, the arguably most common approach to SfM photogrammetry underwater is to calibrate the sensor with a regular camera model and to compensate for refraction using radial distortion. Also, commercial SfM software don't support refraction-based SfM and MVS although it has been implemented in research [75], [76]. Moreover, in this thesis the refraction compensation is done using the radial distortion approach. Without proof, it can be deduced that this solution should work equally well for a line camera (e.g. the HSI) where all rays are within the same plane of refraction. It is worth noting that compensation through radial distortion will give different calibrations depending on the proportions of the camera ray path in air and in water (and glass). This argues for calibrating a camera+underwater housing at approximately the same camera-object distances as those used in photogrammetric

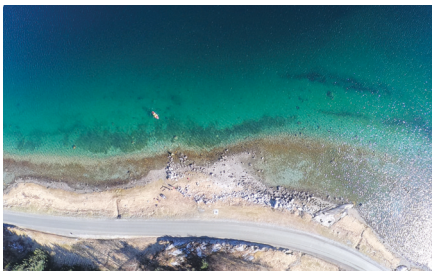

(a) Zoom-in of a GoPro image from a UAV, from the experiment in [36]. Flickering sunglint is seen, caustics on the seafloor, and generally reduced visibility towards deeper water.

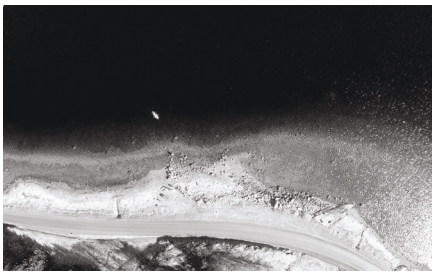

(b) The same image, just the red channel. Strong absorption compared to scattering means that the red band yields dark values for deeper water.

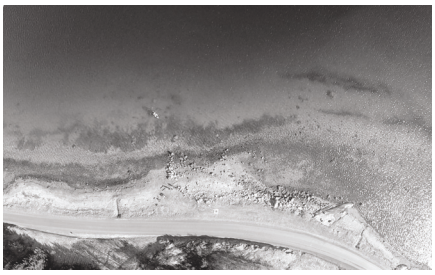

(c) Green channel. The channel has less absorption than red, and less backscatter than blue i.e. better visibility.

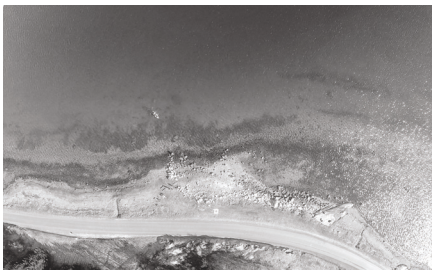

(d) Blue channel. Arguably has more "haze" additive light than the green channel.

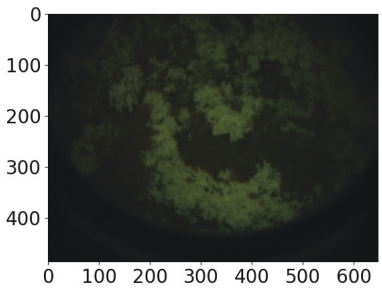

(e) An unprocessed image of cold-water corals from the RGB camera within the UHI-4. The signal clearly weakens out from the center of the image. The image was copied from [34].

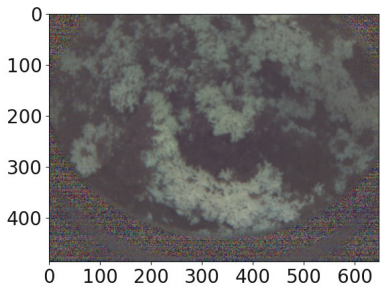

(f) The image after a statistical gray-world colour correction using a high number of images. In terms of Scale-Invariant Feature Transform (SIFT)-feature matching with the next image in the sequence, the unprocessed image yields 22 valid matches while the corrected yields 151 matched features.

Figure 3.3: Some of the effects facing photogrammetry in and through water. An understanding of the underlying radiometry is key.

mapping. It also argues for placing the camera as close as possible to the glass port. The air/water proportions decide how much epipolar lines bend into epipo-

lar curves [77]. This is not that significant for a camera very close to a flat port $d_a << d_w$ in underwater photogrammetry, where d_a and d_w are the distance in air and water. Airborne through-water photogrammetry represents the diagonally opposite where $d_a >> d_w$ and it will be described in Section 3.2.4 how this affects bathymetry estimation.
For evaluating the importance of refractive calibration for the frame camera, two camera calibrations were tested on a subset of the checkerboard-images from J.1. First, a proper refractive calibration procedure of [78], where an in-air calibration of the frame camera first yielded a camera model. Then, an in-water calibration determined the relative orientation of the glass port and the port-focal point distance in a nonlinear refinement. The result was a 0.023° tilt angle and a 7.74 mm in-air distance. The refraction-corrected approach gave a 0.34 pixel reprojection error in water and 0.16 pixels for the in-air calibration. Secondly, a regular camera model was computed using only in-water points and radial distortion compensation. The mean pixel error of the regular camera optimization was 0.24 pixels for in-water points. The in-water comparisons above were made for the same 30 checkerboard images at distances 0.2-0.5 m. Although this may result from effects of calibration errors from e.g. the glass, these results arguably justify the use of the radial distortion approach. Notably the camera tested here is the same RGB camera used in the experiment in J.1 and J.4. An example illustrating the refraction-correction approach is shown in Figure 3.4(a), while the radial distortion approach is shown in Figure 3.4(b).

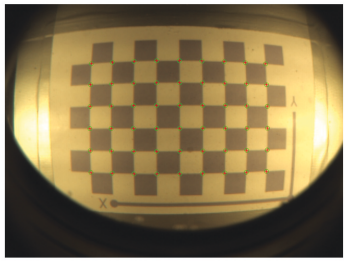

(a) Camera calibration accounting for refraction according to [78].

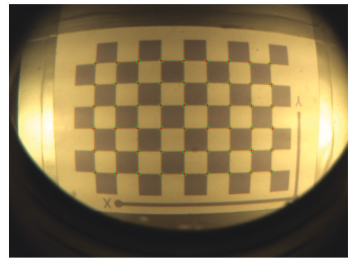

(b) Camera calibration following a standard pinhole calibration model with radial and tangential distortion.

Figure 3.4: The rim of the UHI-4 housing is seen. The green points are detected corners, while the red crosses are predicted locations by the refractive model.

3.2.4 Aerial through-water photogrammetry

This thesis will not look into the SfM, or alignment step of shallow-water photogrammetry, but instead assume that terrestrial points are visible, or that the vehicle is sufficiently close to shore. In fact, in-water points were removed for the SfM alignment step in J.3. Studies like [17] highlighted the importance of PPK accuracy for open-water SfM alignment, while [16] skipped SfM in open-water areas and exploited high-accuracy navigation estimates directly.

MVS makes it possible to reconstruct dense models of the seafloor using images taken from different views. Applying MVS to airborne images of submerged terrain leads to a systematic underestimation of the depth. The water depths estimated by conventional MVS are referred to as apparent water depths, because it is how deep the water appears to be. For the special case of close-to-nadir imagery, the apparent water depths h_a can be converted to true depths by the approximation $h = h_a n_w$ [79] where n_w is the water's index of refraction. For this assumption, there are also no horizontal corrections.

Near-nadir refraction

Assume there are two cameras at equal height, z_a above the sea surface, assumed to be a tangent plane to the instantaneous ellipsoid. Assume further that images are rectified with z axes aligned with the vertical, and x axes in the direction of the baseline, B (from camera 1 to image 2). The following equation describes normalized pixel correspondence between an image coordinate in camera 1 and an image coordinate in camera 2:

$$z_a \begin{bmatrix} \bar{x}_1 \\ \bar{y}_1 \\ 1 \end{bmatrix} + z_w \begin{bmatrix} \bar{x}_1 C(n,\theta_1) \\ \bar{y}_1 C(n,\theta_1) \\ 1 \end{bmatrix} = z_a \begin{bmatrix} \bar{x}_2 \\ \bar{y}_2 \\ 1 \end{bmatrix} + z_w \begin{bmatrix} \bar{x}_2 C(n,\theta_2) \\ \bar{y}_2 C(n,\theta_2) \\ 1 \end{bmatrix} + \begin{bmatrix} B \\ 0 \\ 0 \end{bmatrix}. \tag{3.1}$$

Where z_w is the depth of the water, $\bar{x}, \bar{y}$ are normalized image plane coordinates in the two images, θ signifies the nadir angle and B the baseline. The corrections, $C(n,\theta_1), C(n,\theta_2)$ describe the transformations that happen because of Snell's law:

$$C(n,\theta) = \frac{1}{n} \frac{\sqrt{1 - sin(\theta)^2}}{\sqrt{1 - (sin(\theta)/n)^2}} \tag{3.2}$$

Where $n = n_w/n_a$. The expression in (3.2) reduces to $1/n$ for small θ. For 10 degrees off-nadir it is for instance $0.994(1/n)$. To see (3.1) in the context of stereo matching, the software will search for correspondences along a straight epipolar line $\bar{x}_2 = \bar{x}_1 + d$ and $\bar{y}_1 = \bar{y}_2$ where d is normalized disparity. When both θ_1 and θ_2 are small, it is seen that $C(n,\theta_1) = C(n,\theta_2) \approx 1/n$. This results in

$$\bar{y}_2 = \bar{y}_1 \frac{z_a + z_w C(n,\theta_1)}{z_a + z_w C(n,\theta_2)} \approx \bar{y}_1 \tag{3.3}$$

$$z^*(\bar{x}_1) = \frac{z_a + z_w C(n,\theta_2)}{1 - \frac{z_w \bar{x}_1}{B}(C(n,\theta_1) - C(n,\theta_2))} \approx z_a + z_w C(n,\theta_2) \tag{3.4}$$

$$\approx z_a + z_w \frac{1}{n_w}. \tag{3.5}$$

Where the estimated depth from stereo matching (not water depth) is $z^* = B/(\bar{x}_1 - \bar{x}_2)$ that can be expressed as a function of $\bar{x}_1$ or $\bar{x}_2$. As such, the apparent water depth $h_a = z^* - z_a = z_w C(n,\theta_2)$. Recalling the small angle approximation $C(n,\theta_2) = 1/n$, and renaming actual water depth from z_w to h, we get $h = h_a n_w$ by assuming $n_a = 1$. It was also showed in (3.3) that there will be no horizontal errors in this case. Generalizing (3.3) and (3.5) to multiple images needs no

explanation since the equations are independent of view geometry. So matching image 1 against some image 3 at the same altitude would yield the same depth and no horizontal error. Note that the formulation also is independent of rectification. The description above is in agreement with the approximation in [79]. The assumption of small nadir angles is the most predictable approach in correcting MVS bathymetry. Another important aspect about the near-nadir realm is that georeferencing close-to-nadir images onto an apparent bathymetric surface will yield approximately correct horizontal coordinates coordinates. Or the same coordinates as georeferencing that accounts for refraction onto a true bathymetric surface. As such, it is possible to create horizontally accurate orthomosaics without refraction-induced errors (aside from waves). The disadvantage of near-nadir images are that they have small baselines, or decreasing the ability to resolve depth in stereo matching.

Off-nadir refraction

As pointed out by Dietrich [73], for off-nadir imagery, the correction of the apparent depth depends on the multi-view geometry. More specifically, it depends on the nadir-angles of observing cameras. He suggests computing the total correction factor h/h_a for a point as the average of $1/C(n, \theta_i)$ over all indices i of observing cameras. This is the approach that we used in J.3 for correcting the bathymetry from MVS. In [16] they conduct MVS using 5 subsequent images, and performs a similar correction approach as Dietrich [73], but include estimation of horizontal corrections. In [16] they also compare MVS to regular stereo matching and conclude that MVS yields inherent outlier detection and more accurate bathymetry than regular binocular stereo. The advantage of regular stereo is that the refraction correction is more accurate.
For illustrative purposes, Figure 3.5 shows the view-dependency of correction factors, and a comparison of apparent depths with acoustically measured true depths in Figure 3.6. The data is from J.2.

3.3 Georeferencing

Referencing or registering of hyperspectral images is essentially the assignment of spatial coordinates in a Coordinate Reference System (CRS) to each spectrum. In this thesis it is assumed, as is common for photogrammetry, that one spatial measurement, a spectrum for the HSI, can be defined by a single ray. In principle a ray is a direction describing photon travel in reverse. By finding out where the ray intersects with a surface, the origin of the measured photons on the surface is found. If the surface is the seabed, the spectrum has been referenced or registered to the seabed. Using a global CRS, it can be described as georeferencing or georegistration. It is also reasonable to reference spectra to a vehicle-fixed CRS, as described in J.4 for descriptions of radiative transfer. The methods described in this thesis could enable such modeling since it provides the close-range geometry. The end product of georeferencing is an typically orthomosaic of hyperspectral texture, sometimes called an orthorectified datacube. The advantages of properly georeferenced hyperspectral data includes minimal shape distortions in the recti-

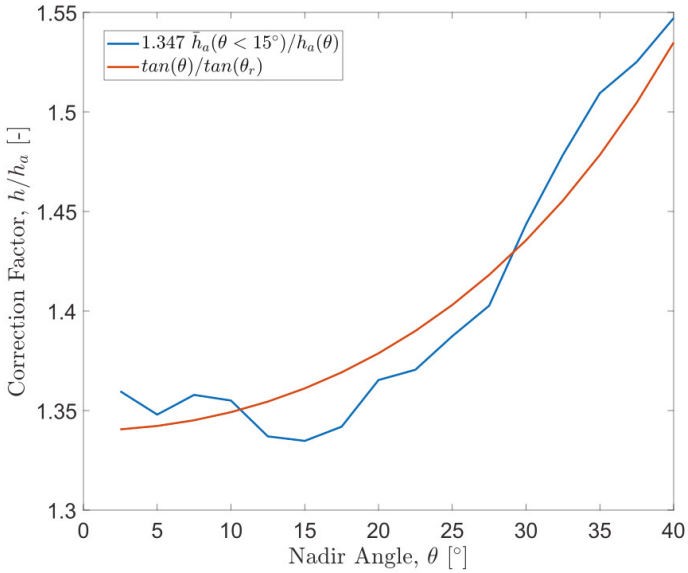

Figure 3.5: Apparent water depth as function of angle. The blue graph is really a ratio of apparent depths near-nadir ($\theta < 15°$) to apparent depths at angles 0°-40°. Multiplying the ratio by a guesstimated near-nadir correction factor of $1.347 \approx n_w$ yields an estimate of correction factors. Comparatively, the relation by Dietrich [73] or $1/C(n, \theta)$ for $n = 1.34$ is shown. The blue graph was drawn based on 1338 points at various depths with 10-100 camera observations per point. The depth value of an observation was extracted by using depth images from the dense image matching step in Agisoft Metashape V 1.6. The data illustrates the significance of view-dependent corrections.

fied datacube and agreement with high-resolution RGB photomosaic. This eases the process of labeling ground truth and better allows for object-based classification of hyperspectral data that exploits shape. The principles and advantages to proper georeferencing are similar for the airborne case and the underwater case, although relative ruggedness probably poses a greater challenge in certain underwater cases.

3.3.1 Ray tracing

The principle for georeferencing of hyperspectral imagery in this work is backwards projection, or ray tracing, from a pixel number u at a timestamp t_j to a seabed point or intersection, $\boldsymbol{p}^e_{sb}$. Conducting the entire process for all measurements yields a 3D point cloud, for example visualized in Figure 3.8 as a pseudo RGB composite point cloud with a photogrammetric mesh model of the seafloor. This example is from the underwater hyperspectral imaging experiment of a deep-water coral reef in J.1. The mesh is, as previously mentioned, an output of the photogrammetry pipeline. In the shallow-water case, it would be the refraction corrected mesh.
To begin with, the rays of the line camera will be described. Here, it is important to make a distinction between the underwater camera model and the airborne camera

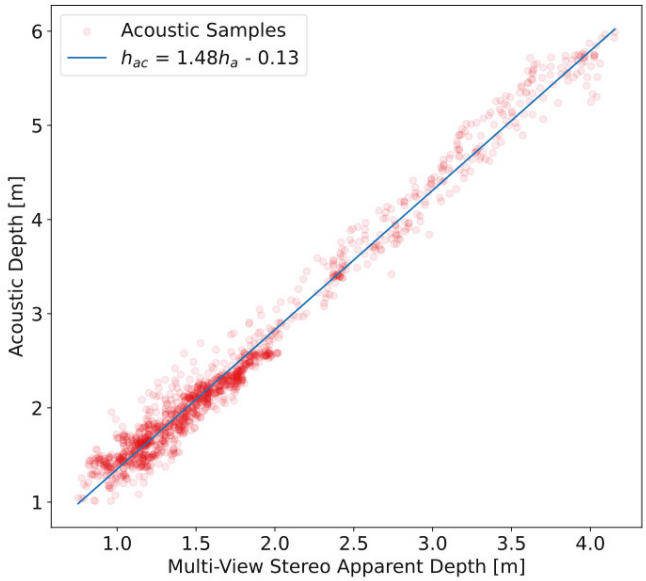

Figure 3.6: Apparent depth h_a on x-axis and acoustic depth h_{ac} on y-axis. The blue line indicates a least squares regression line. There is uncertainty in the regression, but it seems that around 1.48 is a good correction factor. As such, the small-angle approximation with a correction factor of e.g. $n_w = 1.34$ would underestimate the true depth by 9%.

model. They both employ the same camera model, but in the underwater case we let the radial distortion compensate for the refraction as described previously for underwater photogrammetry. In contrast to the photogrammetry, using a refractive model would not add any significant complexity to the ray tracing of hyperspectral measurements. It would also be easy to estimate the necessary parameters of a refractive model using the approach of e.g. [78] as was implemented for the RGB camera.
Moreover, the line camera model used for HSIs in this thesis was adopted from [80], and it can be expressed as

$$u_h = c_{x,h} + \Delta u_h + f_h \bar{x}_h \tag{3.6a}$$
$$\Delta u^h = k_1(u^h - c_x^h)^5 + k_2(u^h - c_x^h)^3 + k_3(u^h - c_x^h)^2 \tag{3.6b}$$
$$\bar{x}_h = (u_h - c_{x,h} - \Delta u_h)/f_h \tag{3.6c}$$
$$\bar{y}_h = 0 \tag{3.6d}$$
$$\hat{\boldsymbol{d}}_h^h = [\bar{x}_h, \bar{y}_h\ , 1]^\top. \tag{3.6e}$$

Where subscript h means hyperspectral, while c_x is the principal point, k_1, k_2 are radial distortion coefficients, while k_3 is a tangential distortion coefficient. (3.6) yields a mapping from a pixel number to a normalized direction vector $\hat{\boldsymbol{d}}_h^h$ in a

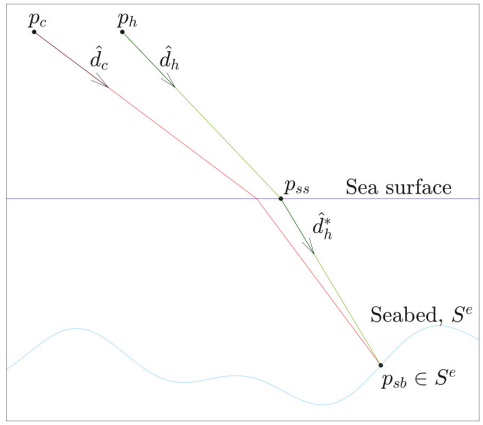

Figure 3.7: The basic principles for georeferencing of a single ray in shallow water. In the case of hyperspectral georeferencing the ray tracing occurs along the green line. The secondary problem, dealt with in J.3 is finding the corresponding pixel direction $\hat{\boldsymbol{d}}_c$ (and pixels u_c, v_c) for an RGB camera at $\boldsymbol{p}_c$.

local frame. The transformation of this direction to some global Euclidean space is entirely decided by the rotation of the HSI at t_j. The global CRS is denoted by superscript e for Earth-Centered Earth Fixed (ECEF). The following equations and Figure 3.7 simply describe ray tracing for shallow-water mapping:

$$\boldsymbol{p}_{ss}^e = \boldsymbol{p}_h^e + \boldsymbol{p}_{ss/h}^e = \boldsymbol{p}_h^e + s_1 \hat{\boldsymbol{d}}_h^e \tag{3.7a}$$

$$\boldsymbol{p}_{sb}^e = \boldsymbol{p}_{ss}^e + s_2 \hat{\boldsymbol{d}}_h^{*e}. \tag{3.7b}$$

Where $\boldsymbol{p}_h^e$ is the global position of the hyperspectral imager at time t_j while $\hat{\boldsymbol{d}}_h^e = \boldsymbol{R}\hat{\boldsymbol{d}}_h^h$, where $\boldsymbol{R}$ is the rotation matrix of the hyperspectral imager. s_1, s_2 are ray scale parameters that describe the intersections with the sea surface and seabed, respectively. $\boldsymbol{p}_{ss}^e, \boldsymbol{p}_{sb}^e$ are intersections with the water surface and seabed, respectively. $\boldsymbol{p}_{ss/h}^e$ is the vector from the hyperspectral imager to the sea surface. Lastly, $\hat{\boldsymbol{d}}_h^{*e}$ is the direction of the ray after refraction with the water surface, which is predictable if ignoring waves. The mathematics is described in detail for the shallow-water case in J.3. Note that the ray tracing, or georeferencing is simplified for the underwater case to

$$\boldsymbol{p}_{sb}^e = \boldsymbol{p}_h^e + s_1 \hat{\boldsymbol{d}}_h^e. \tag{3.8a}$$

Where $\hat{\boldsymbol{d}}_h^e$ is used to describe HSI ray directions because the refraction compensation is implicit in the line camera model in (3.6). In order to find the intersections of the ray tracing, a seabed surface model, $\boldsymbol{S}$ must be supplied, and in this thesis triangular meshes are used. Although there exists multiple tools for intersecting lines and meshes, the Python library Pyvista [81] was used in this work. A subfunction of PyVista for fast ray tracing is called multi_ray_trace and uses the

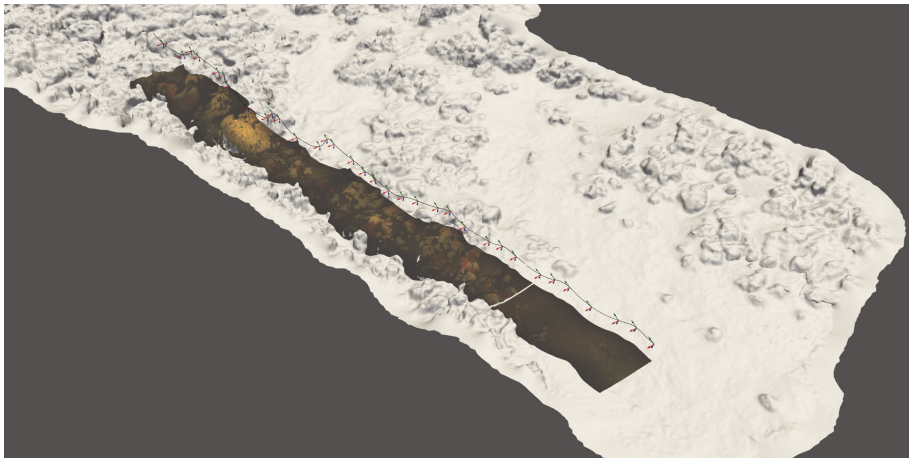

Figure 3.8: Georeferencing of a full hyperspectral datacube onto a seabed model. The representation is a 3D point cloud, where pseudo RGB colour are bands at 590 nm (red), 530 nm (green) and 490 nm (blue). The track of the imager is outlined in black, while axes indicating orientation are shown by the three arrows. The line in the hyperspectral data was a hardware fault skipping some frames.

Embree library [82] for vectorisation and Central Processing Unit (CPU) accelerated ray tracing. As input, the software takes the mesh $\boldsymbol{S}$, the ray directions $\hat{\boldsymbol{d}}_h^e$, starting points $\boldsymbol{p}_h^e$, a max ray length. It returns the seabed intersections $\boldsymbol{p}_{sb}^e$ and cell IDs of the triangles, which can e.g. be used for finding the normal vectors of the triangles, colour (from a texture map) and more. Note that occlusion-issues are avoided by using the first intersection. For example, the ray tracing in Figure 3.8 of 3.3 Million rays on a mesh with 10 Million faces took 20 seconds on a laptop.
For consistency, it is important that $\boldsymbol{S}$ has the same CRS as the navigation. As such, it is recommended to use the appropriate ECEF during ray tracing to avoid challenges with earth curvature. If using a pseudo-3D system such as horizontal Universal Transverse Mercator (UTM) and vertical depth, considerable care must be taken when defining rotation matrix $\boldsymbol{R}$ since e.g. UTM horizontal axis are not exactly aligned with North/East. Moreover, for underwater imaging, it is close to impossible to get the desired consistency ($mm-cm$) between $\boldsymbol{S}$ and navigation unless they are estimated simultaneously using e.g. SfM-MVS photogrammetry. This means that the terrain model should be computed using onboard sensors recording concurrently with the HSI. For aerial hyperspectral imagery with high-accuracy PPK or RTK, it may be possible to use bathymetry from other surveys (e.g. laser or acoustics), particularly if these are accurately georeferenced too. In the absence of accurate bathymetry, it is possible to use a concurrent low cost RGB camera on the UAV as was illustrated in J.3. The water level may also be relevant for georeferencing of hyperspectral images in shallow water. However, as previously shown, it is possible to georeference accurately onto apparent bathymetry in the case that HSI and RGB frame camera record close-to-nadir imagery. The point cloud retrieved from ray tracing has dimension $n \times m \times 3$ where n is the number

of frames in the transect and m are the number of cross-track pixels. So now we know the 3D location of each spectrum in the datacube. The following geometrical information can be extracted for further use in radiometric modeling as illustrated in J.4

- Local intersections: The intersection points can be transformed to the HSI CRS using the HSI poses at the times of each scan $\boldsymbol{p}^h_{sb/h} = \boldsymbol{R}^{-1}(\boldsymbol{p}^e_h - \boldsymbol{p}^e_{sb})$. This information is useful for underwater imaging because illumination is fixed on the vehicle body. Using local intersections, it is possible to describe the path from source-seabed-HSI very simply and solely from $\boldsymbol{p}^h_{sb/h}$ if the position of light sources are known in the vehicle body frame. Another utility, as shown in J.1 is that Euclidean distance $|\boldsymbol{p}^h_{sb/h}|$ can be used for mosaicking overlapping data because a spectrum recorded from a long distance is less reliable than a spectrum recorded from a shorter distance.
- Local surface normals: Since they are directions they are transformed only by rotation $\hat{\boldsymbol{n}}^h_{sb} = \boldsymbol{R}^{-1}\hat{\boldsymbol{n}}^e_{sb}$ where $\hat{\boldsymbol{n}}^e_{sb}$ is the normal of the intersection triangle in the 3D global CRS. These are useful for describing radiative transfer since incident irradiance from a light source is proportional to the cosine of the angle between the normal and incoming light. Since the source-seabed vector is known (previous bullet point) this effect can be computed if the normal is known in the body frame.
- 3D point cloud: The global 3D point cloud can be used for across-transect data correspondence or correspondence with other point data, such as SBES. This is conveniently done using nearest neighbor interpolation. A more important use of the 3D point cloud is to create a georeferenced datacube, for instance in a projected or geographic CRS. This is called orthorectification. Geocentric systems are convenient for the ray tracing (except maybe representation of water surface) but it is desired to work with the data in a rectified raster format in many Geographic Information Systems (GIS) applications.

3.3.2 Orthorectification

This section will describe briefly how to make a 2D hyperspectral map, or an orthorectified datacube, from the 3D point cloud from the georeferencing. This process is by all means the same for the airborne case and the underwater case. It is important to note that the majority of radiometric operations done in this thesis are done with a point cloud representation conducted using the point cloud and the datacube in tandem. As such, the orthorectified datacube has been supplied to the end user, e.g. in J.2 for classification. The rectification process is here considered to consist of point cloud transformation, rasterization and potential overlap handling, also known as mosaicking.
The point cloud transformation takes the geocentric point cloud coordinates and transforms them to a desired projected CRS, for example UTM and geoidal heights if that is of interest.
The point cloud is in an unstructured vector format, but it is desired to represent the data as a raster, where each channel corresponds to a band λ_k. In its

simplest form the rasterization spatially constitutes a one-to-one mapping from $X_{i,j}, Y_{i,j}, Z_{i,j}$ to a pixel coordinate U, V in the raster. Recall that i, j also describe frame number and pixel indices in the datacube. The raster is a k-dimensional image, whose affine transformation describes a mapping between U, V and horizontal projected positions X_U, Y_V. The orthorectification then describes how datacube spectra at $X_{i,j}, Y_{i,j}$ are combined for computing a spectrum in a cell with cell center X_U, Y_V. Although several regression and interpolation approaches can fulfill this objective, two approaches have been used in this thesis for efficiency and convenience, namely arithmetic average and nearest neighbor interpolation.
The first approach means averaging all observations within a raster cell to yield a total spectrum. In terms of SNR, the approach is well able to handle e.g. non-uniform density of points in across- and along-track directions. In a sense it is like the georeferenced equivalent to binning. The disadvantage is that the resolution is slightly decreased since a measurement near the perimeter of the cell has a footprint exceeding cell boundary. This operation is not convenient for inverse mapping, i.e. if it is desired to know the i, j that made the pixel U, V. The arithmetic averaging is done by summing spectra in all cells, and concurrently counting spectra per cell and was used for rectification in J.1.
The one-to-one nearest neighbor mapping is also fast for rectification since it only computes one unique $i, j \leftrightarrow U, V$ correspondence per raster cell. It then inserts the spectrum at datacube index i, j into raster pixel U, V. This avoids mixing of spectra, but suffers from lower SNR if resolutions are different along- and across-track. Moreover, the nearest neighbor mapping allows for thresholding distances (max extra- or interpolation distance from nearest point). We suggest masking the rectified raster by the horizontal footprint of the point cloud using a shape file. The footprint may be approximated by the polygon drawn by the first/last scan lines and all points corresponding to the first and last pixel $u_{min} = 0$ and $u_{max} = max(u)$. The footprint is also useful for evaluating overlap. The main drawback of nearest neighbor interpolation for underwater hyperspectral is that it can result in a low utilization of data if there are non-uniform densities of points in across- and along-track directions. Something that is generally challenging to achieve. As will be seen later Nearest Neighbor (NN) interpolation is well suited for co-registration since it allows direct correspondence between a rectified and unrectified datacube. An example of the transect in Figure 3.8 is shown in Figure 3.9.
When a raster has been made, the orthorectification is finished. It does however seem relevant to describe the last step of handling overlapping rasters transects, sometimes called mosaicking for imagery. Since, datacubes are relatively large data structures ($\approx$ gigabyte) and inconvenient for checking overlap, some smaller representation should be taken in use. In J.1, each spectral raster had a corresponding distance raster describing acquisition distances as a proxy for signal degradation. Both types of rasters were resampled in the same way, thus the distance raster represented the footprint. Potential overlap was first detected using the four corners of each raster bounding box. For overlapping rasters, the footprints of distance rasters were checked. The mosaicking was done by keeping the closest observation, i.e. the least degraded spectrum, for each cell. Corresponding spectra to the largest distance values in the spectral raster were masked out. Lastly,

the masked rasters were restructured to quadratic hyperspectral rasters of an appropriate size with a custom script. In total, the complete mosaicked datacube minimized acquisition distance.

3.3.3 Accuracy evaluation

Absolute accuracy is hard to measure for seabed mapping, but the accuracy of a hyperspectral orthomosaic with respect to a photogrammetric orthomosaic is easier to quantify. The use of Scale-Invariant Feature Transform (SIFT) descriptor for feature matching is common in computer vision, due to its robustness and distinctiveness [83]. From our qualitative experiences with feature matching of hyperspectral-RGB mosaics, the number of valid matches improves significantly with proper georeferencing and radiometric/photometric processing. The latter is highly relevant in underwater imaging where strong vignetting effects and variations in distance cause darker areas to be void of feature matches. The principle of SIFT-based matching is shown in Figure 3.9. Prior to comparison, the RGB mosaic was resampled to the HSI raster grid using cubic convolution. A matched feature will have one pixel position in the hyperspectral raster and one pixel position in the photo raster. The green lines in Figure 3.9 link these pairwise positions. For a perfect georeferencing, the two row and column coordinates are identical, and the green lines are horizontal. The difference in column coordinates can be described as ΔU and the difference in row coordinates as ΔV. Then the registration error of a feature is $[\Delta U, \Delta V]\Delta L = [\Delta X, -\Delta Y]$ where $\Delta X, -\Delta Y$ are the registration errors in the horizontal CRS and ΔL is the resolution.

3.4 Co-registration

Co-registration of the hyperspectral imagery to frame camera imagery is essentially how the georeferencing/georegistration is solved. The hyperspectral imagery is registred (ray-traced) onto the photogrammetric mesh using SfM derived poses. As such, this registration will inherit the biases and errors in the photogrammetry. On the other hand, the hyperspectral registration will inherit the self consistency and accuracy up to a certain level. Notably, the registration of hyperspectral images may require one last step to maximize consistency with the frame camera images, namely calibration of the line camera model. It is necessary to know how the hyperspectral rays are configured with respect to the RGB frame. One way of performing such a calibration is through self-calibration, which is often embedded in the bundle adjustment step of SfM for frame cameras. However, instead of calibrating it to itself it is here calibrated to the RGB imagery. The co-registration of hyperspectral imagery to RGB photogrammetry outputs because they measure the same range of visible light.
The above describes the case where RGB images and hyperspectral images are captured at the same time, or concurrently. Another case could be if the hyperspectral imagery and RGB imagery were captured during two different surveys, or non-concurrently. The concurrent case is the main approach in this thesis, while the non-concurrent approach was used for the aerial mapping that resulted in the

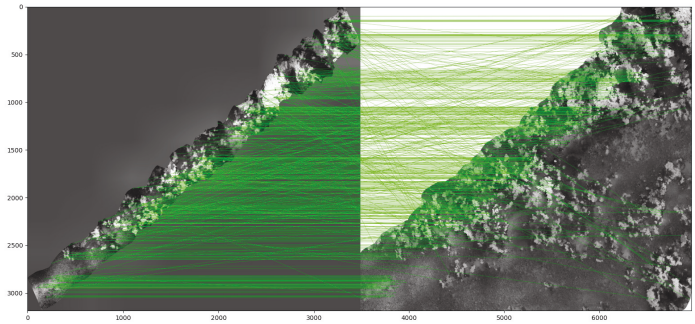

(a) Image matching of a hyperspectral transect from an deep-water coral reef. Looking aside from large outliers, the mean absolute registration error on the reef was 8.8 mm for around 10 thousand features. This is from the data in J.4. The visualizations are gray-scale, since the feature detection we used operated in this colour space.

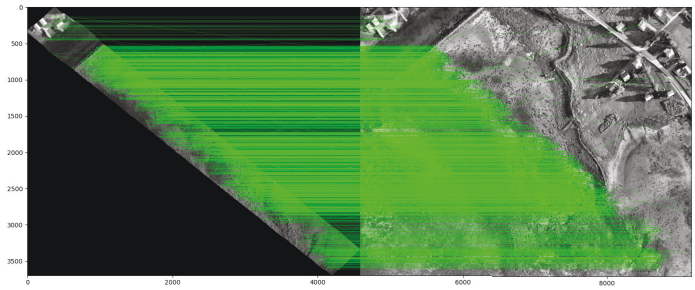

(b) Matching of a hyperspectral transect from a UAV with a photomosaic from photogrammetry. In the darker canal in the upper left of images, there are almost no correspondences. Looking aside from large outliers, the mean absolute registration error here was 5.6 cm for 3497 features.

Figure 3.9: Feature-based accuracy evaluation. All matches are included, also outliers. The outliers are few, particularly for the UAV imagery, and generally extremely easy to remove through a threshold on the registration error.

data [40], which will be described in a future publication. The concurrent and non-concurrent cases are described below:

- Concurrent: If images and scan lines are captured concurrently, the RGB-motion can be used for describing the HSI motion. There are two caveats, difference in acquisition time (unless special synchronization) and difference in CRS between the two sensors. The difference in time must be handled by interpolation (if applicable) or a photogrammetry-consistent navigation filter (e.g. Kalman Smoothing). The difference in CRS for a fixed configuration is a constant rigid-body transformation described by three rotations and three translations. This is the typical case for underwater vehicles. UAVs may employ gimbal stabilization for which this rigidity does not hold true, unless both imagers are on the same gimbal. One of the pioneering systems/pipelines demonstrating the HSI-RGB for UAVs is given in [84]. It was demonstrated for underwater hyperspectral imaging in J.1.
- Non-concurrent: This might seem as an odd-case, but there are cases where it is desired to align data to some previous higher-fidelity photogrammetric survey. In the case that the vehicle of the current survey is equipped with an RGB camera, one potential solution is feature-based SfM alignment of current RGB images to the aligned imagery from the previous high-fidelity survey in a photogrammetry software. Another solution is to directly align push-broom scan lines to the high-fidelity photogrammetry. An example of this was shown in [85] for airborne matching where feature-based HSI-RGB alignment was optimized in a least squares manner by estimating the time-varying errors in the GNSS-aided INS. Since features are sparse in the scan lines, they utilize polynomial interpolation with an assumption that errors are smooth. The estimation of slowly varying GNSS-INS errors allows a flexible, data-driven co-registration approach.

Now that the two basic principles of co-registration are described, it is attempted to solve the last bit of the puzzle. How can in-situ data be used to improve the accuracy of georeferencing with respect to some reference? In this thesis, there has been two main approaches, namely correlation-based calibration and feature-based calibration. There are mainly two things that have been estimated in the co-registration of this thesis. The first is the in-situ, or laboratory based, calibration of HSI line camera parameters and the second is estimation of navigation errors. The first approach has been used throughout this thesis in various forms to enable hyperspectral georeferencing that is well aligned to the georeferencing of photogrammetry.

- HSI line camera calibration: In underwater photogrammetry, a self-calibration may be part of the SfM. It is useful to have an equivalent procedure for the HSI that emphasizes consistency with the photogrammetry. This can also be conducted in a laboratory setup or in the field, and consists in estimating the RGB-relative rigid-body transform of the HSI and the aforementioned line camera model parameters. The transform consists in a

lever arm and a boresight rotation vector $\Delta\boldsymbol{\Theta} \rightarrow \Delta\boldsymbol{R}_c^h$. If a calibration is conducted in the laboratory, it is only valid to the extent that the RGB and HSI are in a fixed configuration and that they are fixed with respect to underwater housing (s) in the case of underwater imaging. However, if the RGB is self-calibrated during SfM, then the HSI parameters should be so too. In the aerial case self calibration of an RGB camera and estimation of HSI boresight is necessary in many cases.

- Navigation error estimation: Assume there is not a concurrent RGB camera on the vehicle and it is desired to improve georeferencing of hyperspectral images with respect to a reference photogrammetric map. This was the case for the data shown in Figure 3.9(b), and before correction this transect had a mean registration error of 1.2 m. A flexible approach is to assume that the registration errors are driven by errors in the navigation data from the GNSS-aided INS. Assuming that the navigation data has slowly varying errors, these can be estimated by parametric curves in order to minimize the aforementioned registration error. Since the HSI is on a gimbal and the INS is very accurate for roll-pitch, only position errors and heading errors were estimated. The errors were parameterized using Gaussian Kriging and equally spaced nodes in time. This methodology was used for data processing in the SeaBee project, and it was inspired by the earlier work by [86] on MBES and the approach of [85] for hyperspectral push-broom imagery.

3.4.1 Correlation-based calibration

A correlation-based co-registration, is based on maximizing the correlation between hyperspectral scan lines and some RGB texture from the photogrammetry. In J.1, J.3, correlation was used for comparing hyperspectral scan lines with RGB images or mesh texture. In J.1 it was conducted for underwater hyperspectral imaging, and for J.3 it was conducted for airborne hyperspectral imaging. Here, only the comparison between hyperspectral scan lines and frame images will be described. Assume that the HSI position and orientation can be decomposed using the RGB pose through

$$\boldsymbol{p}_h^e = \boldsymbol{p}_c^e + \boldsymbol{R}_c \boldsymbol{r}_{h/c}^c \tag{3.9a}$$

$$\boldsymbol{R}_h = \boldsymbol{R}_c \boldsymbol{R}_h^c. \tag{3.9b}$$

Where $\boldsymbol{r}_{h/c}^c, \boldsymbol{R}_h^c$ are the lever arm from HSI to RGB and rotation matrix for rotating from the HSI to the RGB camera's CRS. These are to be estimated along with the HSI line camera parameters. In J.1, all three distortion coefficients, principle point and focal length were also estimated. In the paper it was seen that rotation about the y-axis was ambiguous/correlated to the principal point parameter. Therefore it recommended to set this rotation fixed to zero. Secondly, it is recommended not using the highest order radial distortion coefficient, k_1, as it is susceptible to overfitting. By these measures, the calibration will be more consistent than the tabulated values presented in J.1. In J.3 a small-FoV HSI was used from an aerial vehicle which allowed for a pure pinhole model, only parameterized by rotations and a focal length. As such, the calibrated parameters were much more

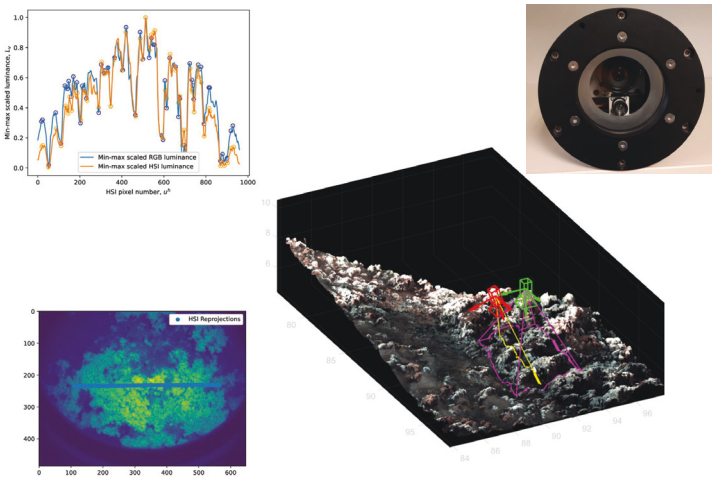

Figure 3.10: An overview of correlation-based optimization for underwater hyperspectral imaging. The green camera is the RGB camera and its pink FoV is intersected with the seabed model. The red camera is the HSI and the yellow FoV is intersected with the seabed. By re-projecting the yellow line onto the RGB image plane (lower left), we can describe the corresponding RGB pixels. Then the luminance from the two sensors can be compared (upper left). The blue luminance is RGB-derived, while the orange luminance is HSI-derived and they are both min-max normalized. The figure is adapted from J.1. The comparison was made by computing the correlation between the signals, which is invariant to min-max scaling.

consistent.

The optimization is based on the assumption that the RGB camera and the HSI are recording the same light, just in different photo- and radiometric forms. By converting the RGB signal to luma and the HSI to luminance, they could be compared. Note that raw RGB images were used and not the colour corrected described in Figure 3.3(f). Figure 3.10 shows how the correlation is computed for an RGB image and HSI scan line is computed. It is worth noting that such pairs were near simultaneous, and that cameras are displaced by 3-4 cm, so the sensors should be recording almost the same radiance field. The mean correlation could then be computed for a set of such pairs, yielding a measure of consistency. This constituted the objective function and the parameters were adjusted to maximize the mean correlation. If we study Figure 3.10 we can notice that both the RGB-based luminance and HSI-based luminance are affected by vignetting. Using the mean scan line correlation, the central measurements will play a larger role in the correlation since they are relatively speaking higher than those to the sides as seen in Figure 3.10. The edges of images play an important role in camera calibration for good constraining of distortion coefficients [87], so this is a potential point of improvement. Lastly, it is worth noting that the correlation based method can be used in a laboratory setting too as demonstrated in J.1, where the ray intersection was reduced to a line-plane computation.

3.4.2 Feature-based calibration

First, the case of a concurrent RGB camera is described. In J.1 we described a feature-based laboratory calibration with a checkerboard, and this approach is applicable to field calibration with some modifications. This is the approach that was utilized in J.4. In [88] they suggested an approach for in-situ estimation of the HSI lever arm/boresight in underwater hyperspectral imaging using manually selected tie points to achieve parameters. Their approach seemed to converge consistently with a small number of features. We will here try to explain a general way in which automated feature-based optimization can be set up against a RGB ground truth in aerial or underwater hyperspectral imaging. There are three main steps, feature matching, defining reprojection/registration error and optimization to minimize the errors.

- Feature matching:
  1. Unrectified datacube: For a stable hyperspectral push-broom motion where across-track and along-track resolutions are fairly constant, direct feature matching between a gray-scale converted datacube and a gray-scale georeferenced reference orthomosaic can be conducted. Although the checkerboard approach in J.1 used a known structure of the checkerboard, this is principally similar. Anyhow, the results from feature matching are non-integer detections in the datacube $[u_h, j]$ and detections in the orthorectified reference raster U, V. For a georeferenced orthophoto we can get global horizontal positions $[X, Y] = T_{aff}([U, V])$, where T_{aff} is the affine transform of the raster. In the photogrammetry pipeline it is also common to generate an orthographic Digital Surface Model (DSM). Using the reverse affine transform of the DSM, we can look-up the Z-value at the corresponding location. Hence, our detections have established a correspondence between the tuple $[u_h, j]$ and global points $[X, Y, Z]$. By means of linear interpolation of position and SLERP of orientation, we can compute RGB positions and rotation matrices $\boldsymbol{p}^e_{c,j}, \boldsymbol{R}_{c,j}$ corresponding with the timestamps t_j. In the case that an INS is used, camera positions are known at a much higher rate, making interpolation more accurate.
     As previously mentioned we would advise transforming to an ECEF CRS to avoid earth-curvature problems or projection distortions. Assume we do that, resulting in $[X^e, Y^e, Z^e] = T^e_{proj}([X, Y, Z])$, where T^e_{proj} describes this CRS transform. In a laboratory setting we would use a CRS based on the checkerboard.
  2. Orthorectified datacube: For accumulating the maximal number of features between the RGB orthomosaic and the HSI data, an orthorectified datacube should be used as shown in Figure 3.9. For UHI this is essential in many cases because the geometry is so distorted in the raw datacube that you would get zero matches. For the gimbal-stabilized UAV case, the unrectified datacube yielded 950 matches, while a directly georeferenced, orthorectified datacube gave 2876 matched features. By directly georeferenced, we mean georeferenced with some qualified guess of geo-

metric parameters. In [85] it is referred to as partial, rather than direct. Since georeferencing (ray tracing) and rectification is relatively time consuming it is not time-efficient to do this for every objective function evaluation. However, a single direct georeferencing should give a sufficient number of features for most cases, in the experiences of this thesis. As for the unrectified case, we get ground truth feature positions $[X^e, Y^e, Z^e]$ from the reference mosaic and DSM. The challenge then lies in finding the corresponding datacube coordinates $[u_h, j]$. The trick lies in the NN orthorectification method which defines a two-way integer index mapping $[u_h, j] \leftrightarrow [U, V]$. Integer raster pixels $[U, V]$ can be mapped to integer datacube locations $[u_h, j]$. To handle decimal locations of features, we use an adapted bi-linear interpolation which was described in J.4. The result of this bi-linear interpolation is camera poses $\boldsymbol{p}^e_{c,j}, \boldsymbol{R}_{c,j}$ at the time of HSI exposure. This whole approach was used in the paper J.4.

- Define reprojection/registration error: Assume the matching gave n correspondence pairs. We now have two "means" of describing the predicted undistorted image plane coordinates of the feature $\hat{\boldsymbol{d}}^h_h$.

  1. Forward computation: With u_h we can compute $\hat{\boldsymbol{d}}^h_h$ using (3.6) with a candidate set of camera model parameters. In the case that the camera parameters are known, these are simply used.
  2. Backward computation: By using some candidate boresight and lever arm parameters $\Delta\boldsymbol{\Theta} \leftrightarrow \boldsymbol{R}^c_h$ and $\boldsymbol{r}^c_{h/c}$, we can compute the HSI pose $\boldsymbol{p}^e_{h,j}, \boldsymbol{R}_{h,j}$ using (3.9). Then we solve (3.8) for $\hat{\boldsymbol{d}}^e_h$ using that $\boldsymbol{p}^e_{sb} = [X^e, Y^e, Z^e]^\top$. Lastly, we compute the local ray direction as $s\hat{\boldsymbol{d}}^h_h = \boldsymbol{R}^{-1}_{h,j}\hat{\boldsymbol{d}}^e_h$ where the scalar s ensures that $\hat{\boldsymbol{d}}^h_h$ is homogeneous.
  3. Backward computation (non-concurrent RGB camera): For the special case of parameterizing the time-varying errors in position $\Delta\boldsymbol{p}^e_h(t_j)$ or orientation $\Delta\boldsymbol{R}(t_j)$, there are no RGB positions and rotation matrices $\boldsymbol{p}^e_{c,j}, \boldsymbol{R}_{c,j}$. In this case, we update the INS estimate using the errors so that $\boldsymbol{p}^e_{h,j} \leftarrow \boldsymbol{p}^e_{h,j} + \Delta\boldsymbol{p}^e_h(t_j)$ and $\boldsymbol{R}_{h,j} \leftarrow \boldsymbol{R}_{h,j}\boldsymbol{R}(t_j)$. Besides from that, the procedure is the same as for boresight/lever arm estimation. An example of some optimized error time-series for positions and orientations are given in Figure 3.11. Notably, this optimization used the North/East errors on ground level by forward intersecting the ray with a virtual horizontal plane at the location of the landmark, or feature. This did not matter that much when the distance to feature points was similar, however for the UHI case, a normalized comparison is used.

- Optimization: Minimize the sum of squared error $|\hat{\boldsymbol{d}}_f - \hat{\boldsymbol{d}}_b|$ between the forward estimate and the backward estimate of the feature locations, denoted by subscript f or b. For a boresight/lever arm/camera calibration this is done in seconds. Note that outliers should be removed prior to optimization. The navigation error estimation such as Figure 3.11 currently takes quite long depending on the total number of nodes for parameterizing the curve. This

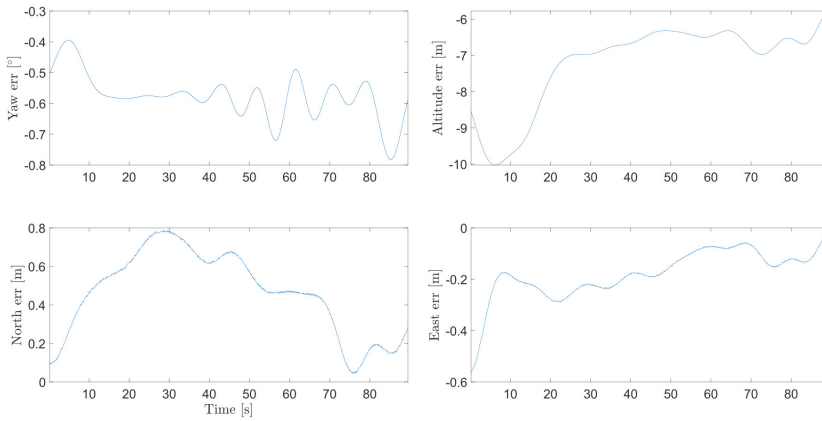

Figure 3.11: Optimized time-varying errors using co-registration, corresponds to the transect in Figure 3.9(b). All parametric curves were parameterized by nodes every 5 s and Gaussian Kriging interpolation with a correlation length of 12 s, and a nugget-to-sill ratio of 0.05. In essence it is close to radial basis interpolation with a Gaussian kernel. Note that even though the estimated altitude error seems large, the corrected altitude is relatively constant, which better reflects the true flying pattern. The full data set that was co-registred in this manner for SeaBee is visualized at [40].

is because the Jacobian becomes large, and is dense since all nodes affect all errors.

Chapter 4

Radiometry

In this thesis water bodies are treated at the macroscopic level, for unpolarized radiative transfer. The case of polarized light is notably interesting for aerial imaging, where polarization filters can remove sea surface scattered light. Moreover, in the macroscopic context, a water body's optical properties are defined by it's IOPs, consisting of bulk absorption and scattering properties. These properties depend on the composition of the water body, including dissolved and particulate matter [69]. It is the relation between the constituents' physical properties and the IOPs that enable optical measurements to infer information about the constituents and visa versa. This is the premise for ocean colour remote sensing. The IOPs of a water body are completely inherent to the medium, meaning that they are independent of environmental conditions (e.g. illumination). An optical measurement is in/through/of water is affected by other interactions at surfaces, e.g. seabed and seafloor, and the incident illumination, e.g. sky irradiance or artificial sources. These are called boundary conditions in the RTE.
The RTE, as a partial differential equation, only has a unique solution when the boundary conditions are defined. It is important to note that the RTE in natural water's generally has no analytical solution, and that numerical solutions are considered the benchmark approach for describing radiative transfer given boundary conditions and IOPs. However, for inverse problems where the IOPs and/or some boundary conditions are to be inferred from optical measurements, SA models are incredibly useful since they are explicitly invertible [46]. In this thesis, which is about seabed mapping of substrate and/or water depth, the semi-analytical model should explicitly contain the bottom reflectance and/or the water depth. For such a model, if the IOPs and water depths are known, the reflectance can be computed. It is in this section assumed that the reader is familiar with geometrical radiometry, including terms such as radiance (L), irradiance (E), radiant intensity (I) and how they are derivatives of radiant flux Φ. It is also assumed that the reader is familiar with hydrologic optics. Arguably, the most comprehensive piece of litterature on hydrologic optics at the time of writing is the open-source "The Oceanic Optics Book" by Mobley [69]. There are two topics emphasized in this chapter:

- Shallow-water: This part gives a brief description of a simple solution of the RTE for shallow-water, and describe the model used in J.3 for bathymetric inversion. This model is for UAV-based mapping.
- Underwater: This part describes the proposed SA solution in J.4 to the RTE for hyperspectral imaging from an underwater vehicle with active light sources. This model was proposed for underwater vehicles.

4.1 Optically shallow-water from air

This section aims to give a brief description of semi-analytical solutions to radiative transfer in shallow-water as relevant for hyperspectral UAV-based mapping. For a reader more interested in the details of coefficients, the reader is referred to the HOPE model in [15], [46].
According to the HOPE model [46], an expression for the sub-surface remote sensing reflectance r_{rs}, or ratio of upwelling radiance L_u^- to downwelling irradiance E_d^-, is expressed as follows:

$$r_{rs} = r_{rs}^{dp}\left[1 - exp[-(K_d + K_u^C)h]\right] + \frac{\rho}{\pi} exp[-(K_d + K_u^B)h]. \tag{4.1}$$

Where ρ is reflectivity of the seafloor, here assuming a Lambertian Bi-Directional Reflectance Distribution Function (BRDF), while r_{rs}^{dp} is the deep-water reflectance, K_d is the diffuse attenuation for downwelling plane irradiance, while K_u^C, K_u^B are the average diffuse attenuation coefficients for upwelling radiance from water column and bottom respectively. h is the water depth. A description of dependencies on view angles and IOPs are given in [15]. Some simple aspects to note are that (4.1) is ρ/π when the water depth approaches zero and r_{rs}^{dp} (the deep ocean "colour") when it is large. For the following, assume the near-nadir view case where the in-water viewing ray is close to the vertical, or $cos(\theta_v) \approx 1$.
By using the numerically calibrated model from [15] and assuming $K_u^C \approx K_u^B$, which holds true for small ratios $u = b_b/(b_b + a)$, this yields a formula of the following form

$$r_{rs} = r_{rs}^{dp}\left[1 - exp[-\alpha h]\right] + \frac{\rho}{\pi} exp[-\alpha h]. \tag{4.2}$$

Where α is a bulk attenuation coefficient for upwelling and downwelling light. This simplified version solution of the RTE is the premise for the physics bathymetry inversion algorithm by Lyzenga, 2006 [89]. Keep in mind that assumptions made here such as a small value of u will be very different depending on wavelength. As such the suitability of water depth inversion will vary.
Neglecting internal reflections effects in (4.2), Lyzenga [89] proposes that the measured upwelling radiance above the surface can be expressed in the following form

$$L(H) = L_s + L_b exp[-\alpha h]. \tag{4.3}$$

Where L_s is upwelling radiance from surface scattering and volumetric scattering and L_b is upwelling radiance from bottom reflectance and volumetric scattering as described in [89]. Assume that correction for sunglint gives gives equivalent entities

$L^{'}$ and $L_s^{'}$. According to [89], (4.3) can then be solved for water depth as follows

$$\hat{h} = \frac{1}{\alpha} ln(L_b) - \frac{1}{\alpha} ln(L^{'} - L_s^{'}). \tag{4.4}$$

Where $\hat{H}$ is the estimated depth. This however, rests upon the assumption that optical properties and bottom reflectance were spatially uniform, which is seldom the case. The proposed algorithm by [89] to accommodate non-uniform bottom and IOPs is as follows

$$\hat{h} = h_0 - \sum_{j=1}^{N} h_j X_j. \tag{4.5}$$

$X_j = ln(L_j^{'} - L_{sj}^{'})$ where j specifies the band index that corresponds to some wavelength λ_j. The regression intercept h_0 and coefficients $h_1 ... h_N$ are found with least squares linear regression during calibration. For a single band, the regression gives a line, for two bands it forms a 2D plane and so on. Once the coefficients are calibrated, they allow for predicting water depths from unseen spectra.
In J.3 it is described how we used the Lyzenga algorithm for estimating water depths with three spectral channels out of more than 100. The coefficients of the multi-band regressor were computed by linear regression using a sparse set of known depths from acoustics. Using a higher number of bands allows fitting the regressor to a higher number of bottom substrate types according to [89]. In J.3 the multiple HSI bands were utilized for selecting the optimal band triplet. That is, all triplets were tested (around 170 thousand) and the triplet with the highest coefficient of determination, R^2 was selected. This might seem excessive but surely improves estimation with a low risk of overfitting.
An example of a Lyzenga depth estimator is given for a two-band combination in Figure 4.1 using data from J.3. It corresponded to the two-band combination with the highest R^2 which were wavelengths 535 nm and 636 nm. The depth predictors X_1 and X_2 correspond with 535 nm and 636 nm, respectively. Two bands are used here because it is the highest dimensional hyperplane that can be visualized nicely. By knowledge of typical optical properties, 535 nm is a deep-penetrating wavelength for coastal waters, and is almost the same wavelength as ALB, 532 nm. On the other hand, assume that the coastal water at 636 nm had a diffuse attenuation of around 0.4 m^{-1} (see Jerlov 1C [90]). This means that for a water depth of 5 m, or path length of 10 m, the 636 nm bottom signal was reduced to 5%. This calculation is crude, but it shows how 636 nm represents a useful trade-off in being sensitive to depth, but not so sensitive that it gets a low SNR. Considering that the depths in the study were in the 0-5 m range, this could be part of the explanation for why it gave a good performance. The chosen wavelengths could also be related to the bottom composition, which was mainly sand and sea grass.

4.2 Semi-analytical model for underwater hyperspectral imaging in deep water

The word optically deep water was intentionally avoided, since it usually describes seafloor visibility from above-water vehicles in the RS community, see e.g. [13].

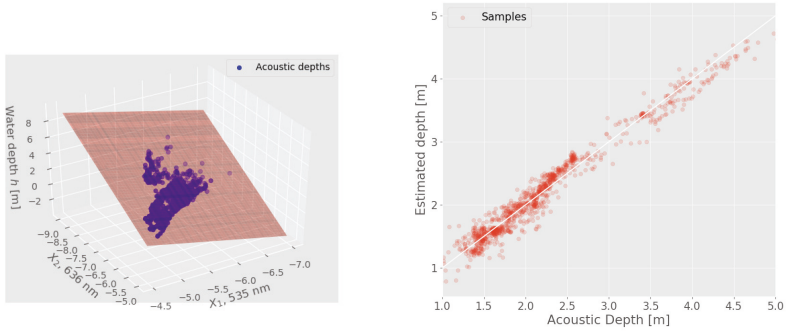

(a) **(b)**

Figure 4.1: The 2D plane in **(a)** shows the Lyzenga regressor for two bands (535 nm, 636 nm) as calibrated to acoustic depths. In **(b)** the depth estimates are plotted against the ground truth acoustics. The mean absolute error of the water depth estimates with respect to acoustic depth was 12 cm.

Here we are talking about depths where sunlight negligible for an underwater vehicle near the seabed. This, as other terms such as "optically shallow", is not a fixed depth and depends on wavelength. It is relevant to note that there is an intermediate depth layer to which there arrives sunlight to the seabed, but aerial observation is infeasible. This is a relevant subdomain for underwater spectral imaging, but it is not covered in this thesis. However, the reader is referred to [31] who demonstrate a practical approach to describing sunlight contributions for spectral measurements in this domain. Below, a solution of the RTE that is tailored towards underwater hyperspectral imaging with artificial light sources is shown. It is the same model that was proposed in J.4. The beauty of these RTE solutions are their additivity. As such, the total light reaching the sensor is e.g. sunlight contribution plus artificial source light contribution. So the presented SA solution can easily be added to an equivalent solution for sunlight.
The SA model described in the coming section was proposed in J.4 and it builds on top of geometry described in Chapter 3 and the journal paper J.1. To give the reader an intuition uncorrected reflectance is shown in Figure 4.2, which is based in data from J.4. In Figure 4.2(a) a distribution of in-situ apparent reflectivity of white *Desmophyllum Pertusum* is drawn along with laboratory spectra of polyp and stem. Apparent here means that scattering and absorption in the water column is not accounted for. For illustration, an image from an RGB camera of *Desmophyllum Pertusum* is also shown. Note that the UHI has a much lower resolution than this camera, meaning that measurements are effectively mixes of polyps and stems. The in-situ spectra were recorded at a typical viewing distance of 2 m. Lastly, the estimated attenuation coefficient κ $[m^{-1}]$, which is an IOP, is shown in Figure 4.2(c). One clear difference between the median apparent reflectivity and the lab spectra is the sudden drop from 580 nm to 600 nm. This is explained by the abrupt increase in pure-seawater absorption, a_w which is an important part of

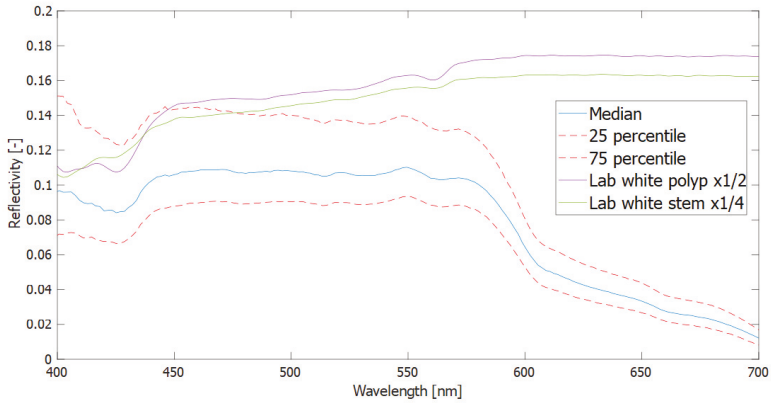

(a)

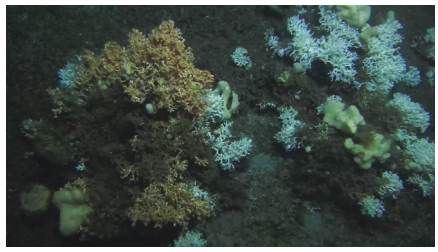

(b)

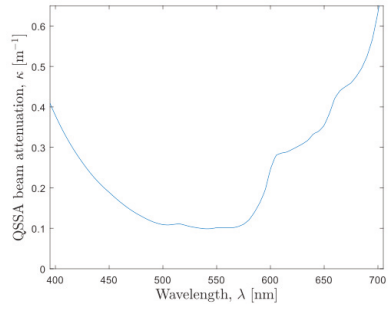

(c)

Figure 4.2: Illustration of hyperspectral data. In Figure 4.2(a) the apparent reflectance median and spread are shown, based on in-situ data from the UHI-4 and the light source characteristics. In Figure 4.2(b) a close-up of *Desmophyllum Pertusum* is shown. The reflectance spectra are from the white corals. Lastly, one of the estimated attenuation coefficients from J.4 is illustrated in Figure 4.2(c).

κ for these wavelengths. The attenuation does not explain all traits of the apparent reflectance, but it plays an important role. The underlying mathematical and physical principles are given next, in Section 4.2.1.

4.2.1 Semi-analytical model

Firstly, we give a 2D illustration of geometric primitives in Figure 4.3. Because the HSI is a line scanner, the 2D representation nicely describes the scan line geometry. All measurements can be described in a 2D scan line plane defined by the x and z axes of the HSI CRS. Note that the light sources are not necessarily in the scan line plane. The figure illustrates why it is convenient to express any seabed point and normal within a CRS fixed to the vehicle. This allows source and HSI positions to be constant with the only variables being the locally defined $\boldsymbol{p}_{sb}$ and $\hat{\boldsymbol{n}}_{sb}$. We choose the CRS of the HSI, i.e. origin in virtual focal center of HSI. For

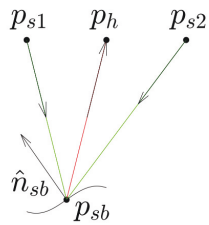

Figure 4.3: The geometric primitives for the SA model. The green and red lines show the flow of quasi-direct photons from the light sources to the HSI via the seafloor.

concisely differing between positions and vectors between positions, the symbol $\boldsymbol{r}$ is used for light paths. For example, the path to from HSI to a seabed point is $\boldsymbol{r}_h = \boldsymbol{R}^{-1}(\boldsymbol{p}_{sb} - \boldsymbol{p}_h)$, i.e. the global point position transformed to the HSI CRS. Also, let $\boldsymbol{r}_{s1}, \boldsymbol{r}_{s2}$ be the equivalent light source positions in the HSI CRS. Assume vector $\boldsymbol{r}$ can be decomposed to a unit-length directional component $\hat{\boldsymbol{d}}$ and Euclidean length l. Lastly, assume that we re-define the surface normal vectors to the HSI frame by rotation, i.e. $\hat{\boldsymbol{n}}_{sb} \leftarrow \boldsymbol{R}^{-1}\hat{\boldsymbol{n}}_{sb}$. These are also unit-length.
The overall model suggested here is partially based on the model developed by McGlamery [71] and implemented for computer simulation by Jaffe [70]. However their description of diffuse attenuation using an empirical PSF and a beam attenuation coefficient was replaced by using an average diffuse attenuation coefficient as done in the HOPE model [46]. The fundamental principle of the model is to use the quasi-single scattering approximation (Quasi-Single-Scattering-Approximation (QSSA), [91]). It takes in use the equations of the single scattering approximation, but treats the forward scattering as no scattering [69]. This means that the QSSA beam attenuation is described as $\kappa = a + b_b$ where a $[m^{-1}]$, b_b $[m^{-1}]$, are the absorption and backscatter coefficients, respectively. Although PSFs are not investigated in this work, it is an interesting and probably more accurate approach for deep-water hyperspectral imaging, given that suitable parametrizations can be defined. For example the simplified model in [92] described from IOPs.
The proposed model, like the Jaffe-McGlamery model, describes the measured signal using two components, namely quasi-direct and backscattered radiance. The quasi-direct light geometry is shown in Figure 4.4(a) and the backscattered light geometry is shown in Figure 4.4(b). Although illustrated equations are for a single light source, the solutions are additive. So the same procedure can be repeated for every light source and the measured radiance is the sum of all the light. Most angles and lengths are described there that are relevant to the computation of radiative transfer. Note that any length l has an equally sub-scripted vector $\boldsymbol{r}$. Since the lengths are from points within the light source and HSI underwater housing, let l' denote equivalent lengths in water.
For brevity we will present the equations and underlying assumptions here and the reader is referred to J.4 for the derivations. The in-water quasi-direct radiance on

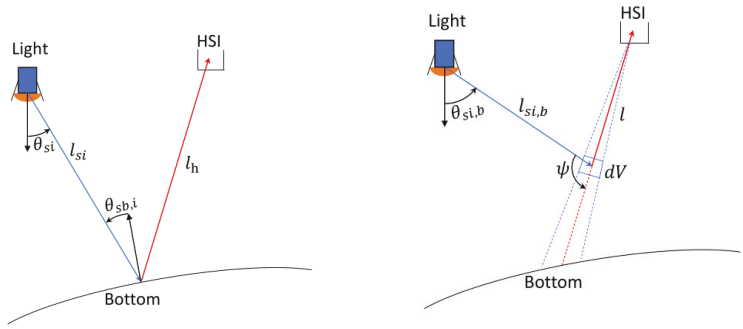

(a) **(b)**

Figure 4.4: Geometry for radiative transfer. Figure 4.4(a) illustrates quasi-direct light while Figure 4.4(b) shows backscattered light.

the outside of the HSI glass, $L_{w,d}$ can be expressed as

$$L_{w,d} = \frac{cos(\theta_{sb,i})\rho}{\pi} E(\theta_{si}) \frac{1}{l_{si}^2} exp(-[D_d \kappa l_{si}^{'} + D_u^B \kappa l_h^{'}]). \tag{4.6}$$

Where spectral dependency is omitted for brevity. The factors are explained below.

- Reflectance: $\rho \in [0, 1]$ is reflectivity. The model assumes a Lambertian BRDF ρ/π $[sr^{-1}]$ and a Dirac-delta (unidirectional) incident radiance distribution. By the definition of the BRDF, it is possible to compute the isotropic reflected radiance with a directional integral. This introduces $cos(\theta_{sb,i})$ which is the angle between the seafloor normal and the average illumination vector. Firstly, the assumption of Lambertian reflectance is prone to overestimation of ρ, because there are in reality hotspots in the BRDF when illumination direction and view direction are similar [93]. This will depend on how displaced source and HSI are relative to seafloor distance. Secondly, the light source is not unidirectional as seen from the seafloor. The average cosine will change through scattering.
- Artificial illumination: Assume that the light source has a center-line, about which it is azimuthally symmetric. That is, the radiant intensity only depends on the angle between the center-line and the illumination vector, θ_{si}. Then $E(\theta_{si})$ $[W/m^2nm]$ represents the irradiance from the source onto a hemispherical shell 1 m from the source's origin. This is what Jaffe [70] refers to as beam pattern BP, and it should be the in-water beam pattern. In J.4 we use a directional Gaussian to represent the pattern. Lastly, the spherical spread, or inverse square law of irradiance cause the term $1/l_{si}^2$. We illustrate a beam pattern in Figure 4.5 using field data. The light source is a DeepSea Multi Sealite 250 W/120 V with a 40° beam angle ($\theta_{50\%} = 20°$). To approximate beam pattern, the median values along-track are used from a data cube with homogeneous sediment. By inspection, the max/midpoint of the source is at 14° and it crosses half maximum (0.5) at -8° suggesting a beam width

of 44°. Meanwhile, a least squares fit of a Gaussian suggests a beam width of 48°. The illustration is very approximate since light source and HSI do not coincide, and radiative transfer is not accounted for.

- Attenuation: The exponential term describes diffuse attenuation on the path from source to seafloor and on the path from seafloor to imager. The premise for the expression is that a path averaged diffuse attenuation coefficient K can be described with a distribution function D as $K = D\kappa$. This is inspired by the HOPE model [46]. D_d, D_u^C are distribution functions for downward heading irradiance and upward heading radiance. Since the light gets diffused, or scattered many times, the diffuse attenuation coefficients are not constant with distance and depend somewhat on the light field. Moreover, the assumption of constant Ds has been used successfully in the HOPE model, and it is suspected to be adequate for an artificial source that is somewhat directionally isotropic.

The backscatter is based on the formulation of the Jaffe-McGlamery model. The total backscattered light is the integral of individual radiance contributions from incremental infinitesimal volumes dV (slab) such as the one in Figure 4.4(b). Assume that $dV = dldA$ where dl is the slab thickness in the direction of l and dA is cross-section area. The total backscattered radiance is expressed using the following equations

$$L_{w,b} = b \int_{l_g}^{l_h} E_i(l)\hat{\beta}(\psi) exp\big[- D_u^C \kappa (l - l_g)\big] dl. \tag{4.7a}$$

$$E_i(l) = E(\theta_{si,b}) \frac{1}{l_{si,b}^2} exp\big[- D_d \kappa l'_{si,b}\big] \tag{4.7b}$$

Factors are summarized below:

- Scattering: The scattering occurs at the slab and it is analogous to the reflectance occurring at the seafloor. The scattering coefficient b $[m^{-1}]$ and total phase function $\hat{\beta}(\psi)$ describe the degree of scattering and the probability of scattering in the direction at and angle ψ. Note that if light source and HSI were at the same place, ψ would be 180°. Note that $\hat{\beta}(\psi)$ is the weighted sum of the known pure water's phase function and a particle phase function. The simplest approach in terms of inversion and computation would be to do as Solonenko and Mobley [90] and use the non-parametric average Petzold phase function [94]. According to [95], the particle backscatter fraction is vital for achieving agreement between modeled and measured in-water light fields. The Fournier-Forand (FF) phase function is regarded as the most physically accurate analytical model of oceanic scattering [69]. Mobley [95] suggests how it can be parameterized only by the particle backscattering coefficient.
- Slab-incident light: We describe the propagation of irradiance E_i by the same principles as for the quasi-direct light. That is, using the beam pattern $E(\theta_{si,b})$ spherical spread $l_{si,b}^2$ and downward attenuation $exp[-D_d \kappa l'_{si,b}]$. Note that E_i is plane irradiance onto a plane perpendicular to the direction

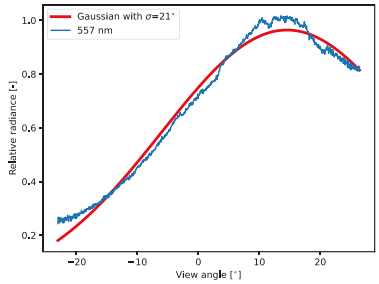

Figure 4.5: Illustration of angular beam spread using field data.

of $l_{si,b}$. For scattering computations, E_i is also considered as a Dirac-delta radiance distribution.

- HSI-incident light: The diffuse attenuation of light along l is described by $exp[-D_u^C \kappa(l-l_g)]$ where D_u^C is a distribution function of water-column scattered light. l_g is the part of l that is not in water. For our purposes we let $D_u^C = D_u^C$, essentially treating slabs in the same way as the seafloor surface.

Now, the total in-water radiance is $L_w = L_{w,b} + L_{w,d}$ from a single light source. If there was one more light source we would repeat the process, only changing the position and beam patterns in the calculations. Assume that doing this for all light sources gives L_w. We can imagine that the non-analytical integral in (4.7a) is "slow" in computation. However, once the IOPs are known one could make accelerated look-up structures (e.g. tables or nonlinear function approximation) replace the integral, or sum of integrals for multiple light sources. This is because we know that $L_{w,b}$ only depends on l_h and pixel number, u_h for a given spectral channel. Of course, the question arises, how do we compute or find out the IOPs?
Here we will think of IOPs as spatially constant for deep-water hyperspectral imaging. In J.4 we used a three-parameter parameterization of IOPs. The parameterization was inspired by the inversion in the HOPE model [15] and the inversion of Jerlov waters by Solonenko and Mobley [90]. The common denominator is that absorption and scattering properties are described by a low number of parameters and exploit measured, analytical and empirical relations. To find the latent parameters of the IOPs we suggest to use two-perspective imagery to estimate them. The idea is that you have two hyperspectral transects that are overlapping, and by associating pairwise measurements across transects, the difference in view geometry makes it possible to find IOPs. This idea was first demonstrated by [96] for underwater RGB imaging. The reason why the two-view approach lets you resolve IOPs is that ρ "cancels out" as an unknown. Using the difference in view geometry of one material to make IOPs "visible" could be implemented in a much simpler way in one special case. For homogeneous-substrate seafloor where ρ was constant everywhere. In that case, one could simply use the seafloor as a big calibration target with one unknown vector ρ and a handful unknown IOP parameters. One could naturally induce an arbitrary number of equations/views by moving the vehicle.

The last approach worth mentioning is inversion aided by a spectral library. In this case, ρ is a categorical (or mix of) variable. The simplest use of this for finding IOPs is presented in the HOPE model [15], where the bottom is represented by a sand spectrum. The clever thing is that the methods 1) needs only one observation to find IOPs and 2) depends on the absolute, not difference in, view geometry. Such methods are certainly interesting for underwater hyperspectral IOP estimation and subsequent classification schemes using the SA model proposed. The method is a powerful tool if one has a sufficiently comprehensive library. An interesting aspect with library-aided inversion is that if IOPs were known, it could be used for simultaneous estimation of geometry and substrate type with the proposed SA model. Now, for many cases SfM-photogrammetry can give the geometry, but for dynamic substrates like Kelp forests, for example in darkness, this seems like a powerful tool. Lastly, no matter which approach is taken for computing IOPs it is worth noting that the scattering integral is asymptotic, or converging. So estimation of b could probably benefit from measurements far from the seafloor, where only the backscattered light is relevant. Conceptually, this approach has been seen in the shallow-water RS community where e.g. [89] used deep-water spectra.
The SA model describes radiative transfer with light sources and it is defined in radiometric terms. It gives the radiance "right outside the glass" of the underwater housing containing the HSI. This is why it is called in-water radiance. The hyperspectral imager is calibrated in air by means of an integrating sphere, meaning that it gives the in-air equivalent radiance, which we can call L_a. Therefore, to relate L_w to L_a we need to account for the immersion effect [45]. Below, we describe how it can be expressed.

4.2.2 Through underwater housing

Radiance transfers through a given interface separating two media according to

$$L_2 = L_1 \frac{t_{12}}{(n_1/n_2)^2}. \tag{4.8a}$$

Where L_1, L_2 is the the incident and transmitted radiance, t_{12} describes the Fresnel transmittance going from medium 1 to 2 and n_1, n_2 are the real indices of refraction of media 1 and 2. Note that (4.8) is called the n-squared law for radiance [69].
If we let L^- denote the inside-housing radiance corresponding to a calibrated in-air radiance recording L_a, we must have the following relations for radiance transfer through air-glass-air (4.9a) and water-glass-air (4.9b)

$$L^- = L_a \frac{t_{ag}}{(n_a/n_g)^2} \frac{t_{ga}}{(n_g/n_a)^2} = L_a t_{ag} t_{ga} \tag{4.9a}$$

$$L^- = L_w \frac{t_{wg}}{(n_w/n_g)^2} \frac{t_{ga}}{(n_g/n_a)^2} = L_a t_{wg} t_{ga} \frac{1}{(n_w/n_a)^2}. \tag{4.9b}$$

Where subscripts a, g, w denote media air, glass and water, respectively. The immersion factor I_f relates $L_a(\theta_u, \lambda)$ to the in-water radiance, $L_w(\theta_u, \lambda)$ through:

$$L_w(\theta_u, \lambda) = L_a(\theta_u, \lambda) I_f(\theta_u, \lambda) \tag{4.10a}$$

$$I_f(\theta_u, \lambda) = \frac{n_w(\lambda)^2}{n_a(\lambda)^2} \frac{t_{ag}(\theta_a, \lambda)}{t_{wg}(\theta_w, \lambda)} \tag{4.10b}$$

Where θ_u is the angle between the ray of pixel u and the glass' surface normal. This can be estimated by a single tilt angle for a flat glass port. As such, an entire description of light's propagation from the source to the HSI measurement has been derived. To describe how L_a is related to digital counts, the reader is referred to J.4 or earlier in this thesis.

4.2.3 Special: photometry and RGB cameras

The described SA model is not unique to a specific sensor, and could be applied for wide-band sensors such as an RGB camera or a multi-spectral imager. However, inversion of ρ is not trivial for such sensors, even if IOPs are known. Consider the following diagnostic description of how inside-housing radiance L^- is integrated

$$L^*(C_i) = \int_0^\infty L^-(\lambda) S(\lambda) d\lambda. \tag{4.11}$$

Where L^* is the response-integrated radiance for a given channel C_i, while $S(\lambda)$ is the aggregate spectral sensitivity response at wavelength λ. As stated in [69], spectral response curves are not easy to get, but we may note that experiments as [97] illustrate an approach for doing it yourself. Assume that $S(\lambda)$ represents a wide-band response, e.g. for the red RGB channel. And assume for simplicity that the radiance spectrum $L^-(\lambda)$ was a spectral Dirac delta (monochromatic, e.g. laser) at 500 nm such that $L^* = S(500nm)$. Let's pretend that $S(450nm) = 0.5S(500nm)$ for this channel. From the measurement alone there would be no way of telling weather your signal came from a 500 nm laser of radiance L or a 400 nm laser of radiance $2L$. In other words, given that you assumed it was monochromatic light, there would be a spectral range from which the light could come from. Using a more narrow channel response S, the range becomes smaller and it is more justified to say that a hyperspectral sensor records monochromatic light. Due to the ambiguity of a broad band sensor, it is ill posed for inversion using IOPs. This is because the IOPs vary within the band. In layman terms, an orange 600 nm substrate and a red 650 nm substrate have different effective attenuation coefficients for the red channel. Therefore it is not possible to compute the true colour of the seafloor unless you had a spectral library. A study of a crude optical property called effective attenuation was presented in [98] for RGB cameras, where they illustrate the complexity of the problem.

Chapter 5

Discussion of Results

In this chapter the results of the articles are discussed in the broader context of the research questions. Each section is a research question. To understand how the research questions came to be, a brief introduction is given below in the context of C.1,J.5. It will be given in the form of a story.
In the autumn of 2019, at the genesis of the PhD, it was decided that the author along with several others were to go to an island called Little Cayman in March 2020. The ambition was to conduct underwater hyperspectral imaging of the seafloor at sites around the island. Therefore, the vehicle described in C.1 was assembled, and tested for an Arctic kelp forest during the polar night, as described in J.1 in January 2020. As most contemporary are aware of, the Corona virus became a pandemic around March, which essentially put the next two years of foreign field work outside the realm of possibilities. It also meant that the vehicle never went to Caribbean. Moreover, through experiences from the field test in the Arctic, the vehicle was developed with a new ambition, namely to conduct under-sea ice mapping. The first proof-of-concept was done in the Barents sea in 2021, and an example of geometrically processed data is given in Figure 5.1.
The idea with the assembled system in C.1 was to have a system for acquisition of underwater hyperspectral imagery. It was also meant to be portable and so that it could be deployed and operated manually. It is not a competing technology with industrial ROV, but rather to serve as an alternative in cases where that is not possible. A lot was learned from the field tests in the Arctic that were described in J.5, and in the context of research questions, both RQ1 and RQ2 can be traced back to these field trials. To explain, recordings of hyperspectral images were made of the kelp forest with the only illumination being a single diving light. Accompanying ground truth reflectances from the laboratory were also recorded. When studying the acquired data it became apparent that georeferencing of hyperspectral data was challenging, and that a lot of assumptions had to be. When studying the hyperspectral data and trying to to relate lab reflectances to field measurements, it was quickly realized how much impact the water body and source-bottom-HSI distance had on the signal. It was understood already then, albeit in basic terms, that there was an intrinsic connection between measurement geometry, radiometric

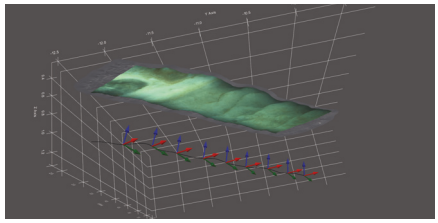

Figure 5.1: A 3D RGB visualization of hyperspectral point cloud data of under-ice data from the Barents Sea, recorded with the vehicle from C.1.

effects and classification. To exemplify, the distances were estimated by use of an acoustic altimeter which did not seem to reflect the kelp canopy, but rather the bottom below. Therefore, a physics-based correction based on these distances did not work very well. Although neither the radiometric, nor geometric processing was particularly advanced in this study it gave rise to RQ1 and RQ2. Today, it seems that a useful radiometric approach would have been an SA model as the one proposed in J.4, where the distance to the canopy was set as an unknown. This would have allowed for a classification scheme like that in [33] where in-water distances (in their case water depth) is computed along with substrate classes.

5.1 Research question 1

RQ1: How can we make geometrically accurate maps in underwater hyperspectral imagery?

The research question is best answered from the following peer-reviewed journal papers:

J.1: H. S. Løvås, A. A. Mogstad, A. J. Sørensen, and G. Johnsen, "A Methodology for Consistent Georegistration in Underwater Hyperspectral Imaging," *IEEE Journal of Oceanic Engineering*, vol. 47, no. 2, pp. 331–349, 2021

J.2: A. A. Mogstad, **H. S. Løvås**, Ø. Sture, G. Johnsen, and M. Ludvigsen, "Remote Sensing of the Tautra Ridge: An Overview of the World's Shallowest Cold-Water Coral Reefs," *Frontiers in Marine Science*, vol. 9, p. 848 888, 2022

Although J.1 explains the methodical steps to achieve accuracy, we include J.2 to get the mapping context and implications of primarily the geometric, but also radiometric processing.
In J.1 we suggested a methodology of how to go from data cubes to a photogrammetry-consistent mosaicked reflectance map. The geometric processing used ray tracing onto a 3D photogrammetric model and co-calibration of HSI with RGB, something that had not previously been done for an underwater push-broom device when the paper was submitted early 2021. However, the use of SfM for estimation of navigation had been done before in [99]. We proposed laboratory and

in-situ approaches to co-calibration using scanline correlations in luminance, and a feature-based approach in the laboratory setting. We presented quantitative results from the laboratory and evaluated in-situ georeferencing using a small number of manually selected features. These gave a roughly 0.5-1 cm mean error. The geometry was also used in computing an attenuation-based correction based on distance. The basic premise was that pixels of bright corals (with known reflectance spectrum) with varying sensor-seabed distances were used to calibrate an empirical log-linear radiance-to-reflectance conversion (based on Beer-Lamberts law). In J.2 the corrected spectra were used in an SVM classification using only a small of samples (800 per species) with a 100 percent cross-validation score for a ten-fold cross validation. Noting that the area consisted of roughly 8 million spectra, this is around 0.01 percent, and a very small job for a human annotator. Arguably, our quantitative results in J.1 suggested that we were able to establish a method for adequate ($\approx$ 1 cm) consistency with a photogrammetry-based reference. This also allowed a "seamless" mosaic of overlapping transects, and a trustworthy map overall in terms of geometry. The use of the intersection geometry in a crude reflectance conversion, also enabled us actually estimate the reflectances in a physics-based manner (although empirical). Figure 5.2 illustrates this by a qualitative comparison of laboratory reflectance spectra of white and orange *Desmophyllum Pertusum* stems and polyps and the in-situ training samples in J.2. Regarding limitations to the geometric methods, there are clearly points of improvement. The correlation-based calibration seemed to give adequate calibration results. It is believed that the laboratory experiments should have tested different parametrizations of the camera model, particularly to minimize edge distortions, a typical problem for high-order polynomial coefficients, and parameter ambiguities. In terms of finding lever arm/boresight, it is believed that the laboratory approach worked sufficiently well, in particular the feature-based approach. Regarding the in-situ calibration, it is believed that feature-based approaches using a partially georeferenced datacube with NN orthorectification, as done in J.4, are better than correlation-based approaches in some cases. They are at least a lot faster and give understandable accuracy metrics. This approach was therefore taken in J.4. To illustrate, two feature-based calibration results are shown in Figure 5.3. The histogram in Figure 5.3(a) is taken from J.4. As seen in Figure 5.3, a pure quantitative accuracy measure not can be compared recklessly between surveys, since this would give the impression that Figure 5.3(b) was 2-3 times more accurate than Figure 5.3(a). The survey in Figure 5.3(a) was exposed to severe motion because of currents and challenging bottom tracking. The survey from Figure 5.3(b) was slow-moving with relatively flat bottom and closer to the seafloor.

Regarding limitations of the radiometric correction in J.1, it was highly crude and empirical and did not account for scattering. We think there could have been an improvement in using a SA model. On the other hand, the use of the intersection geometry for solving the RTE was successfully demonstrated. It is also believed that the mosaicking of overlapping transects using nearest observations helped improve data quality in the final mosaic. The final mosaic arguably had small seamline effects, at least compared to the uncorrected data. For illustrative purposes, a comparison is added here Figure 5.4.

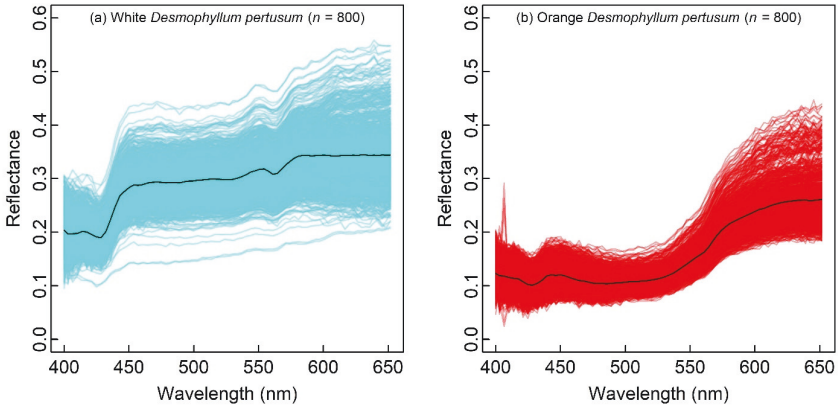

(a) Reflectance-converted training pixels of *Desmophyllum Pertusum* from J.2.

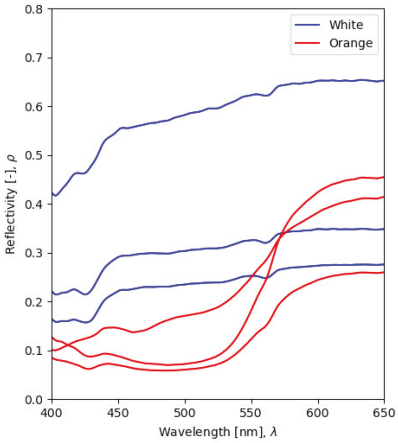

(b) Laboratory spectra of white and orange *Desmophyllum Pertusum*, two of polyps and one of stem for each type.

Figure 5.2: Laboratory and in situ reflectances. By qualitative inspection they seem fairly similar.

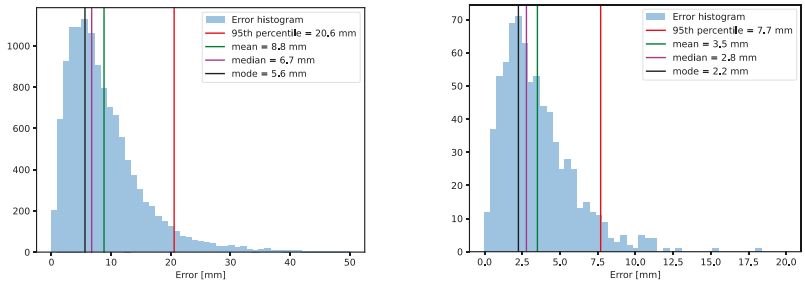

(a) Feature-based calibration residuals for ≈ 10 thousand features on the ground using the Tautra data from J.1 of over 50 transects.

(b) Error histograms from two transects from a historical wreck site (same as that in [42]).

Figure 5.3: Georeferencing Accuracy: Radial error histograms from feature based calibrations of two UHI surveys. As seen, they both follow a Rayleigh distribution, but with very different means etc.

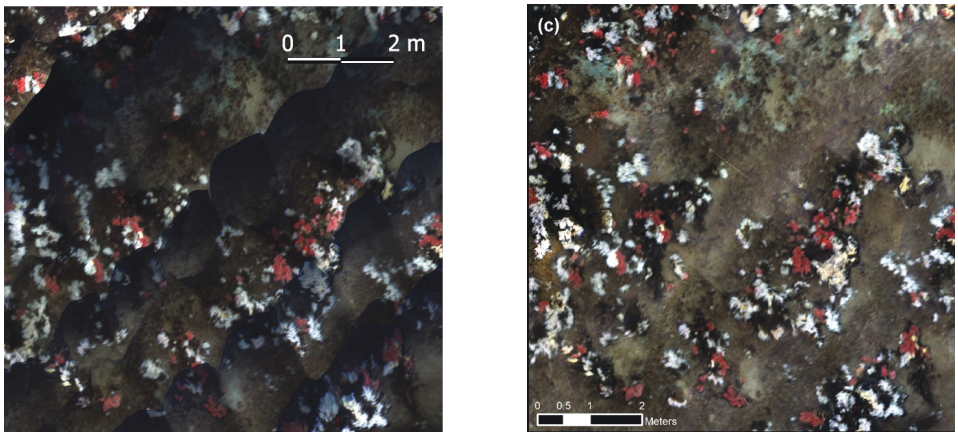

(a) Radiance transects, stacked by sequence.

(b) Reflectance mosaic after radiometric correction and mosaicking.

Figure 5.4: Radiometric correction and overlap compensation. The figures both show 12 overlapping transects in the North-East or South-West directions. Note that mosaicking was conducted using the closest observation.

5.2 Research question 2

RQ2: How can a semi-analytical model be designed for hyperspectral imaging from an underwater vehicle with active light sources? And how can the unknown parameters of that model be determined?

To answer this question, the following submitted journal paper is considered

J.4: H. S. Løvås, M. K. Larsen, O. Pizarro, and A. J. Sørensen (Submitted 29.06.2023), "A semi-analytical model for deep-water hyperspectral imaging," *Applied optics*, 2023

In J.4, a semi-analytical model was proposed for deep water hyperspectral imaging from an underwater vehicle. The model was assembled and adapted from previous work in hydrologic optics, underwater imaging/CV and the shallow-water RS community. To predict seafloor reflectance, the SA model needed 1) geometric information about light paths and 2) 1=IOPs. The geometry was acquired using the methodology of J.1 while the IOPs were described using three parameters, as inspired by the HOPE model. For determining the unknown parameters we proposed using two-perspective observations, as inspired by [96]. In other words, overlapping transects. In order to estimate the parameters we used spectral optimization. After optimization, we evaluated the performance of the SA model using across-perspective cosine similarity and spectrally resolved correlation. The optimization and performance were evaluated on the parts of the same data set as in J.1. For comparative purposes, we included per-channel estimates of κ for which we used the SA model, but fixed the backscatter term to zero.

One of the the main take-away from the study was that we were able to get physically realistic estimates of water body attenuation using per-channel estimates of κ, at least for wavelengths 450 nm-700 nm. This told us that 1) the two-perspective principle was useful for inferring IOPs and 2) the geometry and model for describing direct light in the SA worked adequately. Moreover, using the full three-parameter SA we were able to get consistent estimates of IOPs. We had two data sets, and parameter estimates were consistent within each data set and across data sets. The largest difference across the data sets was in the scattering coefficients. This lead to a slight difference cosine similarity performance. In total the SA model significantly increased across-perspective similarity, both in terms of cosine similarity and correlation.

The limitations of the study are mainly related to the functionality of the two-perspective principle, including the optimization approach and experimental setup. To begin with, our experiment was conducted on a highly rugged, structurally complex coral reef with both bright prominent coral and darker dead coral that were typically seen at further distances (below prominent structures). Arguably, it was not ideal neither geometrically nor radiometrically. It is therefore though that the method has the potential to work quite well in for a variety of seabed compositions. It should be noted that we discuss some criteria in the paper for two-perspective data points to be useful. Moreover, the experiment used a halogen light source which had an increasing spectral power with wavelength. The power was incredibly weak around 400 nm - 450 nm, meaning the bit where e.g. Colored Dissolved Organic Matter (CDOM) absorbs. The low power probably resulted in SNR issues at these wavelengths and potential biases due to e.g. light contamination from steering lights. Since our objective function optimized for similarity in apparent reflectance, i.e. radiance normalized by source spectrum, the low wavelengths potentially got a too high weight. Therefore, it may be better to replace the reflectance in the objective function by just radiance. In Figure 5.5 we show

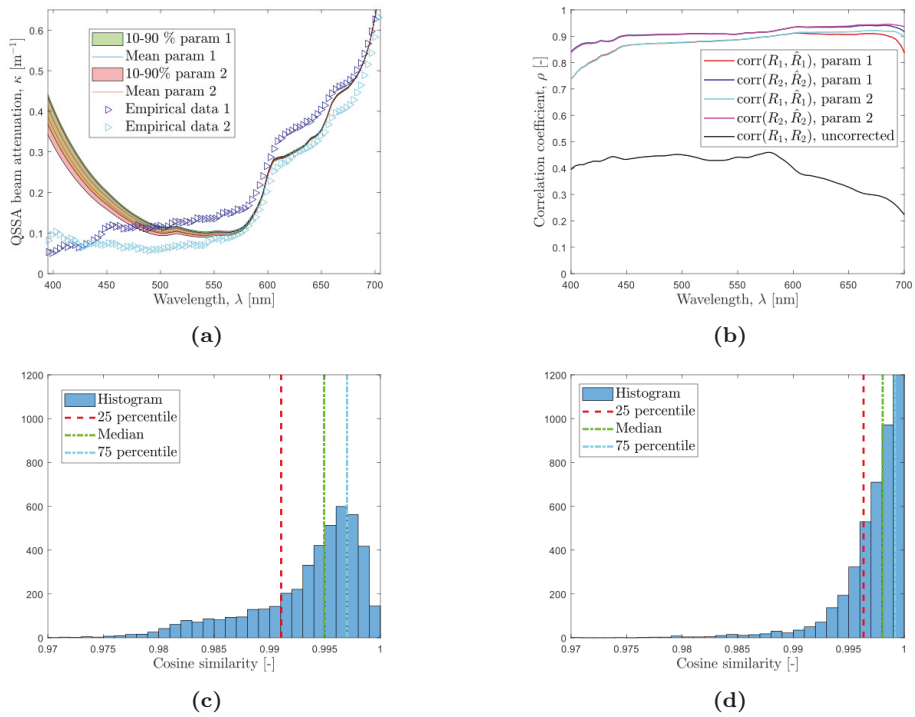

Figure 5.5: Results from J.4. In Figure 5.5(a) we see the estimated attenuation spectra from spectral optimization plotted and the per-channel regression denoted "Empirical". In Figure 5.5(b) we can see the across-perspective correlation before and after. In Figures 5.5(c) and 5.5(d) we display the uncorrected and corrected distributions of cosine similarities across perspectives.

some results including attenuation estimates, and across-perspective correlations and cosine similarities

5.3 Research question 3

RQ3: How can we achieve consistent georeferencing for concurrent RGB and HSI imagery in airborne shallow-water hyperspectral imagery? Can we utilize this to perform concurrent bimodal bathymetry estimation from spectral inversion and photogrammetry?

To answer this question, the following journal paper is considered

J.3: H. S. Løvås, O. Hasler, D. D. Langer, and A. J. Sørensen, "Coregistration of Hyperspectral Imagery With Photogrammetry for Shallow-Water Mapping," *IEEE Transactions on Geoscience and Remote Sensing*, vol. 61, pp. 1–24, 2023

In J.3 a copter UAV equipped with an RGB camera and an HSI were used to map bathymetry that was verified using a SBES measurements from an Unmanned Surface Vehicle (USV). Firstly, we demonstrated a coregistration approach using SfM-photogrammetry pose estimates in an error-state extended Kalman filter that performed filtering forward and backwards. The two estimates were combined by Kalman smoothing. This provided a convenient "interpolation" method that could ensure consistency with SfM-poses. Moreover, the MVS step in photogrammetry pipeline gave apparent bathymetry, where apparent refers to how the bathymetry "appears" when performing regular MVS, not accounting for refraction. An interesting trend when performing MVS was that lower-texture areas (deeper water and sand bottom) would tend to have significantly lower coverage for higher-resolution images, than downsampled versions. This was studied by conducting image matching with 1/2 resolution, 1/4 resolution etc. The final dense point cloud was used with an estimate of the water level to perform view-dependent refraction correction to give refraction-corrected model of the sea floor. On the other hand, the georeferenced hyperspectral data was associated to the sparse SBES water depths, and we calibrated an empirical spectral inversion model to the sparse depths. Lastly, an evaluation of MVS - acoustic and MVS - hyperspectral was conducted.
Arguably, the correlation-based calibration method was successful. In this case due to the the relatively low-geometric fidelity of images caused by motion blur and the small FoV, the correlation-based approach might be better suited than a feature-based approach. In the paper, we gave an optimistic estimate of a mean registration error around 20 cm (altitude of 100 m). Comparatively, the feature-based coregistration conducted on behalf of the SeaBee project had a radial registration error of 6.7 cm for 18000 features from an altitude around 80 m. Data available at [40] and publication is in preparation by Joseph Garrett. The latter had a gimbal and a 50 Hz frame rate, while the former had a 10 Hz frame rate and no gimbal. Nonetheless, the hyperspectral inversion in J.3 gave good results with a low noise level, which may have been higher for a 50 Hz frame rate since it would force a lower exposure time.
Regarding the photogrammetric pipeline, there were several lessons learned. Firstly, it would have been very convenient to have accurate, visible GCPs along the shoreline. It should be noted that this lesson was taken and both GCPs and PPK positioning was used in a subsequent survey in Ny-Ålesund 2022 (publication in preparation by Oliver Hasler). Another thing that should have been done was time synchronization between the GoPro and INS. However, the GoPro had a Global Positioning system (GPS) time stamping (in integer seconds) and fixed acquisition interval, so a constant time shift was computed.
Regarding the overall bathymetry estimation from MVS, the mean absolute error was 14 cm with respect to acoustics and 11 cm with respect to the spectral inversion. As such, we would argue that the method was successful in MVS bathymetry mapping. It should be noted that there was a slight trend that MVS underestimated higher water depths. Considering the various image resolutions in MVS, the trend was that higher resolutions were somewhat more accurate, at the expense of lower coverage. The reason for low coverage is known to arise because of "too high" local variation/inconsistency in depth map estimates. By inspection, it clearly seemed to be low texture sand areas in conjunction with deeper water that caused such

inconsistency. This observation was consistent with other studies [55].
The spectral inversion approach was calibrated to the sparse acoustics with a mean absolute error of 10 cm. Considering the 11 cm mean absolute error and general consistency in water depths between the coregistred spectral inversion and photogrammetry, we would say that we were able to perform concurrent bimodal bathymetry estimation. For ease of interpretation, some main results are shown in Figure 5.6.
The obvious drawback with the inversion method was that it had to be site-calibrated. However, the potential advantage of of such a radiometric-geometric combo is as shown in [55] e.g. low-texture areas where photogrammetry fails. It is possible to imagine that a hyperspectral inversion algorithm is calibrated by the photogrammetry estimates in texture areas, while spectral inversion "fills out" low-texture areas. It is also possible to imagine how photogrammetry-derived water depths could ease the estimation IOPs and help solving the inverse problem by decreasing ambiguity. The concurrency has the advantage that the water level is the same for both modalities, which could also allow for detection/estimation of the waterline/water level.

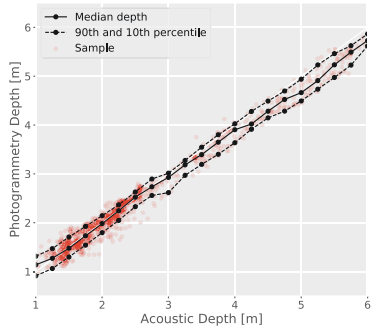

(a) MVS vs acoustic. Acoustic depth h_{ac} on x-axis and photogrammetry depth h_p on y-axis. Exact same median and percentiles as in Figure 5.6(b), except h_{ac} is added.

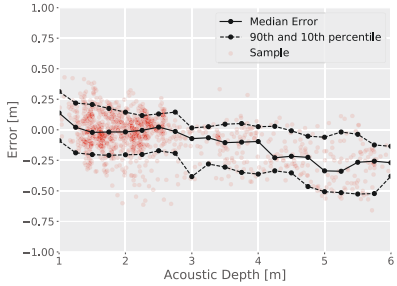

(b) MVS vs acoustic error $e^p_{ac} = h_p - h_{ac}$. There are three lines, the 10th percentile, median and 90th percentile. Total MAE is 14 cm for 1220 points.

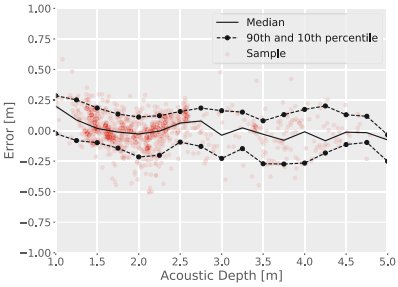

(c) Spectral vs acoustic error $e^s_{ac} = h_s - h_{ac}$. Total MVS is 10 cm for 1029 points. This is the result of the calibration.

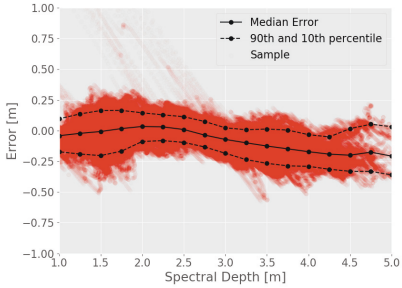

(d) MVS vs spectral error $e^p_s = h_p - h_s$. The large outliers are from a person on a paddle board. Total Mean Absolute Error is 11 cm for 522174 points.

Figure 5.6: Comparison of bathymetry from MVS, spectral inversion and acoustics. All error statistics were computed every 25 cm within a depth window ±25 cm.

Chapter 6

Conclusions and Further Work

6.1 Conclusions

In this thesis optical techniques for facilitating hyperspectral mapping of the seafloor has been developed, with a particular focus on geometric and radiometric processing. One of the key ideas studied has been how RGB cameras and hyperspectral sensors could be used in tandem. In recent years, the RGB sensor and processing technology has become incredibly available and accurate for inferring high-resolution texture and geometry. The thesis has spent time trying to transfer some of the geometrical accuracy to the realm of hyperspectral push-broom imaging through developing methods for georeferencing and co-registration. We started out by demonstrating this for underwater hyperspectral imaging in J.1 and we also showed how this allowed attenuation correction and mosaicking. The resulting hyperspectral mosaic was then used in a larger mapping context in J.2 for mapping a coral reef. In Section J.3 we co-registered hyperspectral imagery with two-media photogrammetry from a UAV for shallow-water mapping. We demonstrated two-modality concurrent bathymetry mapping using a simple spectral technique and multi-view stereo with refraction correction. Lastly in Section J.4, with inspiration from the shallow-water RS community, we proposed a comprehensive semi-analytical model for deep-water hyperspectral imaging. The model utilized accurate geometries from the method in J.1, so that the only unknowns were the IOPs and the bottom reflectances. We demonstrated the use of two-perspective geometry to perform direct estimation of IOPs. This gives an SA model that can compute bottom reflectance or be used for classification schemes.
In the underwater hyperspectral domain, the work has contributed with significant improvements to aspects in geometrical and radiometric processing. The work has looked towards other fields such as underwater computer vision, shallow-water remote sensing and radiative transfer theory, to adapt state-of-the-art methods to the underwater hyperspectral domain. In the work on combining aerial photogrammetry and shallow-water hyperspectral imaging, a novel approach for co-registred, bi-modal bathymetry estimation was demonstrated. The notion of combining hyperspectral imaging with RGB imaging in this manner could have an important

role in improving georeferencing, lowering ambiguity in inversion and more robust bathymetry estimation.

6.2 Recommendations for further work

The recommendations for further work are two-fold, aerial and underwater.

1. Aerial shallow-water: A key recommendation is the further development of robust photogrammetry methods that are easy to take in use. The number of actors in possession of a small aerial vehicle with an RGB camera, low cost etc. makes it a potentially large contribution. One aspect is the direct computation the water surface level, another is minimization and quantification of the refraction correction. In terms of novel low-cost, low-weight hyperspectral imagers, coregistration with an RGB camera seems like an interesting topic for further work. It could allow for the geometrical consistency needed for creating benthic monitoring sites. It could also allow for developing methods that seamlessly integrates geometrical information, e.g. water depth, from photogrammetry to enhance hyperspectral benthic classification.
2. Underwater hyperspectral: In the further development of SA model calibration routines, a natural next step is to do a controlled laboratory study with some ground truth of IOPs. In J.4 it was out of scope to look into in-situ estimation of beam patterns, but this could also be part of such a laboratory experiment. For proper verification of the SA model in a variety of water conditions it seems useful to perform numerical 3D Monte Carlo studies. This would enable appropriate computation of diffuse attenuation coefficients as done in the development of the HOPE model [15]. An interesting application of the SA model is to create benchmark bottom reflectance data sets for evaluating color correction schemes for RGB imagery. The main application for further work would be to use the SA model for inversion-based classification. Lastly, we showed during co-registration that we could extract quite unique geometric SIFT features using three bands. An interesting application would be the study of underwater hyperspectral textural information, meaning the use of pixel neighborhoods rather than individual pixels, for e.g. classification. Potentially, this could be step towards optimal data utilization.

References

[1] M. Pidwirny. ""introduction to the oceans". fundamentals of physical geography, 2nd edition." (2006), [Online]. Available: http://www.physicalgeography.net/fundamentals/8o.html (visited on 05/04/2023).

[2] A. A. Mogstad, "Underwater hyperspectral imaging as a tool for benthic habitat mapping," 2021.

[3] Andreas Tjernshaugen, *Hvaleventyret*. Kagge Forlag, 2018.

[4] R. H. Thurstan, "The potential of historical ecology to aid understanding of human–ocean interactions throughout the Anthropocene," *Journal of Fish Biology*, vol. 101, no. 2, pp. 351–364, 2022.

[5] A. Rice, "1 The Challenger Expedition," *Understanding the Oceans: A Century of Ocean Exploration*, 2013.

[6] L. A. Mayer, "Frontiers in seafloor mapping and visualization," *Marine Geophysical Researches*, vol. 27, pp. 7–17, 2006.

[7] A.-C. Wölfl, H. Snaith, S. Amirebrahimi, C. W. Devey, B. Dorschel, V. Ferrini, V. A. Huvenne, M. Jakobsson, J. Jencks, G. Johnston, *et al.*, "Seafloor mapping–the challenge of a truly global ocean bathymetry," *Frontiers in Marine Science*, p. 283, 2019.

[8] D. T. Sandwell, W. H. Smith, S. Gille, E. Kappel, S. Jayne, K. Soofi, B. Coakley, and L. Géli, "Bathymetry from space: Rationale and requirements for a new, high-resolution altimetric mission," *Comptes Rendus Geoscience*, vol. 338, no. 14-15, pp. 1049–1062, 2006.

[9] OECD. "Marine Protected Areas: Economics, Management and Effective Policy Mixes Policy Highlights." (), [Online]. Available: https://www.oecd.org/environment/resources/Marine-Protected-Areas-Policy-Highlights.pdf (visited on 05/05/2023).

[10] Ø. Sture, M. Ludvigsen, M. S. Scheide, and T. Thorsnes, "Recognition of cold-water corals in synthetic aperture sonar imagery," in *2018 IEEE/OES Autonomous Underwater Vehicle Workshop (AUV)*, IEEE, 2018, pp. 1–6.

[11] J. M. Roberts, C. J. Brown, D. Long, and C. R. Bates, "Acoustic mapping using a multibeam echosounder reveals cold-water coral reefs and surrounding habitats," *Coral Reefs*, vol. 24, pp. 654–669, 2005.

[12] J. H. Fosså, B. Lindberg, O. Christensen, T. Lundälv, I. Svellingen, P. B. Mortensen, and J. Alvsvåg, "Mapping of Lophelia reefs in Norway: experiences and survey methods," *Cold-water corals and ecosystems*, pp. 359–391, 2005.

[13] T. Kutser, J. Hedley, C. Giardino, C. Roelfsema, and V. E. Brando, "Remote sensing of shallow waters–A 50 year retrospective and future directions," *Remote Sensing of Environment*, vol. 240, p. 111 619, 2020.

[14] G. Mandlburger, "A review of airborne laser bathymetry for mapping of inland and coastal waters," 2020.

[15] Z. Lee, K. L. Carder, C. D. Mobley, R. G. Steward, and J. S. Patch, "Hyperspectral remote sensing for shallow waters: 2. Deriving bottom depths and water properties by optimization," *Applied optics*, vol. 38, no. 18, pp. 3831–3843, 1999.

[16] G. Mandlburger, "Through-water dense image matching for shallow water bathymetry," *Photogrammetric Engineering & Remote Sensing*, vol. 85, no. 6, pp. 445–455, 2019.

[17] R. Slocum, W. Wright, C. Parrish, B. Costa, M. Sharr, and T. Battista, "Guidelines for bathymetric mapping and orthoimage generation using sUAS and SfM, an approach for conducting nearshore coastal mapping," 2019.

[18] J. D. Hedley, C. M. Roelfsema, I. Chollett, A. R. Harborne, S. F. Heron, S. J. Weeks, W. J. Skirving, A. E. Strong, C. M. Eakin, T. R. Christensen, *et al.*, "Remote sensing of coral reefs for monitoring and management: A review," *Remote Sensing*, vol. 8, no. 2, p. 118, 2016.

[19] G. De'Ath, K. E. Fabricius, H. Sweatman, and M. Puotinen, "The 27–year decline of coral cover on the Great Barrier Reef and its causes," *Proceedings of the National Academy of Sciences*, vol. 109, no. 44, pp. 17 995–17 999, 2012.

[20] S. B. Williams, O. R. Pizarro, M. V. Jakuba, C. R. Johnson, N. S. Barrett, R. C. Babcock, G. A. Kendrick, P. D. Steinberg, A. J. Heyward, P. J. Doherty, *et al.*, "Monitoring of benthic reference sites: Using an autonomous underwater vehicle," *IEEE Robotics & Automation Magazine*, vol. 19, no. 1, pp. 73–84, 2012.

[21] G. Mandlburger, M. Pfennigbauer, R. Schwarz, S. Flöry, and L. Nussbaumer, "Concept and performance evaluation of a novel UAV-borne topo-bathymetric LiDAR sensor," *Remote Sensing*, vol. 12, no. 6, p. 986, 2020.

[22] V. Chirayath and A. Li, "Next-generation optical sensing technologies for exploring ocean worlds—NASA FluidCam, MiDAR, and NeMO-Net," *Frontiers in Marine Science*, vol. 6, p. 521, 2019.

[23] A. Papakonstantinou, C. Stamati, and K. Topouzelis, "Comparison of True-Color and Multispectral Unmanned Aerial Systems Imagery for Marine Habitat Mapping Using Object-Based Image Analysis," *Remote Sensing*, vol. 12, no. 3, 2020. DOI: 10.3390/rs12030554.

[24] M. Parsons, D. Bratanov, K. J. Gaston, and F. Gonzalez, "UAVs, hyperspectral remote sensing, and machine learning revolutionizing reef monitoring," *Sensors*, vol. 18, no. 7, p. 2026, 2018.

[25] T. Kwasnitschka, K. Köser, J. Sticklus, M. Rothenbeck, T. Weiß, E. Wenzlaff, T. Schoening, L. Triebe, A. Steinführer, C. Devey, *et al.*, "DeepSurveyCam—a deep ocean optical mapping system," *Sensors*, vol. 16, no. 2, p. 164, 2016.

[26] D. M. Price, K. Robert, A. Callaway, C. Lo Lacono, R. A. Hall, and V. A. Huvenne, "Using 3D photogrammetry from rov video to quantify cold-water coral reef structural complexity and investigate its influence on biodiversity and community assemblage," *Coral Reefs*, vol. 38, pp. 1007–1021, 2019.

[27] D. Stanley, A. Bodenmann, M. Massot-Campos, and B. Thornton, "Autocalibration of line-laser structured-light seafloor mapping systems," in *OCEANS 2021: San Diego–Porto*, IEEE, 2021, pp. 1–6.

[28] H. Liu, J. V. Büscher, K. Köser, J. Greinert, H. Song, Y. Chen, and T. Schoening, "Automated activity estimation of the cold-water coral Lophelia Pertusa by multispectral imaging and computational pixel classification," *Journal of Atmospheric and Oceanic Technology*, vol. 38, no. 2, pp. 141–154, 2021.

[29] A. A. Mogstad, H. S. Løvås, Ø. Sture, G. Johnsen, and M. Ludvigsen, "Remote Sensing of the Tautra Ridge: An Overview of the World's Shallowest Cold-Water Coral Reefs," *Frontiers in Marine Science*, vol. 9, p. 848 888, 2022.

[30] Ø. Sture, M. Ludvigsen, L. M. S. Aas, *et al.*, "Autonomous underwater vehicles as a platform for underwater hyperspectral imaging," in *Oceans 2017-Aberdeen*, IEEE, 2017, pp. 1–8.

[31] D. L. Bongiorno, M. Bryson, T. C. Bridge, D. G. Dansereau, and S. B. Williams, "Coregistered hyperspectral and stereo image seafloor mapping from an autonomous underwater vehicle," *Journal of Field Robotics*, vol. 35, no. 3, pp. 312–329, 2018.

[32] C. D. Mobley, L. K. Sundman, C. O. Davis, J. H. Bowles, T. V. Downes, R. A. Leathers, M. J. Montes, W. P. Bissett, D. D. Kohler, R. P. Reid, *et al.*, "Interpretation of hyperspectral remote-sensing imagery by spectrum matching and look-up tables," *Applied Optics*, vol. 44, no. 17, pp. 3576–3592, 2005.

[33] R. A. Garcia, Z. Lee, and E. J. Hochberg, "Hyperspectral shallow-water remote sensing with an enhanced benthic classifier," *Remote Sensing*, vol. 10, no. 1, p. 147, 2018.

[34] H. S. Løvås, A. A. Mogstad, A. J. Sørensen, and G. Johnsen, "A Methodology for Consistent Georegistration in Underwater Hyperspectral Imaging," *IEEE Journal of Oceanic Engineering*, vol. 47, no. 2, pp. 331–349, 2021.

[35] SeaBee. "Norwegian Infrastructure for Drone-based Research, Mapping and Monitoring in the Coastal Zone." (), [Online]. Available: https://seabee.no/ (visited on 05/08/2023).

[36] H. S. Løvås, O. Hasler, D. D. Langer, and A. J. Sørensen, "Coregistration of Hyperspectral Imagery With Photogrammetry for Shallow-Water Mapping," *IEEE Transactions on Geoscience and Remote Sensing*, vol. 61, pp. 1–24, 2023.

[37] H. S. Løvås, M. K. Larsen, O. Pizarro, and A. J. Sørensen (Submitted 29.06.2023), "A semi-analytical model for deep-water hyperspectral imaging," *Applied optics*, 2023.

[38] N. Summers, G. Johnsen, A. Mogstad, H. Løvås, G. Fragoso, and J. Berge, "Underwater hyperspectral imaging of Arctic macroalgal habitats during the polar night using a novel mini-ROV-UHI portable system," *Remote sensing*, vol. 14, no. 6, p. 1325, 2022.

[39] H. S. Løvås, A. J. Sørensen, and M. Ludvigsen, "Framework for Combining Multiple Lightweight Underwater Vehicles into Super Underwater Vehicle," in *2020 IEEE/OES Autonomous Underwater Vehicles Symposium (AUV)*, IEEE, 2020, pp. 1–6.

[40] SeaBee. "RGB, multispectral and hyperspectral mapping of Remøy, Norway." (), [Online]. Available: https://geonode.seabee.sigma2.no/catalogue/#/map/29 (visited on 05/09/2023).

[41] Arctic frontiers. "Arctic Frontiers Book of Abstracts." (), [Online]. Available: https://www.arcticfrontiers.com/wp-content/uploads/2022/07/bookofabstractsscience2022.pdf (visited on 05/10/2023).

[42] E. Diamanti, H. S. Løvås, M. K. Larsen, and Ø. Ødegård, "A multi-camera system for the integrated documentation of Underwater Cultural Heritage of high structural complexity; The case study of M/S Helma wreck," *IFAC-PapersOnLine*, vol. 54, no. 16, pp. 422–429, 2021.

[43] O. Hasler, H. Løvås, T. H. Bryne, and T. A. Johansen, "Direct georeferencing for Hyperspectral Imaging of ocean surface," in *2023 IEEE Aerospace Conference*, IEEE, 2023, pp. 1–19.

[44] M. B. Henriksen, E. F. Prentice, T. A. Johansen, and F. Sigernes, "Prelaunch calibration of the HYPSO-1 cubesat hyperspectral imager," in *2022 IEEE Aerospace Conference (AERO)*, IEEE, 2022, pp. 1–9.

[45] G. Zibordi and M. Darecki, "Immersion factors for the RAMSES series of hyper-spectral underwater radiometers," *Journal of Optics A: Pure and Applied Optics*, vol. 8, no. 3, p. 252, 2006.

[46] Z. Lee, K. L. Carder, C. D. Mobley, R. G. Steward, and J. S. Patch, "Hyperspectral remote sensing for shallow waters. I. A semianalytical model," *Applied optics*, vol. 37, no. 27, pp. 6329–6338, 1998.

[47] F. Sigernes, "Basic hyperspectral imaging," *TTK20 Hyperspectral remote sensing-lecture notes, Norwegian University of Science and Technology, Trondheim*, 2018.

[48] Applied Underwater Robotics Laboratory. "ROV 30K description." (), [Online]. Available: https://www.ntnu.edu/aur-lab/rov30k (visited on 05/10/2023).

[49] F. Sigernes, M. Syrjäsuo, R. Storvold, J. Fortuna, M. E. Grøtte, and T. A. Johansen, "Do it yourself hyperspectral imager for handheld to airborne operations," *Opt. Express*, vol. 26, no. 5, pp. 6021–6035, Mar. 2018. DOI: 10.1364/OE.26.006021.

[50] M. B. Henriksen, E. F. Prentice, C. M. van Hazendonk, F. Sigernes, and T. A. Johansen, "Do-it-yourself VIS/NIR pushbroom hyperspectral imager with C-mount optics," *Opt. Continuum*, vol. 1, no. 2, pp. 427–441, Feb. 2022. DOI: 10.1364/OPTCON.450693.

[51] A. A. Mogstad and G. Johnsen, "Spectral characteristics of coralline algae: A multi-instrumental approach, with emphasis on underwater hyperspectral imaging," *Applied Optics*, vol. 56, no. 36, pp. 9957–9975, 2017.

[52] Ø. Sture, B. Snook, and M. Ludvigsen, "Obtaining hyperspectral signatures for seafloor massive sulphide exploration," *Minerals*, vol. 9, no. 11, p. 694, 2019.

[53] I. Dumke, A. Purser, Y. Marcon, S. M. Nornes, G. Johnsen, M. Ludvigsen, and F. Søreide, "Underwater hyperspectral imaging as an in situ taxonomic tool for deep-sea megafauna," *Scientific reports*, vol. 8, no. 1, p. 12 860, 2018.

[54] D. R. Thompson, E. J. Hochberg, G. P. Asner, R. O. Green, D. E. Knapp, B.-C. Gao, R. Garcia, M. Gierach, Z. Lee, S. Maritorena, *et al.*, "Airborne mapping of benthic reflectance spectra with Bayesian linear mixtures," *Remote sensing of Environment*, vol. 200, pp. 18–30, 2017.

[55] R. K. Slocum, C. E. Parrish, and C. H. Simpson, "Combined geometric-radiometric and neural network approach to shallow bathymetric mapping with UAS imagery," *ISPRS Journal of Photogrammetry and Remote Sensing*, vol. 169, pp. 351–363, 2020.

[56] O. J. Woodman, "An introduction to inertial navigation," University of Cambridge, Computer Laboratory, Tech. Rep., 2007.

[57] R. Mur-Artal and J. D. Tardós, "Visual-Inertial Monocular SLAM With Map Reuse," *IEEE Robotics and Automation Letters*, vol. 2, no. 2, pp. 796–803, 2017. DOI: 10.1109/LRA.2017.2653359.

[58] T. Takasu and A. Yasuda, "Development of the low-cost RTK-GPS receiver with an open source program package RTKLIB," in *International symposium on GPS/GNSS*, International Convention Center Jeju Korea Seogwipo-si, Korea, vol. 1, 2009, pp. 1–6.

[59] H. Zhang, E. Aldana-Jague, F. Clapuyt, F. Wilken, V. Vanacker, and K. Van Oost, "Evaluating the potential of post-processing kinematic (PPK) georeferencing for UAV-based structure-from-motion (SfM) photogrammetry and surface change detection," *Earth Surface Dynamics*, vol. 7, no. 3, pp. 807–827, 2019. DOI: 10.5194/esurf-7-807-2019.

[60] A. Tal, I. Klein, and R. Katz, "Inertial Navigation System/Doppler Velocity Log (INS/DVL) Fusion with Partial DVL Measurements," *Sensors*, vol. 17, no. 2, 2017. DOI: 10.3390/s17020415.

[61] F. Dukan and A. J. Sørensen, "Sea floor geometry approximation and altitude control of ROVs," *Control Engineering Practice*, vol. 29, pp. 135–146, 2014.

[62] R. Szeliski, *Computer vision: algorithms and applications*. Springer Science & Business Media, 2010.

[63] L. Zhou, X. Cheng, Y. Zhu, and Y. Lu, "Terrain aided navigation for long-range AUVs using a new bathymetric contour matching method," in *2015 IEEE International Conference on Advanced Intelligent Mechatronics (AIM)*, IEEE, 2015, pp. 249–254.

[64] P. Norgren and R. Skjetne, "A multibeam-based slam algorithm for iceberg mapping using auvs," *IEEE Access*, vol. 6, pp. 26 318–26 337, 2018.

[65] M. K. Larsen, O. Pizarro, and M. Ludvigsen, "Geometric Registration of Benthic Imagery for Learning Appearance-Based Place Recognition over Multiple Sessions," in *2023 IEEE Underwater Technology (UT)*, IEEE, 2023, pp. 1–10.

[66] P. Groves, "Principles of GNSS, Inertial, and Multisensor Integrated Navigation Systems, Second Edition," in Artech House, 2008, ch. 3, pp. 90–91.

[67] H. Hirschmuller, "Stereo processing by semiglobal matching and mutual information," *IEEE Transactions on pattern analysis and machine intelligence*, vol. 30, no. 2, pp. 328–341, 2007.

[68] P. Merrell, A. Akbarzadeh, L. Wang, P. Mordohai, J.-M. Frahm, R. Yang, D. Nister, and M. Pollefeys, "Real-Time Visibility-Based Fusion of Depth Maps," in *2007 IEEE 11th International Conference on Computer Vision*, 2007, pp. 1–8. DOI: 10.1109/ICCV.2007.4408984.

[69] C. Mobley *et al.*, "The Oceanic Optics Book," 2022.

[70] J. S. Jaffe, "Computer modeling and the design of optimal underwater imaging systems," *IEEE Journal of Oceanic Engineering*, vol. 15, no. 2, pp. 101–111, 1990.

[71] B. McGlamery, "A computer model for underwater camera systems," in *Ocean Optics VI*, SPIE, vol. 208, 1980, pp. 221–231.

[72] C. D. Mobley, *Light and water: radiative transfer in natural waters*. Academic press, 1994.

[73] J. T. Dietrich, "Bathymetric structure-from-motion: Extracting shallow stream bathymetry from multi-view stereo photogrammetry," *Earth Surface Processes and Landforms*, vol. 42, no. 2, pp. 355–364, 2017.

[74] Y.-H. Kwon, "Object plane deformation due to refraction in two-dimensional underwater motion analysis," *Journal of Applied Biomechanics*, vol. 15, no. 4, pp. 396–403, 1999.

[75] A. Jordt-Sedlazeck and R. Koch, "Refractive structure-from-motion on underwater images," in *Proceedings of the IEEE international Conference on Computer Vision*, 2013, pp. 57–64.

[76] A. Jordt-Sedlazeck, D. Jung, and R. Koch, "Refractive plane sweep for underwater images," in *Pattern Recognition: 35th German Conference, GCPR 2013, Saarbrücken, Germany, September 3-6, 2013. Proceedings 35*, Springer, 2013, pp. 333–342.

[77] H.-G. Maas, "On the accuracy potential in underwater/multimedia photogrammetry," *Sensors*, vol. 15, no. 8, pp. 18 140–18 152, 2015.

[78] G. Telem and S. Filin, "Photogrammetric modeling of underwater environments," *ISPRS journal of photogrammetry and remote sensing*, vol. 65, no. 5, pp. 433–444, 2010.

[79] A. Woodget, P. Carbonneau, F. Visser, and I. P. Maddock, "Quantifying submerged fluvial topography using hyperspatial resolution UAS imagery and structure from motion photogrammetry," *Earth Surface Processes and Landforms*, vol. 40, no. 1, pp. 47–64, 2015.

[80] B. Sun, J. Zhu, L. Yang, S. Yang, and Z. Niu, "Calibration of line-scan cameras for precision measurement," *Applied optics*, vol. 55, no. 25, pp. 6836–6843, 2016.

[81] The PyVista Developers. "PyVista: 3D plotting and mesh analysis through a streamlined interface for the Visualization Toolkit (VTK)." (), [Online]. Available: https://docs.pyvista.org/version/stable/index.html (visited on 05/14/2023).

[82] I. Wald, S. Woop, C. Benthin, G. S. Johnson, and M. Ernst, "Embree: A kernel framework for efficient CPU ray tracing," *ACM Transactions on Graphics (TOG)*, vol. 33, no. 4, pp. 1–8, 2014.

[83] K. Mikolajczyk and C. Schmid, "A performance evaluation of local descriptors," *IEEE transactions on pattern analysis and machine intelligence*, vol. 27, no. 10, pp. 1615–1630, 2005.

[84] J. Suomalainen, N. Anders, S. Iqbal, G. Roerink, J. Franke, P. Wenting, D. Hünniger, H. Bartholomeus, R. Becker, and L. Kooistra, "A lightweight hyperspectral mapping system and photogrammetric processing chain for unmanned aerial vehicles," *Remote Sensing*, vol. 6, no. 11, pp. 11 013–11 030, 2014.

[85] A. Habib, W. Xiong, F. He, H. L. Yang, and M. Crawford, "Improving orthorectification of UAV-based push-broom scanner imagery using derived orthophotos from frame cameras," *IEEE Journal of Selected Topics in Applied Earth Observations and Remote Sensing*, vol. 10, no. 1, pp. 262–276, 2016.

[86] Ø. Sture, "Autonomous Exploration for Marine Minerals," Ph.D. dissertation, Norwegian University of Science and Technology Trondheim, Norway, 2022, pp. 131–152.

[87] calib.io. "Camera Calibration Best Practices." (), [Online]. Available: https://calib.io/blogs/knowledge-base/calibration-best-practices (visited on 05/15/2023).

[88] P. Kumar, N. Gracias, K. Istenič, R. Garcia, A. Arnaubec, M. Ferrera, and T. Bajjouk, "Combined use of a frame and a linear pushbroom camera for deep-sea 3D hyperspectral mapping," in *OCEANS 2021: San Diego–Porto*, IEEE, 2021, pp. 1–9.

[89] D. R. Lyzenga, N. P. Malinas, and F. J. Tanis, "Multispectral bathymetry using a simple physically based algorithm," *IEEE Transactions on Geoscience and Remote Sensing*, vol. 44, no. 8, pp. 2251–2259, 2006.

[90] M. G. Solonenko and C. D. Mobley, "Inherent optical properties of Jerlov water types," *Applied optics*, vol. 54, no. 17, pp. 5392–5401, 2015.

[91] A. Gordon and M. R. Knittel, "Underwater Multiple Scattering of Light for System Designers. Part 1. An Exponential Multiple-Scattering Mode. Part 2. Evaluation of the Exponential Multiple-Scattering Model," NAVAL UNDERSEA CENTER SAN DIEGO CA, Tech. Rep., 1973.

[92] W. Hou, D. J. Gray, A. D. Weidemann, and R. A. Arnone, "Comparison and validation of point spread models for imaging in natural waters," *Optics Express*, vol. 16, no. 13, pp. 9958–9965, 2008.

[93] C. D. Mobley, H. Zhang, and K. J. Voss, "Effects of optically shallow bottoms on upwelling radiances: Bidirectional reflectance distribution function effects," *Limnology and Oceanography*, vol. 48, no. 1part2, pp. 337–345, 2003.

[94] T. J. Petzold, "Volume scattering functions for selected ocean waters," Scripps Institution of Oceanography La Jolla Ca Visibility Lab, Tech. Rep., 1972.

[95] C. D. Mobley, L. K. Sundman, and E. Boss, "Phase function effects on oceanic light fields," *Applied optics*, vol. 41, no. 6, pp. 1035–1050, 2002.

[96] M. Bryson, M. Johnson-Roberson, O. Pizarro, and S. B. Williams, "True color correction of autonomous underwater vehicle imagery," *Journal of Field Robotics*, vol. 33, no. 6, pp. 853–874, 2016.

[97] F. Sigernes, J. M. Holmes, M. Dyrland, D. A. Lorentzen, T. Svenøe, K. Heia, T. Aso, S. Chernouss, and C. S. Deehr, "Sensitivity calibration of digital colour cameras for auroral imaging," *Optics express*, vol. 16, no. 20, pp. 15 623–15 632, 2008.

[98] D. Akkaynak, T. Treibitz, T. Shlesinger, Y. Loya, R. Tamir, and D. Iluz, "What is the space of attenuation coefficients in underwater computer vision?" In *Proceedings of the IEEE Conference on Computer Vision and Pattern Recognition*, 2017, pp. 4931–4940.

[99] I. Dumke, S. M. Nornes, A. Purser, Y. Marcon, M. Ludvigsen, S. L. Ellefmo, G. Johnsen, and F. Søreide, "First hyperspectral imaging survey of the deep seafloor: High-resolution mapping of manganese nodules," *Remote Sensing of Environment*, vol. 209, pp. 19–30, 2018.

Chapter 7

Collection of Articles

J.1 A Methodology for Consistent Georegistration in Underwater Hyperspectral Imaging

J.2 Remote Sensing of the Tautra Ridge: An Overview of the World's Shallowest Cold-Water Coral Reefs

frontiers in Marine Science

ORIGINAL RESEARCH
published: 28 March 2022
doi: 10.3389/fmars.2022.848888

Remote Sensing of the Tautra Ridge: An Overview of the World's Shallowest Cold-Water Coral Reefs

Aksel Alstad Mogstad[1], Håvard Snefjellå Løvås[2], Øystein Sture[2], Geir Johnsen[1,3] and Martin Ludvigsen[2]*

[1] Centre for Autonomous Marine Operations and Systems, Department of Biology, Norwegian University of Science and Technology (NTNU), Trondheim, Norway, [2] Centre for Autonomous Marine Operations and Systems, Department of Marine Technology, Norwegian University of Science and Technology (NTNU), Trondheim, Norway, [3] Arctic Biology Department, University Centre in Svalbard (UNIS), Longyearbyen, Norway

OPEN ACCESS

Edited by:
Anthony Grehan, National University of Ireland Galway, Ireland

Reviewed by:
Erik Cordes, Temple University, United States
Alessandra Savini, University of Milano-Bicocca, Italy

****Correspondence:***
Aksel Alstad Mogstad
aksel.a.mogstad@ntnu.no

Specialty section:
This article was submitted to Deep-Sea Environments and Ecology, a section of the journal Frontiers in Marine Science

Received: *05 January 2022*
Accepted: *01 March 2022*
Published: *28 March 2022*

Citation:
Mogstad AA, Løvås HS, Sture Ø, Johnsen G and Ludvigsen M (2022) Remote Sensing of the Tautra Ridge: An Overview of the World's Shallowest Cold-Water Coral Reefs. Front. Mar. Sci. 9:848888. doi: 10.3389/fmars.2022.848888

On the Tautra Ridge – a 39-100 m deep morainic sill located in the middle of the Trondheimsfjord, Norway – some of the world's shallowest known occurrences of the scleractinian cold-water coral (CWC) *Desmophyllum pertusum* can be found. The earliest *D. pertusum* records from the Tautra Ridge date back to the 18th century, and since then, the location has provided easy access to physical coral specimens for numerous scientific studies. In 2013, the ridge was declared a marine protected area by the Norwegian Government due to its unique CWC reefs. However, few attempts have to our knowledge yet been made to characterize the distribution, extent and condition of these reefs extensively. The aim of the current study was therefore to add geospatial context to the Tautra CWC reef complex. In the study, data from multibeam echo sounding, synthetic aperture sonar imaging and underwater hyperspectral imaging are used to assess CWC reef occurrences from multiple perspectives. The study demonstrates how complementary remote sensing techniques can be used to increase knowledge generation during seafloor mapping efforts. Ultimately, predictive modeling based on seafloor geomorphometry is used to estimate both distribution and areal coverage of *D. pertusum* reefs along the majority of the Tautra Ridge. Our findings suggest that *D. pertusum* reef distribution on the Tautra Ridge is affected by several geomorphometric seafloor properties, and that the total reef extent in the area likely is close to 0.64 km^2. Better description of current patterns across the Tautra Ridge will improve our understanding of the interaction between hydrography and geomorphology at the Tautra CWC reef complex in the future.

Keywords: cold-water corals, *Desmophyllum pertusum*, *Lophelia pertusa*, habitat mapping, predictive modeling, multibeam echo sounding (MBES), synthetic aperture sonar (SAS) imaging, underwater hyperspectral imaging (UHI)

1 INTRODUCTION

Situated between 63°40'N 9°45'E and 64°0'N 11°30'E, the 135 km long Trondheimsfjord is one of Norway's largest fjord systems. The fjord system consists of three main basins: the 617 m deep outer basin, the 440 m deep middle basin and the 270 m deep inner basin (Jacobson, 1983). These basins – respectively denoted as B1, B2 and B3 in **Figure 1A** – are separated by morainic sills of glacial debris deposited during the Younger Dryas cooling period (Sakshaug and Sneli, 2000). Whereas the surface layer of the Trondheimsfjord (0-25 m deep) to a large extent is characterized by freshwater influx from surrounding rivers, the fjord's deeper water layers (>50 m during summer) are dominated by a mixture of saline and well-oxygenated Atlantic water (AW) and Norwegian coastal water (NCW). The annual influx of AW and NCW into the fjord system exchanges all water masses below the surface layer twice a year. This provides a relatively stable deep-water environment, with salinities >34, temperatures typically ranging from 7 to 7.5°C and oxygen levels >6 mL L^{-1} throughout the year (Sakshaug and Sneli, 2000). At the morainic sills, the fjord's rapid water exchange rate and semidiurnal tidal patterns are manifested as strong currents with speeds typically ranging from 0.4 to 1m s^{-1} (Jacobson, 1983). These currents, and the suspended food particles they carry, provide suitable conditions for sessile suspension feeders, and at the sill separating the outer basin from the middle basin – the Tautra Ridge – a particularly spectacular suspension feeder assemblage can be found (Sakshaug and Sneli, 2000; Mortensen and Fosså, 2001).

Extending from 63°36'30"N 10°30'E to 63°34'N 10°35'E, the ~6-km Tautra Ridge supports some of the world's shallowest cold-water coral (CWC) reefs (39 m; Brooke and Järnegren, 2013). A reef is here defined as a biogenic framework consisting of both living and dead coral. Radiocarbon labelling suggests that the Tautra Ridge was formed 10,800-10,500 ^{14}C years BP (Reite, 1995; Lysså et al., 2008), and with depths generally ranging from 39 to 100 m, it spans the full width of the Trondheimsfjord (**Figure 1B**). The CWCs associated with the Tautra Ridge do not form a continuous reef structure, but rather a complex of discrete, adjacent CWC build-ups ranging from 10 to 10^5 m^2 in size (Mortensen and Fosså, 2001). The currents across the ridge are influenced by season, tide and local bathymetry, but can invariably be considered strong. At 80-m depth, eastward currents with speeds up to 0.7 m s^{-1} have for instance been recorded (Jacobson, 1983). Over the past decades, the biological value of the Tautra Ridge has become increasingly acknowledged by the Norwegian Government, and in 2013, the ridge was named one of Norway's first marine protected areas (MPAs; Lovdata, 2013).

The species that dominates the Tautra CWC reef complex is the scleractinian coral *Desmophyllum pertusum* (Linnaeus, 1758), formerly known as *Lophelia pertusa*. *Desmophyllum pertusum* is a cosmopolitan coral species that so far has proven to be particularly abundant in the North Atlantic and its associated fjord systems (Davies et al., 2008). Its known depth range spans all the way from 39 m at the Tautra Ridge to a maximum recorded depth of 3,383 m in the Northwest Atlantic (Squire, 1959). On the Norwegian continental shelf, *D. pertusum*

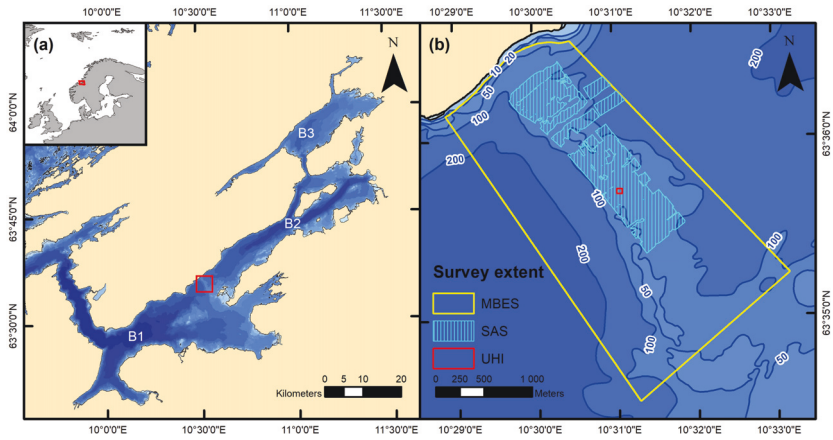

FIGURE 1 | The area surveyed in the current study. Panel **(A)** shows a map of the Trondheimsfjord with the fjord's geographic position indicated in the upper left corner. B1, B2 and B3 correspond to the fjord's outer, middle and inner basin, respectively. The red square indicates the position of the Tautra Ridge and the extent of panel **(B)**. Panel **(B)** shows a depth contour map of the most pronounced part of the Tautra Ridge (depths are given in meters) and the spatial extent of the datasets utilized in the study. The data were obtained using three different techniques: multibeam echo sounding (MBES), synthetic aperture sonar (SAS) imaging and underwater hyperspectral imaging (UHI). The maps were created in ArcMap (v. 10.8; Esri Inc., Redlands, USA; https://desktop.arcgis.com/en/arcmap/). The depth contour maps are based on data from the Norwegian Mapping Authority (Kartverket), available at https://kartkatalog.geonorge.no/Metadata/dybdedata/2751aacf-5472-4850-a208-3532a51c529a under CC BY 4.0 license. Projection: UTM 32N. Datum: WGS 1984.

is most common at 200-400-m depths, but in Norwegian fjords, it is frequently encountered in shallower waters (Mortensen et al., 1995; Fosså et al., 2002). On a general basis, *D. pertusum* can be considered relatively tolerant with respect to environmental variables (Järnegren and Kutti, 2014). In the Northeast Atlantic, it does, however, seem to prefer salinities close to 35, temperatures of 6-9°C and oxygen levels of 6.0-6.2 mL L^{-1} (Davies et al., 2008; Roberts et al., 2009), which coincides well with the environmental conditions at the Tautra Ridge.

Desmophyllum pertusum's ability to create complex, three-dimensional reef structures makes it an important ecosystem engineer in cold waters (Jones et al., 1994; Mortensen et al., 2010). Despite its slow growth rate (typically <1 cm $year^{-1}$; Sabatier et al., 2012), the species is capable of forming vast bioherms, and the biggest *D. pertusum* reef complex known to date is the ~40 km long Røst Reef off the coast of northern Norway (Fosså et al., 2005). As a structure-forming ecosystem engineer, *D. pertusum* provides substrate and shelter to a range of benthic and demersal organisms. In the Northeast Atlantic as a whole, it is known to co-occur with >1,300 species (Roberts et al., 2006), and at the Tautra Ridge, >120 macrofaunal species have so far been documented (Mortensen and Fosså, 2001; Costello et al., 2005; Mortensen and Fosså, 2006). Historically, published studies of the Tautra CWC reef complex have relied heavily on physical point sampling. However, there also exist non-invasive methods of obtaining coral information that hitherto have remained relatively unexplored in the current study area.

Desmophyllum pertusum's eco-geographical preferences and morphological properties make the Tautra CWC reef complex an interesting target for acoustic remote sensing surveys. From a geomorphometric perspective, *D. pertusum* in the Northeast Atlantic is for instance known to be associated with bathymetric highs, steep slopes and irregular seafloor surfaces (Mortensen et al., 2001; Davies et al., 2008; Davies et al., 2017), all of which are seafloor variables that can be quantified using, e.g., multibeam echo sounding (MBES; Wilson et al., 2007). Furthermore, the corals themselves may on multiple levels serve as suitable targets for acoustic detection. Firstly, being a scleractinian coral species, *D. pertusum* deposits calcium carbonate in the form of aragonite in order to grow. In Norwegian waters, the solid aragonite skeletons of dense *D. pertusum* frameworks have been shown to produce stronger MBES backscatter than, e.g., soft-bottom sediments, which may provide a partial means of reef identification (Fosså et al., 2005). It should, however, be noted that this is not necessarily thought to be the case if the corals grow in less dense frameworks. Secondly, vertical coral growth may generate abrupt angles between the reef perimeter and the surrounding seafloor. This is an attribute that can be identified by side-scanning sonar systems, which produce imagery where protruding seafloor features typically display strong acoustic backscatter and cast distinctive acoustic shadows (Fosså et al., 1997; Blondel, 2009). Finally, and perhaps most importantly, *D. pertusum*'s complex three-dimensionality potentially gives its reefs characteristic acoustic signatures in sonar imagery. In Norwegian waters, *D. pertusum* often has a tightly branching and hemispherical growth pattern, which typically is manifested as noisy, rough-textured areas, sometimes referred to as "cauliflower patterns" (Freiwald et al., 2002; Fosså et al., 2005; De Clippele et al., 2018). In 2012, the Tautra Ridge was acoustically surveyed using a HUGIN 1000 autonomous underwater vehicle (AUV) from Kongsberg Maritime AS (Kongsberg, Norway). The HUGIN AUV was equipped with a synthetic aperture sonar (SAS), and the recorded sonar imagery clearly revealed the presence of cauliflower-patterned reef structures (Ludvigsen et al., 2014). Sture et al. (2018) later demonstrated that these *D. pertusum* reefs could be accurately identified in SAS imagery by applying a convolutional neural network (CNN) classification algorithm.

The morphological properties of *D. pertusum* also permit reef detection by means of optical remote sensing. Most notably, *D. pertusum* is known to have two distinct color phenotypes: white and orange. Both phenotypes spectrally differ considerably from dead coral structures, which potentially may constitute >70% of the reef framework (Vad et al., 2017). The reason as to why the two phenotypes exist and grow side by side is currently a topic under investigation. What is known, is that the color difference as such likely is caused by carotenoid pigments, such as astaxanthin, which are more than twice as abundant in the orange phenotype (Elde et al., 2012). What is yet to be determined, is the exact mechanism behind the difference in carotenoid contents. One of the leading hypotheses is currently that the coloration is linked to the bacterial composition of the *D. pertusum* mucus layer, which further is thought to influence the coral's nutritional uptake (Neulinger et al., 2008; Provan et al., 2016). From a physiological perspective, the difference between the two phenotypes is also unclear, but findings from a recent study by Büscher et al. (2019) suggest that the orange phenotype may be more resistant to stress than its white counterpart. At present, only a few published studies feature optical survey results from the Tautra CWC reef complex. In September 2000, the northwestern part of the Tautra Ridge was optically investigated using a remotely operated vehicle (ROV) equipped with two video cameras (Mortensen and Fosså, 2001). The survey was performed by the Norwegian Institute of Marine Research and aimed to map *D. pertusum* occurrences and associated biodiversity. In total, ~6,200 m of video transect were analyzed, and the documented biodiversity was found to be greater than that of equivalent seafloor areas on the Norwegian continental shelf. In 2012, a small area (200-300 m^2) of the Tautra Ridge was surveyed in detail using an ROV equipped with two video cameras, a downward-facing digital camera and an underwater hyperspectral imager (Ludvigsen et al., 2014; Johnsen et al., 2016). During the survey, *D. pertusum* was optically confirmed to be present, but the resulting data were not analyzed extensively. More recently, ROV-acquired video from the Tautra Ridge was used to verify coral presence in acoustic SAS imagery (Sture et al., 2018). Here, the optical information served as a useful qualitative guide, but the video data were not assessed quantitatively.

Over the past decade, the Norwegian University of Science and Technology (NTNU) has collected both acoustic and optical

remote sensing datasets from the Tautra Ridge and its associated *D. pertusum* reefs. However, very little of this material has to date been published in a geospatial context. The aim of the current study was therefore to synthesize available data to provide enhanced insight into the frequently referenced but poorly documented Tautra CWC reef complex.

The study utilized data from three major remote sensing techniques: (1) ship-based MBES, (2) AUV-based SAS imaging and (3) ROV-based underwater hyperspectral imaging (UHI; **Figure 1B**). Data from the first of these techniques were used to estimate seven geomorphometric seafloor variables covering most of the Tautra Ridge, whereas data from the latter two techniques were used to outline and characterize *D. pertusum* occurrences at two different spatial scales. Ultimately, geomorphometric variable values from areas with and without corals present were compared, and an attempt was made to predict CWC reef distribution along the ridge. **Figure 2** shows a flowchart that outlines the steps presented in the *Materials and Methods* section.

2 MATERIALS AND METHODS

2.1 MBES Data

In April 2016, a georeferenced MBES point cloud from the most pronounced part of the Tautra Ridge was obtained from the Norwegian Mapping Authority's Hydrographic Service (Kartverket Sjødivisjonen, Stavanger, Norway). The point cloud had been collected using a Kongsberg EM 710 MBES system (Kongsberg Maritime AS, Kongsberg, Norway) onboard the survey vessel MS Hydrograf. The data were initially classified, but approved for release to NTNU's Applied Underwater Robotics Laboratory (AURLab) for the purpose of research and education. The released MBES data featured detailed bathymetric information but did not contain information on acoustic backscatter intensity. Based on the MBES point cloud, a gridded bathymetric dataset with a spatial resolution of 2 m x 2 m was generated. This dataset covered an area of 6.23 km^2 and served as the basis for all geomorphometric analyses presented herein.

2.2 SAS Data

The SAS data utilized in the current study were collected in December 2012 during a joint research cruise arranged by NTNU's AURLab and the Norwegian Defense Research Establishment (FFI, Kjeller, Norway). To record sonar imagery, a Kongsberg HiSAS 1030 synthetic aperture sonar system (Kongsberg Maritime AS, Kongsberg, Norway) was deployed on a HUGIN 1000 AUV. As opposed to regular side-scanning sonar systems, SAS systems utilize more than a single ping to reconstruct a given location in the output imagery, which improves spatial resolution both across- and along-track (Hansen et al., 2004; Sture et al., 2018). Using the SAS-equipped HUGIN AUV, the northwestern region of the Tautra Ridge was surveyed in a systematic lawnmower pattern at a mean seafloor altitude of 26 m. The resulting imagery was post-processed in Kongsberg Maritime's "Reflection" software, and ultimately georeferenced at a pixel resolution of 4 cm x 4 cm. The final SAS mosaic covered a seafloor area of ~1 km^2.

2.3 UHI Data

A Tautra Ridge CWC reef situated at 80-m depth at approximately 63°35'43"N 10°31'3"E was optically surveyed by NTNU's AURLab in March 2017. The survey utilized a SUB-fighter 30k ROV (Sperre AS, Notodden, Norway) equipped with a 4th generation underwater hyperspectral imager (UHI-4) from Ecotone AS (Trondheim, Norway). UHI-4 is an optical imager that contains two cameras: (1) a regular digital camera (red, green, blue; RGB) and (2) a hyperspectral push-broom scanner capable of recording imagery where each pixel holds a

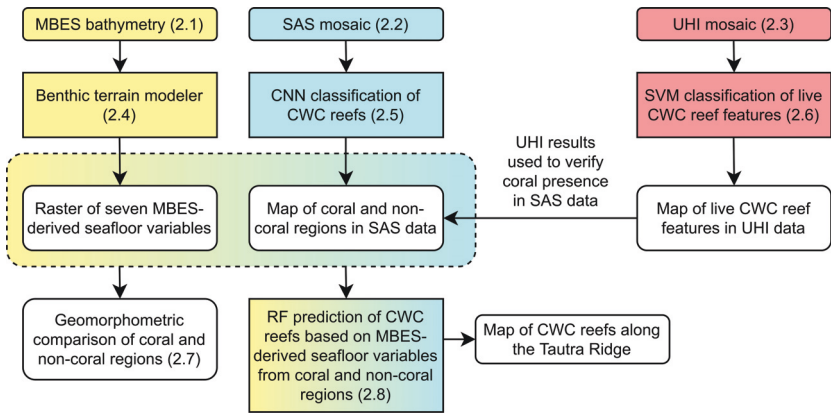

FIGURE 2 | Flowchart of the steps presented in the *Materials and Methods* Section (sections *2.1-2.8*). CNN, convolutional neural network; CWC, cold-water coral; MBES, multibeam echo sounding; SAS, synthetic aperture sonar; SVM, support-vector machine; UHI, underwater hyperspectral imaging.

contiguous light spectrum as opposed to an RGB value. The high spectral resolution of the technique potentially provides an enhanced data foundation with potential for the identification of spectral signatures ("fingerprints") that may be useful for automated mapping of seafloor features based on color. Being a push-broom scanner, the latter camera operates by capturing hyperspectral pixel rows through a narrow light entrance slit at a fixed frame rate. To provide spatially coherent hyperspectral imagery, UHI-4 must therefore be maneuvered in straight lines across the given area of interest, with the light entrance slit of the hyperspectral camera oriented perpendicularly to the instrument platform's heading. Over the past decade, UHI-based seafloor studies have been carried out within a variety of fields (e.g., marine biology and archaeology), and for an overview of the technique, see Liu et al. (2020) and Montes-Herrera et al. (2021).

For the current study's optical survey, UHI-4 was mounted on the SUB-fighter 30k ROV in a nadir viewing position, with two downward-facing 250-W Deep Multi SeaLite halogen lamps (DeepSea Power & Light LLC, San Diego, USA) placed 35 cm port and starboard of the instrument. The ROV was subsequently deployed at the survey location, using NTNU's research vessel, RV Gunnerus. To provide geospatial context to the data acquisition, the ROV utilized a dynamic positioning system (Sørensen et al., 2012) and a navigation filter aided by an acoustic ultra-short baseline (USBL) positioning system mounted on the surface vessel. This permitted the ROV to follow a pre-programmed lawnmower pattern at a seafloor altitude of 2 m. The pattern consisted of 13 parallel, partially overlapping transects and covered a reef area of approximately 800 m^2. While following the pattern, UHI-4 captured optical imagery according to the settings specified in **Table 1**.

Following the optical data acquisition, the imagery was processed in a succession of steps, according to the procedure described in Løvås et al. (2021). First, the acquired RGB imagery (a total of 21,702 images) was used to generate a three-dimensional (3D) model of the survey area in the photogrammetry software Agisoft Metashape Professional (v. 1.6.2; Agisoft LLC, St. Petersburg, Russia). This model provided highly detailed estimates of UHI-4's position (northing, easting and depth) and orientation (pitch, roll and yaw) over the course of the survey. Using these estimates, the underwater hyperspectral imagery was subsequently ray-casted onto the 3D model according to the hyperspectral push-broom scanner's known geometric model relative to the RGB camera. By estimating the geographic intersections between the 3D model and the push-broom scanner's field of view (FOV), the hyperspectral imagery was georeferenced on a pixel-specific basis at a spatial resolution of 1 cm x 1 cm. Ultimately, the georeferenced UHI data were converted from spectral radiance ($L(\lambda)$) to spectral reflectance ($R(\lambda)$) using Beer-Lambert's law for non-scattering media modified from Mobley (1994). The final UHI mosaic covered an area of ~787 m^2 (see **Supplementary Figure S1**).

2.4 Estimation of Geomorphometric MBES Variables

The MBES-derived depth data from the Tautra Ridge were analyzed in the geospatial processing software ArcMap (v. 10.8; Esri Inc., Redlands, USA) using the Benthic Terrain Modeler (BTM) 3.0 plug-in (Walbridge et al., 2018). In addition to depth, six geomorphometric variables were estimated: broad bathymetric position index (BPI broad), fine bathymetric position index (BPI fine), slope, ruggedness, eastness and northness. While depth corresponds to a grid cell's vertical position relative to the sea surface, BPIs are calculated based on neighborhood analyses and indicate a grid cell's bathymetric position relative to its surroundings. The exact value range of a BPI will depend on the dataset as well as the chosen analysis settings. Positive and negative values respectively denote bathymetric highs (e.g., ridges and mounds) and lows (e.g., valleys and troughs), whereas values close to 0 represent flat or constantly sloping seafloor areas (Weiss, 2001). As a rule, finer-scale BPIs (smaller neighborhood sizes) are potentially capable of picking up smaller bathymetric features of interest. In the current study, the broad- and fine-scale BPIs were standardized according to Weiss (2001). The slope variable indicates the maximum rate of bathymetric change between a grid cell and its neighbors. Slope is typically given in degrees (°), and possible values range from 0 (flat areas) to 90 (vertical drops). Ruggedness can be characterized as the degree of three-dimensional variation within a grid cell neighborhood. It is calculated based on dispersion of orthogonal grid cell vectors within the given neighborhood, and possible values range from 0 (completely homogeneous surface) to 1 (completely heterogeneous surface). Finally, the variables eastness and northness both relate to the aspect (direction) of a grid cell's downslope. Possible values for the two variables range from -1 to 1, where -1 denotes an entirely westward (eastness) or southward (northness) downslope direction and 1 denotes an entirely eastward (eastness) or northward (northness) downslope direction. The settings used to derive the geomorphometric variables in the BTM 3.0 ArcMap plug-in are listed in **Table 2**.

TABLE 1 | UHI-4 specifications relevant for the 2017 cold-water coral (CWC) survey on the Tautra Ridge.

UHI-4 survey specifications	RGB camera	Hyperspectral push-broom scanner
Spectral properties	3 wavebands (RGB)	380-750 nm spectral range, 1.65-nm spectral resolution (224 bands)
Spatial resolution	648 x 486 pixels	960 x 1 pixels
Bit resolution	8-bit	12-bit
Field of view (FOV)	62.2° transversal, 48.7° longitudinal	54.1° transversal, 0.4° longitudinal
Frame rate	5 Hz	50 Hz
Exposure time	10 ms	20 ms

TABLE 2 | Settings used to estimate six geomorphometric variables in the Benthic Terrain Modeler (BTM) 3.0 ArcMap plug-in.

Geomorphometric variable	Neighborhood (grid cells)	Neighborhood (size)
BPI broad (standardized)	225-cell radius	450-m radius
BPI fine (standardized)	75-cell radius	150-m radius
Slope (°) [0, 90]	3 x 3 cell grid	36 m^2
Ruggedness [0, 1]	3 x 3 cell grid	36 m^2
Eastness [-1, 1]	3 x 3 cell grid	36 m^2
Northness [-1, 1]	3 x 3 cell grid	36 m^2

The variables were calculated based on multibeam echo sounding (MBES)-derived depth data from the most pronounced part of the Tautra Ridge. The gridded bathymetric dataset had a spatial resolution of 2 m x 2 m.

2.5 Estimation of CWC Reef Distribution in SAS Imagery

CWC reef distribution in the full Tautra Ridge SAS mosaic from 2012 was estimated using a CNN classifier. In recent years, CNNs have grown to become powerful deep learning tools for classifying data that are structured in multiple arrays (e.g., two-dimensional imagery; LeCun et al., 2015). A CNN consists of a set of alternating convolution and pooling layers. During training, each kernel-based convolution layer generates a set of unique feature maps, which subsequently are downsampled in a pooling layer to reduce computational time in the next round of convolutions. Ultimately, all feature maps and their neural couplings are assembled to one or more fully connected layers capable of recognizing patterns based on the utilized training data. When new data are provided to a pre-trained CNN classifier, the output is typically a vector or matrix of probabilistic values corresponding to the input data's likelihood of belonging to different classes.

The CNN classifier used in the current study was implemented in TensorFlow Keras (Abadi et al., 2016). Structurally, the CNN consisted of four blocks of convolution/pooling, followed by two fully connected layers. The classifier was trained on a selection of SAS image subsets (100 x 100 pixels) from three different HUGIN AUV deployments. All training data had a spatial pixel resolution of 4 cm x 4 cm, and the total CNN training set consisted of >30,000 images distributed among two classes: images with *D. pertusum* present and images with *D. pertusum* absent. Of the full training set, 20% of the images were set aside for model validation, and for the final classification model, an accuracy of 95% was reported. For further details on the development and training of the CNN, see Sture et al. (2018).

Applying the pre-trained CNN to the full Tautra Ridge SAS mosaic yielded a CWC reef distribution map with a spatial resolution of 80 cm x 80 cm, where each grid cell contained a georeferenced probability (0-1) of coral presence. These probabilities were subsequently labeled into three discrete classes: the coral class (grid cells with a probability of coral presence >0.99), the control class (grid cells with a probability of coral presence <0.50) and the intermediate class (all remaining grid cells). The thresholds used to define the classes were chosen subjectively based on their perceived ability to accurately isolate coral regions (the coral class) from non-coral regions (the control class). The seafloor regions outlined by the coral class and the control class later provided the basis for the assessment of geomorphometric trends related to *D. pertusum* coverage on the Tautra Ridge.

2.6 Estimation of Live CWC Reef Coverage in Underwater Hyperspectral Imagery

To estimate live CWC reef coverage in the UHI survey area, the underwater hyperspectral imagery was analyzed using support-vector machine (SVM) classification with a radial basis function (RBF) kernel. The SVM algorithm uses vector-defined decision surfaces to maximize the margins between the provided training set classes and is known to be well-suited for high-dimensional datasets (Cortes and Vapnik, 1995; Mountrakis et al., 2011). It has also performed favorably in previous seafloor mapping studies featuring UHI (Chennu et al., 2017; Dumke et al., 2018; Mogstad et al., 2020). During the optical CWC survey in March 2017, the live fraction of the present CWC reef framework was observed to primarily consist of white *D. pertusum*, orange *D. pertusum* and the sponge *Mycale* cf. *lingua* (Bowerbank, 1866). The spectral signatures of these species were consequently chosen as supervised classification targets.

For the SVM classification, the georeferenced UHI mosaic was spectrally subset to the range of 400-650 nm and binned down to a spectral resolution of 3.3 nm, resulting in a total of 75 color bands (wavelengths). This was done to remove wavelengths with low signal-to-noise ratio and to make the ensuing spectral classification computationally less intensive. SVM training data were subsequently obtained from pixel regions of the UHI mosaic corresponding to white *D. pertusum*, orange *D. pertusum* and *Mycale* cf. *lingua*. The total training set consisted of 2,400 pixels, evenly distributed among the three spectral targets (the $R(\lambda)$ signatures of the different targets are shown in **Supplementary Figure S2**). By performing a ten-fold cross-validation on the selected training data in the statistical software environment R (v. 4.0.2; R Foundation for Statistical Computing, Vienna, Austria) using the package "e1071" (Meyer et al., 2020), the optimal values for RBF-SVM parameters γ (kernel width) and C (degree of regularization) were in the current study found to be 1e-05 and 1e06, respectively (cross-validation accuracy = 100%). Using these parameter values, the SVM classification algorithm was ultimately applied to the full UHI mosaic in the software application ENVI (Environment for Visualizing Images, v. 5.6; Harris Geospatial Solutions Inc., Broomfield, USA). The full classification was performed with a probability threshold of 0.95, implying that only pixels with probabilities of belonging to a training set class beyond 0.95 were classified.

2.7 Geomorphometric Comparison of Coral and Non-Coral Regions

For the geomorphometric comparison of coral and non-coral regions, all MBES-derived seafloor variables (depth, BPI broad, BPI fine, slope, ruggedness, eastness and northness) were combined into a single 7-band raster. From the combined raster, values from grid cells covered entirely by either the coral class or the control class of the classified CNN coral distribution map were subsequently extracted for analysis. The extracted dataset consisted of 24,388 coral cells and 122,963 control cells (each cell corresponding to a 2 m x 2 m area). For each MBES-derived variable, the median and interquartile range was calculated for both classes, and a two-sided Mann-Whitney rank sum test was performed to investigate whether coral regions differed significantly from control regions.

2.8 Geomorphometric CWC Reef Classification

To assess the feasibility of CWC reef identification by means of geomorphometry alone, the dataset extracted in *Geomorphometric Comparison of Coral and Non-Coral Regions* was also used to generate a random forest (RF) prediction model. An RF is an assemblage of decision trees created from randomly selected subsets (bootstrapped samples) of the provided training data (Breiman, 2001). For classification purposes, RF training data are typically composed of one categorical response variable (class) and a set of corresponding explanatory variables (predictors). When an unclassified sample is provided to a pre-trained RF prediction model, all decision trees individually vote for the most likely class based on the values of the provided predictors. These votes are subsequently pooled together, and the final output from the RF algorithm is the class that obtained the majority vote (the dichotomization may alternatively be decided by a user-defined probability cutoff). In the current study, the RF algorithm was chosen due to its ability to handle complex interactions, correlated predictors and irregular variable distributions (Cutler et al., 2007). In addition, the RF algorithm has yielded promising results in previous attempts to classify CWC reef structures in MBES-derived data (De Clippele et al., 2017; Diesing and Thorsnes, 2018).

For the RF classification, the extracted data were randomly partitioned into a training set (80% of the samples), a validation set (10% of the samples) and a test set (10% of the samples). The ratio of coral samples to control samples was equal in all partitions (approximately 1:5). The RF prediction model was developed in the statistical software environment R using the package "randomForest" (Liaw and Wiener, 2002). RF modeling requires specification of two parameters: the number of decision trees to grow (n_{tree}) and the number of features (predictor variables) to consider during each split (m_{try}). These parameters were optimized using ten-fold cross-validation, which revealed that n_{tree} = 1000 and m_{try} = 5 yielded the best tradeoff between accuracy (out-of-bag error rate = 0.08) and processing time. By subsequently maximizing the model's overall classification accuracy (OCA) based on the validation set, the optimal probability cutoff for differentiating coral samples from control samples was found to be 0.42 (i.e., samples receiving >42% of the decision tree votes in favor of the coral class were considered to be coral). The final RF prediction model was applied to the test set, and the results were evaluated with respect to the performance metrics listed in **Table 3**.

Ultimately, CWC reef distribution was estimated along the Tautra Ridge by applying the RF prediction model to all regions of the full 7-band MBES raster that contained variable values inside the range of the RF training set (amounting to 4.55 km^2 of the full raster; regions with variable values exceeding the training set were omitted because RF predictions are known to be unreliable for samples outside the modeled range). For this classification, the results were dichotomized at three different probability cutoffs: maximized validation set OCA (probability cutoff = 0.42), validation set negative predictive value (NPV) = 0.95 (probability cutoff = 0.39) and validation set positive predictive value (PPV) = 0.95 (probability cutoff = 0.72). The former cutoff was chosen to provide a CWC reef coverage estimate with optimized accuracy. The latter two cutoffs were chosen to provide realistic upper and lower boundaries to the optimized estimate. The rationale behind choosing 0.39 as the upper boundary, was that at NPV = 0.95, at least 95% of the negative (control) predictions could be expected to be correct. Similarly, the rationale behind choosing 0.72 as the lower boundary, was that at PPV = 0.95, at least 95% of the positive (coral) predictions could be expected to be correct.

3 RESULTS

3.1 MBES and SAS Results

Figure 3A shows the MBES-derived bathymetric map used to acquire geomorphometric information from the Tautra Ridge. The structure of the ridge was evident in the map, with the ridge crest oriented perpendicularly to the fjord's direction (see **Figures 1**, **3A**) and notable downward slopes towards the southwest and northeast. Geographic heatmaps of the variables BPI broad, BPI fine, slope, ruggedness, eastness and northness are shown in **Supplementary Figure S3**.

The AUV-acquired SAS dataset covered ~1 km^2 of the 6.23 km^2 MBES-surveyed area (**Figure 3B**), and acoustic cauliflower patterns assumed to correspond to reef structures were interspersed throughout the SAS survey area (an example is shown in **Supplementary Figure S4**). Based on the results of the CNN prediction model (**Figure 3C**) and the classification thresholds defined in *Estimation of CWC Reef Distribution in SAS Imagery*, CWC reefs (the coral class) were estimated to cover 0.12 km^2 of the SAS-surveyed area, whereas non-coral regions (the control class) were estimated to cover 0.63 km^2 (**Figure 3D**). The intermediate class covered the remaining 0.25 km^2.

3.2 UHI Results

Overall, the UHI results agreed well with the acoustic findings from the SAS analysis. The georeferenced UHI mosaic covered an area of 786.7 m^2, and 661.5 m^2 of this area corresponded to regions acoustically identified as coral by the CNN classifier

TABLE 3 | Descriptions of performance metrics used to evaluate the random forest (RF) prediction model.

Performance metric	Description
Overall classification accuracy (OCA)	The proportion of correctly classified outcomes.
Sensitivity	The proportion of correctly classified positive outcomes (coral samples).
Specificity	The proportion of correctly classified negative outcomes (control samples).
Positive predictive value (PPV)	The proportion of correct positive predictions (also known as precision).
Negative predictive value (NPV)	The proportion of correct negative predictions.
Kappa coefficient	A measure of overall classification accuracy (OCA) adjusted for the accuracy that could be expected due to chance alone. A kappa of 1 indicates 100% classification accuracy, whereas a kappa of 0 indicates that the classifier performs no better than a random classifier. For further details, see Landis and Koch (1977).
Area under the receiver operating characteristic (AUROC) curve	The integrated area under the curve obtained by plotting true positive rate (sensitivity) as a function of false positive rate (1 – specificity). The higher the AUROC curve value (with 1 being the maximum value), the better the classifier is at discriminating between positive and negative outcomes. An AUROC curve value of 0.5 indicates that the classifier performs no better than a random classifier.
Mean decrease in accuracy (MDA)	The individual contribution of a given variable to the accuracy of a random forest (RF) prediction model. The MDA is estimated by calculating the mean decrease in prediction accuracy (among individual decision trees) that occurs when the values of the variable under investigation are permuted (randomized). The result is typically scaled by its standard deviation. Higher MDA values indicate higher variable importance, but the units are arbitrary, and the output should not be treated quantitatively.

(**Figure 4A**). Based on the hyperspectral SVM classification (**Figure 4B**), live reef structures (i.e., white *D. pertusum*, orange *D. pertusum* and the sponge *Mycale* cf. *lingua*) were estimated to cover 15.5% of the total UHI survey area and 17.3% of the UHI survey area identified as coral acoustically (**Table 4**). Within the surveyed area, white *D. pertusum* was estimated to be considerably more abundant than both orange *D. pertusum* and sponges (**Table 4**).

3.3 Geomorphometric Comparison of Coral and Non-Coral Regions

Probability densities of the geomorphometric variable values extracted from coral and control regions on the Tautra Ridge are shown in **Figure 5**. For all MBES-derived variables, the distribution differed significantly between the two classes (**Table 5**). Furthermore, for all but one of the variables (BPI broad being the exception), slightly elevated values were associated with the coral class. For the exception – BPI broad – the coral class displayed the highest median value, but the lowest overall value distribution (**Figure 5B**). The magnitude of the observed class difference varied between variables, and the most significant class discrepancies were observed for depth, slope, ruggedness and eastness (**Table 5**).

3.4 Geomorphometric CWC Reef Classification

The test set performance of the RF prediction model is summarized in the **Table 6** confusion matrix. In total, the model performed well, with an OCA of 0.92 and an area under the receiver operating characteristic (AUROC) curve value of 0.95 (**Figure 6A**). Moreover, the obtained kappa coefficient of 0.71 indicated substantial agreement between predictions and true sample identities (Landis and Koch, 1977). However, the model was not without imperfections, and based on the observed sensitivity, specificity, PPV and NPV (**Table 6**), the model appeared to display a slight tendency towards underestimating coral abundance.

In terms of individual predictor importance, the variable slope contributed the most to the prediction model's accuracy (**Figure 6B**). In descending order, the variables depth, eastness, BPI broad and ruggedness made intermediate contributions, whereas northness and BPI fine contributed the least. The significance of these findings is further discussed in *Geomorphometric CWC Coverage Trends*.

Applying the RF prediction model to the 7-band MBES raster with the probability cutoffs defined in **Figure 7A** yielded the CWC reef coverage estimates displayed in **Figure 7B** and **Table 7**. The returned estimates ranged from 0.19 km^2 to 0.72 km^2, with the optimized OCA estimate suggesting a Tautra Ridge CWC reef coverage of 0.64 km^2. **Figure 8** shows a spatial representation of the RF classification results. Predicted CWC reef units were interspersed along the entire ridge, and within the regions surveyed by SAS and UHI, estimated coral coverage largely appeared to agree between the different remote sensing techniques (**Supplementary Figure S4**).

4 DISCUSSION

4.1 Survey Techniques and Assumptions

The current study illustrated the value of applying multiple remote sensing techniques during the investigation and mapping of CWC reefs. At present, MBES systems (typically deployed on surface vessels) arguably represent the most efficient way of geospatially mapping ≥km-scale benthic habitats dominated by large biogenic structures. In previous CWC studies, MBES-derived data have for instance been used to

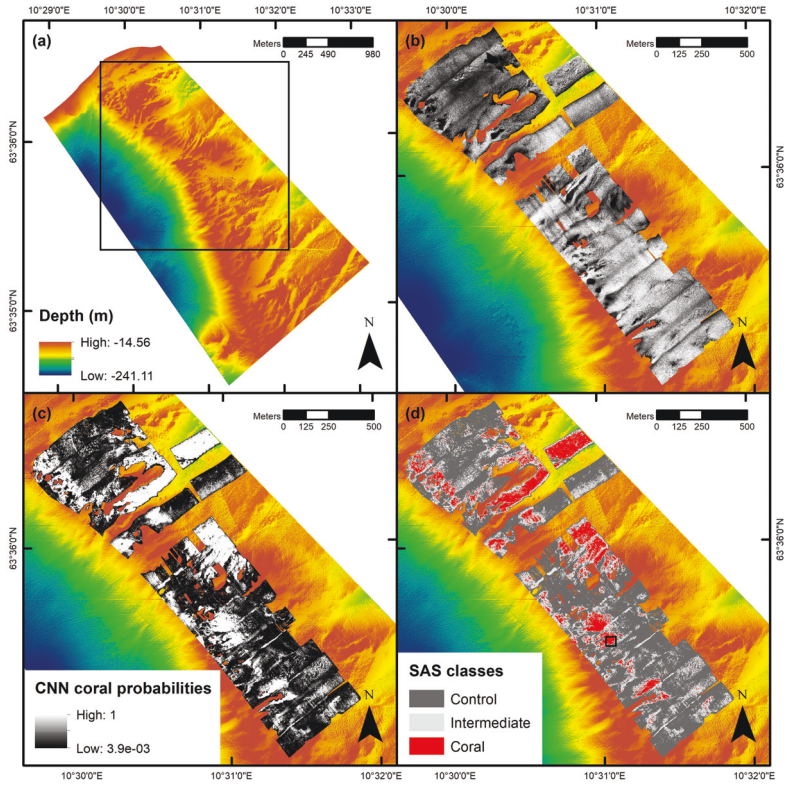

FIGURE 3 | Multibeam echo sounding (MBES) and synthetic aperture sonar (SAS) imaging results. Panel **(A)** shows the MBES-derived bathymetric map of the most pronounced part of the Tautra Ridge (declassified bathymetry, map courtesy of the Norwegian Mapping Authority). The black square indicates the spatial extent of panels (B-D). Panel **(B)** shows the Tautra Ridge SAS mosaic. Panel **(C)** shows the georeferenced probabilities of coral presence obtained from the convolutional neural network (CNN). Panel **(D)** shows the classified coral distribution map generated based on the probabilities in panel **(C)** and the thresholds defined in *Estimation of CWC Reef Distribution in SAS Imagery*. The black square indicates the position of the underwater hyperspectral imaging (UHI) mosaic presented in **Figure 4**. The maps were created in ArcMap (v. 10.8; Esri Inc., Redlands, USA; https://desktop.arcgis.com/en/arcmap/). Projection: UTM 32N. Datum: WGS 1984.

address issues ranging from localized distribution of CWC reefs (Roberts et al., 2005; Guinan et al., 2009a; De Clippele et al., 2017; Diesing and Thorsnes, 2018) to *D. pertusum* habitat suitability along the entire Norwegian continental shelf (Sundahl et al., 2020). MBES also proved valuable in the current assessment of the Tautra Ridge, especially with respect to its superior capacity for areal coverage. To fully capitalize on its potential, a sufficiently extensive ground truth dataset was, however, a vital prerequisite. As shown in this study, the ground truthing requirements concerning MBES mapping of *D. pertusum* reefs could be fulfilled by combining AUV-based SAS imaging with an ROV-based UHI survey. These two ground truthing techniques represented incremental steps towards increased level of detail in the remote sensing pyramid of observation. In the first step, distinct acoustic patterns assumed to belong to *D. pertusum* permitted estimation of CWC reef coverage in a ~1-km^2 subset of the MBES-surveyed area. In the second step, the identity of the acoustic patterns assumed to belong to *D. pertusum* was verified optically in an ~800-m^2 area. This optical verification increased the confidence not only in the SAS classification accuracy, but also the georeferencing of the SAS dataset, which eventually were to guide the MBES-based CWC reef classification along the entire Tautra Ridge. In summary, all remote sensing techniques employed in the current study played complementary roles in the quest for holistic knowledge: ROV-based optical imaging provided data with unprecedented spatial resolution and ground truthing accuracy but was limited in terms of areal coverage; AUV-based sonar imaging could detect acoustically distinct biogenic structures in large areas but provided little information besides from the geographic extent of the targets of interest; ship-based MBES was limited with respect to spatial resolution but generated data that covered the entire area of interest and brought geomorphometric context to the identified targets. The potential value of using data from multiple sensors and platforms during

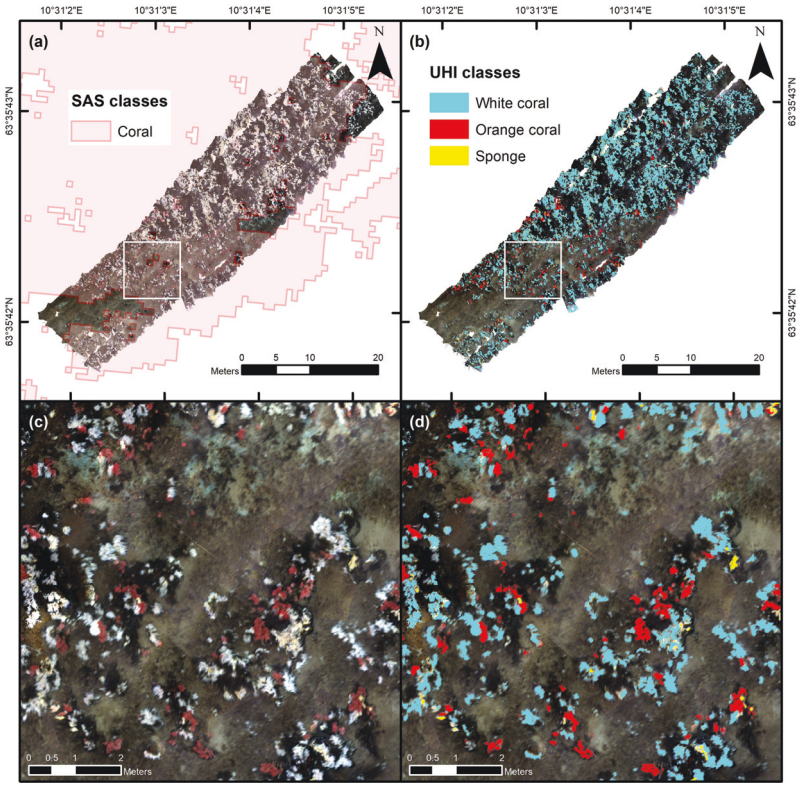

FIGURE 4 | Underwater hyperspectral imaging (UHI) results. Panel **(A)** shows the georeferenced UHI mosaic visualized in red (R; 590 nm), green (G; 530 nm) and blue (B; 460 nm). Regions in the synthetic aperture sonar (SAS) imagery classified as "coral" by the convolutional neural network (CNN) classifier (see *Estimation of CWC Reef Distribution in SAS Imagery*) are highlighted in pink for comparison. Panel **(B)** shows the results of the hyperspectral support-vector machine (SVM) classification of UHI classes corresponding to live reef structures. Panels **(C, D)** show the areas indicated by white squares in panels **(A, B)**, respectively. The maps were created in ArcMap (v. 10.8; Esri Inc., Redlands, USA; https://desktop.arcgis.com/en/arcmap/). Projection: UTM 32N. Datum: WGS 1984.

marine exploration efforts is further elaborated in, e.g., the integrated mapping and monitoring approach proposed by Nilssen et al. (2015), and in the future, application of such approaches will likely become increasingly more important.

The validity of the presented Tautra Ridge findings rests on two principal assumptions. Firstly, it was assumed that the georeferencing of the different remote sensing datasets was consistent. As in any marine seafloor survey, minor geospatial discrepancies were expected, but upon inspection, the alignment of the MBES-, SAS- and UHI-acquired data was considered more than sufficient for the scope of the work. **Supplementary Figure S4** exemplifies the observed positional coherence. Secondly, it was

TABLE 4 | Results of the support-vector machine (SVM) classification of the underwater hyperspectral imaging (UHI) dataset from the Tautra Ridge.

UHI data selection	Total area		White coral		Orange coral		Sponge		Live reef	
	m^2	%	m^2	%	m^2	%	m^2	%	m^2	%
Full UHI mosaic	786.68	100	111.19	14.13	8.21	1.04	2.49	0.32	121.89	15.49
Acoustically identified coral regions*	661.47	100	103.95	15.71	7.82	1.18	2.39	0.36	114.16	17.26

*The table shows the estimated areal coverage (m^2 and %) of different spectral targets. The class "live reef" corresponds to "white coral", "orange coral" and "sponge" combined. The second row of the table only considers UHI data from geographic regions acoustically classified as "coral" by the convolutional neural network (CNN) classifier (see Estimation of CWC Reef Distribution in SAS Imagery and **Figure 4A**).*

The regions of the UHI dataset encompassed by the acoustic "coral" class in **Figure 4A.*

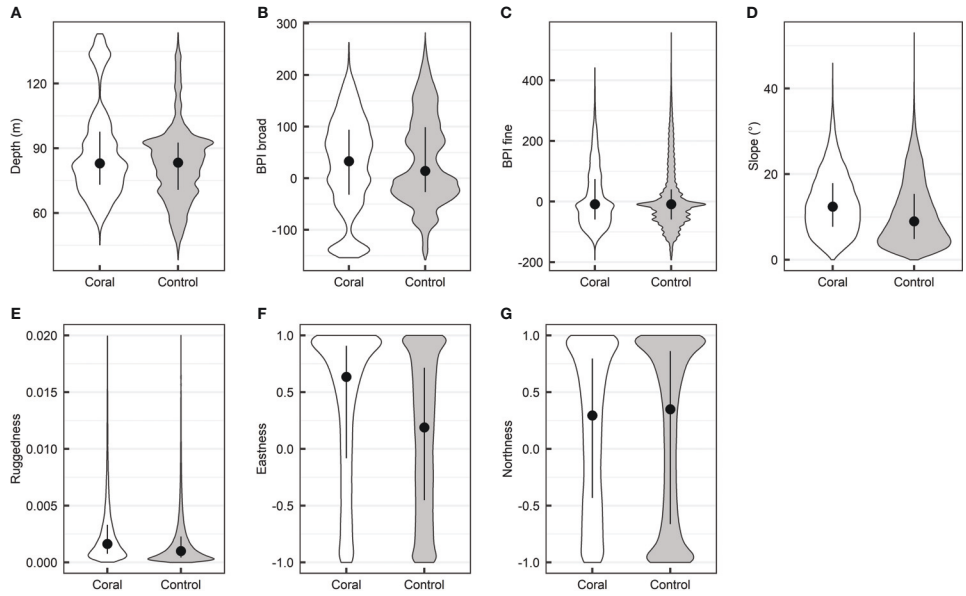

FIGURE 5 | Geomorphometric comparison of coral (n = 24,388 grid cells) and non-coral (control; n = 122,963 grid cells) regions on the Tautra Ridge. The data were obtained from areas classified as "coral" and "control" by the convolutional neural network (CNN) classifier (see *Estimation of CWC Reef Distribution in SAS Imagery*). The figure shows the class-specific median, interquartile range and probability density of seven multibeam echo sounding (MBES)-derived seafloor variables.

assumed that *D. pertusum* reef extent on the Tautra Ridge was unaltered between the acquisition of the first (December 2012) and the last (March 2017) dataset utilized in the study. It should be noted that this is an inherently erroneous assumption. However, considering *D. pertusum*'s slow growth rate (<1 cm year^{-1}; Sabatier et al., 2012), and that the Tautra Ridge is an MPA where physical seafloor intervention is prohibited, it was nevertheless deemed reasonable for the analyses presented herein.

4.2 Optical CWC Coverage Trends

ROV-based UHI proved to be a valuable ground truthing technique for optical verification of acoustic CWC reef predictions. This is exemplified in **Figure 4A** and **Supplementary Figure S4**, where the CWC reef contours predicted by the acoustic CNN classifier closely match the coral distribution that can be observed in the recorded hyperspectral imagery. In addition to serving as a means of verifying reef presence, the optical UHI survey provided useful information on the survey area's biological reef composition. Hyperspectral SVM classification for instance indicated that live *D. pertusum* and associated sponges covered ~17% of the regions in the survey area acoustically classified as coral (**Table 4**). Although this estimate only is based on spatially two-dimensional image analyses from a bird's-eye view, it is exceptionally consistent with findings from a study by Vad et al. (2017), in which the ratio of live *D. pertusum* to whole colony size (i.e., both live and dead coral structures) ranged from 0.10 to 0.27, with a mean value of 0.17. The study by Vad et al. was carried out off the west coast of Scotland at relatively remote locations. If these locations are assumed to represent healthy CWC habitats and the estimated proportion of live coral (~17%) is used as a proxy for health, it can further be speculated that the Tautra Ridge CWC reef optically surveyed in the current study was in good condition. Regarding *D. pertusum* phenotype distribution, hyperspectral SVM classification revealed that the white *D. pertusum* phenotype was an order of magnitude more abundant than the orange phenotype within the UHI survey area (**Figure 4B** and **Table 4**). This trend is in accordance with observations from several other *D. pertusum* studies (Roberts, 2002; Larcom et al., 2014; Kellogg et al., 2017; Büscher et al., 2019), but its underlying cause remains to be determined. Overall, the UHI results showed that live *D. pertusum* easily could be mapped based on its spectral properties. One of the main benefits of applying UHI for the purpose of optical coral mapping was that live coral coverage accurately could be estimated using supervised classification (**Figures 4C, D**). Notably, the hyperspectral SVM classification only utilized a training set of 2,400 labeled pixels, which merely corresponded to 0.03% of the total UHI mosaic. This vastly increased data processing efficiency and firmly illustrated the value of employing automated approaches to optical seafloor mapping. In the future, we recommend conducting similar optical surveys at other CWC reefs on the Tautra Ridge. This will help substantiate the trends observed in the current study and

TABLE 5 | Geomorphometric comparison of coral and non-coral (control) regions on the Tautra Ridge.

Seafloor variable	Coral(*n* = 24,388 grid cells)			Control(*n* = 122,963 grid cells)			Mann-Whitney rank sum test (*p*-value)	Median sample difference
	Q1	Median	Q3	Q1	Median	Q3		
Depth (m)	73.10	83.00	97.68	70.70	83.35	92.58	<2.2e-16	2.76
BPI broad	-32.00	33.00	94.00	-27.00	14.00	99.00	2.7e-05	-4.00
BPI fine	-59.00	-9.00	74.00	-59.00	-9.00	40.00	2.1e-04	2.4e-06
Slope (°)	7.71	12.41	17.87	4.84	8.99	15.37	<2.2e-16	2.72
Ruggedness	7.7e-04	1.6e-03	3.4e-03	4.3e-04	1.0e-03	2.3e-03	<2.2e-16	4.5e-04
Eastness	-0.08	0.63	0.91	-0.45	0.19	0.71	<2.2e-16	0.24
Northness	-0.43	0.29	0.80	-0.66	0.35	0.86	1.3e-04	9.2e-03

The data were obtained from areas classified as "coral" and "control" by the convolutional neural network (CNN) classifier (see Estimation of CWC Reef Distribution in SAS Imagery). The class-specific median and interquartile range is shown for seven multibeam echo sounding (MBES)-derived seafloor variables. The latter two columns show the results of variable-specific, two-sided Mann-Whitney rank sum tests comparing the two classes. The median sample difference is reported relative to the control class.

improve our understanding of the Tautra CWC reef complex as a whole.

4.3 Geomorphometric CWC Coverage Trends

The comparison of coral and non-coral regions on the Tautra Ridge revealed that *D. pertusum* appeared to have certain preferences with respect to local geomorphometric seafloor variables. In the Mann-Whitney rank sum tests performed to compare coral-covered regions to their surroundings, the value distributions of all investigated variables were for instance found to significantly differ between the two seafloor classes (**Table 5**). However, some variables displayed more pronounced trends than others, and in terms of the observed probability densities, the variables slope and eastness stood out the most (**Figures 5D, F**). Specifically, the coral class was associated with steeper slopes (median = 12.41°; median sample difference = 2.72°) and more eastward-oriented terrain (median = 0.63; median sample difference = 0.24) than the control class. The former observation agrees well with findings from previous CWC studies from the Northeast Atlantic, which also suggest that *D. pertusum* prefers sloping terrain (Davies et al., 2008; Guinan et al., 2009b; Howell et al., 2011). The main reason for this preference is thought to be that slope-induced hydrodynamic phenomena (e.g., localized current patterns) may enhance the availability of suspended food particles (Frederiksen et al., 1992; Thiem et al., 2006; Davies et al., 2009). The interpretation of the latter observation is less clear-cut, as any preference with respect to aspect direction (in this case eastness) likely is linked to the directional dynamics of the surrounding currents. Being sessile suspension feeders, CWCs are often found to be associated with enhanced bottom currents (White and Dorschel, 2010). However, laboratory-based studies by Purser et al. (2010) and Orejas et al. (2016) suggest that excessive current velocities may impede *D. pertusum*'s food uptake. These findings are supported by a recent *in situ* study by Lim et al. (2020), in which current velocities ≥75 cm s^{-1} were found to restrict live *D. pertusum* coverage. Furthermore, at the Piddington Mound – a coral mound in the Porcupine Seabight exposed to current velocities of ~40 cm s^{-1} – live CWC reef framework was primarily found on the lee side of the mound (Lim et al., 2017). Interestingly, the interval of 40-75 cm s^{-1} coincides almost perfectly with the maximum bottom current speeds measured across the Tautra Ridge over the course of June 1974 (Jacobson, 1983). Since it also is known that the prevailing direction of these currents is eastward (Jacobson, 1983), a possible explanation for *D. pertusum*'s apparent inclination towards eastness on the Tautra Ridge (i.e., the lee side of the ridge) is therefore that it reduces current exposure to a level that facilitates the corals' food uptake. To further investigate this hypothesis, we recommend deploying acoustic Doppler current profilers (ADCPs) at multiple locations on the Tautra Ridge over time, so that the spatiotemporal complexities of the *in situ* current patterns can be elucidated. In addition, routine surveys with ADCP-equipped AUVs along the ridge should be carried out, so that site-specific current measurements can be put into a broader spatial perspective.

Although less pronounced, some noteworthy coral coverage trends were also observed for the variables depth, BPI broad and ruggedness. Overall, the coral class was for instance found to be associated with slightly deeper waters and slightly lower BPI broad scores (**Figures 5A, B** and **Table 5**) than the control class. This initially seemed counterintuitive, as *D. pertusum* commonly is known to occur on bathymetric highs (Davies et al., 2008). However, these observations are, in fact, in accordance with the

TABLE 6 | Confusion matrix displaying the test set performance of the random forest (RF) prediction model.

Predicted class	True class		Total
	Coral (positive)	Control (negative)	
Coral (positive)	1,777	484	2,261
Control (negative)	661	11,812	12,473
Total	2,438	12,296	14,734

Accuracy metrics are summarized below the table. The probability cutoff utilized for differentiating coral samples from control samples was 0.42 (see Geomorphometric CWC Reef Classification).

Overall classification accuracy (OCA): 0.92; sensitivity: 0.73; specificity: 0.96; positive predictive value (PPV): 0.79; negative predictive value (NPV): 0.95; kappa coefficient: 0.71.

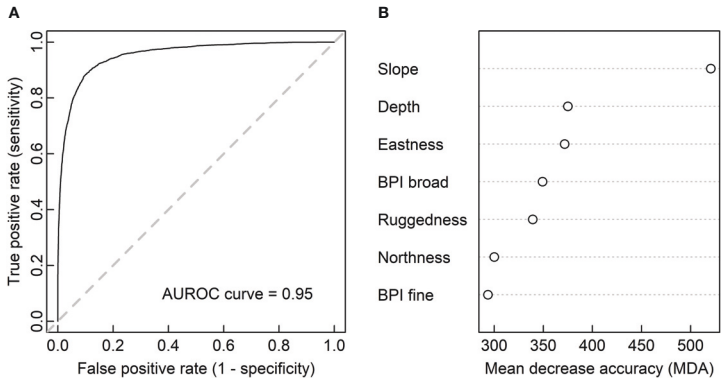

FIGURE 6 | Results of the random forest (RF) coral classification. Panel **(A)** shows the prediction model's area under the receiver operating characteristic (AUROC) curve for the test set. The dashed diagonal line symbolizes a hypothetical AUROC curve value of 0.5 (no ability to discriminate between coral and control samples). Panel **(B)** shows the RF prediction model's mean decrease in accuracy (MDA; scaled by standard deviation) among decision trees when individual variables are randomized. Higher MDA values indicate higher variable contributions to the model's performance.

hypothesis stated in the previous paragraph: assuming the currents across the Tautra Ridge are strong enough to potentially impede *D. pertusum*'s food uptake or inflict unnecessary physical strain, it would be suboptimal for the corals to settle on the summit of the ridge. This could partially explain the observed patterns. It should be noted that the values of both depth and BPI broad displayed highly irregular probability densities, and their interpretation should consequently be treated with caution. Regarding ruggedness, the coral class was associated with significantly higher values than the control class (**Table 5**). This agrees with coarse-scale studies by Guinan et al. (2009b) and Davies et al. (2008), where *D. pertusum* also was found to be associated with irregular bathymetry. More importantly, it agrees with acoustic findings from a fine-scale CWC study by De Clippele et al. (2017), which was performed at a spatial resolution of 2 m. The reason for this tendency could be that bathymetric complexity is linked to increased access to suspended nutrition, reduced levels of sedimentation and/or a wider variability of substrate types (possibly favoring larval settling). However, at the high spatial resolution utilized in the current study (**Table 2**), the enhanced ruggedness could also be attributed to the three-dimensionality

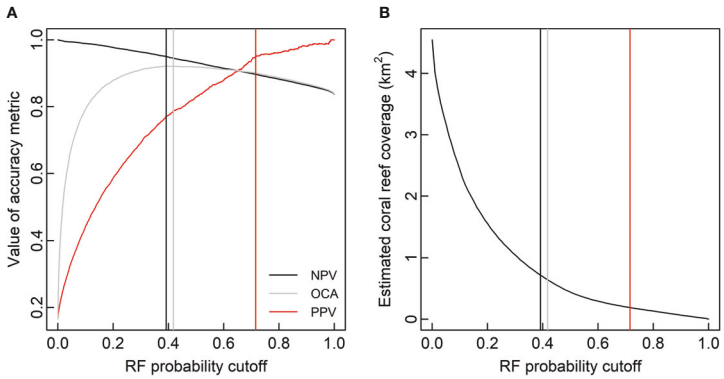

FIGURE 7 | Cold-water coral (CWC) reef coverage along the Tautra Ridge estimated by the random forest (RF) prediction model at different probability cutoffs. Panel **(A)** shows the RF prediction model's validation set negative predictive value (NPV), overall classification accuracy (OCA) and positive predictive value (PPV) plotted as functions of probability cutoff. The black, gray and red vertical lines respectively correspond to probability cutoffs where NPV = 0.95, OCA is maximized (0.92) and PPV = 0.95. Panel **(B)** shows estimated CWC reef coverage along the Tautra Ridge plotted as a function of RF probability cutoff. The vertical lines correspond to the three cutoffs defined in panel **(A)**.

TABLE 7 | Tautra Ridge cold-water coral (CWC) reef coverage estimated by the random forest (RF) prediction model at three different probability cutoffs.

RF probability cutoff	Rationale behind chosen cutoff	Estimated CWC reef coverage (m^2)	Estimated proportion of CWC reefs in raster regions within the modeled RF range (%)
0.39	Validation set negative predictive value (NPV) = 0.95	719,288	15.82
0.42*	Maximized validation set overall classification accuracy (OCA; 0.92)	642,932	14.14
0.72	Validation set positive predictive value (PPV) = 0.95	190,248	4.18

Cutoff used to evaluate test set performance (Table 6**).*

of the *D. pertusum* reef structures themselves. For instance, Price et al. (2019) and Price et al. (2021) recently utilized 3D models with sub-cm resolution to show that the structural complexity of CWC reefs often is considerably greater than that of surrounding non-reef regions. The least significant geomorphometric trends were observed for BPI fine and northness (**Figures 5C, G** and **Table 5**). For these variables, the coral class and the control class displayed highly similar median values and probability densities. This suggests that neither conveyed indispensable information with respect to CWC reef distribution in the current study.

4.4 Performance of the Geomorphometric CWC Reef Prediction Model

The RF model created to predict CWC reef coverage along the Tautra Ridge performed very well on the test set. As an example, all obtained accuracy metrics (**Figure 6A** and **Table 6**) were comparable to or exceeded those reported in similar studies by De Clippele et al. (2017) and Diesing and Thorsnes (2018). The RF probability cutoff that yielded the highest OCA resulted in a sensitivity of 0.73, a specificity of 0.96, a PPV of 0.79 and an NPV of 0.95. These results – specifically that sensitivity < PPV and specificity > NPV – indicate that the model was inclined to predict false negatives (type II errors) rather than false positives (type I errors). This may be interpreted as the model being conservative rather than exaggerated. The five predictors that contributed the most to the accuracy of the model were the variables slope, depth, eastness, BPI broad and ruggedness (**Figure 6B**). This was not surprising, considering that these were also the variables where the greatest differences between coral and non-coral regions had been observed previously (**Figure 5** and **Table 5**). As the RF model applied in the current study only was based on seven geomorphometric variables derived from the same MBES dataset, its favorable performance can likely be attributed to the quality and size of the utilized training set. This emphasizes the importance of high-quality ground truthing, and attests to the value of applying multiple sensors and platforms in future studies of CWC reefs. Because the Tautra Ridge represents an unusual CWC habitat, it is unlikely that the utilized model can be directly applied to other locations. However, as the model was built and implemented in open-source software, the methodology can easily be adapted for other situations, provided that similar remote sensing data are available. An interesting future project would be to apply equivalent acoustic prediction models to CWC habitats where

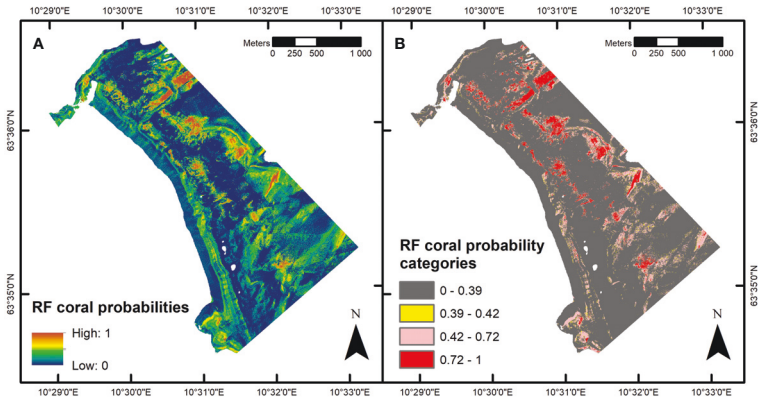

FIGURE 8 | Estimated cold-water coral (CWC) reef distribution along the Tautra Ridge. Panel **(A)** shows floating point probabilities of coral presence estimated by the random forest (RF) prediction model. Panel **(B)** shows CWC reef distribution estimated at different probability cutoffs (see *Geomorphometric CWC Reef Classification* and **Figure 7**). The maps were generated in ArcMap (v. 10.8; Esri Inc., Redlands, USA; https://desktop.arcgis.com/en/arcmap/). Projection: UTM 32N. Datum: WGS 1984.

D. pertusum is known to form other reef frameworks than the dense cauliflower patterns present on the Tautra Ridge. Examples of such frameworks include fan-like growth patterns found in the Mediterranean Sea and columnar growth patterns found in the Gulf of Mexico and the Florida Straits (Sanna and Freiwald, 2021).

Although the RF prediction model performed favorably, inclusion of certain additional predictors could likely have enhanced its performance. Howell et al. (2011) for instance found substrate type to be highly important for predictive modeling of *D. pertusum* at coarser scales in the Northeast Atlantic. Similarly, Georgian et al. (2014) found that the availability of hard substrate was an important *D. pertusum* predictor in the Gulf of Mexico. In the current study, it is possible that acoustic backscatter intensity from MBES could have improved the coral prediction model by serving as a proxy for substrate type or capturing characteristic acoustic properties associated with coral presence (Fosså et al., 2005; Roberts et al., 2005). In addition to substrate, bottom current speed and direction have also proven to be useful variables in previous attempts to model CWC distribution (Davies et al., 2008; De Clippele et al., 2017; Sundahl et al., 2020). Unfortunately, sufficiently detailed data on the aforementioned variables were to our knowledge not available during the writing of this study. To increase the accuracy of future prediction models, it is therefore recommended that maps of substrate distribution, MBES backscatter intensity and current patterns on the Tautra Ridge are acquired.

5 CONCLUSIONS

The motivation behind the current study was to provide enhanced insight into the Tautra CWC reef complex, and based on the presented work, we believe the following can be presumed. Firstly, optical UHI analyses suggest that CWC reefs on the Tautra Ridge are dominated by the white *D. pertusum* phenotype. However, optical data were only acquired from a limited area, and further information is thus needed to support this claim. The underlying reason for the skewed phenotype distribution is also a topic that warrants further investigation. Secondly, acoustic analyses indicate that *D. pertusum* reef distribution on the Tautra Ridge is partially determined by bathymetric features. Specifically, relatively steep, eastward-sloping areas that are situated off the summit of the ridge appear to facilitate coral growth. The ultimate cause of this is likely linked to the patterns of the prevailing bottom currents, and further data on the surrounding hydrodynamic conditions can likely help elucidate the observed trends. Lastly, predictive modeling based on seafloor geomorphometry suggests that the following three conclusions can be drawn regarding *D. pertusum* reef extent on the Tautra Ridge: (1) *D. pertusum* reefs cover at least 0.19 km^2 of the Tautra Ridge; (2) it is likely that *D. pertusum* reef extent on the Tautra Ridge is close to 0.64 km^2; and (3) it is unlikely that *D. pertusum* reef extent on the Tautra Ridge currently exceeds 0.72 km^2.

To our knowledge, this is the first attempt to characterize distribution and areal coverage of *D. pertusum* reefs on the Tautra Ridge extensively. Consequently, there are few data available to verify CWC reef predictions beyond the areas surveyed by SAS and UHI in the current study. Nevertheless, we believe the modeled estimates presented herein represent a valuable knowledge basis that decision-making authorities may refer to in efforts to govern the Tautra Ridge MPA sustainably. Furthermore, the results of this study may serve as a foundation for future research carried out in the area. Although *D. pertusum* is thought to be a relatively tolerant CWC species, its slow growth rate and high importance as an ecosystem engineer makes it a primary conservation target. In an era of climate change and increasing anthropogenic pressure, mapping and monitoring of such targets can arguably be considered more important than ever. In the future, it is therefore recommended that systematic ground truthing surveys are conducted along the entire Tautra Ridge so that the coral estimates presented in this study can be further refined. This will provide baseline information that should be considered essential not only for satisfactory MPA management, but also the continued existence of some of the world's least conventional CWC reefs.

DATA AVAILABILITY STATEMENT

The raw data supporting the conclusions of this article will be made available by the authors, without undue reservation.

AUTHOR CONTRIBUTIONS

AM: developed the idea, participated in the data acquisition, performed data analysis and wrote the manuscript. HL and ØS: participated in the data acquisition, performed data analysis and provided textual input to the manuscript. GJ and ML: participated in the data acquisition and provided textual input to the manuscript. All authors contributed to the article and approved the submitted version.

FUNDING

This work has been carried out at the Centre for Autonomous Marine Operations and Systems (NTNU AMOS). This work was supported by the Research Council of Norway through the Centres of Excellence funding scheme (grant no. 223254 – NTNU AMOS).

ACKNOWLEDGMENTS

The authors would like to thank the Norwegian Mapping Authority's Hydrographic Service for providing MBES data from the Tautra Ridge. The authors would also like to thank the Norwegian Defense Research Establishment, NTNU's

AURLab and the crew of RV Gunnerus for their valuable contributions concerning data collection and preparation.

SUPPLEMENTARY MATERIAL

The Supplementary Material for this article can be found online at: https://www.frontiersin.org/articles/10.3389/fmars.2022.848888/full#supplementary-material.

Supplementary Figure 1 | The georeferenced underwater hyperspectral imaging (UHI) mosaic from the Tautra Ridge visualized in red (R; 590 nm), green (G; 530 nm) and blue (B; 460 nm). The map was created in ArcMap (v. 10.8; Esri Inc., Redlands, USA; https://desktop.arcgis.com/en/arcmap/). Projection: UTM 32N. Datum: WGS 1984.

Supplementary Figure 2 | The training data used for support-vector machine (SVM) classification of underwater hyperspectral imagery from the Tautra Ridge. Panels **(A-C)** show the spectral reflectance ($R(\lambda)$) signatures of white *Desmophyllum pertusum*, orange *D. pertusum* and the sponge *Mycale* cf. *lingua*, respectively (n = 800 hyperspectral image pixels per class). Mean $R(\lambda)$ signatures are shown in black. Panel **(D)** shows all mean $R(\lambda)$ signatures plotted together for comparison.

Supplementary Figure 3 | Maps of six multibeam echo sounding (MBES)-derived geomorphometric variables covering the majority of the Tautra Ridge (maps based on declassified bathymetry, courtesy of the Norwegian Mapping Authority). BPI, bathymetric position index. The maps were created in ArcMap (v. 10.8; Esri Inc., Redlands, USA; https://desktop.arcgis.com/en/arcmap/). Projection: UTM 32N. Datum: WGS 1984.

Supplementary Figure 4 | Comparison of different mapping techniques. Panels **(A, B)** show results of the synthetic aperture sonar (SAS) survey. Panels **(C, D)** show results of the underwater hyperspectral imaging (UHI) survey. Panels **(E, F)** show results of the multibeam echo sounding (MBES)-based random forest (RF) prediction model. All panels correspond to the same geographic area. The maps were created in ArcMap (v. 10.8; Esri Inc., Redlands, USA; https://desktop.arcgis.com/en/arcmap/). Projection: UTM 32N. Datum: WGS 1984.

REFERENCES

Abadi, M., Barham, P., Chen, J., Chen, Z., Davis, A., Dean, J., et al. (2016). "TensorFlow: A System for Large-Scale Machine Learning," in *12th USENIX Symposium on Operating Systems Design and Implementation (OSDI 16)* (USA).

Blondel, P. (2009). *The Handbook of Sidescan Sonar* (Berlin: Springer).

Breiman, L. (2001). Random Forests. *Mach. Learn.* 45, 5–32. doi: 10.1023/A:1010933404324

Brooke, S., and Järnegren, J. (2013). Reproductive Periodicity of the Scleractinian Coral *Lophelia pertusa* From the Trondheim Fjord, Norway. *Mar. Biol.* 160, 139–153. doi: 10.1007/s00227-012-2071-x

Büscher, J. V., Wisshak, M., Form, A. U., Titschack, J., Nachtigall, K., and Riebesell, U. (2019). *In Situ* Growth and Bioerosion Rates of *Lophelia pertusa* in a Norwegian Fjord and Open Shelf Cold-Water Coral Habitat. *PeerJ* 7, e7586. doi: 10.7717/peerj.7586

Chennu, A., Färber, P., De'ath, G., de Beer, D., and Fabricius, K. E. (2017). A Diver-Operated Hyperspectral Imaging and Topographic Surveying System for Automated Mapping of Benthic Habitats. *Sci. Rep.* 7, 7122. doi: 10.1038/s41598-017-07337-y

Cortes, C., and Vapnik, V. (1995). Support-Vector Networks. *Mach. Learn.* 20, 273–297. doi: 10.1007/BF00994018

Costello, M. J., McCrea, M., Freiwald, A., Lundälv, T., Jonsson, L., Bett, B. J., et al. (2005). "Role of Cold-Water Lophelia pertusa Coral Reefs as Fish Habitat in the NE Atlantic," in *Cold-Water Corals and Ecosystems*. Eds. A. Freiwald and J. M. Roberts (Berlin: Springer), 771–805.

Cutler, D. R., Edwards, T. C.Jr., Beard, K. H., Cutler, A., Hess, K. T., Gibson, J., et al. (2007). Random Forests for Classification in Ecology. *Ecology* 88, 2783–2792. doi: 10.1890/07-0539.1

Davies, A. J., Duineveld, G. C., Lavaleye, M. S., Bergman, M. J., van Haren, H., and Roberts, J. M. (2009). Downwelling and Deep-Water Bottom Currents as Food Supply Mechanisms to the Cold-Water Coral *Lophelia pertusa* (Scleractinia) at the Mingulay Reef Complex. *Limnol. Oceanogr.* 54, 620–629. doi: 10.4319/lo.2009.54.2.0620

Davies, J. S., Guillaumont, B., Tempera, F., Vertino, A., Beuck, L., Ólafsdóttir, S. H., et al. (2017). A New Classification Scheme of European Cold-Water Coral Habitats: Implications for Ecosystem-Based Management of the Deep Sea. *Deep Sea Res. II* 145, 102–109. doi: 10.1016/j.dsr2.2017.04.014

Davies, A. J., Wisshak, M., Orr, J. C., and Roberts, J. M. (2008). Predicting Suitable Habitat for the Cold-Water Coral *Lophelia pertusa* (Scleractinia). *Deep Sea Res. I* 55, 1048–1062. doi: 10.1016/j.dsr.2008.04.010

De Clippele, L. H., Gafeira, J., Robert, K., Hennige, S., Lavaleye, M. S., Duineveld, G. C. A., et al. (2017). Using Novel Acoustic and Visual Mapping Tools to Predict the Small-Scale Spatial Distribution of Live Biogenic Reef Framework in Cold-Water Coral Habitats. *Coral Reefs* 36, 255–268. doi: 10.1007/s00338-016-1519-8

De Clippele, L. H., Huvenne, V. A., Orejas, C., Lundälv, T., Fox, A., Hennige, S. J., et al. (2018). The Effect of Local Hydrodynamics on the Spatial Extent and Morphology of Cold-Water Coral Habitats at Tisler Reef, Norway. *Coral Reefs* 37, 253–266. doi: 10.1007/s00338-017-1653-y

Diesing, M., and Thorsnes, T. (2018). Mapping of Cold-Water Coral Carbonate Mounds Based on Geomorphometric Features: An Object-Based Approach. *Geosciences* 8, 34. doi: 10.3390/geosciences8020034

Dumke, I., Nornes, S. M., Purser, A., Marcon, Y., Ludvigsen, M., Ellefmo, S. L., et al. (2018). First Hyperspectral Imaging Survey of the Deep Seafloor: High-Resolution Mapping of Manganese Nodules. *Remote Sens. Environ.* 209, 19–30. doi: 10.1016/j.rse.2018.02.024

Elde, A. C., Pettersen, R., Bruheim, P., Järnegren, J., and Johnsen, G. (2012). Pigmentation and Spectral Absorbance Signatures in Deep-Water Corals From the Trondheimsfjord, Norway. *Mar. Drugs* 10, 1400–1411. doi: 10.3390/md10061400

Fosså, J. H., Furevik, D., and Mortensen, P. B. (1997). *Methods for Detecting and Mapping of Lophelia Coral Banks: Preliminary Results. ICES CM 1997/L:7* (Gdynia: ICES Benthos Ecology Working Group).

Fosså, J. H., Lindberg, B., Christensen, O., Lundälv, T., Svellingen, I., Mortensen, P. B., et al. (2005). "Mapping of Lophelia Reefs in Norway: Experiences and Survey Methods," in *Cold-Water Corals and Ecosystems*. Eds. A. Freiwald and J. M. Roberts (Berlin: Springer), 359–391.

Fosså, J. H., Mortensen, P. B., and Furevik, D. M. (2002). The Deep-Water Coral *Lophelia pertusa* in Norwegian Waters: Distribution and Fishery Impacts. *Hydrobiologia* 471, 1–12. doi: 10.1023/A:1016504430684

Frederiksen, R., Jensen, A., and Westerberg, H. (1992). The Distribution of the Scleractinian Coral *Lophelia pertusa* Around the Faroe Islands and the Relation to Internal Tidal Mixing. *Sarsia* 77, 157–171. doi: 10.1080/00364827.1992.10413502

Freiwald, A., Hühnerbach, V., Lindberg, B., Wilson, J. B., and Campbell, J. (2002). The Sula Reef Complex, Norwegian Shelf. *Facies* 47, 179–200. doi: 10.1007/BF02667712

Georgian, S. E., Shedd, W., and Cordes, E. E. (2014). High-Resolution Ecological Niche Modelling of the Cold-Water Coral *Lophelia pertusa* in the Gulf of Mexico. *Mar. Ecol. Prog. Ser.* 506, 145–161. doi: 10.3354/meps10816

Guinan, J., Brown, C., Dolan, M. F., and Grehan, A. J. (2009a). Ecological Niche Modelling of the Distribution of Cold-Water Coral Habitat Using Underwater Remote Sensing Data. *Ecol. Inform.* 4, 83–92. doi: 10.1016/j.ecoinf.2009.01.004

Guinan, J., Grehan, A. J., Dolan, M. F., and Brown, C. (2009b). Quantifying Relationships Between Video Observations of Cold-Water Coral Cover and Seafloor Features in Rockall Trough, West of Ireland. *Mar. Ecol. Prog. Ser.* 375, 125–138. doi: 10.3354/meps07739

Hansen, R. E., Sæbø, T. O., and Hagen, P. E. (2004). "Development of Synthetic Aperture Sonar for the HUGIN AUV," in *Proceedings of the Seventh European Conference on Underwater Acoustics, ECUA 2004* (Netherlands: Delft University of Technology).

Howell, K. L., Holt, R., Endrino, I. P., and Stewart, H. (2011). When the Species Is Also a Habitat: Comparing the Predictively Modelled Distributions of *Lophelia pertusa* and the Reef Habitat it Forms. *Biol. Conserv.* 144, 2656–2665. doi: 10.1016/j.biocon.2011.07.025

Jacobson, P. (1983). Physical Oceanography of the Trondheimsfjord. *Geophys. Astrophys. Fluid Dyn.* 26, 3–26. doi: 10.1080/03091928308221761

Järnegren, J., and Kutti, T. (2014). *Lophelia pertusa in Norwegian Waters. What Have We Learned Since 2008? NINA Report 1028* (Trondheim: Norwegian Institute for Nature Research).

Johnsen, G., Ludvigsen, M., Sørensen, A. J., and Aas, L. M. S. (2016). The Use of Underwater Hyperspectral Imaging Deployed on Remotely Operated Vehicles-Methods and Applications. *IFAC-PapersOnLine* 49, 476–481. doi: 10.1016/j.ifacol.2016.10.451

Jones, C. G., Lawton, J. H., and Shaehak, M. (1994). Organisms as Ecosystem Engineers. *Oikos* 69, 373–386. doi: 10.1007/978-1-4612-4018-1_14

Kellogg, C. A., Goldsmith, D. B., and Gray, M. A. (2017). Biogeographic Comparison of *Lophelia*-Associated Bacterial Communities in the Western Atlantic Reveals Conserved Core Microbiome. *Front. Microbiol.* 8, 796. doi: 10.3389/fmicb.2017.00796

Løvås, H. S., Mogstad, A. A., Sørensen, A. J., and Johnsen, G. (2021). A Methodology for Consistent Georegistration in Underwater Hyperspectral Imaging. *IEEE J. Oceanic Eng.* doi: 10.1109/JOE.2021.3108229.

Landis, J. R., and Koch, G. G. (1977). The Measurement of Observer Agreement for Categorical Data. *Biometrics* 33, 159–174. doi: 10.2307/2529310

Larcom, E. A., McKean, D. L., Brooks, J. M., and Fisher, C. R. (2014). Growth Rates, Densities, and Distribution of *Lophelia pertusa* on Artificial Structures in the Gulf of Mexico. *Deep Sea Res. I* 85, 101–109. doi: 10.1016/j.dsr.2013.12.005

LeCun, Y., Bengio, Y., and Hinton, G. (2015). Deep Learning. *Nature* 521, 436–444. doi: 10.1038/nature14539

Liaw, A., and Wiener, M. (2002). Classification and Regression by Randomforest. *R News* 2, 18–22.

Lim, A., Wheeler, A. J., and Arnaubec, A. (2017). High-Resolution Facies Zonation Within a Cold-Water Coral Mound: The Case of the Piddington Mound, Porcupine Seabight, NE Atlantic. *Mar. Geol.* 390, 120–130. doi: 10.1016/j.margeo.2017.06.009

Lim, A., Wheeler, A. J., Price, D. M., O'Reilly, L., Harris, K., and Conti, L. (2020). Influence of Benthic Currents on Cold-Water Coral Habitats: A Combined Benthic Monitoring and 3D Photogrammetric Investigation. *Sci. Rep.* 10, 19433. doi: 10.1038/s41598-020-76446-y

Liu, B., Liu, Z., Men, S., Li, Y., Ding, Z., He, J., et al. (2020). Underwater Hyperspectral Imaging Technology and Its Applications for Detecting and Mapping the Seafloor: A Review. *Sensors* 20, 4962. doi: 10.3390/s20174962

Lovdata. (2013). *Forskrift Om Vern Av Tauterryggen Marine Verneområde, Frosta Og Leksvik Kommuner, Nord-Trøndelag*. Available at: https://lovdata.no/dokument/LTII/forskrift/2013-06-21-693 (Accessed February 15, 2022).

Ludvigsen, M., Johnsen, G., Sørensen, A. J., Lågstad, P. A., and Ødegård, Ø. (2014). Scientific Operations Combining ROV and AUV in the Trondheim Fjord. *Mar. Technol. Soc J.* 48, 59–71. doi: 10.4031/MTSJ.48.2.3

Lyså, A., Hansen, L., Christensen, O., L`Heureux, J. S., Longva, O., Olsen, H. A., et al. (2008). Landscape Evolution and Slide Processes in a Glacioisostatic Rebound Area; a Combined Marine and Terrestrial Approach. *Mar. Geol.* 248, 53–73. doi: 10.1016/j.margeo.2007.10.008

Meyer, D., Dimitriadou, E., Hornik, K., Weingessel, A., and Leisch, F. (2020) *E1071: Misc Functions of the Department of Statistics, Probability Theory Group (Formerly: E1071), TU Wien. R Package Version 1.7-4*. Available at: https://CRAN.R-project.org/package=e1071 (Accessed 15 April 2021).

Mobley, C. D. (1994). *Light and Water: Radiative Transfer in Natural Waters* (San Diego: Academic Press).

Mogstad, A. A., Ødegård, Ø., Nornes, S. M., Ludvigsen, M., Johnsen, G., Sørensen, A. J., et al. (2020). Mapping the Historical Shipwreck Figaro in the High Arctic Using Underwater Sensor-Carrying Robots. *Remote Sens.* 12, 997. doi: 10.3390/rs12060997

Montes-Herrera, J. C., Cimoli, E., Cummings, V., Hill, N., Lucieer, A., and Lucieer, V. (2021). Underwater Hyperspectral Imaging (UHI): A Review of Systems and Applications for Proximal Seafloor Ecosystem Studies. *Remote Sens.* 13, 3451. doi: 10.3390/rs13173451

Mortensen, P. B., and Fosså, J. H. (2001). *Korallrev Og Andre Bunnhabitater På Tautraryggen I Trondheimsfjorden. Fisken Og Havet Report 7* (Bergen: Norwegian Institute of Marine Research).

Mortensen, P. B., and Fosså, J. H. (2006). "Species Diversity and Spatial Distribution of Invertebrates on Deep-Water Lophelia Reefs in Norway," in *Proceedings of 10th International Coral Reef Symposium* (Japan: International Society for Reef Studies, Japanese Coral Reef Society).

Mortensen, P. B., Hovland, M., Brattegard, T., and Farestveit, R. (1995). Deep Water Bioherms of the Scleractinian Coral *Lophelia pertusa* (L.) at 64°N on the Norwegian Shelf: Structure and Associated Megafauna. *Sarsia* 80, 145–158. doi: 10.1080/00364827.1995.10413586

Mortensen, P. B., Hovland, M. T., Fosså, J. H., and Furevik, D. M. (2001). Distribution, Abundance and Size of *Lophelia pertusa* Coral Reefs in Mid-Norway in Relation to Seabed Characteristics. *J. Mar. Biol. Assoc. UK* 81, 581–597. doi: 10.1017/S002531540100426X

Mortensen, L. B., Vanreusel, A., Gooday, A. J., Levin, L. A., Priede, I. G., Mortensen, P. B., et al. (2010). Biological Structures as a Source of Habitat Heterogeneity and Biodiversity on the Deep Ocean Margins. *Mar. Ecol.* 31, 21–50. doi: 10.1111/j.1439-0485.2010.00359.x

Mountrakis, G., Im, J., and Ogole, C. (2011). Support Vector Machines in Remote Sensing: A Review. *ISPRS J. Photogramm. Remote Sens.* 66, 247–259. doi: 10.1016/j.isprsjprs.2010.11.001

Neulinger, S. C., Järnegren, J., Ludvigsen, M., Lochte, K., and Dullo, W. C. (2008). Phenotype-Specific Bacterial Communities in the Cold-Water Coral *Lophelia pertusa* (Scleractinia) and Their Implications for the Coral's Nutrition, Health, and Distribution. *Appl. Environ. Microbiol.* 74, 7272–7285. doi: 10.1128/AEM.01777-08

Nilssen, I., Ødegård, Ø., Sørensen, A. J., Johnsen, G., Moline, M. A., and Berge, J. (2015). Integrated Environmental Mapping and Monitoring, a Methodological Approach to Optimise Knowledge Gathering and Sampling Strategy. *Mar. Pollut. Bull.* 96, 374–383. doi: 10.1016/j.marpolbul.2015.04.045

Orejas, C., Gori, A., Rad-Menéndez, C., Last, K. S., Davies, A. J., Beveridge, C. M., et al. (2016). The Effect of Flow Speed and Food Size on the Capture Efficiency and Feeding Behaviour of the Cold-Water Coral *Lophelia pertusa*. *J. Exp. Mar. Biol. Ecol.* 481, 34–40. doi: 10.1016/j.jembe.2016.04.002

Price, D. M., Lim, A., Callaway, A., Eichhorn, M. P., Wheeler, A. J., Lo Iacono, C., et al. (2021). Fine-Scale Heterogeneity of a Cold-Water Coral Reef and Its Influence on the Distribution of Associated Taxa. *Front. Mar. Sci.* 8, 556313. doi: 10.3389/fmars.2021.556313

Price, D. M., Robert, K., Callaway, A., Hall, R. A., and Huvenne, V. A. (2019). Using 3D Photogrammetry From ROV Video to Quantify Cold-Water Coral Reef Structural Complexity and Investigate Its Influence on Biodiversity and Community Assemblage. *Coral Reefs* 38, 1007–1021. doi: 10.1007/s00338-019-01827-3

Provan, F., Nilsen, M. M., Larssen, E., Uleberg, K. E., Sydnes, M. O., Lyng, E., et al. (2016). An Evaluation of Coral *Lophelia pertusa* Mucus as an Analytical Matrix for Environmental Monitoring: A Preliminary Proteomic Study. *J. Toxicol. Environ. Health A* 79, 647–657. doi: 10.1080/15287394.2016.1210494

Purser, A., Larsson, A. I., Thomsen, L., and van Oevelen, D. (2010). The Influence of Flow Velocity and Food Concentration on *Lophelia pertusa* (Scleractinia) Zooplankton Capture Rates. *J. Exp. Mar. Biol. Ecol.* 395, 55–62. doi: 10.1016/j.jembe.2010.08.013

Reite, A. J. (1995). Deglaciation of the Trondheimsfjord Area, Central Norway. *Bull. Nor. Geol. Unders.* 427, 19–21.

Roberts, J. M. (2002). The Occurrence of the Coral *Lophelia pertusa* and Other Conspicuous Epifauna Around an Oil Platform in the North Sea. *Underwat. Technol.* 25, 83–92. doi: 10.3723/175605402783219163

Roberts, J. M., Brown, C. J., Long, D., and Bates, C. R. (2005). Acoustic Mapping Using a Multibeam Echosounder Reveals Cold-Water Coral Reefs and Surrounding Habitats. *Coral Reefs* 24, 654–669. doi: 10.1007/s00338-005-0049-6

Roberts, J. M., Wheeler, A. J., and Freiwald, A. (2006). Reefs of the Deep: The Biology and Geology of Cold-Water Coral Ecosystems. *Science* 312, 543–547. doi: 10.1126/science.1119861

Roberts, J. M., Wheeler, A. J., Freiwald, A., and Cairns, S. (2009). *Cold-Water Corals: The Biology and Geology of Deep-Sea Coral Habitats* (Cambridge: Cambridge University Press).

Sørensen, A. J., Dukan, F., Ludvigsen, M., Fernandes, D. A., and Candeloro, M. (2012). "Development of Dynamic Positioning and Tracking System for the ROV Minerva," in *Further Advances in Unmanned Marine Vehicles*. Eds. G. N. Roberts and R. Sutton (London: Institution of Engineering and Technology), 113–128.

Sabatier, P., Reyss, J. L., Hall-Spencer, J. M., Colin, C., Frank, N., Tisnerat-Laborde, N., et al. (2012). ^{210}Pb-^{226}Ra Chronology Reveals Rapid Growth Rate of *Madrepora oculata* and *Lophelia pertusa* on World's Largest Cold-Water Coral Reef. *Biogeosciences* 9, 1253–1265. doi: 10.5194/bg-9-1253-2012

Sakshaug, E., and Sneli, J. A. (2000). *Trondheimsfjorden* (Trondheim: Tapir Academic Press).

Sanna, G., and Freiwald, A. (2021). Deciphering the Composite Morphological Diversity of *Lophelia pertusa*, A Cosmopolitan Deep-Water Ecosystem Engineer. *Ecosphere* 12, e03802. doi: 10.1002/ecs2.3802

Squires, D. F. (1959). Deep Sea Corals Collected by the Lamont Geological Observatory. 1 Atlantic Corals. *Am. Mus. Novit.* 1965, 1–42.

Sture, Ø., Ludvigsen, M., Scheide, M. S., and Thorsnes, T. (2018). "Recognition of Cold-Water Corals in Synthetic Aperture Sonar Imagery," in *2018 IEEE/OES Autonomous Underwater Vehicle Workshop (AUV)* [Portugal: Institute of Electrical and Electronics Engineers (IEEE)].

Sundahl, H., Mortensen, P. B., and Mortensen, L. B. (2020). Distribution and Suitable Habitat of the Cold-Water Corals *Lophelia pertusa*, *Paragorgia arborea*, and *Primnoa resedaeformis* on the Norwegian Continental Shelf. *Front. Mar. Sci.* 7, 213. doi: 10.3389/fmars.2020.00213

Thiem, Ø., Ravagnan, E., Fosså, J. H., and Berntsen, J. (2006). Food Supply Mechanisms for Cold-Water Corals Along a Continental Shelf Edge. *J. Mar. Syst.* 60, 207–219. doi: 10.1016/j.jmarsys.2005.12.004

Vad, J., Orejas, C., Moreno-Navas, J., Findlay, H. S., and Roberts, J. M. (2017). Assessing the Living and Dead Proportions of Cold-Water Coral Colonies: Implications for Deep-Water Marine Protected Area Monitoring in a Changing Ocean. *PeerJ* 5, e3705. doi: 10.7717/peerj.3705

Walbridge, S., Slocum, N., Pobuda, M., and Wright, D. J. (2018). Unified Geomorphological Analysis Workflows With Benthic Terrain Modeler. *Geosciences* 8, 94. doi: 10.3390/geosciences8030094

Weiss, A. D. (2001). "Topographic Position and Landforms Analysis," in *21st Annual ESRI User Conference* (San Diego: ESRI).

White, M., and Dorschel, B. (2010). The Importance of the Permanent Thermocline to the Cold Water Coral Carbonate Mound Distribution in the NE Atlantic. *Earth Planet Sci. Lett.* 296, 395–402. doi: 10.1016/j.epsl.2010.05.025

Wilson, M. F., O'Connell, B., Brown, C., Guinan, J. C., and Grehan, A. J. (2007). Multiscale Terrain Analysis of Multibeam Bathymetry Data for Habitat Mapping on the Continental Slope. *Mar. Geod.* 30, 3–35. doi: 10.1080/01490410701295962

Conflict of Interest: The authors declare that the research was conducted in the absence of any commercial or financial relationships that could be construed as a potential conflict of interest.

Publisher's Note: All claims expressed in this article are solely those of the authors and do not necessarily represent those of their affiliated organizations, or those of the publisher, the editors and the reviewers. Any product that may be evaluated in this article, or claim that may be made by its manufacturer, is not guaranteed or endorsed by the publisher.

J.3 Coregistration of Hyperspectral Imagery With Photogrammetry for Shallow-Water Mapping

J.4 A semi-analytical model for deep-water hyperspectral imaging (submitted to Applied Optics 29.06.2023)

A semi-analytical model for deep-water hyperspectral imaging

HÅVARD SNEFJELLÅ LØVÅS[*,1,2], MARTIN KVISVIK LARSEN[2], OSCAR PIZARRO[1,2,3], AND ASGEIR J. SØRENSEN[1,2]

[1] *Centre for Autonomous Marine Operations and Systems (AMOS), Norwegian University of Science and Technology (NTNU), Trondheim, Norway*
[2] *Department of Marine Technology, NTNU, Trondheim, Norway*
[3] *Australian Center for Field Robotics, University of Sydney, Sydney, Australia*
[*] *havard.s.lovas@ntnu.no*

Abstract: In this paper we propose a semi-analytical (SA) model for relating seafloor reflectance to measured radiance in deep-water hyperspectral imaging for artificially illuminated scenes. Utilizing accurate sensor-seafloor geometry from photogrammetry and the principle of two-perspective observation, we allow for estimation of the inherent optical properties (IOPs) of the water column. We demonstrate the SA model and estimation of IOPs for hyperspectral imaging of a deep-water coral reef from a remotely operated vehicle. For the calibrated SA model, evaluation of across-perspective similarity demonstrates the model's ability to compensate for water column and light source effects.

1. Introduction

Hyperspectral imaging of the seafloor is severely affected by the annihilation and redirection of photons in the water column. These processes are governed by the Radiative Transfer Equation (RTE), along with boundary conditions and the Inherent Optical Properties (IOPs), describing bulk absorption and scattering properties. Determination of the true bottom reflectance requires solving the RTE with numerical simulation, an empirical model, or a Semi-Analytical (SA) model. As stated in [1], the SA model is explicitly invertible in contrast to the numerical approaches. This makes SA models attractive for shallow-water remote sensing applications since they allow computationally feasible analytical inversion of water depths, IOPs and bottom reflectances. Even with an SA model, the inversion problem for shallow-water remote sensing is inherently underdetermined [2]. By establishing spectral relations for the IOPs and using site knowledge about reflectance spectra (e.g. a spectral library), the problem can be made solvable. This was first presented in the SA model called Hyperspectral Optimization Processing Exemplar (HOPE) by Lee et al. [2] for shallow-water hyperspectral remote sensing.

Similarly for hyperspectral imaging in deep water with artificial light sources, it is expected that an SA model could allow for accurate inversion of light path geometry, IOPs, and bottom reflectances. The inversion topic has been studied extensively in the remote sensing community for shallow-water hyperspectral imaging [3], typically with the goals of retrieving bottom types and bathymetry. On the other hand, the underwater computer vision community has studied radiative transfer solutions in the context of image enhancement [4] and color correction for Red-Green-Blue (RGB) frame cameras [5] [6]. Furthermore, the computer vision community has provided tools for image alignment and Multiview-Stereo (MVS), allowing for highly consistent camera-bottom-light source geometries. This allows for removing the in-water distances and light paths as unknowns in the inversion problem. Software for performing such Structure-from-Motion (SfM) photogrammetry are readily available and provides a simple-to-use and low-cost alternative for consistent localization and seabed mapping. Recently, accurate geometries in underwater hyperspectral imaging with a push-broom scanner has been achieved by exploiting a concurrent RGB frame camera and SfM-MVS pipeline [7] [8] [9]. This motivates the development of solutions to the RTE that make use of such geometries in deep-water hyperspectral

imaging.
In earlier work on RTE solutions for underwater color correction, [5, 6, 10, 11] and hyperspectral reflectance correction [12], scaled seabed-camera geometry has been obtained from SfM photogrammetry or stereo imagery and used for describing radiative transfer. In [5] the geometry for the case of only artificial illumination, i.e. deep water, was been described for RGB color correction. They estimated Apparent Optical Properties (AOPs) based on the geometry and inverted raw signals to true bottom color. Note that we call them AOPs, since wide-band RGB signals transfers according to optical properties that depend on the bottom reflectance, distance, and more [13]. Moreover, the aggregate inversion of these AOPs along with the bottom reflectances is an underdetermined problem. One way of solving it, is to record multiple-perspective observations of points on the seafloor as was done by [5, 11]. If the seafloor has a simple Lambertian reflectance, the multiple perspectives reduce the number of unknowns and make the aggregate inversion into a determined problem. For 2D frame camera imaging, multi-perspective is easily achieved for sequential image frames. However, due to the 1D acquisition of the hyperspectral push-broom scanner, there is not overlap between sequential frames during an area scan, also called a transect. However, through two overlapping transects, two perspectives of each overlapping seabed point could be achieved, allowing inversion of IOPs. Once the IOPs are solved for, the SA model can be used for computation of bottom reflectance or classification schemes with low ambiguity, as has been demonstrated in the shallow-water remote sensing community [14].
The scientific contribution of this paper is to develop an SA model for deep-water hyperspectral imaging of the seafloor. The SA model makes use of accurate geometries from SfM photogrammetry for describing light paths. Therefore, the IOPs are the only unknowns to make the model complete. By complete we mean that the model allows direct computation of bottom reflectance from a radiance measurement. To resolve the unknown IOPs, we use overlapping two-perspective geometry, inspired by [5], to effectively cancel out the effect of varying bottom reflectances and render IOPs observable. To lower the ambiguity of estimation, we use a low number of latent parameters to represent the spectral IOPs, as inspired by the HOPE model [1] and the parameterization in [15].

2. Methods

This section describes the SA model and the methods used for determining the geometry and IOPs of that model. We first describe how the geometrical primitives were acquired in Sec. 2.1 and quantify the quality of this geometry. Since the approach is a modification of a previous work, descriptions are relatively brief. This geometry is utilized in the SA model. Then, in Sec. 2.2 we describe the proposed SA model in detail, including parameterization of IOPs and the two-perspective optimization for finding these. The main contributions of the paper are described in this section.

2.1. Geometry

The geometric processing is based on the methodology and data from [7], where photogrammetry, co-calibration of the Hyperspectral Imager (HSI) and ray casting were used to do accurate georeferencing for deep-water hyperspectral imaging. The following modifications were made as improvements to the method in Løvås et al. [7]:

- Photogrammetric alignment aided by stereo imagery, described in Sec. 2.1.1.
- Feature-based calibration of the HSI parameters, described in Sec. 2.1.2.
- Automatic feature-based accuracy validation, described in Sec. 2.1.3.

Arguably, the modification of the calibration methodology is not necessarily better than that in [7] in terms of accuracy, but it is simpler to implement, and much faster and easier to optimize. It also gives a more interpretable error metric. Please note that we also upgraded the ray tracing software solution to multi_ray_trace from PyVista which uses the Embree library [16] for vectorization of the ray traces.

2.1.1. Alignment

One day prior to the hyperspectral survey, a high-resolution stereo camera survey was conducted using the same vehicle system as described in [7]. This imagery was aligned in Agisoft Metashape v.1.6 as a rigid camera rig and with the keep key points option. The idea is that the key points form accurate geometry, particularly in terms of scale, which is a challenge for monocular photogrammetry. During the hyperspectral survey the next day, described in [7], we had a lower resolution monocular RGB camera right next to the HSI, running at 5 Hz. We aligned the monocular images to the accurate stereo key points in the alignment step. This way, the stereo points aid the scale estimation for the monocular camera. Onward, the monocular camera is referred to as RGB camera, and the stereo imagery is not used further.
In the alignment process, we re-calibrated the RGB camera model. Afterwards we created a 3D mesh model for ray tracing, a Digital Elevation Model (DEM), and an orthomosaic from the RGB imagery in Agisoft. We will be using this orthomosaic for feature-based comparison to hyperspectral imagery, so to avoid confusion it will be called photomosaic to emphasize that it is from photogrammetry. It is worth noting that we used spherical linear interpolation for interpolating rotational motion from the 5 Hz camera images to the 50 Hz timestamps of hyperspectral images. Looking at time-plots of the data, this constant rotational velocity assumption seemed justifiable for the large vehicle with slow dynamics.

2.1.2. Calibration of HSI line camera model

Since the RGB camera model was re-calibrated, the HSI line camera model should be re-calibrated so that they are consistent. Instead of using correlation-based photoconsistency as in [7] for comparing HSI imagery with RGB imagery, we here utilize Scale-Invariant Feature Transform (SIFT) features [17]. The method is conceptually similar to the checkerboard-corner calibration method in [7] but modified to in-situ use. The idea is that a partially rectified data cube can give a sufficient geometric fidelity that it can be compared to the photomosaic through SIFT matching [18]. By partially rectified, we mean that the data cube is georeferenced using a rough estimate for the camera parameters. For simplicity, we only perform the partial rectification using three bands, namely 590 nm, 530 nm and 490 nm, and this representation of a data cube can be called a psuedo-RGB raster. The georeferencing is conducted with ray casting as in [7], and we use nearest neighbor to resample the 3D point cloud to a raster in an orthographic grid. Keep in mind that nearest neighbor gives an invertible mapping between a pixel in the raster and the original data cube.
We denote the pseudo-RGB orthographic raster as $\boldsymbol{M}_k$, where k is a raster index and letter $\boldsymbol{M}$ is for match image. For a given $\boldsymbol{M}_k$, we resample the photomosaic to the grid of $\boldsymbol{M}_k$, resulting in a raster $\boldsymbol{R}_k$ or reference image. Extracted SIFT features from $\boldsymbol{M}_k$ are matched with extracted features from $\boldsymbol{R}_k$, where we consider $\boldsymbol{R}_k$ as the ground truth. A matched feature in $\boldsymbol{R}_k$ has associated horizontal coordinates and we can extract the vertical coordinate from the DEM, giving $[X_i, Y_i, Z_i]$ for the ith feature. These points are equivalent to the "world" positions of checkerboard corners in [7].
Since we utilized the nearest neighbor resampling, an integer pixel location in $\boldsymbol{M}_k$ can be mapped back to a frame number (i.e. timestamp) and a pixel number in the raw data cube. At the timestamp we know the pose of the concurrent RGB camera. To account for decimal SIFT feature locations in $\boldsymbol{M}_k$, we perform such the mapping for the 4 adjacent orthorectified pixels,

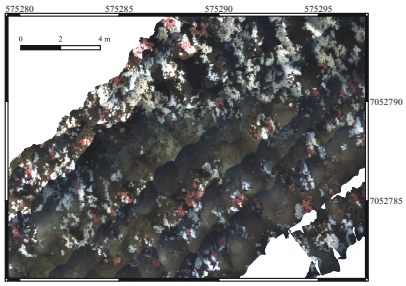

Fig. 1. Orthographic rasters of the raw hyperspectral data. Fine-scale detail on white and orange coral is seen in Fig. 2.

giving 4 poses and 4 pixel numbers. To get one pose and one pixel number we perform bi-linear interpolation of the 4 poses and 4 pixel numbers. This gives one RGB pose and one pixel number corresponding to $[X_i, Y_i, Z_i]$. Assume that this is done for all features i in all rasters k. The HSI line camera parameters are then found by minimizing the sum of squared reprojection error for all the features, equivalent to objective function J_1 in [7]. This is also similar to the approach in [9]. It is possible to repeat the partial rectification process with refined geometric parameters and re-do the calibration process, which could give more feature matches. In practice it did not seem to make much of a difference when the initial guess was decent. Note that we omitted the highest order radial distortion coefficient (k_1 in [7]) and set the relative roll angle to zero due to ambiguity with the principal point. Hence, we adjusted two boresight rotations and three line camera parameters using around 10 000 features correspondences with nonlinear least squares optimization.

2.1.3. Accuracy validation

We conduct the modified calibration approach and evaluate the georeferencing for the data set presented in [7]. The hyperspectral data set is from the Tautra cold-water coral reef, Norway, and was recorded in March 2017 at around 80 m depth. It has previously been used in [7, 19]. Fig. 1 shows a partial view of the 12 overlapping hyperspectral transects recorded in a mow-the-lawn pattern in the South-West/North-East direction. The vehicle was programmed to keep a 2 m distance to the seafloor, which is equivalent to around 2 m swath for the hyperspectral imager. At 2 m distance the approximate feasible resolution is 10 mm for the HSI, see [7] for details. Moreover, the transects were pre-programmed to 1 m line spacing, giving on average 50 % overlap. In reality the overlap varied between 0-100 %.

The hyperspectral transects in Fig. 1 are represented as georeferenced and orthorectified pseudo-RGB rasters, i.e. $\boldsymbol{M}_k$s using the calibrated HSI model. The individual rasters were stacked according to sequence. A close-up RGB photo is shown in Fig. 2 to show the typical seafloor composition. Furthermore, the same individual $\boldsymbol{M}_k$s were used for computing horizontal errors with respect to the equivalent $\boldsymbol{R}_k$. For each $\boldsymbol{M}_k$, the photomosaic is resampled to $\boldsymbol{R}_k$ with cubic convolution to $\boldsymbol{M}_k$'s raster grid of resolution 5 mm prior to the matching. Then the SIFT feature extraction and matching is conducted, and differences in features' pixel placements can be directly transformed to horizontal registration errors using the raster transform. This is done for all individual rasters to produce the histogram of registration error magnitudes in Fig. 3 of around 10 000 features. Seeing that most errors are below 6.7 mm, which is less than the feasible resolution, we consider it sufficiently accurate.

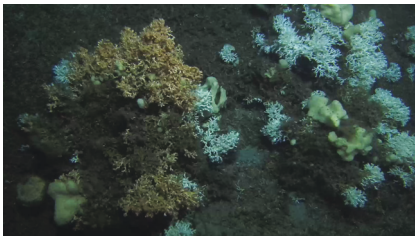

Fig. 2. An image representative for key substrates in the data including orange and white *Desmophyllum Pertusum* coral, yellow rounded sponges and brown matter.

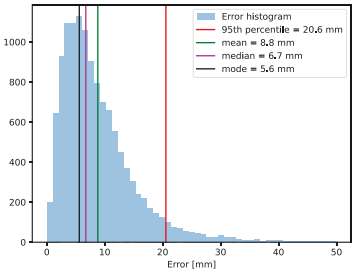

Fig. 3. Distribution of registration error magnitudes between hyperspectral and RGB based on matching SIFT features.

2.1.4. Geometric primitives for radiative transfer

Onward in this paper we do not work with the orthorectified format of measurements, but instead use the 3D point cloud representation. From the georeferencing, or ray casting of a measurement onto a mesh, we can extract the seabed intersection point $\boldsymbol{p}_{sb}$ and a surface normal vector $\hat{\boldsymbol{n}}_{sb}$ for each intersection in a global coordinate reference system. The global 3D point cloud is useful for finding data correspondences for overlapping transects. For studying radiative transfer, it is more practical to represent $\boldsymbol{p}_{sb}$ and $\hat{\boldsymbol{n}}_{sb}$ in a vehicle-fixed coordinate reference system.
All intersection points $\boldsymbol{p}_{sb}$ constitute a global 3D point cloud per transect. For associating pairwise spectra across transects (i.e. two-perspective approach), we utilize georeferenced point clouds and find point-to-point correspondences by 3D nearest neighbor interpolation. This provides pairwise correspondence for radiance spectra, point locations, surface normals, and other attributes. Invalid correspondences are determined with a max Euclidean distance threshold of 20 mm. Given that there are n valid correspondences, we get $2n$ spectra and $2n$ of any geometric attribute. In the radiometric derivations of Sec. 2.2 it has no practical significance whether spectra/geometries belong to the first or second observation, but it is revisited for the two-perspective optimization in Sec. 2.2.3.
A 2D illustration of the measurement geometry with two light sources is given in Fig. 4. Since the HSI is a line scanner, such 2D drawings nicely describe scanline geometry in the HSI frame. Naturally, the light sources $\boldsymbol{p}_{s1}, \boldsymbol{p}_{s2}$, may be located outside of the scanning plane. In our case, we had two light sources that were approximately within the scanning plane, so the figure conceptually shows how our light sources were placed with respect to the HSI. As a vehicle-fixed

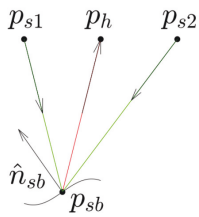

Fig. 4. The geometries acquired from ray intersections. The arrows show the flow of unscattered light from two light sources to the HSI.

frame for radiative transfer we choose the HSI frame, for which the x, y, z axes were fairly well aligned with the left, forward, and downward directions of the vehicle, respectively. In addition, $\boldsymbol{p}_h$ represents the origin of the frame. Let $\boldsymbol{r}_{s1}, \boldsymbol{r}_{s2}$ be the equivalent light source positions in HSI frame. Defining this is challenging as the HSI origin is a virtual convergence point in the underwater housing and the source origin is a virtual convergence point inside the light source. It is however easy to measure lever arms using the outsides of source/HSI glass. We will get back to how we approximate the geometry inside these glass containers. We express the vector from the HSI origin to a seabed point as $\boldsymbol{r}_h = \boldsymbol{R}^{-1}(\boldsymbol{p}_{sb} - \boldsymbol{p}_h)$. The surface normal is only a unit-length direction vector, and it can be rotated to the HSI frame through $\hat{\boldsymbol{n}}_{sb} \leftarrow \boldsymbol{R}^{-1}\hat{\boldsymbol{n}}_{sb}$. $\boldsymbol{R}$ is the rotation matrix expressing the orientation of the HSI, and $\boldsymbol{p}_h$ is the position of the HSI origin with respect to the geocentric coordinate reference system.

2.2. Radiometry

Sec. 2.2.1 describes the semi-analytical model of radiative transfer, Sec. 2.2.2 describes the chosen parameterization of IOPs, and Sec. 2.2.3 describes the two-perspective optimization.

2.2.1. Semi-analytical model

Our description of radiative transfer is in part based on the simulation model of McGlamery [20] and Jaffe [21]. However, their modeling of diffuse attenuation uses an empirical point spread function and a beam attenuation coefficient. In contrast, we choose to model it with average diffuse attenuation coefficients, as in the HOPE model [1]. The fundamental principle here is to use the Quasi-Single Scattering Approximation (QSSA) [22]. The approach uses the equations of the single-scattering approximation, but treats forward scatter as no scattering [23]. Therefore the QSSA expresses the beam attenuation as $\kappa = a + b_b$, where a $[1/m]$ is the absorption coefficient and b_b $[1/m]$ is the backscatter coefficient, both IOPs. The approximation is quite accurate for hydrologic optics because of the highly peaked nature of the Volume Scattering Function (VSF) [23].

In this section, we will describe how irradiance and radiance propagates from a light source to radiance right outside the underwater housing, L_w $[W/(m^2\ sr\ nm)]$. To accompany the mathematical explanations here, we add figures 5a and 5b to describe quasi-direct light and backscattered light, respectively. The figures describe most of the angles and lengths relevant for describing the light's propagation from source to HSI. Note that the letter l is used to describe equivalent Euclidean distance corresponding to a 3D vector $\boldsymbol{r}$. Similar to [5], we assume that our light source's directional radiant intensity I $[W/(sr\ nm)]$ can be approximated with a directional

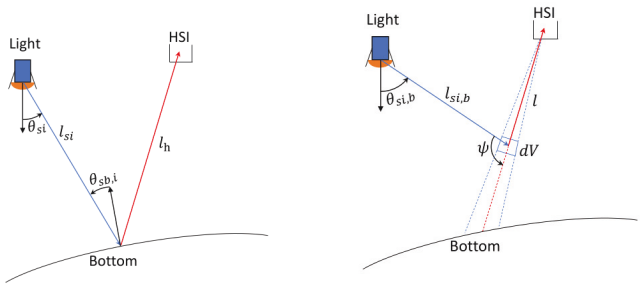

Fig. 5. Geometry for radiative transfer. Fig. 5a illustrates quasi-direct light while Fig. 5b shows backscattered light.

Gaussian as

$$I(\theta_{si}, \lambda) = I_0(0, \lambda) e^{-\frac{\theta_{si}^2}{2\sigma_{si}^2}} \tag{1a}$$

$$\sigma_{si} = \sqrt{\frac{\theta_{50\%}^2}{-2ln(0.5)}} \tag{1b}$$

$$cos(\theta_{si}) = \hat{\boldsymbol{n}}_{\boldsymbol{si}} \cdot \hat{\boldsymbol{d}}_{\boldsymbol{si}} \tag{1c}$$

$$\hat{d}_{si} = \boldsymbol{r}_{si} / l_{si}. \tag{1d}$$

Where $\hat{\boldsymbol{n}}_{\boldsymbol{si}}$ is the direction of the center-line, and subscript i denotes the light source index. $\theta_{50\%}$ is the off center-line angle at which the I is half of max. The used light source type is a DeepSea Multi Sealite 250 W/120 V with a 40° beam angle meaning that $\theta_{50\%} = 20°$. As such, $\sigma_{si} \approx 17°$. The manufacturer also delivered integrating sphere measurements of radiant power $\Phi(\lambda)$ $[W/nm]$ [24]. As such, we let the center-line irradiance 1 meter from the source's origin, $E_0(\lambda)$ $[W/m^2\ nm]$ be expressed as

$$E_0(\theta_{si} = 0, l_{si} = 1) = I_0 = K\Phi, \tag{2}$$

where $K \approx 2.1$ $[1/m^2]$ is an unknown that was determined using a reflectance plaque and a checkerboard underwater. Theoretically, performing a spherical integral of Eq. (1a) over all directions and equating it to Φ, K should be around 1.9. Using E_0 we may express the irradiance on a tangent plane to a hemisphere at a distance l_{si} as

$$E(l_{si}, \theta_{si}, \lambda) = \frac{E_0(\lambda)}{l_{si}^2} e^{-\frac{\theta_{si}^2}{2\sigma_{si}^2}} = \frac{E(\theta_{si}, \lambda)}{l_{si}^2}. \tag{3}$$

In polar coordinates, the origin of a hemispherical source is displaced by a positive distance $l_{g,s}$ with respect to the source's glass surface. In other words, the light beams has a virtual origin/convergence point $l_{g,s}$ inside the source glass. The simple heuristic used for finding $l_{g,s}$ in this paper was to use the source's diameter and beam angle. In our case, the source diameter was around 0.08 m, which gives $l_{g,s} \approx 0.1$ m for a beam angle of 40°.
Recall that $\boldsymbol{r}_{si}$ is the equivalent vector from the light source origin to the seabed so that $|\boldsymbol{r}_{si}| = l_{si}$. The attenuation of light then depends on the path length in water $l'_{si} = l_{si} - l_{g,s}$ and the diffuse

attenuation coefficient $K_d(\lambda)$ $[1/m]$. K_d is the path-averaged diffuse attenuation denoted by subscript d to indicate that it is downward-heading light. It describes the evolution of plane irradiance onto a plane perpendicular to $\boldsymbol{r}_{si}$. According to the QSSA, κ is used as the beam attenuation coefficient. As for the HOPE model, we here describe diffuse attenuation K through κ and a distribution function D [-] as

$$K(\lambda) = D(\lambda)\kappa(\lambda). \tag{4}$$

In [1] the Ds are parameterized spectrally by using the IOPs. For now, let $K_d = D_d\kappa$ for downward-heading light, and we will come back to choices of D_d. We should emphasize that K_d is an average attenuation coefficient as long as there is scattering. This is due to the fact that the average cosine of the light field is changing along a path from the light source through scattering. We express the incident irradiance from a light source, E_i arriving at the seafloor as

$$E_i = E(\theta_{si})\frac{1}{l_{si}^2} exp\big[-D_d\kappa l_{si}^{'}\big] \tag{5}$$

Moreover, we define $E(\theta_{si})$ as the beam pattern on a hemispherical shell at unit distance, as denoted BP in Jaffe's paper [21].
For a Lambertian surface, we have that the Bi-directional Reflectance Distribution Function (BRDF) $[1/sr]$ is constant and equal to ρ/π where $\rho(\lambda)$ $[-] \in [0, 1]$ is the reflectivity of the surface. By the definition of the BRDF and integration over all directions, we may express the isotropic reflected radiance L_r as

$$L_r = \frac{\rho E_i cos(\theta_{sb,i})}{\pi} \tag{6a}$$

$$cos(\theta_{sb,i}) = \hat{\boldsymbol{d}}_{\boldsymbol{si}} \cdot \hat{\boldsymbol{n}}_{\boldsymbol{sb}}. \tag{6b}$$

$\theta_{sb,i}$ is the angle between the seabed's surface normal and the direction of incident light. To be specific, the average illumination vector is used, effectively modeling radiance distribution from the source as a Dirac-delta directionally (unidirectional). Moreover, according to [25], the modeling of bottom substrates as Lambertian typically leads to errors of $<<$ 10 % for passive near-nadir viewing instruments. However, an important non-Lambertian phenomenon of rough surfaces are hotspot effects, or retroflection when incident illumination and observer are aligned. Active optical systems where the source is close to the camera are faced with observations of the BRDF hot spot. In worst case, the received light can be two times (or more for highly slanted rays) the radiance that could be received if the bottom was Lambertian [25]. For underwater hyperspectral imaging this predicts that the Lambertian assumption will overestimate reflectivity, with increasing effect for increasing angles $\theta_{sb,i}$. We will not model BRDF hotspots in this study. We will, however, note it as a source of directional inconsistency for two-view comparison.
We can now describe the direct light as

$$L_d = L_r exp\big[-K_u^B l_h^{'}\big], \tag{7}$$

where $l_h^{'}$ is the in-water distance from the seafloor to the glass port of the underwater housing. The in-water distance for a flat glass port can be expressed $l_h^{'} \approx l_h - l_g$, where l_h is the distance from the virtual center of the HSI camera model to the seafloor. The virtual center-to-glass distance $l_g = z_g l_h / z_h$ where $z_g = 0.05$ m is the approximate distance along the optical axis to the glass-water interface in our case. z_h is the z-component of $\boldsymbol{r}_h$. Furthermore, $K_u^B(\lambda)$ $[1/m]$ is a path-averaged diffuse attenuation coefficient for upward-heading bottom radiance which is modeled as $K_u^B = D_u^B\kappa$, where D_u^B is a distribution function. The notation is adapted from [1].

Furthermore, using K_u^B we can describe the quasi-direct in-water radiance outside the HSI glass, $L_{w,d}$ as

$$L_{w,d} = \frac{1}{\pi}\rho E(\theta_{si})\frac{cos(\theta_{sb,i})}{l_{si}^2} exp(-[D_d \kappa l_{si}^{'} + D_u^B \kappa l_h^{'}]). \tag{8}$$

Where spectral dependence is omitted for brevity.

For backscatter we adapt the formulation of the Jaffe-McGlamery model [20,21]. Our backscatter formulation can be derived from their equations using the fundamental radiometric relation [26]. The total backscattered radiance is a discrete sum of slab-scattered, or small water volume-scattered radiance. One such discrete water volume dV with illumination geometry is shown in Fig. 5b for ease in readability. The reflected radiance from a single slab dV in the direction of the HSI is expressed as

$$dL_{bs,i} = E_{i,b}\beta\frac{dz}{cos(\theta)}. \tag{9}$$

Where $\beta\ [1/(m\ sr)]$ is the total VSF of the water body, and $E_{i,b}$ is incident light onto a plane perpendicular to $\boldsymbol{r}_{si,b}$ the light source and dz is the slab thickness along the camera's optical axis. θ is as defined in [20] the off-optical axis angle so that $l = z/cos(\theta)$. We substitute distance along optical axis z with the camera-slab distance l. Then dl is the thickness of the slab in the direction $\hat{\boldsymbol{d}}_h$. We can then express the total backscattered radiance as the following integral

$$L_{w,b} = b\int_{l_g}^{l_h} E_{i,b}(l)\hat{\beta}(\psi)exp\big[-K_u^C(l-l_g)\big]dl. \tag{10}$$

Where $E_{i,b}(l)$ is the incident irradiance onto the small volume element of thickness dl. The average upwelling diffuse attenuation for backscattered radiance is expressed by $K_u^C = \kappa D_u^C$. Moreover, $\hat{\beta}\ [1/sr] = \beta/b$ is the phase function describing the directional probabilities of scattering (given a scattering event) at an angle ψ, while $b\ [1/m]$ is the scattering coefficient. We can express the source-slab vector $\boldsymbol{r}_{si,b} = l\hat{\boldsymbol{d}}_h - \boldsymbol{r}_{si}$. Then ψ is the angle between the vector $\boldsymbol{r}_{si,b}$ and the vector $\boldsymbol{r}_{b,h} = -l\hat{\boldsymbol{d}}_h$. We can express $E_{i,b}(l)$ as

$$E_{i,b}(l) = E(\theta_{si,b})\frac{1}{l_{si,b}^2}exp\big[-\kappa D_d l_{si,b}^{'}\big] \tag{11a}$$

$$cos(\theta_{si,b}) = \frac{\hat{\boldsymbol{n}}_{\boldsymbol{si}}\cdot\boldsymbol{r}_{si,b}}{l_{si,b}}. \tag{11b}$$

Where $l_{si,b} = |\boldsymbol{r}_{si,b}|$ is the source origin-slab distance, while $l_{si,b}^{'} = l_{si,b} - l_{g,s}$ is the equivalent distance in water. In a numerical context, notice how most factors of Eq. (10) and Eq. (11) can be pre-computed since the geometry is known. We also use a "typical" average particle phase function to pre-compute $\hat{\beta}_p(\psi)$ and the water's phase function $\hat{\beta}_w(\psi)$ is known. As such, given a discretization of l, it is possible to pre-compute all entities except terms with the unknowns κ and b. Once the SA model is calibrated so that b and κ are known, it is possible to design a look-up table or other structures to enable fast computation of $L_{w,b}$. These would depend on values of l, u, λ. For the computations in this paper related to finding IOPs, we choose $dl \approx \Delta l = 0.02$ m, and compute the non-analytical integral in Eq. (10) as a discrete summation. Lastly, we should mention that the non-analytical integral converges to an asymptotic with increasing distance for a given u and λ. Although not studied here, using spectral images far from the seafloor could essentially allow measurement of this asymptotic "image". This could benefit estimation of IOPs, in particular b. A conceptually similar approach has been used in aerial shallow-water mapping using deep-water measurements [27].

To conclude the radiative transfer solution for one light source, we express the total in-water radiance as $L_w = L_{w,d} + L_{w,b}$. If there is more than one light source, we compute $L_{w,i}$ for the

ith light source and sum the contributions over all i.
A hyperspectral imager does not measure L_w by default, and therefore it seems suitable to describe how a measurement relates to L_w in the case that the HSI is calibrated in air. If so, the HSI measures digital counts $\hat{N}_m(u,\lambda)$ [-] at spatial pixel u and a spectral channel with a central wavelength λ [nm]. We can express the in-air radiance measurement as

$$L(u,\lambda) = \frac{\hat{N}_m(u,\lambda) - \hat{N}_d(u,\lambda)}{C(u,\lambda)t}. \tag{12}$$

Where $L(u,\lambda)$ is the average in-air radiance entering the radiometer during the exposure time, t. $\hat{N}_d(u,\lambda)$ is the dark count and $C(u,\lambda)$ is a radiometric calibration gain. The reader is referred to e.g. [28] for details on the characteristics of hyperspectral push-broom measurement.
If the spectral imager is calibrated in air, it is necessary to compensate for the immersion factor, $I_f(u,\lambda)$ [-] [29]. The difference in air and in water is at the medium-glass boundary on the outside of the underwater housing. The immersion effect is due to Snell's law and changes in transmittance at the glass-medium interface. Assume that pixel u corresponds to either an in-water intersection angle θ_w or an in-air angle θ_a at the medium-glass boundary. This association can be approximated using the calibrated line camera model or manufacturer data. Snell's law provides the relation between θ_w and θ_a. Then, the immersion factor relating $L(u,\lambda)$ to the in-water radiance $L_w(u,\lambda)$ can be expressed through

$$L_w(u,\lambda) = L(u,\lambda) I_f(u,\lambda) \tag{13a}$$

$$I_f(u,\lambda) = n_w(\lambda)^2 \frac{t_{ag}(\theta_a,\lambda)}{t_{wg}(\theta_w,\lambda)}. \tag{13b}$$

Where t_{ag}, t_{wg} are the Fresnel transmittance at the air-glass and water-glass surfaces, respectively. The beams' corresponding reflectance losses are $r_{ag} = 1 - t_{ag}$ and $r_{wg} = 1 - t_{wg}$. The Fresnel reflectance can be computed using only the incident angle to the glass and the refractive indices of the of the glass and the medium. Therefore, the immersion factor has a dependence on the intersection angle of each ray with the glass and a dependence on the wavelength due to variations in refractive indices. For the hyperspectral imager in this study with an in-water field-of-view of 50°, relevant intersection angles approximately range from $\theta_w = 0° - 25°$. Assume that we use the 400-700 nm mean refractive index of water, $n_w \approx 1.34$ (with script from [30]), and a fused silica glass $n_g \approx 1.46$ (see [31]). Then the transmittance ratio in Eq. (13b), t_{ag}/t_{wg} ranges from 0.967-0.965. Meanwhile, the wavelength dependent n_w^2 ranges from 1.82-1.79 for 400-700 nm. Based on these factors we used a wavelength independent immersion factor $I_f \approx 1.74$. This is because the same wavelength dependent effect n_w^2 occurs to a light source (depending on geometry) and cancels out by division in later computations. It is also not a large potential error for the purposes of this paper.

2.2.2. IOP parameterization

The unknowns in the proposed SA model are the spectral IOPs $\kappa, b, \hat{\beta}$ and spectral distribution functions D_d, D_u^B, D_u^C, where $\hat{\beta}$ has an unknown angular distribution for each channel. By spectral we mean that there is one unknown per spectral channel. Due to the small spatial scales at which we operated in this study, we assume that the IOPs are constant. Here, we will use a minimalist parameterization adapted from the approaches in [15] and [2]. The following

equations describe the IOPs relevant for the QSSA in this work

$$a_g = Ge^{-S(\lambda-440)} \tag{14a}$$

$$b_l = 0.3411\left[\frac{400}{\lambda}\right]^{0.3} \tag{14b}$$

$$b_s = 1.513\left[\frac{400}{\lambda}\right]^{1.7} \tag{14c}$$

$$b_p = B_s b_s + B_l b_l \tag{14d}$$

$$\hat{\beta}_p = \hat{\beta}_{petz} \tag{14e}$$

$$b = b_w + b_p \tag{14f}$$

$$a = a_\phi + a_g + a_w \tag{14g}$$

$$\eta = \frac{b_w}{b_w + b_p} \tag{14h}$$

$$\hat{\beta} = \eta\hat{\beta}_w + (1-\eta)\hat{\beta}_p \tag{14i}$$

$$b_b = 0.5b_w\eta + 0.019b_p(1-\eta). \tag{14j}$$

Where all equations describe spectral quantities. We will assume chlorophyll concentrations, i.e. a_ϕ to be insignificant for deep waters in March when the recordings were made in Norway. We use the absorption model for Colored Dissolved Organic Matter (CDOM), a_g, suggested by [32], and we use a slope value, $S = 0.015\ [1/nm]$, as a mean value for CDOM and non-algal particles from the data presented in [33]. The parameter $G\ [1/m]$ is the absorption at 440 nm. We used a_w from [34] and b_w from [35]. We use, as in [15], the Petzold average particle phase function, $\hat{\beta}_{petz}$, based on Petzold's measurements [36]. We downloaded $\hat{\beta}_{petz}$ from [37]. The particle scattering coefficient b_p is expressed as contributions from small and large particles [38] denoted by subscript s, l respectively. $B_s, B_l\ [g/m^3]$ are the particle concentrations, while lowercase $b_l, b_s\ [m^2/g]$ are the specific scattering coefficients. The pure-water molecular scattering fraction η is used for linear weighting of the phase functions and backscattering coefficients. We can note that 0.019 represents the backscatter fraction of $\hat{\beta}_{petz}$ [39], while 0.5 is the backscatter fraction of seawater since it is an isotropic scatterer. The model for describing water's phase function $\hat{\beta}_w$ is well known and is described in e.g. [40]. In total we have the parameter vector, $\boldsymbol{\beta} = [G, B_s, B_l]$, and would have had four in the case of phytoplankton using the one-parameter model in e.g. [1]. The low parameterization helps with constraining the optimization problem into physically realistic values.

Lastly, for describing the relation between the various diffuse attenuation coefficients and κ, lets first allow $D_u^B = D_u^C = D_u$. This is a logical assumption for our integral-of-slabs formulation since each discrete slab behaves like a reflecting surface. Moreover, we will use $D_u = 1$ and $D_d = 1.0395$ for which the latter is compatible with the plane irradiance diffuse attenuation coefficient of Gordon [41]. We can note that this model is quite similar to the HOPE model parameterization

$$D_d = 1 \tag{15a}$$

$$D_u^B = 1.04(1 + 5.4U)^{0.5} \tag{15b}$$

$$U = \frac{b_b}{a + b_b}, \tag{15c}$$

for small values of U. The main difference is then that their D_d equates our D_u^B and vice versa. We are aware that our simplistic parameterization of distribution functions is a limitation, particularly in highly scattering waters, but it seems that numerical studies are needed for properly describing these, as was done for the HOPE model.

2.2.3. Two-perspective optimization

Given that observations are pairwise of the same substrates, it is possible to omit bottom reflectance as an unknown and compare L_1 and L_2. Given a set of parameters $\boldsymbol{\beta}$, and the geometric variables $\boldsymbol{x} = [\boldsymbol{r}_h, \hat{\boldsymbol{n}}_{sb}]$, we can use the described SA model as a two-term linear model relating in-water radiance L_w and reflectivity ρ as

$$L_w = F(\boldsymbol{\beta}, \boldsymbol{x})\rho + G(\boldsymbol{\beta}, \boldsymbol{x}). \tag{16}$$

Where the nonlinear functions $F = L_{w,d}/\rho$ from Eq. (8) and $G = L_{w,b}$ from Eq. (10) are directly computed. In other words, F is Eq. (8) without ρ. For a point seen by two perspectives, assume that F_1, G_1 denotes the first observation while F_2, G_2 denotes the second observation. In fact, the use of subscripts $1, 2$ will here-on forward refer to the first and second transect which is synonym to the first and second overlapping observation. For a visual intuition of two-perspective, or two-transect observation, see Fig. 6a. If we want to compare two measurements L_1, L_2 we can e.g. use our model to predict what L_2 would be from L_1. Let this model estimate be called $\hat{L}_2$. Note that the in-water subscript w was omitted for brevity. $\hat{L}_2$ is expressed as

$$\hat{L}_2 = \frac{F_2}{F_1}(L_1 - G_1) + G_2. \tag{17}$$

This result is achieved by first solving for the estimated bottom reflectivity $\hat{\rho}_1$ in Eq. (16) using L_1, F_1, G_1 and then expressing $\hat{L}_2$ using $\hat{\rho}_1, F_2, G_2$. If we assume that L_w has measurement noise with standard deviation $\sigma_w(\lambda)$, this too must be scaled accordingly. By the rules of variance propagation, we can express the variance of the residual $L_2 - \hat{L}_2$ as

$$Var(L_2 - \hat{L}_2) = \sigma_r^2 = \left[1 + \left(\frac{F_2}{F_1}\right)^2\right]\sigma_w^2. \tag{18}$$

Where σ_r is the standard deviation of the residual. Here, we model spectral channels independently without accounting for covariance in measurement errors meaning that all entities are scalar. We note that better measurement uncertainty modeling could be incorporated along with modeling of process noise to improve estimation. We will not attempt to model the exact measurement noise σ_w but rather the relevant variations for pixels u and spectral channels, λ. We know from Eq. (12) how digital counts are converted to in-air-radiances. With this in mind, we can let

$$\sigma_w^2 = \left(\frac{1}{C(u, \lambda)}\right)^2 \left(\frac{1}{t}\right)^2. \tag{19}$$

Where we can recall that C is a radiometric gain, while t is the exposure time. If t was equal for both observations, it could be removed. Essentially, we can interpret that a low C gives high variance. The main point of computing σ_r is that observation pairs for a given wavelength are weighted suitably given F_1, F_2. The modeling of σ_w further allows for including calibration knowledge. Note that the immersion factor could go into σ_w, but a constant scaling makes no difference.

For setting up an optimization function, we make a slight adaption to the error index employed by HOPE [2]. For the ith spectrum, we define the scalar error index

$$err_{i,2} = \frac{\sqrt{\left(\sum_{j=1}^{k} w_i(\lambda_j)\left[R_2^i(\lambda_j) - \hat{R}_2^i(\lambda_j)\right]^2\right)}}{\sum_{j=1}^{k} \hat{R}_2^i(\lambda_j)}. \tag{20}$$

Where Rs are the equivalent reflectances obtained by dividing radiances Ls by a 565 nm normalized light source spectrum. The modification compared to the HOPE error index is

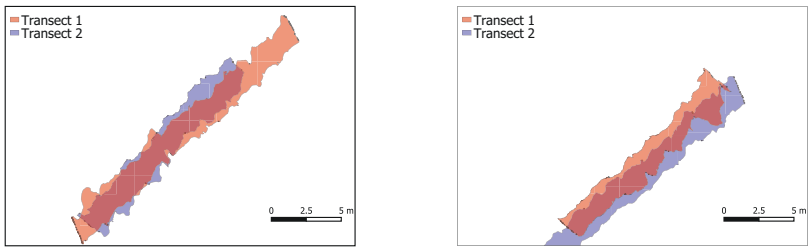

(a) (b)

Fig. 6. Overlap in hyperspectral data sets. Fig. 6a and Fig. 6b show orthorectified footprints of DS1 and DS2, respectively. The footprints are drawn slightly transparent so that overlapping area gets a purple color. The x, y axes are aligned with UTM 32 East/North.

the variance weighting $w_i(\lambda_j) = 1/\sigma_r^2$. Note that $err_{i,2}$ is the error index for $R_2, \hat{R}_2$, and we compute the error index $err_{i,1}$ for $R_1, \hat{R}_1$ in the same way. The indices i, j are used for sample numbers and spectral band numbers, respectively. Lastly, we suggest finding the parameters that minimizes the expression

$$\arg\min_{\beta} \frac{1}{n}\sum_{i=1}^{n} |err_{i,1}(\boldsymbol{\beta})| + \frac{1}{n}\sum_{i=1}^{n} |err_{i,2}(\boldsymbol{\beta})|. \tag{21}$$

Where n are the number of samples. The absolute value is used to prevent a solution with negative error indices. We use simulated annealing in MATLAB for minimization with default settings. An important comment to the objective function is that we use the first norm of the error indices to reduce the impact of outliers. The division by a light source spectrum and using reflectance R rather than radiance L applies a noise transformation that we are not accounting for. Our light sources used halogen bulbs emitting a power spectrum that grew significantly with wavelength. The power was for instance 10 times as high for around 630 nm as for 400 nm. As such, the noise's standard deviation grew by 10 times as much for 400 nm as for 630 nm through the division. On the other hand, it can also be seen as a form of importance weighting that significantly increased the impact of the lower wavelengths, as these would otherwise have close-to no impact in estimation of IOPs.

3. Results

To conduct the validation and processing, we utilized two pairs of overlapping transects. These will be referred to as Data Set 1 (DS1) and Data Set 2 (DS2). DS1 is illustrated in Fig. 6a, while DS2 is shown in Fig. 6b.

3.1. Initial attenuation estimation

The main strategy in this paper is to use the spectral optimization of the semi-analytical model to find the previously described parameters. However, due to complex illumination patterns and other factors, we think that a per-channel optimization can be a good step for initial data exploration. We will call this an empirical regression since it does not conserve the known spectral relations. For this step, we ignore scattering (i.e. $L_{b,w} = 0$) and attempt empirical estimation of κ_j for all bands λ_j. So how do we best estimate the attenuation? There are several occluding factors, such as an inaccurate beam pattern model, non-Lambertian reflectance, and so

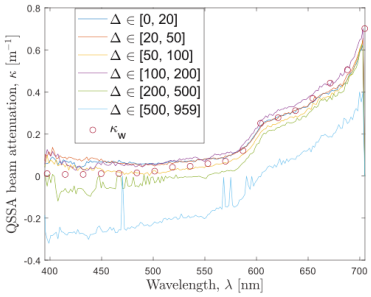

Fig. 7. Attenuation from empirical regression. The figure shows κ estimates for varying constraints on intervals of $\Delta = |u_1 - u_2|$ and the QSSA beam attenuation for pure water, κ_w. The κ-estimates are negative and noisy for $\Delta > 200$. For lower values of Δ it seems that $\kappa \approx \kappa_w$ when λ is 600 nm-700 nm.

on. The advantage of using the overlap concept is that we have much data, and that we can be selective when comparing data. Therefore, we think that the ideal comparison of L_1, L_2 would be to compare pixels with similar illumination geometry but varying distance.

With this rationale, we hypothesize that it is convenient to limit the absolute pixel distance $\Delta = |u_1 - u_2|$ between the two radiance observations L_1, L_2 with associated spatial pixels u_1, u_2. We test this hypothesis by optimization using different intervals of Δ, shown in Fig. 7. Each optimization used 5000 random spectral pairs from DS1. For this initial study, we used a robust variance-weighted nonlinear least squares minimizing $(L_2 - \hat{L}_2)^2/\sigma_r^2$ and let $\sigma_w = 1$ for the optimization. This was implemented using the MATLAB function nonlinfit and robust weighting function bisquare. Arguably, the most important trend in Fig. 7 seemed to be that using pixels with a large Δ resulted in a significant underestimation of the attenuation. Here we will not dig deeper into the underlying errors, but instead conclude that a suitably low Δ seemed to be more robust against such errors. Moving on, we will use $\Delta = 50$ pix as a trade-off between data diversity and quality.

Another takeaway from the comparison in Fig. 7 was that the attenuation, κ took a reasonable shape close to the attenuation of pure water, κ_w with a low amount of noise. It must be taken into account that separate calibrations were done over 181 channels without incorporating any relations between the channels. We also did not conduct any smoothing prior to this particular estimation.

It should be mentioned that prior to making Fig. 7, a slight correction to the spectral calibration for the HSI was made. It was apparent that the spectral calibration suffered from some nanometers systematic shift. This was particularly apparent when comparing κ to κ_w. By using manually selected spectral features, an ad-hoc second order polynomial was fit to correct the factory spectral calibration. We used 15 spectral features from 427 nm to 690 nm and the resulting corrections were in the range -4 nm to 5 nm for the 400 nm – 700 nm range. In comparison, the band width was 2.2-5.5 nm according to the manufacturer.

3.2. Semi-analytical optimization

In this section it is attempted to optimize the parameters for the SA model, $\boldsymbol{\beta} = [G, B_s, B_l]$. We constrained all the parameters to be positive due to their physical meaning. Further, we constrained the CDOM absorption at 440 nm G to be below 0.4 $1/m$, B_l to 3.8 g/m^3 and B_s to 1.5 g/m^3. The first upper bound was slightly above the $a(440nm)$ derived for Jerlov water

Label	n_{tot} [$\times 10^3$]	n [$\times 10^3$]	$\mathbb{E}(l_{h,1})[m]$	$\mathbb{E}(l_{h,2})[m]$	$\mathbb{E}(\lvert l_{h,1} - l_{h,2}\rvert)[m]$
DS1	2536	68 (2.7 %)	2.25 ± 0.31	2.16 ± 0.54	0.50 ± 0.23
DS2	1272	48 (3.8 %)	2.64 ± 0.45	2.55 ± 0.45	0.52 ± 0.20

Table 1. Key metrics for selected data points. n_{tot}, n are total number of pairs and selected number of pairs, respectively. Percentages corresponding to n/n_{tot} are shown in parenthesis. The symbol $\mathbb{E}$ shows the mean with standard deviation after the $\pm$ symbol.

5C in [15]. The B_s value was the highest value for Jerlov waters I-5C in [15]. The max value for B_l was acquired as the highest value for Jerlov waters I-5C derived in [42]. In total, these upper/lower bounds should have represented the relevant parameter space, since we expected the visibility to be much better than for water type 5C.
We used the wavelength range 400 nm - 700 nm for a total of 181 spectral channels. The following pre-processing was done to the spectra:

- Spectral Savitzky–Golay quadratic smoothing was conducted using a window size of 11 with the MATLAB function smoothdata. Edge artifacts of the smoothing were not a big problem since we included the 10 channels before 400 nm and the 34 channels after 700 nm in the smoothing. The smoothing was seen to have a very positive effect on the similarity of overlapping spectral measurements.
- Criterion 1: Data was constrained to $\Delta < 50$ pixels.
- Criterion 2: Observations with pairwise difference in HSI-seabed distance $|l_{h,1} - l_{h,2}|$ less than 25 cm were excluded. This was because small $|l_{h,1} - l_{h,2}|$ gives small effect of IOPs.
- Criterion 3: A heuristic thresholding was done by defining a brightness metric as the spectral integral of radiance. The scalar threshold was set as the 25th percentile brightness of the darkest transect. This eliminates very dark/far away targets with a low Signal-to-Noise Ratio (SNR).
- Data satisfying the above criteria defined the population from which we drew samples. A quantitative description of the data sets is given in Tab. 1.
- Outlier removal mechanism: It was hard to make any assumptions about outliers in the data as this depended on a myriad of factors. From data exploration, it was seen that the residuals from Eq. (21) produced some very high outliers, around 5 percent of the selected population. As a simple outlier filtration approach, we used the inter-quartile method to remove high outliers. It removed around 5-10 percent of the data. To implement outlier rejection, an optimization was first ran on the selected data in Tab. 1. Then, using optimized parameters, the inter-quartile method removed the outliers and the optimization was run again.

The function randomperm in MATLAB was employed for selecting 1000 arbitrary and unique pairs from the n samples of the distribution in Tab. 1. For each optimization, randomperm was re-initialized to create a different set of samples. The initial parameters were also randomly initialized for each optimization, and the optimization was limited to 400 iterations. We ran the simulated annealing optimization 10 times and evaluated the resulting parameters. The results of the optimizations are shown in Tab. 2 for DS1 and DS2. Parameter subscripts 1, 2 refer to data set number. We added the median in parentheses for μ and the Median Absolute Deviation (MAD)

	μ (median)	σ (MAD)	$c(G)$	$c(B_s)$
$G_1[m^{-1}]$	0.20 (0.20)	0.01 (0.01)	1	0.48
$G_2[m^{-1}]$	0.19 (0.19)	0.02 (0.02)	1	0.90
$B_{s,1}$ $[g/m^3]$	0.31 (0.35)	0.10 (0.07)	0.48	1
$B_{s,2}$ $[g/m^3]$	0.20 (0.19)	0.07 (0.06)	0.90	1
$B_{l,1}$ $[g/m^3]$	0.29 (0.22)	0.25 (0.15)	-0.29	-0.92
$B_{l,2}$ $[g/m^3]$	0.27 (0.27)	0.18 (0.15)	-0.90	-0.97

Table 2. Parameter estimate summary. The mean, spread and correlations of parameter estimates for the two data sets.

in parentheses for μ and σ, respectively. $c(G)$ and $c(B_s)$ were the parameters' correlations with G and B_s estimates, respectively. Note that the correlation must be seen in context with the standard deviations. For example $B_{s,2}$ could very well explain the variance of G_2, but the variance was small. We used the 10 parameter estimates per data set to compute corresponding IOPs, including a, b and κ spectra. For comparison showed the IOPs of the clearest coastal Jerlov waters and some open-ocean types derived by Solonenko and Mobley [15]. The comparisons of our absorption, scattering and attenuation coefficients are shown in figures 8a to 8c. We denoted the parameter sets for DS1 and DS2 as param 1 and param 2, respectively. In Fig. 8c we included empirical per-channel optimization where we estimated $\kappa(\lambda)$ instead of the SA parameters. For this optimization it was assumed that there was no backscattered light. Simultaneous estimation of κ and b was tried but gave clearly ambiguous results. Therefore b was fixed to zero. The empirical regression was conducted using 5000 observations from each data set. The objective function was a per-channel equivalent to Eq. (20) without the division by $\hat{R}(\lambda_j)$ in Eq. (20). We used simulated annealing and omitted outlier rejection since it had a low effect.
In terms of evaluating the calibrated SA model, we chose to make comparisons across-perspective, as we did in the objective function. We could also have studied inverted bottom spectra of targets with semi-known laboratory reflective properties. In making comparisons across transects there is an assumption that two observations measure the same Lambertian seafloor point. The assumption is undoubtedly wrong, and we would expect a baseline level of error to arise from this alone. One way to try and isolate this is through comparing measurements $|l_{h,1} - l_{h,2}| \approx 0$. In this case, the only difference between two measurements are the surface normal angles and slight differences in illumination pattern within Δ. The similarity achieved in that case is approximately the ceiling of performance. Naturally, a finite interval was needed and we used $|l_{h,1} - l_{h,2}| < 0.1\ m$. To evaluate performance, we studied two chosen normalized distance metrics, $\in [0, 1]$.

- Spectrally resolved correlation: For each channel we described the correlation, $corr$, between measurements and model predictions, evaluated using all samples. If the model is consistent, it explains more of the variance, and thus gives higher correlation. Unfortunately, the metric is not robust over the samples, meaning that outlier samples could lower the correlation by an disproportional amount.

- Sample cosine similarity: For each pair of sample spectra, we evaluated the cosine similarity $cossim$ between measurements and model predictions. Evaluating it for all samples yields a distribution. The cosine similarity distribution is robust to sample outliers, but not robust to systemic outliers in a spectral channel.

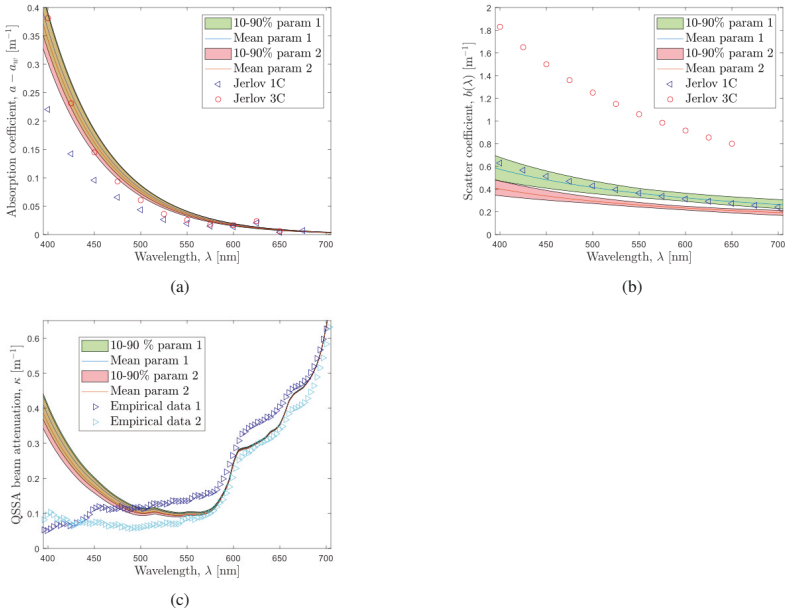

Fig. 8. IOPs estimation results. Fig. 8a shows the constituent absorption $a - a_w$, Fig. 8b shows the total scattering coefficient b, and Fig. 8c shows the total QSSA beam attenuation κ. The spread of the IOPs' estimates are shown with pink and green transparent color, which appears brown for overlapping areas.

In Fig. 9a we show the spectrally resolved correlation between model predictions and measurements. The correlations were computed for param 1 and 2, and the set-averaged values were displayed. For comparison, we included the correlations of measurements without making model-based corrections, $corr(R_1, R_2)$. The correlation results would have been identical if we had used radiances. The correlations were evaluated using 5000 spectral pairs that were chosen from DS1 within the aforementioned criteria. For comparison we added the expected performance ceiling case in Fig. 9b which was based on 5000 spectral pairs were the criterion for $|l_{h,1} - l_{h,2}| < 0.1\ m$. Note that the reason why the uncorrected performed best for Fig. 9b was due to seafloor cosines $cos(\theta_{sb,i})$, and without these factors, the corrected approaches would give the highest correlation. In other words, it seemed that $cos(\theta_{sb,i})$ caused some outliers that shifted the corrected correlations in Fig. 9b slightly down. Histograms of cosine similarity are shown in Sec. 3.2 for the same 5000 pairs from DS1. The exception is the ceiling of performance in Fig. 10d that used the 5000 spectral pairs with the modified criterion for $|l_{h,1} - l_{h,2}| < 0.1\ m$. Fig. 10a shows uncorrected cosine similarity between measured spectra $cossim(\boldsymbol{L}_1^i, \boldsymbol{L}_2^i)$, where i denotes index. Fig. 10b and Fig. 10c illustrate corrected cosine similarity $cossim$. For the ith spectral pair was computed as the mean of $cossim(\boldsymbol{L}_1^i, \hat{\boldsymbol{L}}_1^i)$ and $cossim(\boldsymbol{L}_2^i, \hat{\boldsymbol{L}}_2^i)$. The $cossim$ was computed using the median of param 1 and 2. We used radiances instead of reflectances for $cossim$ because it gave a higher cosine similarity, i.e. better agreement in the spectral shape. Again, this was likely because the division by the halogen spectrum in Eq. (20) magnified noise for lower wavelengths.

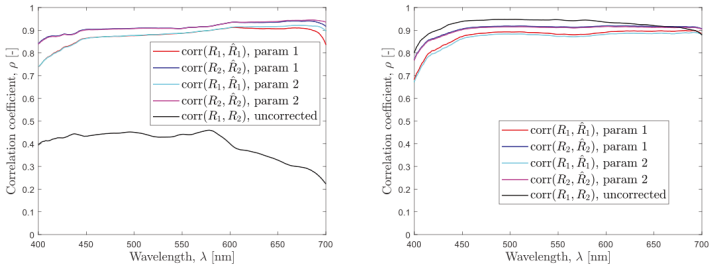

(a) (b)

Fig. 9. Spectrally resolved correlation, denoted $corr$, between measurements and model predictions. The actual evaluation is seen in Fig. 9a while Fig. 9a comparatively shows the ceiling of performance.

4. Discussion

From Fig. 7 we were able to get physically realistic estimates of water body attenuation using two-perspective measurements and empirical per-channel regression. Note that the curves of "empirical data" in Fig. 8c illustrated this further, at least for wavelengths 450-700 nm. This tells us that 1) the two-perspective principle was useful for inferring IOPs and 2) the geometry and model for describing direct light in the SA was useful. It must be kept in mind that these regressions ignored additive, backscattered light, so they are expected to work better for absorption dominated wavelengths/water types as well as cases where there was a strong bottom reflectance. What Fig. 7 also showed was that it seemed useful to compare measurements with pixel positions, in order to mitigate direction-dependent model errors such as non-Lambertian phenomena or errors in light source beam patterns.

The results from optimizing the IOPs' parameters for the SA model showed that we were able to estimate the IOPs in a consistent manner, and that the calibrated semi-analytical model improved similarity significantly for overlapping observations compared to no model correction. Since we did not have in-situ ground truth, it is hard say anything about accuracy of the IOPs. It is worth noting that the absorption and scattering coefficients were of similar magnitude as the coastal Jerlov waters 1C and 3C from Solonenko and Mobley [15]. Parameter estimates were consistent within each data set, although some differences were observed between the two data sets. The absorption estimates differed only by a small amount, which almost solely constituted the difference in κ. The difference was the result of $G_1 - G_2 \approx 0.01\ m^{-1}$. Due to the exponential model of CDOM absorption, a_g, the difference in a is below $0.01\ m^{-1}$ for wavelengths over 440 nm, which we deem insignificant considering other uncertainties of the experiment. Lastly, comparing the per-channel κ estimates in Fig. 8c, these have an offset of between $0.04 - 0.07\ m^{-1}$ for wavelengths 450 nm and upwards, i.e. an almost constant positive offset. However, below 450 nm the offset ranged from -0.05 to $0.04\ m^{-1}$. Comparing the per-channel estimates to the SA derived ones, there was a significant difference below 450 nm. In particular, the SA model suggested a significant increase in κ towards 400 nm that was not seen in the per-channel estimates. Considering that we did not have ground truth and the low SNR for lower wavelengths, it was hard make any definite conclusions.

The most significant difference in the experiment was seen by the mean scattering coefficients in Fig. 8b which differed by $0.07 - 0.17\ m^{-1}$ between the two data sets. In fractional terms, b_1/b_2 varied between $1.36 - 1.43$ where b_1 was the scattering coefficient from param 1, while b_2 was the same from param 2. It was hard to pinpoint what caused the systematic difference,

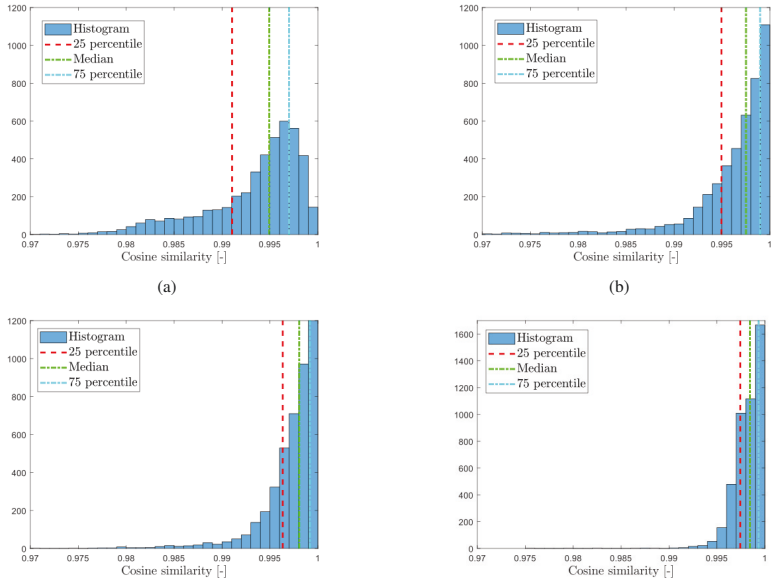

Fig. 10. Pairwise spectral cosine similarity. Fig. 10a shows the uncorrected cosine similarity, while figures 10b and 10c show SA model corrected cosine similarities for param 1 and 2, respectively. The ceiling of performance is shown by Fig. 10d using param 2.

besides a different weighting of the scattering integral. Since the scattering is most important for targets at a longer distances or darker substrates, it could be that the distribution of these variables explained the discrepancy. It could also be that backscatter was hard to estimate in the sense that it had a small detectable effect.

When both parameter sets were applied to the same data set in Fig. 9a we saw that the performance was similar. We also saw that the SA model improved accuracy a lot compared to the uncorrected measurements. In Sec. 3.2 we could see the effect of the SA model on the distribution of the spectral cosine similarity. The largest difference was that the SA-corrected distributions had a 75 percentile that was highly shifted towards 1. This is equivalent to stating that some observations became very similar after correction. However, for both parameter sets the distribution had a tail of low similarity on the distribution that was not seen for the ceiling of performance in Fig. 10d. In fact the differences between the distributions in Fig. 10c and Fig. 10d were arguably driven by SA model errors that grew with difference $|l_{h,1} - l_{h,2}|$. Moreover, from comparing Fig. 10b and Fig. 10c we saw that param 2 outperformed the param 1 in terms of cosine similarity. This was somewhat surprising since the param 1 was calibrated on DS1. We also saw slightly lower performance for the first parameter set in Fig. 9a for wavelengths 600 nm-700 nm. Given that the parameter sets gave similar estimated absorption, this meant that it was the higher scattering coefficient b_1 that caused the dip in correlation for wavelengths 600 nm-700 nm. A potential reason why the optimization for DS1 let this happen, was that our objective function ended up giving too little weight to the high wavelengths. This was because 1) high wavelengths were

heavily attenuated and 2) we divided radiances by the halogen power spectrum which was strong for higher wavelengths. These observations suggest that the objective function and error indices should be re-evaluated and potentially revised. For example substituting reflectances in the error indices of Eq. (20) with radiances.

5. Conclusions and further work

In this paper we have proposed a semi-analytical model for relating measured radiance to bottom reflectance in underwater hyperspectral imaging. Using accurate geometric information derived from SfM-photogrammetry, we used two-perspective observations of seafloor and optimization to retrieve the IOPs. The optimization method gave consistent, and physically realistic IOPs for the water body. The calibrated semi-analytical model resulted in a great increase in across-perspective similarity, suggesting that it successfully compensated for water column and light source effects. As such, the suggested semi-analytical model, geometry and IOPs were successfully demonstrated as a proof of concept.

Our results suggest that it is possible to estimate the IOPs on site using two-perspective observation and a semi-analytical model. The main recommendation for further work would be controlled laboratory experiments with high-accuracy ground truth to further develop the SA model along with mode robust calibration for estimating IOPs and light source geometries. When such methods are mature, it is believed that an SA model with calibrated IOPs in deep-water hyperspectral imaging can provide reliable, robust and low-ambiguity classifiers. Another application is accurate computation of hyperspectral bottom reflectance and co-registration with RGB imagery for creating benchmark data sets with true reflectance data for color correction in RGB underwater imaging.

Funding. This work was supported by the Research Council of Norway through the Centre of Excellence funding scheme, NTNU AMOS, project number 223254.

Acknowledgments. We would like to thank Hongbo Liu from the University in Bergen for being helpful with his knowledge of the hyperspectral sensor and the immersion factor. We would also like to thank former PhD students Aksel Alstad Mogstad and Stein Nornes for the acquisition of the data.

Disclosures. The authors declare no conflicts of interest.

Data availability. Data underlying the results presented in this paper are not publicly available at this time but may be obtained from the authors upon reasonable request.

References

1. Z. Lee, K. L. Carder, C. D. Mobley, R. G. Steward, and J. S. Patch, "Hyperspectral remote sensing for shallow waters. i. A semianalytical model," Appl. optics **37**, 6329–6338 (1998).
2. Z. Lee, K. L. Carder, C. D. Mobley, R. G. Steward, and J. S. Patch, "Hyperspectral remote sensing for shallow waters: 2. Deriving bottom depths and water properties by optimization," Appl. optics **38**, 3831–3843 (1999).
3. T. Kutser, J. Hedley, C. Giardino, C. Roelfsema, and V. E. Brando, "Remote sensing of shallow waters–a 50 year retrospective and future directions," Remote. Sens. Environ. **240**, 111619 (2020).
4. W. Hou, D. J. Gray, A. D. Weidemann, and R. A. Arnone, "Comparison and validation of point spread models for imaging in natural waters," Opt. Express **16**, 9958–9965 (2008).
5. M. Bryson, M. Johnson-Roberson, O. Pizarro, and S. B. Williams, "True color correction of autonomous underwater vehicle imagery," J. Field Robotics **33**, 853–874 (2016).
6. D. Akkaynak and T. Treibitz, "Sea-thru: A method for removing water from underwater images," in *Proceedings of the IEEE/CVF conference on computer vision and pattern recognition,* (2019), pp. 1682–1691.
7. H. S. Løvås, A. A. Mogstad, A. J. Sørensen, and G. Johnsen, "A Methodology for Consistent Georegistration in Underwater Hyperspectral Imaging," IEEE J. Ocean. Eng. **47**, 331–349 (2021).
8. M. Ferrera, A. Arnaubec, K. Istenič, N. Gracias, and T. Bajjouk, "Hyperspectral 3D mapping of underwater environments," in *Proceedings of the IEEE/CVF International Conference on Computer Vision,* (2021), pp. 3703–3712.
9. P. Kumar, N. Gracias, K. Istenič, R. Garcia, A. Arnaubec, M. Ferrera, and T. Bajjouk, "Combined use of a frame and a linear pushbroom camera for deep-sea 3D hyperspectral mapping," in *OCEANS 2021: San Diego–Porto,* (IEEE, 2021), pp. 1–9.
10. M. Bryson, M. Johnson-Roberson, O. Pizarro, and S. B. Williams, "Colour-consistent structure-from-motion models using underwater imagery," Robotics: Sci. Syst. VIII **33** (2013).

11. C. Boittiaux, R. Marxer, C. Dune, A. Arnaubec, M. Ferrera, and V. Hugel, "SUCRe: Leveraging Scene Structure for Underwater Color Restoration," arXiv preprint arXiv:2212.09129 (2022).
12. D. L. Bongiorno, M. Bryson, T. C. Bridge, D. G. Dansereau, and S. B. Williams, "Coregistered hyperspectral and stereo image seafloor mapping from an autonomous underwater vehicle," J. Field Robotics **35**, 312–329 (2018).
13. D. Akkaynak and T. Treibitz, "A revised underwater image formation model," in *Proceedings of the IEEE conference on computer vision and pattern recognition,* (2018), pp. 6723–6732.
14. R. A. Garcia, Z. Lee, and E. J. Hochberg, "Hyperspectral shallow-water remote sensing with an enhanced benthic classifier," Remote. Sens. **10**, 147 (2018).
15. M. G. Solonenko and C. D. Mobley, "Inherent optical properties of Jerlov water types," Appl. optics **54**, 5392–5401 (2015).
16. I. Wald, S. Woop, C. Benthin, G. S. Johnson, and M. Ernst, "Embree: a kernel framework for efficient cpu ray tracing," ACM Trans. on Graph. (TOG) **33**, 1–8 (2014).
17. D. G. Lowe, "Object recognition from local scale-invariant features," in *Proceedings of the seventh IEEE international conference on computer vision,* vol. 2 (IEEE, 1999), pp. 1150–1157.
18. A. Habib, Y. Han, W. Xiong, F. He, Z. Zhang, and M. Crawford, "Automated ortho-rectification of uav-based hyperspectral data over an agricultural field using frame rgb imagery," Remote. Sens. **8**, 796 (2016).
19. A. A. Mogstad, H. S. Løvås, Ø. Sture, G. Johnsen, and M. Ludvigsen, "Remote Sensing of the Tautra Ridge: An Overview of the World's Shallowest Cold-Water Coral Reefs," Front. Mar. Sci. **9**, 848888 (2022).
20. B. McGlamery, "A computer model for underwater camera systems," in *Ocean Optics VI,* vol. 208 (SPIE, 1980), pp. 221–231.
21. J. S. Jaffe, "Computer modeling and the design of optimal underwater imaging systems," IEEE J. Ocean. Eng. **15**, 101–111 (1990).
22. A. Gordon and M. R. Knittel, "Underwater Multiple Scattering of Light for System Designers. Part 1. An Exponential Multiple-Scattering Mode. Part 2. Evaluation of the Exponential Multiple-Scattering Model," Tech. rep., NAVAL UNDERSEA CENTER SAN DIEGO CA (1973).
23. C. Mobley *et al.*, *The Oceanic Optics Book* (International Ocean Colour Coordinating Group (IOCCG), 2022), pp. 366–366.
24. DeepSea, "Multi SeaLite | DeepSea," https://www.deepsea.com/multi-sealite/ (2023). (Accessed: 2023-05-30).
25. C. D. Mobley, H. Zhang, and K. J. Voss, "Effects of optically shallow bottoms on upwelling radiances: Bidirectional reflectance distribution function effects," Limnol. Oceanogr. **48**, 337–345 (2003).
26. R. Szeliski, *Computer vision: algorithms and applications* (Springer Science & Business Media, 2010), pp. 64–65.
27. D. R. Lyzenga, N. P. Malinas, and F. J. Tanis, "Multispectral bathymetry using a simple physically based algorithm," IEEE Trans. on Geosci. Remote. Sens. **44**, 2251–2259 (2006).
28. M. B. Henriksen, E. F. Prentice, T. A. Johansen, and F. Sigernes, "Pre-launch calibration of the HYPSO-1 cubesat hyperspectral imager," in *2022 IEEE Aerospace Conference (AERO),* (IEEE, 2022), pp. 1–9.
29. G. Zibordi, "Immersion factor of in-water radiance sensors: assessment for a class of radiometers," J. Atmospheric Ocean. Technol. **23**, 302–313 (2006).
30. R. Slocum, "Seawater water index of refraction python code," https://github.com/hokiespurs/water_ior/ (2023). (Accessed: 2023-05-30).
31. J. Wray and J. T. Neu, "Refractive index of several glasses as a function of wavelength and temperature," JOSA **59**, 774–776 (1969).
32. A. Bricaud, A. Morel, L. Prieur *et al.*, "Absorption by dissolved organic matter of the sea (yellow substance) in the UV and visible domains," Limnol. Ocean. **26**, 43–53 (1981).
33. C. Mobley *et al.*, *The Oceanic Optics Book* (International Ocean Colour Coordinating Group (IOCCG), 2022), pp. 267–270.
34. R. M. Pope and E. S. Fry, "Absorption spectrum (380–700 nm) of pure water. ii. Integrating cavity measurements," Appl. optics **36**, 8710–8723 (1997).
35. A. Morel, "Optical properties of pure water and pure seawater," Opt. aspects oceanography (1974).
36. T. J. Petzold, "Volume scattering functions for selected ocean waters," Tech. rep., Scripps Institution of Oceanography La Jolla Ca Visibility Lab (1972).
37. C. Mobley, "Petzold VSF and phase function data," https://www.oceanopticsbook.info/packages/iws_l2h/conversion/files/Petzold_data.txt (2023). (Accessed: 2023-06-01).
38. V. I. Haltrin, "Chlorophyll-based model of seawater optical properties," Appl. Opt. **38**, 6826–6832 (1999).
39. A. Morel and H. Loisel, "Apparent optical properties of oceanic water: dependence on the molecular scattering contribution," Appl. Opt. **37**, 4765–4776 (1998).
40. C. Mobley *et al.*, *The Oceanic Optics Book* (International Ocean Colour Coordinating Group (IOCCG), 2022), pp. 106–106.
41. H. R. Gordon, "Can the Lambert-Beer law be applied to the diffuse attenuation coefficient of ocean water?" Limnol. Oceanogr. **34**, 1389–1409 (1989).
42. C. A. Williamson and R. C. Hollins, "Measured IOPs of Jerlov water types," Appl. Opt. **61**, 9951–9961 (2022).

J.5 Underwater Hyperspectral Imaging of Arctic Macroalgal Habitats During the Polar night using a Novel mini-ROV-UHI Portable System

remote sensing

MDPI

Article

Underwater Hyperspectral Imaging of Arctic Macroalgal Habitats during the Polar Night Using a Novel Mini-ROV-UHI Portable System

Natalie Summers [1,*], Geir Johnsen [1,2], Aksel Mogstad [1], Håvard Løvås [3], Glaucia Fragoso [1] and Jørgen Berge [1,2,4]

[1] Centre for Autonomous Marine Operations and Systems (AMOS), Trondheim Biological Station, Department of Biology, Norwegian University of Science and Technology (NTNU), 7018 Trondheim, Norway; geir.johnsen@ntnu.no (G.J.); aksel.a.mogstad@ntnu.no (A.M.); glaucia.m.fragoso@ntnu.no (G.F.); jorgen.berge@uit.no (J.B.)
[2] Department of Arctic Biology, University Centre in Svalbard (UNIS), 9170 Longyearbyen, Norway
[3] Centre for Autonomous Marine Operations and Systems (AMOS), Department of Marine Technology, Norwegian University of Science and Technology (NTNU), 7491 Trondheim, Norway; havard.s.lovas@ntnu.no
[4] Faculty of Biosciences, Fisheries and Economics, Arctic University of Norway (UiT), 9037 Tromsø, Norway
* Correspondence: natalie.summers@ntnu.no

Abstract: We describe an Underwater Hyperspectral Imager (UHI) deployed on an instrument-carrying platform consisting of two interconnected mini-ROVs (Remotely Operated Vehicle) for the mapping and monitoring of Arctic macroalgal habitats in Kongsfjorden (Svalbard) during the Polar Night. The mini-ROV-UHI system is easy to transport, assemble and deploy from shore, even under the dark, icy and cold conditions of the Arctic Polar Night. The system can be operated by two persons, keeping the operational costs low. In vivo hyperspectral reflectance of collected specimens of brown, red and green macroalgae was measured with a spectrometer in the lab to provide a spectral library for supervised pigment group classification based on UHI photomosaics. The in situ UHI-photomosaics provided detailed information of the areal coverage of the seafloor substrate (16%), as well as brown (51% habitat cover), red (18%), and green (14%) macroalgae, with spatial resolution in the range of cm and spectral resolution of 2 nm. The collected specimens from the mapped area were also used for species identification and health state evaluation. This innovative UHI sampling method provides significant information about macroalgal distribution and physiology, and due to its flexibility in terms of deployment, it is applicable to a variety of environments.

Keywords: underwater hyperspectral imaging (UHI); mini ROV (Remotely Operated Vehicle); in situ/in vivo spectral reflectance; underwater habitat mapping; Svalbard; arctic; phaeophytes; chlorophytes; rhodophytes; polar night

Citation: Summers, N.; Johnsen, G.; Mogstad, A.; Løvås, H.; Fragoso, G.; Berge, J. Underwater Hyperspectral Imaging of Arctic Macroalgal Habitats during the Polar Night Using a Novel Mini-ROV-UHI Portable System. *Remote Sens.* **2022**, *14*, 1325. https://doi.org/10.3390/rs14061325

Academic Editor: Shubha Sathyendranath

Received: 31 January 2022
Accepted: 4 March 2022
Published: 9 March 2022

1. Introduction

The use of underwater hyperspectral imaging (UHI) was first published in 2013 [1,2] and first reviewed by [3,4], covering the use of UHI for the identification and mapping of different bio-geo-chemical Objects of Interest (OOI). UHI has been conducted from different instrument-carrying platforms, such as SCUBA diving [2,5] landers [6], underwater slides [1], remotely operated vehicles (ROV) operating from the surface and down to 4200 m [5,7–10], autonomous underwater vehicles (AUV) [11] and unmanned surface vehicles (USV), [12]. Aerial hyperspectral imaging of kelp forests in the Arctic was performed for the first time by using a two engine Dornier airplane carrying a prototype hyperspectral imager (HI) [13]. The airborne campaign was conducted in concert with kelp forest measurements (in situ spectral reflectance) in Kongsfjorden, May 2004 [13]. The current study with mini-ROV-UHI was conducted in the same area [13] in January

2020 during the Polar Night (Figure 1). However, these airborne methods (passive remote sensing) are limited by solar illumination (March to October in Kongsfjorden) making passive remote sensing impossible from November to February due to the Polar Night [14]. In addition, water clarity is low during summertime due to glacial run-off of particles and phytoplankton blooms [13,15], restricting reflected light from macroalgae to be detected by aerial remote sensing. In contrast, during the Polar Night, in situ mapping is restricted to active remote sensing using artificial light sources, which has not been achieved previously.

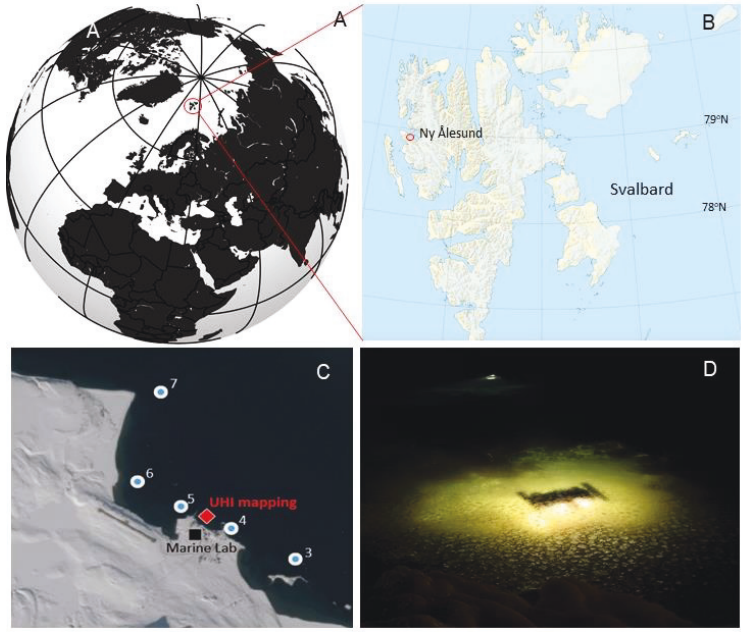

Figure 1. (**A**,**B**) Geoposition of Svalbard. (**C**) The ROV-UHI study site outside the Marine Lab, Ny Ålesund in Kongsfjord. Current UHI survey site (red diamond) in front of the Marine Lab (black square). Aerial hyperspectral imaging study sites from [13] are shown as blue points (3–7). (**D**) ROV-UHI underneath pancake ice. Credits: (**A**,**B**) based on [14]; (**C**) N. Summers (modified from https://geokart.npolar.no/, accessed 16 September 2022) and (**D**) N. Summers.

Macroalgal systematics in Kongsfjorden during the summer season have previously been reviewed [16]. A review of the light regime during the summer season in air and water was carried out by [17]. Polar Night macroalgal biodiversity, ecology, and environmental variables from Kongsfjorden have been reviewed by [15]. Knowledge about macroalgal dynamics (presence, composition, health state) during the three months of Polar Night darkness remains limited to a few species of brown algae [15]. Ecologically relevant light regime data (intensity, spectral composition, and day length), the most important environmental variable for photosynthetic organisms, was provided from the ArcLight observatory in Kongsfjorden for 2017–2020, with 1 h temporal resolution [14].

Fast, precise, and affordable approaches for the identification, mapping and monitoring of marine habitats are needed to provide knowledge and information for nature management and policy-making decisions in marine environments [7]. In situ sampling and mapping of seabed natural communities involving divers, ship-based acoustics, box corers, trawls, RGB photography and video are usually spectrally limited [4]. Satellite-based ocean colour techniques only cover surface waters, while information from the deep habitats is missing.

With the double mini-ROV system described here, we were able to map a macroalgal habitat with a spatial resolution in the range of centimetres with a corresponding spectral

resolution of 2 nm. Because our system (double mini-ROV with the UHI attached) is light (35 kg), it does not require large research vessels and deployment is possible from land or from a small boat. As the system is developed towards becoming more autonomous, the spatial range of data collection will increase from tens of meters to hundreds of meters. By being successful in creating maps in extreme areas, such as during the Arctic Polar Night with dark, cold and icy conditions, this system should also work elsewhere, globally, in less hostile environments [18].

This paper describes a double, interconnected mini-ROV system, comprising a UHI, a battery-powered light source, and an altimeter (estimation of distance between UHI and seafloor) for the identification, mapping and monitoring of seafloor habitats. The ROV-UHI unit comprises two mini-ROVs and a UHI, which can easily be disassembled into three boxes (volume of mid-size suitcases) for transport by car, boat, or airplane and quickly assembled in the field. We describe a battery-powered mini-ROV-UHI system to create useful habitat maps in extreme conditions of the Arctic Polar Night when other methods are limited due the dependence on solar illumination and large robotic systems requiring expensive logistics.

2. Materials and Methods

2.1. Study Area

The study was carried out at 1–2 m depth along the coastal line outside the Marine Laboratory in Ny-Ålesund, Kongsfjorden, Spitsbergen (78°55′40.0″ N 11°55′52.9″ E) on the 11–12 January 2020 (Figure 1). The macroalgal habitat was dominated by the kelp species *Saccharina nigripes* (often indicated as *Laminaria digitata*, see discussion of this species complex in [16]), *Saccharina latissima* and *Alaria esculenta*. The seabed was characterised by a rocky bottom and coarse sand covered by three major macroalgal pigment groups belonging to algal classes Phaeophyceae (brown algae), Chlorophyceae (green algae) and Rhodophyceae (red algae), detailed in [15,16]. Ice-scouring of macroalgae was observed in the shallowest parts close to shore. During the mapping survey, the weather was calm (air temperature −15 °C to −20 °C) with corresponding water temperatures of −1.8 °C, resulting in the formation of pancake ice on the surface, Figure 1D).

2.2. Mini ROV Platform as UHI Carrier

The overall line-up of the interconnected mini-ROVs-UHI system is detailed in [19] and has a total weight in air of 35 kg. Each Blueye Pioneer ROV (Blueye AS, Trondheim, Norway) weighs 9 kg in air, and is able to carry the underwater hyperspectral imager UHI-4 (Ecotone AS, Trondheim, Norway) that also weighs 9 kg in air (Figure 2). The ROV has a 96 Wh lithium-ion smart battery, avoiding the need for a "Dangerous Goods Declaration" (DGD) for air transport (DGD needed for lithium batteries > 100 Wh). The battery time was 2 h at 20 °C but reduced by 50% due to the cold conditions in which they were used (−15 °C air temperature and −1.8 °C water temperature).

The UHI was connected to an underwater electronic housing (Figure 2 #4) containing the UHI battery and a Raspberry Pi computer. The UHI typically consumed 20 W with a maximum of 35 W (UHI-4 manual, Ecotone AS). The electronic housing and the two ROVs were then connected to a surface modem through a "twisted pair" tether containing two wires to transmit and receive data. We then used Wi-Fi to communicate from the modem to a Dell field laptop connected to a power source from the Marine Lab. The UHI captured images using a scientific complementary metal-oxide-semiconductor (sCMOS) camera sensor with a 12-bit radiometric resolution (dynamic range) through an 8 mm fore lens providing a field of view of 60° (transversal) and 0.4° (longitudinal). The spatial resolution of the spectrograph camera was 1936 spatial pixels (image slit) with a spectral resolution of 0.5 nm in the range of 380–750 nm. Prior to providing the UHI transect line, the spectral and spatial binning was set to 2 nm and 968 pixels, respectively, through Ecotone's "Immersion" UHI software (Ecotone AS, Trondheim, Norway). We used a 105 W Keldan Video 8 M CRI LED (light- emitting diode) lamp (KELDAN GmbH, Brügg, Switzerland) to provide

"broadband white light", optimized for underwater imaging. The light was mounted facing down on the aft of the ROV, providing even seafloor illumination using a 90° diffuser for 50 min at full capacity (Figure 3). One person operated the UHI acquisition by using the "Immersion" software, while another operator controlled the ROV via a gamepad that communicated with the field laptop through Bluetooth.

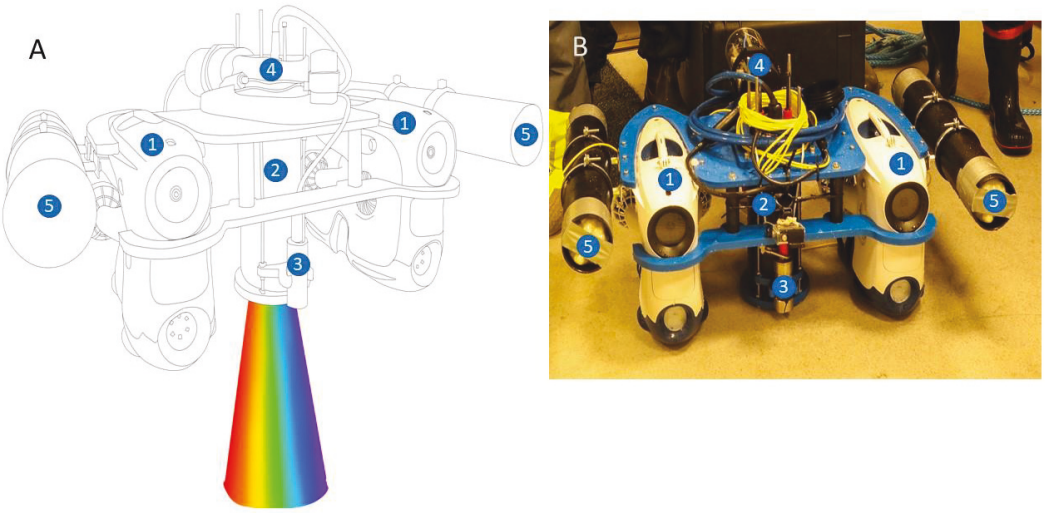

Figure 2. (**A**) Schematic front view of the double mini-ROV rig used (Blueye Pioneer, Blueye), as a carrier for an Underwater Hyperspectral Imager (UHI-4, Ecotone). 1. Mini-ROV, 2. UHI, 3. Altimeter, 4. Underwater electronic housing, 5. Buoyancy tubes (PVC tubes filled with incompressible foam). (**B**) Front view of the mini-ROV rig. Credits: (**A**) by Malin Bø Nevstad, (**B**) by Geir Johnsen.

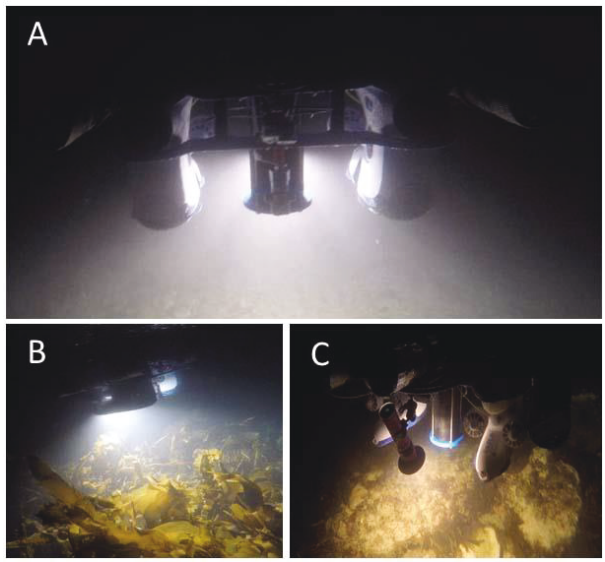

Figure 3. In situ images of mini-ROV UHI survey. (**A**) Front view of ROV-UHI rig showing illumination from lamp during kelp forest mapping. (**B**) Side view of the mini-ROV-UHI over the kelp forest habitat during the transect. (**C**) Aft view of ROV with lamp and UHI over the seafloor. Credits: (**A**–**C**) by Geir Johnsen.

There was no global positioning on the vehicle (and the magnetic compass gave faulty measurements due to closeness to the magnetic North pole). Navigation was, therefore, conducted manually using visual landmarks to assess heading and speed. For data processing purposes, we assume that the ROV track was a straight line moving at a constant speed and heading. An acoustic altimeter measured the altitude from the seafloor (below the macroalgae). Lastly, we used the altitude with the flat seabed assumption for estimating the position of measurements across-track. The main transect line was estimated to be 28 m in length and the vehicle had a constant depth control at 0.5 m depth with an altitude to the seafloor varying between 0.6–1.5 m. The ROV-UHI transect speed was estimated to be 0.3 m s^{-1} based on 3 min for a 60 m transect.

At the beginning of each transect, the UHI was scanning over a Spectralon reflectance standard (SRT-99-050 from Labsphere Inc., North Sutton, USA, providing 99% light reflection from 400–700 nm) placed in an open seafloor area. Given multiple measurements of the Spectralon at varying distances, we estimated the normalized spectral light beam attenuation, c(λ). Immersion software converted the UHI data to absolute radiance. Furthermore, all radiance spectra were normalized by the radiance at 574 nm (high signal-to-noise ratio) to remove baseline effects (wavelength-independent effects) and converted to reflectance taking into account inherent optical properties (IOP) and light source spectra using the following Equation (1) [20]. Each UHI-based pixel has reflectance spectra that can be compared to the lab-based reflectance spectra for classification.

$$R(\lambda) = [L_{u\,OOI}(\lambda)]/L_0(\lambda)] \times e^{(2c(\lambda)(d-d_0))} \quad (1)$$

where: R: Normalised spectral reflectance, $L_{u\,OOI}$: Normalized in situ upwelling radiance measurement of the OOI; L_0: Normalized in situ radiance measurement of reflectance standard at distance d_0; c(λ): Normalized light beam attenuation coefficient; d: Distance to OOI.

2.3. Classification of UHI Data

After optical corrections described above and geometrical correction based on the pitch and roll of the mini ROV [19], the UHI-based reflectance spectra were classified using a two-step classification procedure. The first step was applying the spectral angle mapper (SAM) algorithm based on the spectral library of macroalgal reflectance spectra (green, red and brown macroalgae) measured in the lab beforehand. The spectral library also featured reflectance spectra of various minerals/rocks), as well as coralline algae and calcium carbonate covered in green-algal biofilm. The SAM classification was performed within the spectral interval of 490–690 nm using a narrow maximum angle threshold of 0.09 radians. The interval of 490–690 nm was chosen to eliminate wavelengths with low signal-to-noise ratio in parts of the recorded UHI data, whereas the narrow maximum angle threshold was chosen to make sure only pixel spectra very closely resembling a library spectrum were classified [1].

In the second step, pixels identified by the SAM algorithm were extracted and used as training data for a full-scale Support Vector Machine (SVM) classification with a radial basis function kernel [1]. SVM was chosen due to its previous performances with UHI data [7–10,12]. The training data were categorized into four classes based on their spectral signatures: (1) green algae (green algae and calcium carbonate covered with green alga-like biofilm), (2) red algae (leafy red algae and coralline red algae), (3) brown algae and (4) substrate (different minerals). The classifier was tuned using ten-fold cross-validation, which found that a γ (kernel width) of 10^{-6} in combination with a C (regularization degree) of 10^6 yielded the best classification results (100% cross-validation accuracy). Ultimately, the tuned SVM classifier was applied to the full UHI dataset, yielding a macroalgal map of the survey area. The spectral classification was carried out in the software application ENVI (Environment for Visualizing Images, v. 5.6; Harris Geospatial Solutions Inc., Broomfield, CO, USA), while the SVM tuning was performed in the software environment R, using the package "e1071" [21].

2.4. Ground-Truthing

Two snorkelers collected three specimens of each of the seven most common macroalgal species (Figure 4). Chlorophyceae: *Ulva sp.*, Rhodophyceae: *Palmaria palmata*, Phaeophyceae: *Laminaria digitata/S. nigripes*, *Alaria esculenta*, *Saccharina latissima*, *Fucus distichus*, and *Desmarestia aculeata*. The samples were kept in nets on site at approximately 2 m depth during sampling and stored in 10-L plastic buckets of freezing seawater in a cold room (4 °C) on board until they were processed.

A QE Pro spectrometer (Ocean Insight Inc., Orlando, FL, USA), equipped with an HL-2000-HP high-power tungsten halogen light source from Ocean Insight Inc. (Ocean Insight Inc., Orlando, FL, USA) was used to measure in vivo reflectance spectra between 400 to 700 nm on subsamples from new and old tissue of each macroalgal specimen. The reflectance was measured using a QR 400-7-VIS-BX reflection probe with optical fibres (Ocean Insight Inc., Orlando, FL, USA) and was normalized to a white WS-1 reflectance standard (Ocean Insight Inc., Orlando, FL, USA). Live specimens were also used for photosynthesis measurements and the tissues were frozen in −80 °C for High Performance Liquid Chromatography (HPLC) analysis of pigments (in prep).

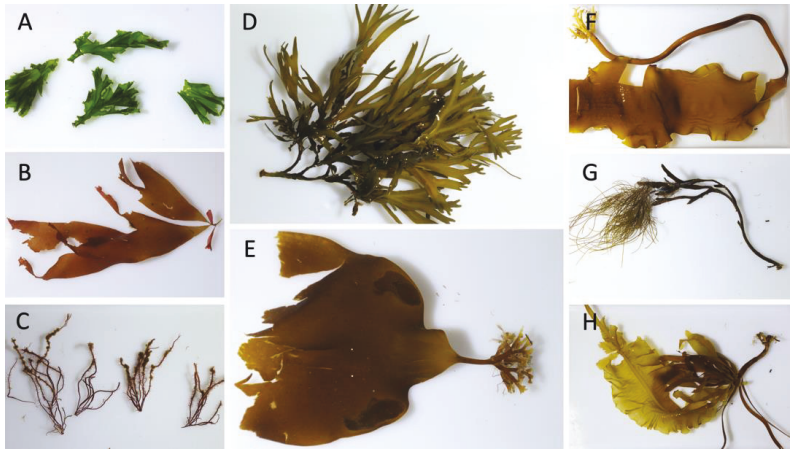

Figure 4. The 8 major macroalgal species sampled from Kongsfjorden macroalgal habitat in January 2020. (**A**) Chlorophyte *Ulva* sp.; (**B**) Rhodophytes *Palmaria palmata*; (**C**) unknown Rhodophyte. (**D**–**H**) Phaeophytes: (**D**) *Fucus distichus*, (**E**) *Laminaria digitata*, (**F**) *Saccharina latissima*, (**G**) *Desmarestia aculeata* and (**H**) *Alaria esculenta*.

3. Results

The in vivo reflectance spectra, R(λ), of collected macroalgae, measured in the laboratory reflected the pigment signatures from three macroalgal classes (herein referred to as "pigment groups", Figure 5). High pigment absorption was observed as low R(λ) at 650 nm (chl b) and 677 nm for green algae, 530–570 nm (phycoerythrin) and 680 nm (chl a) for red algae and 535 nm (fucoxanthin), 630 nm (chl c) and 674 nm (chl a) for brown algae (Figure 5).

Using the reflectance data, the spectra from the hyperspectral images of the seafloor habitat were classified into 4 categories: green, red and brown algae and substrate (minerals). Minerals covered 16.06%, red algae 18.14%, green algae 14.10% and brown algae 51.70% of the UHI transect (Figure 5). Verification (ground-truthing) of collected specimens confirmed the correct identification of algal group and indicated that the estimation of algal cover was accurate (Figure 5).

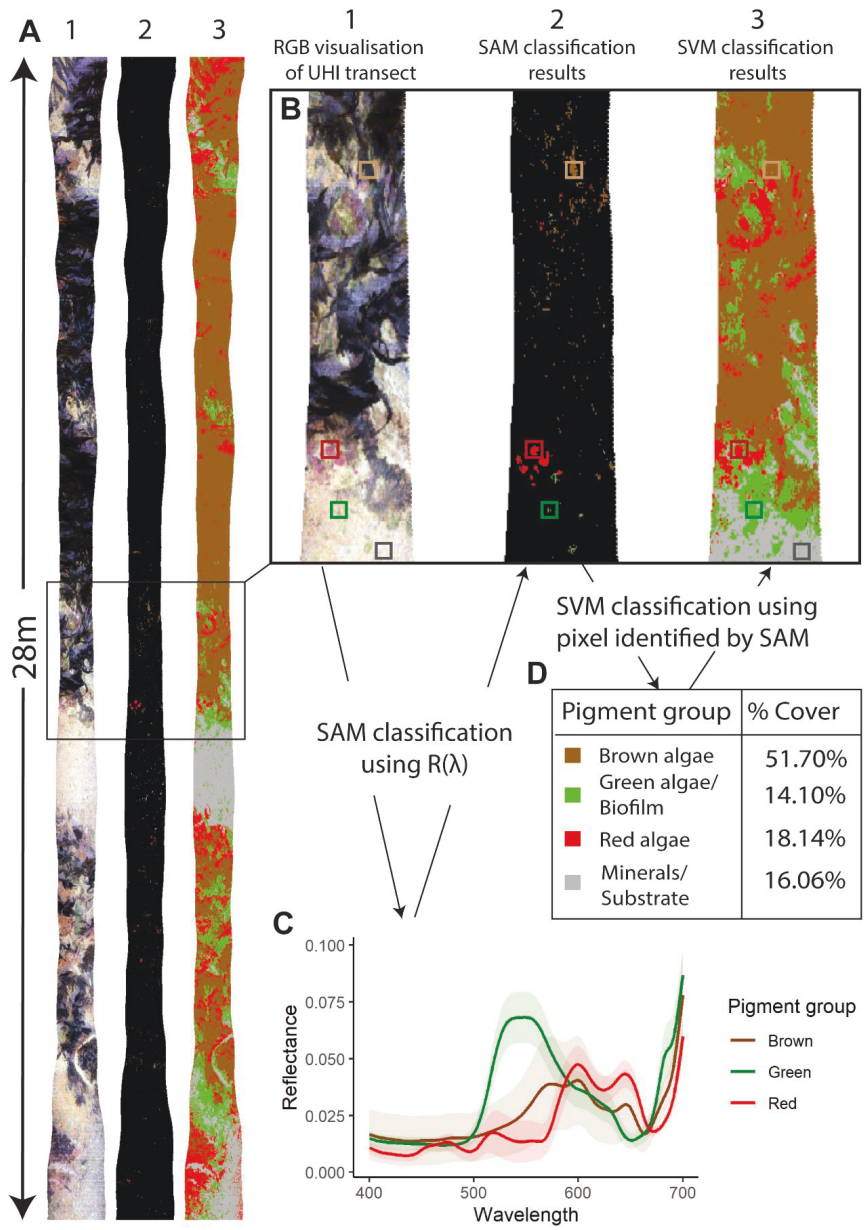

Figure 5. (**A**,**B**) Stages (1–3) for making a map of the macroalgal habitat. Stage 1, RGB visualisation of the UHI transect; Stage 2, Application of spectral angle mapper (SAM) algorithm based on the spectral library of brown, red and green macroalgal in vivo reflectance spectra taken in the lab (**C**); Stage 3, Support Vector Machine (SVM) classification of all remaining pixel into green, brown, red macroalgae and substrate using from SAM pixels as training data. (**C**) In vivo reflectance spectra (R(λ)) with standard error of the mean for each pigment group, measured with a spectrometer. Low R(λ) indicates high absorption at 650 nm (chl b) and 677 nm for green algae, 530–570 nm (phycoerythrin) and 680 nm (chl a) for red algae and lastly 535 nm (fucoxanthin), 630 nm (chl c) and 674 nm (chl a) for brown algae. (**D**) Percent areal cover of each OOI.

4. Discussion

4.1. ROV-UHI Macroalgal Habitat Mapping during the Polar Night

We here report a novel ROV-UHI-survey indicating that the majority of brown, green and red macroalgal species were healthy during the Polar Night. This was indicated by appearance (Figure 4), in vivo R(λ) (showing major functional pigment absorption signature of all pigments, Figure 5), absence of degraded pigments evident in all tissues (HPLC, in prep) and the 8 major species were also able to perform photosynthesis when artificial actinic light was provided (Pulse Amplitude Modulated fluorometry, in prep). The mapped macroalgal habitat in Kongsfjorden was dominated by the brown algae, *Laminaria digitata*, *Alaria esculenta*, *Saccharina latissima*, *Fucus distichus*, and *Desmarestia aculeata*, covering 51.70% of the examined area. The corresponding red and green algal cover comprised 18% and 14% of the mapped area, respectively (Figure 5).

Our study strongly indicates that many algal species, comprising red, green and brown algae, thrived during the dark period (Polar Night). The 8 species examined survived and thrived for >3 months under an irradiance far below the limits for photosynthetic activity (actinic light). Actinic light is generally defined as percent hours per month (H%) with downwelling irradiance higher than 0.01 µmol m^{-2} s^{-1} [14]. The actinic light in Kongsfjorden increases very rapidly in February and March reaching 100 H% in April-August (midnight sun) [14]. Previous studies have shown that the brown algal species *Laminaria solidungula* and *S. latissima* can survive during the Polar Night [15].

The double mini-ROV system presented provides a stable UHI carrier which is easy to transport (35 kg and small size), can be used and deployed from shore by 2 persons and can be disassembled and reassembled. Other ROV systems carrying an UHI typically weigh between 250 kg (inspection ROV, [5,10]) and 3500 kg (work class ROV, [9]). We deployed the system in a water temperature of −1.8 °C with pancake ice forming on the surface. At the surface, the pancake ice interfered with the ROV thrusters creating air bubbles and ice particles resulting in blurry images. To avoid this problem, we operated the ROV from 10 to 50 cm below the surface. The buoyancy tubes (Figure 2 #5) enhance the buoyancy control and stability of the ROV in ice-free water surfaces and at discrete depths. Seeing the live feed (real-time) UHI (data collection) and RGB video acquisition from the ROV (navigation purposes) during our survey was important and was required for online adjustments, such as ROV speed, illumination, altitude to seafloor. The current system's ROVs had about 1 h operational time in these cold conditions. However, the battery packs are easily replaceable without dissembling the whole set-up. The current system is fully manually controlled. Future updates will include automated depth, speed and heading control. This will facilitate route planning, resulting in a more systematic approach to underwater mapping. This study is a proof-of-concept of the mini-ROV-UHI for mapping and monitoring macroalgal habitats in the Arctic. In addition, the system allows us to gather data during the Polar Night when the dark and icy conditions limit the use of other instrument-carrying platforms (such as satellites, airplanes, drones and USV).

During the Polar Night, the water column is usually quite clear, which is optimal for seafloor imaging. High water transparency is caused by low phytoplankton biomass (<0.01 mg chl a m^{-3}), low concentration of coloured dissolved organic matter (cDOM) and total suspended matter (TSM) [15].

There were several factors that affected the in situ reflectance signal of the macroalgae, primarily the distance between the algae and the UHI. The effect of the inherent optical properties (IOP) of the water caused by the absorption and scattering properties of phytoplankton, cDOM and TSM causes variance in the intensity and shape of the spectral signal of the macroalgae and water properties [1]. This potential variation in the IOPs may be higher than the variability of bio-optical properties between species of the same macroalgae pigment group. As a result, we were not able to distinguish between species of the same pigment class.

Another challenge with in situ mapping of macroalgae habitats is that thallus and lamina of larger species (especially kelp) are constantly moving due to wave action and

tidally driven currents. Although the movement did not create any issue regarding the image quality in our study, the fact that the orientation and movement of the lamina were constantly changing during imaging may have introduced errors in the UHI-based percent areal cover estimates. This is especially evident with large kelp species, which have a lamina length that can extend up to 5 m in this area, often twisted and swaying (due to current and swell) in the macroalgal habitat [15,16]. For smaller species, such as wrack (brown algae), red and green algae, this is not a major issue compared to the large kelp species.

4.2. In Vivo Bio-Optical Characteristics of Macroalgae

The shape of the in vivo R(λ) and its intensity (related to pigment concentration in tissue) were used to estimate underwater coverage of brown, red and green macroalgae [15]. Both in situ and in vivo laboratory R(λ) on collected algal specimens indicated the major pigments found in the brown, red and green macroalgae (Figures 4 and 5).

Brown algae is distinguished from the green and red algae by the presence of chl c with peak absorption at 460 nm and minor peaks at 585 and 635 nm [22]. These chromophytes (chl c-containing algae) also contain fucoxanthin that has distinct absorption shoulders at 480, 520 and 545 nm [22].

Red algae are mainly distinguished from brown and green algae by the presence of the phycobiliprotein phycoerythrin that absorbs between 500–600 nm. These absorption peaks are detected as dips in the reflectance data, indicating the corresponding high absorption by pigments (Figure 5C). Figure 5B shows that the SAM algorithm classified coralline algae in the red algae class with *P. palmata* due to similar R(λ) related to their pigment composition [8,15].

The green algae were characterized by the absorption peaks (or reflectance dip) corresponding to the following pigments: chl a, chl b and lutein. This is seen by in vivo R(λ) dips at 400–500 nm due to all major pigments of green algae, and at 650 nm due to chl b (Figure 5). Our findings regarding optical fingerprints from R(λ) from in situ and in vivo specimens are in agreement with in vivo absorption properties of the same macroalgal groups found in the Trondheim fjord, Norway [15,22], where leafy green algae such as *Ulva* spp. are characterized by the major pigments chl a, chl b and lutein. For green algae, chl a has absorption peaks in vivo at 440 nm, 630 nm and 675 nm. Chl b has in vivo absorption peaks at 470 nm, 600 nm and 650 nm and the carotenoid lutein has an in vivo absorption peak at 460 nm and 485 nm [22]. The indication of green algae, seen as reflectance of biofilm-like structures, is likely caused by the chl b. Biofilms are important to the ecosystem, providing food to other organisms and potentially "seeds" for micro- and macroalgae when light becomes available in the spring [15]. Future research on this topic could offer important insights on biofilm composition and the role of algal dynamics in the Arctic.

5. Conclusions

The UHI has shown potential for the identification of macroalgal groups that are hard to see or identify with the human eye or with an RGB camera (such as coralline algae and biofilm). In addition, the optical correction described here (Equation (1)) allowed us to classify pixels directly based on in vivo reflectance signatures. This automated classification, using spectral fingerprints to classify individual pixels, greatly reduces the time needed to create maps of OOI. The maps created by the UHI can be a base to select areas of interest for more detailed experiments.

The relatively small size and weight of this ROV and UHI system may reduce the user threshold and cost for mapping of seafloor and facilitate the logistics for field work in remote areas. Future improvement of the software can make the navigation system more autonomous and able to follow a survey pattern. Currently, work with additional IOP sensors will allow us to correct for spectral attenuation of constituents of seawater itself and its optical active constituents to improve the OOI signatures. The current use of the acoustic altimeter gave us the ability to stay at a fixed depth. Ongoing work to estimate the

distance from the instrument-carrying robot to the habitat/OOI is challenging in a kelp forest due to the movement of macroalgae caused by waves and currents. This challenge may be solved by other types of non-acoustic altimeters based on optics, such as Lidars.

We have shown that our innovative ROV-UHI rig can function in extreme conditions of the Polar Night, at −2 °C water temperature and under sea-ice formation. The setup is simple to transport, making it ideal for in situ OOI identification, mapping and monitoring. Thus, the system should work with great ease in less hostile environments around the globe. Future updates will include enhanced altitude control (distance from the seafloor or other surface), more automated navigation, and heading control and speed control, making the system more versatile. These in situ hyperspectral habitat maps, using UHI as an active remote sensing sensor (equipped with its own light source), provide data when airborne platforms cannot, such as when there is a lack of ambient light, cloud cover or for deeper seafloor mapping. In addition, the data collected can be used to verify/ground truth remotely sensed RGB-, multi- or hyperspectral images collected from these airborne platforms.

Author Contributions: Conceptualization, N.S., G.J., A.M. and H.L.; Formal analysis, N.S., A.M. and H.L.; Funding acquisition, G.J. and J.B.; Investigation, N.S., G.J., A.M. and H.L.; Methodology, N.S., G.J., A.M. and H.L.; Project administration, G.J. and J.B.; Supervision, G.J. and G.F.; Visualization, N.S., G.J. and A.M.; Writing—original draft, N.S.; Writing—review and editing, N.S., G.J., A.M., H.L., G.F. and J.B. All authors have read and agreed to the published version of the manuscript.

Funding: This work was carried out at the Centre of Autonomous Marine Operations and Systems (AMOS, NTNU). This research was funded by the Research Council of Norway (NFR), through the centres of excellence funding scheme, grant numbers 223254 (AMOS), 276730 (Nansen Legacy), 245923 (Arctic ABC-D) and 315514 (MoniTare).

Acknowledgments: The authors want to thank the crew of R/V Helmer Hanssen and the engineers of NTNU Applied Underwater Robotics Laboratory (AUR Lab).

Conflicts of Interest: The authors declare no conflict of interest. The funders had no role in the design of the study; in the collection, analyses, or interpretation of data; in the writing of the manuscript, or in the decision to publish the results.

References

1. Johnsen, G.; Volent, Z.; Dierssen, H.; Pettersen, R.; Van Ardelan, M.; Søreide, F.; Fearns, P.; Ludvigsen, M.; Moline, M. Underwater hyperspectral imagery to create biogeochemical maps of seafloor properties. In *Subsea Optics and Imaging*; Woodhead Publishing: Sawston, UK, 2013; pp. 508–535; ISBN 9780857093417.
2. Chennu, A.; Färber, P.; Volkenborn, N.; Al-Najjar, M.A.A.; Janssen, F.; de Beer, D.; Polerecky, L. Hyperspectral imaging of the microscale distribution and dynamics of microphytobenthos in intertidal sediments. *Limnol. Oceanogr. Methods* **2013**, *11*, 511–528. [CrossRef]
3. Liu, B.; Liu, Z.; Men, S.; Li, Y.; Ding, Z.; He, J.; Zhao, Z. Underwater Hyperspectral Imaging Technology and Its Applications for Detecting and Mapping the Seafloor: A Review. *Sensors* **2020**, *20*, 4962. [CrossRef] [PubMed]
4. Montes-Herrera, J.C.; Cimoli, E.; Cummings, V.; Hill, N.; Lucieer, A.; Lucieer, V. Underwater hyperspectral imaging (UHI): A review of systems and applications for proximal seafloor ecosystem studies. *Remote Sens.* **2021**, *13*, 3451. [CrossRef]
5. Johnsen, G.; Ludvigsen, M.; Sørensen, A.; Sandvik Aas, L.M. The use of underwater hyperspectral imaging deployed on remotely operated vehicles—methods and applications. *IFAC-PapersOnLine* **2016**, *49*, 476–481. [CrossRef]
6. Dumke, I.; Ludvigsen, M.; Ellefmo, S.L.; Søreide, F.; Johnsen, G.; Murton, B.J. Underwater Hyperspectral Imaging Using a Stationary Platform in the Trans-Atlantic Geotraverse Hydrothermal Field. *IEEE Trans. Geosci. Remote Sens.* **2019**, *57*, 2947–2962. [CrossRef]
7. Johnsen, G.; Mogstad, A.A.; Berge, J.; Cohen, J.H. Operative habitat mapping and monitoring in the polar night. In *Polar Night Marine Ecology: Life and Light in the Dead of Night*; Berge, J., Johnsen, G., Cohen, J.H., Eds.; Springer International Publishing: Cham, Switzerland, 2020; pp. 277–305; ISBN 978-3-030-33208-2.
8. Mogstad, A.A.; Johnsen, G. Spectral characteristics of coralline algae: A multi-instrumental approach, with emphasis on underwater hyperspectral imaging. *Appl. Opt.* **2017**, *56*, 9957. [CrossRef]
9. Dumke, I.; Nornes, S.M.; Purser, A.; Marcon, Y.; Ludvigsen, M.; Ellefmo, S.L.; Johnsen, G.; Søreide, F. First hyperspectral imaging survey of the deep seafloor: High-resolution mapping of manganese nodules. *Remote Sens. Environ.* **2018**, *209*, 19–30. [CrossRef]
10. Ødegård, Ø.; Mogstad, A.A.; Johnsen, G.; Sørensen, A.J.; Ludvigsen, M. Underwater hyperspectral imaging: A new tool for marine archaeology. *Appl. Opt.* **2018**, *57*, 3214. [CrossRef] [PubMed]

11. Sture, Ø.; Ludvigsen, M.; Søreide, F.; Aas, L.M.S. Autonomous underwater vehicles as a platform for underwater hyperspectral imaging. In Proceedings of the OCEANS 2017, Aberdeen, UK, 19–22 June 2017; pp. 1–8.
12. Mogstad, A.A.; Johnsen, G.; Ludvigsen, M. Shallow-water habitat mapping using Underwater Hyperspectral Imaging from an Unmanned Surface Vehicle: A pilot study. *Remote Sens.* **2019**, *11*, 685. [CrossRef]
13. Volent, Z.; Johnsen, G.; Sigernes, F. Kelp forest mapping by use of airborne hyperspectral imager. *J. Appl. Remote Sens.* **2007**, *1*, 011503. [CrossRef]
14. Johnsen, G.; Zolich, A.; Grant, S.; Bjørgum, R.; Cohen, J.H.; McKee, D.; Kopec, T.P.; Vogedes, D.; Berge, J. All-sky camera system providing high temporal resolution annual time series of irradiance in the Arctic. *Appl. Opt.* **2021**, *60*, 6456. [CrossRef] [PubMed]
15. Johnsen, G.; Leu, E.; Gradinger, R. Marine micro- and macroalgae in the polar night. In *Polar Night Marine Ecology: Life and Light in the Dead of Night*; Berge, J., Johnsen, G., Cohen, J.H., Eds.; Springer International Publishing: Cham, Switzerland, 2020; pp. 67–112; ISBN 978-3-030-33208-2.
16. Fredriksen, S.; Karsten, U.; Bartsch, I.; Woelfel, J.; Koblowsky, M.; Schumann, R.; Moy, S.R.; Steneck, R.S.; Wiktor, J.M.; Hop, H.; et al. Biodiversity of benthic macro- and microalgae from svalbard with special focus on kongsfjorden. In *The Ecosystem of Kongsfjorden, Svalbard*; Hop, H., Wiencke, C., Eds.; Springer International Publishing: Cham, Switzerland, 2019; pp. 331–371; ISBN 978-3-319-46425-1.
17. Pavlov, A.K.; Leu, E.; Hanelt, D.; Bartsch, I.; Karsten, U.; Hudson, S.R.; Gallet, J.-C.; Cottier, F.; Cohen, J.H.; Berge, J.; et al. The underwater light climate in Kongsfjorden and its ecological implications. In *The Ecosystem of Kongsfjorden, Svalbard*; Hop, H., Wiencke, C., Eds.; Springer International Publishing: Cham, Switzerland, 2019; pp. 137–170; ISBN 978-3-319-46425-1.
18. Sørensen, A.J. Testination north. In *Whither the Arctic Ocean? Research, Knowledge Needs and Development en Route to the New Arctic*; Paul, W., Ed.; Fundacion BBVA: Bilbao, Spain, 2021; pp. 165–175; ISBN 978-84-92937-82-0.
19. Lovas, H.S.; Sorensen, A.J.; Ludvigsen, M. Framework for combining multiple lightweight underwater vehicles into super underwater vehicle. In Proceedings of the 2020 IEEE/OES Autonomous Underwater Vehicles Symposium (AUV), St. Johns, NL, Canada, 30 September–2 October 2020. [CrossRef]
20. Lovas, H.S.; Mogstad, A.A.; Sorensen, A.J.; Johnsen, G. A Methodology for Consistent Georegistration in Underwater Hyperspectral Imaging. *IEEE J. Ocean. Eng.* **2021**, 1–19. [CrossRef]
21. Meyer, D.; Dimitriadou, E.; Hornik, K.; Weingessel, A.; Leisch, F. e1071: Misc Functions of the Department of Statistics, Probability Theory Group (Formerly: E1071). TU Wien. R Package Version 1.7-1. Available online: https://CRAN.R-project.org/package=e (accessed on 31 January 2022).
22. Grzymski, J.; Johnsen, G.; Sakshaug, E. The significance of intracellular self-shading on the biooptical properties of brown, red, and green macroalgae. *J. Phycol.* **1997**, *33*, 408–414. [CrossRef]

C.1 Framework for combining multiple lightweight underwater vehicles into super underwater vehicle

Previous PhD theses published at the Department of Marine Technology

Previous PhD theses published at the Department of Marine Technology (earlier: Faculty of Marine Technology)
NORWEGIAN UNIVERSITY OF SCIENCE AND TECHNOLOGY

Report No.	Author	Title
	Kavlie, Dag	Optimization of Plane Elastic Grillages, 1967
	Hansen, Hans R.	Man-Machine Communication and Data-Storage Methods in Ship Structural Design, 1971
	Gisvold, Kaare M.	A Method for non-linear mixed -integer programming and its Application to Design Problems, 1971
	Lund, Sverre	Tanker Frame Optimalization by means of SUMT-Transformation and Behaviour Models, 1971
	Vinje, Tor	On Vibration of Spherical Shells Interacting with Fluid, 1972
	Lorentz, Jan D.	Tank Arrangement for Crude Oil Carriers in Accordance with the new Anti-Pollution Regulations, 1975
	Carlsen, Carl A.	Computer-Aided Design of Tanker Structures, 1975
	Larsen, Carl M.	Static and Dynamic Analysis of Offshore Pipelines during Installation, 1976
UR-79-01	Brigt Hatlestad, MK	The finite element method used in a fatigue evaluation of fixed offshore platforms. (Dr.Ing. Thesis)
UR-79-02	Erik Pettersen, MK	Analysis and design of cellular structures. (Dr.Ing. Thesis)
UR-79-03	Sverre Valsgård, MK	Finite difference and finite element methods applied to nonlinear analysis of plated structures. (Dr.Ing. Thesis)
UR-79-04	Nils T. Nordsve, MK	Finite element collapse analysis of structural members considering imperfections and stresses due to fabrication. (Dr.Ing. Thesis)
UR-79-05	Ivar J. Fylling, MK	Analysis of towline forces in ocean towing systems. (Dr.Ing. Thesis)
UR-79- x	Finn Gunnar Nielsen, MH	Hydrodynamic problems related to oil barriers for offshore application
UR-80-06	Nils Sandsmark, MM	Analysis of Stationary and Transient Heat Conduction by the Use of the Finite Element Method. (Dr.Ing. Thesis)
UR-80-09	Sverre Haver, MK	Analysis of uncertainties related to the stochastic modeling of ocean waves. (Dr.Ing. Thesis)

UR-81-15	Odland, Jonas	On the Strength of welded Ring stiffened cylindrical Shells primarily subjected to axial Compression
UR-82-17	Engesvik, Knut	Analysis of Uncertainties in the fatigue Capacity of Welded Joints
UR-82-18	Rye, Henrik	Ocean wave groups
UR-83-30	Eide, Oddvar Inge	On Cumulative Fatigue Damage in Steel Welded Joints
UR-83-33	Mo, Olav	Stochastic Time Domain Analysis of Slender Offshore Structures
UR-83-34	Amdahl, Jørgen	Energy absorption in Ship-platform impacts
UR-84-37	Mørch, Morten	Motions and mooring forces of semi submersibles as determined by full-scale measurements and theoretical analysis
UR-84-38	Soares, C. Guedes	Probabilistic models for load effects in ship structures
UR-84-39	Aarsnes, Jan V.	Current forces on ships
UR-84-40	Czujko, Jerzy	Collapse Analysis of Plates subjected to Biaxial Compression and Lateral Load
UR-85-46	Alf G. Engseth, MK	Finite element collapse analysis of tubular steel offshore structures. (Dr.Ing. Thesis)
UR-86-47	Dengody Sheshappa, MP	A Computer Design Model for Optimizing Fishing Vessel Designs Based on Techno-Economic Analysis. (Dr.Ing. Thesis)
UR-86-48	Vidar Aanesland, MH	A Theoretical and Numerical Study of Ship Wave Resistance. (Dr.Ing. Thesis)
UR-86-49	Heinz-Joachim Wessel, MK	Fracture Mechanics Analysis of Crack Growth in Plate Girders. (Dr.Ing. Thesis)
UR-86-50	Jon Taby, MK	Ultimate and Post-ultimate Strength of Dented Tubular Members. (Dr.Ing. Thesis)
UR-86-51	Walter Lian, MH	A Numerical Study of Two-Dimensional Separated Flow Past Bluff Bodies at Moderate KC-Numbers. (Dr.Ing. Thesis)
UR-86-52	Bjørn Sortland, MH	Force Measurements in Oscillating Flow on Ship Sections and Circular Cylinders in a U-Tube Water Tank. (Dr.Ing. Thesis)
UR-86-53	Kurt Strand, MM	A System Dynamic Approach to One-dimensional Fluid Flow. (Dr.Ing. Thesis)
UR-86-54	Arne Edvin Løken, MH	Three Dimensional Second Order Hydrodynamic Effects on Ocean Structures in Waves. (Dr.Ing. Thesis)
UR-86-55	Sigurd Falch, MH	A Numerical Study of Slamming of Two-

		Dimensional Bodies. (Dr.Ing. Thesis)
UR-87-56	Arne Braathen, MH	Application of a Vortex Tracking Method to the Prediction of Roll Damping of a Two-Dimension Floating Body. (Dr.Ing. Thesis)
UR-87-57	Bernt Leira, MK	Gaussian Vector Processes for Reliability Analysis involving Wave-Induced Load Effects. (Dr.Ing. Thesis)
UR-87-58	Magnus Småvik, MM	Thermal Load and Process Characteristics in a Two-Stroke Diesel Engine with Thermal Barriers (in Norwegian). (Dr.Ing. Thesis)
MTA-88-59	Bernt Arild Bremdal, MP	An Investigation of Marine Installation Processes – A Knowledge - Based Planning Approach. (Dr.Ing. Thesis)
MTA-88-60	Xu Jun, MK	Non-linear Dynamic Analysis of Space-framed Offshore Structures. (Dr.Ing. Thesis)
MTA-89-61	Gang Miao, MH	Hydrodynamic Forces and Dynamic Responses of Circular Cylinders in Wave Zones. (Dr.Ing. Thesis)
MTA-89-62	Martin Greenhow, MH	Linear and Non-Linear Studies of Waves and Floating Bodies. Part I and Part II. (Dr.Techn. Thesis)
MTA-89-63	Chang Li, MH	Force Coefficients of Spheres and Cubes in Oscillatory Flow with and without Current. (Dr.Ing. Thesis
MTA-89-64	Hu Ying, MP	A Study of Marketing and Design in Development of Marine Transport Systems. (Dr.Ing. Thesis)
MTA-89-65	Arild Jæger, MH	Seakeeping, Dynamic Stability and Performance of a Wedge Shaped Planing Hull. (Dr.Ing. Thesis)
MTA-89-66	Chan Siu Hung, MM	The dynamic characteristics of tilting-pad bearings
MTA-89-67	Kim Wikstrøm, MP	Analysis av projekteringen for ett offshore projekt. (Licenciat-avhandling)
MTA-89-68	Jiao Guoyang, MK	Reliability Analysis of Crack Growth under Random Loading, considering Model Updating. (Dr.Ing. Thesis)
MTA-89-69	Arnt Olufsen, MK	Uncertainty and Reliability Analysis of Fixed Offshore Structures. (Dr.Ing. Thesis)
MTA-89-70	Wu Yu-Lin, MR	System Reliability Analyses of Offshore Structures using improved Truss and Beam Models. (Dr.Ing. Thesis)
MTA-90-71	Jan Roger Hoff, MH	Three-dimensional Green function of a vessel with forward speed in waves. (Dr.Ing. Thesis)
MTA-90-72	Rong Zhao, MH	Slow-Drift Motions of a Moored Two-Dimensional Body in Irregular Waves. (Dr.Ing. Thesis)
MTA-90-73	Atle Minsaas, MP	Economical Risk Analysis. (Dr.Ing. Thesis)

MTA-90-74	Knut-Aril Farnes, MK	Long-term Statistics of Response in Non-linear Marine Structures. (Dr.Ing. Thesis)
MTA-90-75	Torbjørn Sotberg, MK	Application of Reliability Methods for Safety Assessment of Submarine Pipelines. (Dr.Ing. Thesis)
MTA-90-76	Zeuthen, Steffen, MP	SEAMAID. A computational model of the design process in a constraint-based logic programming environment. An example from the offshore domain. (Dr.Ing. Thesis)
MTA-91-77	Haagensen, Sven, MM	Fuel Dependant Cyclic Variability in a Spark Ignition Engine - An Optical Approach. (Dr.Ing. Thesis)
MTA-91-78	Løland, Geir, MH	Current forces on and flow through fish farms. (Dr.Ing. Thesis)
MTA-91-79	Hoen, Christopher, MK	System Identification of Structures Excited by Stochastic Load Processes. (Dr.Ing. Thesis)
MTA-91-80	Haugen, Stein, MK	Probabilistic Evaluation of Frequency of Collision between Ships and Offshore Platforms. (Dr.Ing. Thesis)
MTA-91-81	Sødahl, Nils, MK	Methods for Design and Analysis of Flexible Risers. (Dr.Ing. Thesis)
MTA-91-82	Ormberg, Harald, MK	Non-linear Response Analysis of Floating Fish Farm Systems. (Dr.Ing. Thesis)
MTA-91-83	Marley, Mark J., MK	Time Variant Reliability under Fatigue Degradation. (Dr.Ing. Thesis)
MTA-91-84	Krokstad, Jørgen R., MH	Second-order Loads in Multidirectional Seas. (Dr.Ing. Thesis)
MTA-91-85	Molteberg, Gunnar A., MM	The Application of System Identification Techniques to Performance Monitoring of Four Stroke Turbocharged Diesel Engines. (Dr.Ing. Thesis)
MTA-92-86	Mørch, Hans Jørgen Bjelke, MH	Aspects of Hydrofoil Design: with Emphasis on Hydrofoil Interaction in Calm Water. (Dr.Ing. Thesis)
MTA-92-87	Chan Siu Hung, MM	Nonlinear Analysis of Rotordynamic Instabilities in Highspeed Turbomachinery. (Dr.Ing. Thesis)
MTA-92-88	Bessason, Bjarni, MK	Assessment of Earthquake Loading and Response of Seismically Isolated Bridges. (Dr.Ing. Thesis)
MTA-92-89	Langli, Geir, MP	Improving Operational Safety through exploitation of Design Knowledge - an investigation of offshore platform safety. (Dr.Ing. Thesis)
MTA-92-90	Sævik, Svein, MK	On Stresses and Fatigue in Flexible Pipes. (Dr.Ing. Thesis)
MTA-92-91	Ask, Tor Ø., MM	Ignition and Flame Growth in Lean Gas-Air Mixtures. An Experimental Study with a Schlieren

		System. (Dr.Ing. Thesis)
MTA-86-92	Hessen, Gunnar, MK	Fracture Mechanics Analysis of Stiffened Tubular Members. (Dr.Ing. Thesis)
MTA-93-93	Steinebach, Christian, MM	Knowledge Based Systems for Diagnosis of Rotating Machinery. (Dr.Ing. Thesis)
MTA-93-94	Dalane, Jan Inge, MK	System Reliability in Design and Maintenance of Fixed Offshore Structures. (Dr.Ing. Thesis)
MTA-93-95	Steen, Sverre, MH	Cobblestone Effect on SES. (Dr.Ing. Thesis)
MTA-93-96	Karunakaran, Daniel, MK	Nonlinear Dynamic Response and Reliability Analysis of Drag-dominated Offshore Platforms. (Dr.Ing. Thesis)
MTA-93-97	Hagen, Arnulf, MP	The Framework of a Design Process Language. (Dr.Ing. Thesis)
MTA-93-98	Nordrik, Rune, MM	Investigation of Spark Ignition and Autoignition in Methane and Air Using Computational Fluid Dynamics and Chemical Reaction Kinetics. A Numerical Study of Ignition Processes in Internal Combustion Engines. (Dr.Ing. Thesis)
MTA-94-99	Passano, Elizabeth, MK	Efficient Analysis of Nonlinear Slender Marine Structures. (Dr.Ing. Thesis)
MTA-94-100	Kvålsvold, Jan, MH	Hydroelastic Modelling of Wetdeck Slamming on Multihull Vessels. (Dr.Ing. Thesis)
MTA-94-102	Bech, Sidsel M., MK	Experimental and Numerical Determination of Stiffness and Strength of GRP/PVC Sandwich Structures. (Dr.Ing. Thesis)
MTA-95-103	Paulsen, Hallvard, MM	A Study of Transient Jet and Spray using a Schlieren Method and Digital Image Processing. (Dr.Ing. Thesis)
MTA-95-104	Hovde, Geir Olav, MK	Fatigue and Overload Reliability of Offshore Structural Systems, Considering the Effect of Inspection and Repair. (Dr.Ing. Thesis)
MTA-95-105	Wang, Xiaozhi, MK	Reliability Analysis of Production Ships with Emphasis on Load Combination and Ultimate Strength. (Dr.Ing. Thesis)
MTA-95-106	Ulstein, Tore, MH	Nonlinear Effects of a Flexible Stern Seal Bag on Cobblestone Oscillations of an SES. (Dr.Ing. Thesis)
MTA-95-107	Solaas, Frøydis, MH	Analytical and Numerical Studies of Sloshing in Tanks. (Dr.Ing. Thesis)
MTA-95-108	Hellan, Øyvind, MK	Nonlinear Pushover and Cyclic Analyses in Ultimate Limit State Design and Reassessment of Tubular Steel Offshore Structures. (Dr.Ing. Thesis)
MTA-95-109	Hermundstad, Ole A., MK	Theoretical and Experimental Hydroelastic Analysis of High Speed Vessels. (Dr.Ing. Thesis)

MTA-96-110	Bratland, Anne K., MH	Wave-Current Interaction Effects on Large-Volume Bodies in Water of Finite Depth. (Dr.Ing. Thesis)
MTA-96-111	Herfjord, Kjell, MH	A Study of Two-dimensional Separated Flow by a Combination of the Finite Element Method and Navier-Stokes Equations. (Dr.Ing. Thesis)
MTA-96-112	Æsøy, Vilmar, MM	Hot Surface Assisted Compression Ignition in a Direct Injection Natural Gas Engine. (Dr.Ing. Thesis)
MTA-96-113	Eknes, Monika L., MK	Escalation Scenarios Initiated by Gas Explosions on Offshore Installations. (Dr.Ing. Thesis)
MTA-96-114	Erikstad, Stein O., MP	A Decision Support Model for Preliminary Ship Design. (Dr.Ing. Thesis)
MTA-96-115	Pedersen, Egil, MH	A Nautical Study of Towed Marine Seismic Streamer Cable Configurations. (Dr.Ing. Thesis)
MTA-97-116	Moksnes, Paul O., MM	Modelling Two-Phase Thermo-Fluid Systems Using Bond Graphs. (Dr.Ing. Thesis)
MTA-97-117	Halse, Karl H., MK	On Vortex Shedding and Prediction of Vortex-Induced Vibrations of Circular Cylinders. (Dr.Ing. Thesis)
MTA-97-118	Igland, Ragnar T., MK	Reliability Analysis of Pipelines during Laying, considering Ultimate Strength under Combined Loads. (Dr.Ing. Thesis)
MTA-97-119	Pedersen, Hans-P., MP	Levendefiskteknologi for fiskefartøy. (Dr.Ing. Thesis)
MTA-98-120	Vikestad, Kyrre, MK	Multi-Frequency Response of a Cylinder Subjected to Vortex Shedding and Support Motions. (Dr.Ing. Thesis)
MTA-98-121	Azadi, Mohammad R. E., MK	Analysis of Static and Dynamic Pile-Soil-Jacket Behaviour. (Dr.Ing. Thesis)
MTA-98-122	Ulltang, Terje, MP	A Communication Model for Product Information. (Dr.Ing. Thesis)
MTA-98-123	Torbergsen, Erik, MM	Impeller/Diffuser Interaction Forces in Centrifugal Pumps. (Dr.Ing. Thesis)
MTA-98-124	Hansen, Edmond, MH	A Discrete Element Model to Study Marginal Ice Zone Dynamics and the Behaviour of Vessels Moored in Broken Ice. (Dr.Ing. Thesis)
MTA-98-125	Videiro, Paulo M., MK	Reliability Based Design of Marine Structures. (Dr.Ing. Thesis)
MTA-99-126	Mainçon, Philippe, MK	Fatigue Reliability of Long Welds Application to Titanium Risers. (Dr.Ing. Thesis)
MTA-99-127	Haugen, Elin M., MH	Hydroelastic Analysis of Slamming on Stiffened Plates with Application to Catamaran Wetdecks. (Dr.Ing. Thesis)
MTA-99-	Langhelle, Nina K., MK	Experimental Validation and Calibration of

128		Nonlinear Finite Element Models for Use in Design of Aluminium Structures Exposed to Fire. (Dr.Ing. Thesis)
MTA-99-129	Berstad, Are J., MK	Calculation of Fatigue Damage in Ship Structures. (Dr.Ing. Thesis)
MTA-99-130	Andersen, Trond M., MM	Short Term Maintenance Planning. (Dr.Ing. Thesis)
MTA-99-131	Tveiten, Bård Wathne, MK	Fatigue Assessment of Welded Aluminium Ship Details. (Dr.Ing. Thesis)
MTA-99-132	Søreide, Fredrik, MP	Applications of underwater technology in deep water archaeology. Principles and practice. (Dr.Ing. Thesis)
MTA-99-133	Tønnessen, Rune, MH	A Finite Element Method Applied to Unsteady Viscous Flow Around 2D Blunt Bodies With Sharp Corners. (Dr.Ing. Thesis)
MTA-99-134	Elvekrok, Dag R., MP	Engineering Integration in Field Development Projects in the Norwegian Oil and Gas Industry. The Supplier Management of Norne. (Dr.Ing. Thesis)
MTA-99-135	Fagerholt, Kjetil, MP	Optimeringsbaserte Metoder for Ruteplanlegging innen skipsfart. (Dr.Ing. Thesis)
MTA-99-136	Bysveen, Marie, MM	Visualization in Two Directions on a Dynamic Combustion Rig for Studies of Fuel Quality. (Dr.Ing. Thesis)
MTA-2000-137	Storteig, Eskild, MM	Dynamic characteristics and leakage performance of liquid annular seals in centrifugal pumps. (Dr.Ing. Thesis)
MTA-2000-138	Sagli, Gro, MK	Model uncertainty and simplified estimates of long term extremes of hull girder loads in ships. (Dr.Ing. Thesis)
MTA-2000-139	Tronstad, Harald, MK	Nonlinear analysis and design of cable net structures like fishing gear based on the finite element method. (Dr.Ing. Thesis)
MTA-2000-140	Kroneberg, André, MP	Innovation in shipping by using scenarios. (Dr.Ing. Thesis)
MTA-2000-141	Haslum, Herbjørn Alf, MH	Simplified methods applied to nonlinear motion of spar platforms. (Dr.Ing. Thesis)
MTA-2001-142	Samdal, Ole Johan, MM	Modelling of Degradation Mechanisms and Stressor Interaction on Static Mechanical Equipment Residual Lifetime. (Dr.Ing. Thesis)
MTA-2001-143	Baarholm, Rolf Jarle, MH	Theoretical and experimental studies of wave impact underneath decks of offshore platforms. (Dr.Ing. Thesis)
MTA-2001-144	Wang, Lihua, MK	Probabilistic Analysis of Nonlinear Wave-induced Loads on Ships. (Dr.Ing. Thesis)
MTA-2001-145	Kristensen, Odd H. Holt, MK	Ultimate Capacity of Aluminium Plates under Multiple Loads, Considering HAZ Properties.

		(Dr.Ing. Thesis)
MTA-2001-146	Greco, Marilena, MH	A Two-Dimensional Study of Green-Water Loading. (Dr.Ing. Thesis)
MTA-2001-147	Heggelund, Svein E., MK	Calculation of Global Design Loads and Load Effects in Large High Speed Catamarans. (Dr.Ing. Thesis)
MTA-2001-148	Babalola, Olusegun T., MK	Fatigue Strength of Titanium Risers – Defect Sensitivity. (Dr.Ing. Thesis)
MTA-2001-149	Mohammed, Abuu K., MK	Nonlinear Shell Finite Elements for Ultimate Strength and Collapse Analysis of Ship Structures. (Dr.Ing. Thesis)
MTA-2002-150	Holmedal, Lars E., MH	Wave-current interactions in the vicinity of the sea bed. (Dr.Ing. Thesis)
MTA-2002-151	Rognebakke, Olav F., MH	Sloshing in rectangular tanks and interaction with ship motions. (Dr.Ing. Thesis)
MTA-2002-152	Lader, Pål Furset, MH	Geometry and Kinematics of Breaking Waves. (Dr.Ing. Thesis)
MTA-2002-153	Yang, Qinzheng, MH	Wash and wave resistance of ships in finite water depth. (Dr.Ing. Thesis)
MTA-2002-154	Melhus, Øyvin, MM	Utilization of VOC in Diesel Engines. Ignition and combustion of VOC released by crude oil tankers. (Dr.Ing. Thesis)
MTA-2002-155	Ronæss, Marit, MH	Wave Induced Motions of Two Ships Advancing on Parallel Course. (Dr.Ing. Thesis)
MTA-2002-156	Økland, Ole D., MK	Numerical and experimental investigation of whipping in twin hull vessels exposed to severe wet deck slamming. (Dr.Ing. Thesis)
MTA-2002-157	Ge, Chunhua, MK	Global Hydroelastic Response of Catamarans due to Wet Deck Slamming. (Dr.Ing. Thesis)
MTA-2002-158	Byklum, Eirik, MK	Nonlinear Shell Finite Elements for Ultimate Strength and Collapse Analysis of Ship Structures. (Dr.Ing. Thesis)
IMT-2003-1	Chen, Haibo, MK	Probabilistic Evaluation of FPSO-Tanker Collision in Tandem Offloading Operation. (Dr.Ing. Thesis)
IMT-2003-2	Skaugset, Kjetil Bjørn, MK	On the Suppression of Vortex Induced Vibrations of Circular Cylinders by Radial Water Jets. (Dr.Ing. Thesis)
IMT-2003-3	Chezhian, Muthu	Three-Dimensional Analysis of Slamming. (Dr.Ing. Thesis)
IMT-2003-4	Buhaug, Øyvind	Deposit Formation on Cylinder Liner Surfaces in Medium Speed Engines. (Dr.Ing. Thesis)
IMT-2003-5	Tregde, Vidar	Aspects of Ship Design: Optimization of Aft Hull with Inverse Geometry Design. (Dr.Ing. Thesis)

IMT-2003-6	Wist, Hanne Therese	Statistical Properties of Successive Ocean Wave Parameters. (Dr.Ing. Thesis)
IMT-2004-7	Ransau, Samuel	Numerical Methods for Flows with Evolving Interfaces. (Dr.Ing. Thesis)
IMT-2004-8	Soma, Torkel	Blue-Chip or Sub-Standard. A data interrogation approach of identity safety characteristics of shipping organization. (Dr.Ing. Thesis)
IMT-2004-9	Ersdal, Svein	An experimental study of hydrodynamic forces on cylinders and cables in near axial flow. (Dr.Ing. Thesis)
IMT-2005-10	Brodtkorb, Per Andreas	The Probability of Occurrence of Dangerous Wave Situations at Sea. (Dr.Ing. Thesis)
IMT-2005-11	Yttervik, Rune	Ocean current variability in relation to offshore engineering. (Dr.Ing. Thesis)
IMT-2005-12	Fredheim, Arne	Current Forces on Net-Structures. (Dr.Ing. Thesis)
IMT-2005-13	Heggernes, Kjetil	Flow around marine structures. (Dr.Ing. Thesis
IMT-2005-14	Fouques, Sebastien	Lagrangian Modelling of Ocean Surface Waves and Synthetic Aperture Radar Wave Measurements. (Dr.Ing. Thesis)
IMT-2006-15	Holm, Håvard	Numerical calculation of viscous free surface flow around marine structures. (Dr.Ing. Thesis)
IMT-2006-16	Bjørheim, Lars G.	Failure Assessment of Long Through Thickness Fatigue Cracks in Ship Hulls. (Dr.Ing. Thesis)
IMT-2006-17	Hansson, Lisbeth	Safety Management for Prevention of Occupational Accidents. (Dr.Ing. Thesis)
IMT-2006-18	Zhu, Xinying	Application of the CIP Method to Strongly Nonlinear Wave-Body Interaction Problems. (Dr.Ing. Thesis)
IMT-2006-19	Reite, Karl Johan	Modelling and Control of Trawl Systems. (Dr.Ing. Thesis)
IMT-2006-20	Smogeli, Øyvind Notland	Control of Marine Propellers. From Normal to Extreme Conditions. (Dr.Ing. Thesis)
IMT-2007-21	Storhaug, Gaute	Experimental Investigation of Wave Induced Vibrations and Their Effect on the Fatigue Loading of Ships. (Dr.Ing. Thesis)
IMT-2007-22	Sun, Hui	A Boundary Element Method Applied to Strongly Nonlinear Wave-Body Interaction Problems. (PhD Thesis, CeSOS)
IMT-2007-23	Rustad, Anne Marthine	Modelling and Control of Top Tensioned Risers. (PhD Thesis, CeSOS)
IMT-2007-24	Johansen, Vegar	Modelling flexible slender system for real-time

		simulations and control applications
IMT-2007-25	Wroldsen, Anders Sunde	Modelling and control of tensegrity structures. (PhD Thesis, CeSOS)
IMT-2007-26	Aronsen, Kristoffer Høye	An experimental investigation of in-line and combined inline and cross flow vortex induced vibrations. (Dr. avhandling, IMT)
IMT-2007-27	Gao, Zhen	Stochastic Response Analysis of Mooring Systems with Emphasis on Frequency-domain Analysis of Fatigue due to Wide-band Response Processes (PhD Thesis, CeSOS)
IMT-2007-28	Thorstensen, Tom Anders	Lifetime Profit Modelling of Ageing Systems Utilizing Information about Technical Condition. (Dr.ing. thesis, IMT)
IMT-2008-29	Refsnes, Jon Erling Gorset	Nonlinear Model-Based Control of Slender Body AUVs (PhD Thesis, IMT)
IMT-2008-30	Berntsen, Per Ivar B.	Structural Reliability Based Position Mooring. (PhD-Thesis, IMT)
IMT-2008-31	Ye, Naiquan	Fatigue Assessment of Aluminium Welded Box-stiffener Joints in Ships (Dr.ing. thesis, IMT)
IMT-2008-32	Radan, Damir	Integrated Control of Marine Electrical Power Systems. (PhD-Thesis, IMT)
IMT-2008-33	Thomassen, Paul	Methods for Dynamic Response Analysis and Fatigue Life Estimation of Floating Fish Cages. (Dr.ing. thesis, IMT)
IMT-2008-34	Pákozdi, Csaba	A Smoothed Particle Hydrodynamics Study of Two-dimensional Nonlinear Sloshing in Rectangular Tanks. (Dr.ing.thesis, IMT/ CeSOS)
IMT-2007-35	Grytøyr, Guttorm	A Higher-Order Boundary Element Method and Applications to Marine Hydrodynamics. (Dr.ing.thesis, IMT)
IMT-2008-36	Drummen, Ingo	Experimental and Numerical Investigation of Nonlinear Wave-Induced Load Effects in Containerships considering Hydroelasticity. (PhD thesis, CeSOS)
IMT-2008-37	Skejic, Renato	Maneuvering and Seakeeping of a Singel Ship and of Two Ships in Interaction. (PhD-Thesis, CeSOS)
IMT-2008-38	Harlem, Alf	An Age-Based Replacement Model for Repairable Systems with Attention to High-Speed Marine Diesel Engines. (PhD-Thesis, IMT)
IMT-2008-39	Alsos, Hagbart S.	Ship Grounding. Analysis of Ductile Fracture, Bottom Damage and Hull Girder Response. (PhD-thesis, IMT)
IMT-2008-40	Graczyk, Mateusz	Experimental Investigation of Sloshing Loading and Load Effects in Membrane LNG Tanks Subjected to Random Excitation. (PhD-thesis, CeSOS)

IMT-2008-41	Taghipour, Reza	Efficient Prediction of Dynamic Response for Flexible amd Multi-body Marine Structures. (PhD-thesis, CeSOS)
IMT-2008-42	Ruth, Eivind	Propulsion control and thrust allocation on marine vessels. (PhD thesis, CeSOS)
IMT-2008-43	Nystad, Bent Helge	Technical Condition Indexes and Remaining Useful Life of Aggregated Systems. PhD thesis, IMT
IMT-2008-44	Soni, Prashant Kumar	Hydrodynamic Coefficients for Vortex Induced Vibrations of Flexible Beams, PhD thesis, CeSOS
IMT-2009-45	Amlashi, Hadi K.K.	Ultimate Strength and Reliability-based Design of Ship Hulls with Emphasis on Combined Global and Local Loads. PhD Thesis, IMT
IMT-2009-46	Pedersen, Tom Arne	Bond Graph Modelling of Marine Power Systems. PhD Thesis, IMT
IMT-2009-47	Kristiansen, Trygve	Two-Dimensional Numerical and Experimental Studies of Piston-Mode Resonance. PhD-Thesis, CeSOS
IMT-2009-48	Ong, Muk Chen	Applications of a Standard High Reynolds Number Model and a Stochastic Scour Prediction Model for Marine Structures. PhD-thesis, IMT
IMT-2009-49	Hong, Lin	Simplified Analysis and Design of Ships subjected to Collision and Grounding. PhD-thesis, IMT
IMT-2009-50	Koushan, Kamran	Vortex Induced Vibrations of Free Span Pipelines, PhD thesis, IMT
IMT-2009-51	Korsvik, Jarl Eirik	Heuristic Methods for Ship Routing and Scheduling. PhD-thesis, IMT
IMT-2009-52	Lee, Jihoon	Experimental Investigation and Numerical in Analyzing the Ocean Current Displacement of Longlines. Ph.d.-Thesis, IMT.
IMT-2009-53	Vestbøstad, Tone Gran	A Numerical Study of Wave-in-Deck Impact usin a Two-Dimensional Constrained Interpolation Profile Method, Ph.d.thesis, CeSOS.
IMT-2009-54	Bruun, Kristine	Bond Graph Modelling of Fuel Cells for Marine Power Plants. Ph.d.-thesis, IMT
IMT 2009-55	Holstad, Anders	Numerical Investigation of Turbulence in a Sekwed Three-Dimensional Channel Flow, Ph.d.-thesis, IMT.
IMT 2009-56	Ayala-Uraga, Efren	Reliability-Based Assessment of Deteriorating Ship-shaped Offshore Structures, Ph.d.-thesis, IMT
IMT 2009-57	Kong, Xiangjun	A Numerical Study of a Damaged Ship in Beam Sea Waves. Ph.d.-thesis, IMT/CeSOS.
IMT 2010-58	Kristiansen, David	Wave Induced Effects on Floaters of Aquaculture Plants, Ph.d.-thesis, CeSOS.

IMT 2010-59	Ludvigsen, Martin	An ROV-Toolbox for Optical and Acoustic Scientific Seabed Investigation. Ph.d.-thesis IMT.
IMT 2010-60	Hals, Jørgen	Modelling and Phase Control of Wave-Energy Converters. Ph.d.thesis, CeSOS.
IMT 2010- 61	Shu, Zhi	Uncertainty Assessment of Wave Loads and Ultimate Strength of Tankers and Bulk Carriers in a Reliability Framework. Ph.d. Thesis, IMT/ CeSOS
IMT 2010-62	Shao, Yanlin	Numerical Potential-Flow Studies on Weakly-Nonlinear Wave-Body Interactions with/without Small Forward Speed, Ph.d.thesis,CeSOS.
IMT 2010-63	Califano, Andrea	Dynamic Loads on Marine Propellers due to Intermittent Ventilation. Ph.d.thesis, IMT.
IMT 2010-64	El Khoury, George	Numerical Simulations of Massively Separated Turbulent Flows, Ph.d.-thesis, IMT
IMT 2010-65	Seim, Knut Sponheim	Mixing Process in Dense Overflows with Emphasis on the Faroe Bank Channel Overflow. Ph.d.thesis, IMT
IMT 2010-66	Jia, Huirong	Structural Analysis of Intect and Damaged Ships in a Collission Risk Analysis Perspective. Ph.d.thesis CeSoS.
IMT 2010-67	Jiao, Linlin	Wave-Induced Effects on a Pontoon-type Very Large Floating Structures (VLFS). Ph.D.-thesis, CeSOS.
IMT 2010-68	Abrahamsen, Bjørn Christian	Sloshing Induced Tank Roof with Entrapped Air Pocket. Ph.d.thesis, CeSOS.
IMT 2011-69	Karimirad, Madjid	Stochastic Dynamic Response Analysis of Spar-Type Wind Turbines with Catenary or Taut Mooring Systems. Ph.d.-thesis, CeSOS.
IMT - 2011-70	Erlend Meland	Condition Monitoring of Safety Critical Valves. Ph.d.-thesis, IMT.
IMT – 2011-71	Yang, Limin	Stochastic Dynamic System Analysis of Wave Energy Converter with Hydraulic Power Take-Off, with Particular Reference to Wear Damage Analysis, Ph.d. Thesis, CeSOS.
IMT – 2011-72	Visscher, Jan	Application of Particla Image Velocimetry on Turbulent Marine Flows, Ph.d.Thesis, IMT.
IMT – 2011-73	Su, Biao	Numerical Predictions of Global and Local Ice Loads on Ships. Ph.d.Thesis, CeSOS.
IMT – 2011-74	Liu, Zhenhui	Analytical and Numerical Analysis of Iceberg Collision with Ship Structures. Ph.d.Thesis, IMT.
IMT – 2011-75	Aarsæther, Karl Gunnar	Modeling and Analysis of Ship Traffic by Observation and Numerical Simulation. Ph.d.Thesis, IMT.

Imt – 2011-76	Wu, Jie	Hydrodynamic Force Identification from Stochastic Vortex Induced Vibration Experiments with Slender Beams. Ph.d.Thesis, IMT.
Imt – 2011-77	Amini, Hamid	Azimuth Propulsors in Off-design Conditions. Ph.d.Thesis, IMT.
IMT – 2011-78	Nguyen, Tan-Hoi	Toward a System of Real-Time Prediction and Monitoring of Bottom Damage Conditions During Ship Grounding. Ph.d.thesis, IMT.
IMT- 2011-79	Tavakoli, Mohammad T.	Assessment of Oil Spill in Ship Collision and Grounding, Ph.d.thesis, IMT.
IMT- 2011-80	Guo, Bingjie	Numerical and Experimental Investigation of Added Resistance in Waves. Ph.d.Thesis, IMT.
IMT- 2011-81	Chen, Qiaofeng	Ultimate Strength of Aluminium Panels, considering HAZ Effects, IMT
IMT- 2012-82	Kota, Ravikiran S.	Wave Loads on Decks of Offshore Structures in Random Seas, CeSOS.
IMT- 2012-83	Sten, Ronny	Dynamic Simulation of Deep Water Drilling Risers with Heave Compensating System, IMT.
IMT- 2012-84	Berle, Øyvind	Risk and resilience in global maritime supply chains, IMT.
IMT- 2012-85	Fang, Shaoji	Fault Tolerant Position Mooring Control Based on Structural Reliability, CeSOS.
IMT- 2012-86	You, Jikun	Numerical studies on wave forces and moored ship motions in intermediate and shallow water, CeSOS.
IMT- 2012-87	Xiang ,Xu	Maneuvering of two interacting ships in waves, CeSOS
IMT- 2012-88	Dong, Wenbin	Time-domain fatigue response and reliability analysis of offshore wind turbines with emphasis on welded tubular joints and gear components, CeSOS
IMT- 2012-89	Zhu, Suji	Investigation of Wave-Induced Nonlinear Load Effects in Open Ships considering Hull Girder Vibrations in Bending and Torsion, CeSOS
IMT- 2012-90	Zhou, Li	Numerical and Experimental Investigation of Station-keeping in Level Ice, CeSOS
IMT- 2012-91	Ushakov, Sergey	Particulate matter emission characteristics from diesel enignes operating on conventional and alternative marine fuels, IMT
IMT- 2013-1	Yin, Decao	Experimental and Numerical Analysis of Combined In-line and Cross-flow Vortex Induced Vibrations, CeSOS

IMT-2013-2	Kurniawan, Adi	Modelling and geometry optimisation of wave energy converters, CeSOS
IMT-2013-3	Al Ryati, Nabil	Technical condition indexes doe auxiliary marine diesel engines, IMT
IMT-2013-4	Firoozkoohi, Reza	Experimental, numerical and analytical investigation of the effect of screens on sloshing, CeSOS
IMT-2013-5	Ommani, Babak	Potential-Flow Predictions of a Semi-Displacement Vessel Including Applications to Calm Water Broaching, CeSOS
IMT-2013-6	Xing, Yihan	Modelling and analysis of the gearbox in a floating spar-type wind turbine, CeSOS
IMT-7-2013	Balland, Océane	Optimization models for reducing air emissions from ships, IMT
IMT-8-2013	Yang, Dan	Transitional wake flow behind an inclined flat plate-----Computation and analysis, IMT
IMT-9-2013	Abdillah, Suyuthi	Prediction of Extreme Loads and Fatigue Damage for a Ship Hull due to Ice Action, IMT
IMT-10-2013	Ramìrez, Pedro Agustìn Pèrez	Ageing management and life extension of technical systems- Concepts and methods applied to oil and gas facilities, IMT
IMT-11-2013	Chuang, Zhenju	Experimental and Numerical Investigation of Speed Loss due to Seakeeping and Maneuvering. IMT
IMT-12-2013	Etemaddar, Mahmoud	Load and Response Analysis of Wind Turbines under Atmospheric Icing and Controller System Faults with Emphasis on Spar Type Floating Wind Turbines, IMT
IMT-13-2013	Lindstad, Haakon	Strategies and measures for reducing maritime CO2 emissons, IMT
IMT-14-2013	Haris, Sabril	Damage interaction analysis of ship collisions, IMT
IMT-15-2013	Shainee, Mohamed	Conceptual Design, Numerical and Experimental Investigation of a SPM Cage Concept for Offshore Mariculture, IMT
IMT-16-2013	Gansel, Lars	Flow past porous cylinders and effects of biofouling and fish behavior on the flow in and around Atlantic salmon net cages, IMT
IMT-17-2013	Gaspar, Henrique	Handling Aspects of Complexity in Conceptual Ship Design, IMT
IMT-18-2013	Thys, Maxime	Theoretical and Experimental Investigation of a Free Running Fishing Vessel at Small Frequency of Encounter, CeSOS
IMT-19-2013	Aglen, Ida	VIV in Free Spanning Pipelines, CeSOS

IMT-1-2014	Song, An	Theoretical and experimental studies of wave diffraction and radiation loads on a horizontally submerged perforated plate, CeSOS
IMT-2-2014	Rogne, Øyvind Ygre	Numerical and Experimental Investigation of a Hinged 5-body Wave Energy Converter, CeSOS
IMT-3-2014	Dai, Lijuan	Safe and efficient operation and maintenance of offshore wind farms ,IMT
IMT-4-2014	Bachynski, Erin Elizabeth	Design and Dynamic Analysis of Tension Leg Platform Wind Turbines, CeSOS
IMT-5-2014	Wang, Jingbo	Water Entry of Freefall Wedged – Wedge motions and Cavity Dynamics, CeSOS
IMT-6-2014	Kim, Ekaterina	Experimental and numerical studies related to the coupled behavior of ice mass and steel structures during accidental collisions, IMT
IMT-7-2014	Tan, Xiang	Numerical investigation of ship's continuous- mode icebreaking in leverl ice, CeSOS
IMT-8-2014	Muliawan, Made Jaya	Design and Analysis of Combined Floating Wave and Wind Power Facilities, with Emphasis on Extreme Load Effects of the Mooring System, CeSOS
IMT-9-2014	Jiang, Zhiyu	Long-term response analysis of wind turbines with an emphasis on fault and shutdown conditions, IMT
IMT-10-2014	Dukan, Fredrik	ROV Motion Control Systems, IMT
IMT-11-2014	Grimsmo, Nils I.	Dynamic simulations of hydraulic cylinder for heave compensation of deep water drilling risers, IMT
IMT-12-2014	Kvittem, Marit I.	Modelling and response analysis for fatigue design of a semisubmersible wind turbine, CeSOS
IMT-13-2014	Akhtar, Juned	The Effects of Human Fatigue on Risk at Sea, IMT
IMT-14-2014	Syahroni, Nur	Fatigue Assessment of Welded Joints Taking into Account Effects of Residual Stress, IMT
IMT-1-2015	Bøckmann, Eirik	Wave Propulsion of ships, IMT
IMT-2-2015	Wang, Kai	Modelling and dynamic analysis of a semi-submersible floating vertical axis wind turbine, CeSOS
IMT-3-2015	Fredriksen, Arnt Gunvald	A numerical and experimental study of a two-dimensional body with moonpool in waves and current, CeSOS
IMT-4-2015	Jose Patricio Gallardo Canabes	Numerical studies of viscous flow around bluff bodies, IMT

IMT-5-2015	Vegard Longva	Formulation and application of finite element techniques for slender marine structures subjected to contact interactions, IMT
IMT-6-2015	Jacobus De Vaal	Aerodynamic modelling of floating wind turbines, CeSOS
IMT-7-2015	Fachri Nasution	Fatigue Performance of Copper Power Conductors, IMT
IMT-8-2015	Oleh I Karpa	Development of bivariate extreme value distributions for applications in marine technology,CeSOS
IMT-9-2015	Daniel de Almeida Fernandes	An output feedback motion control system for ROVs, AMOS
IMT-10-2015	Bo Zhao	Particle Filter for Fault Diagnosis: Application to Dynamic Positioning Vessel and Underwater Robotics, CeSOS
IMT-11-2015	Wenting Zhu	Impact of emission allocation in maritime transportation, IMT
IMT-12-2015	Amir Rasekhi Nejad	Dynamic Analysis and Design of Gearboxes in Offshore Wind Turbines in a Structural Reliability Perspective, CeSOS
IMT-13-2015	Arturo Jesùs Ortega Malca	Dynamic Response of Flexibles Risers due to Unsteady Slug Flow, CeSOS
IMT-14-2015	Dagfinn Husjord	Guidance and decision-support system for safe navigation of ships operating in close proximity, IMT
IMT-15-2015	Anirban Bhattacharyya	Ducted Propellers: Behaviour in Waves and Scale Effects, IMT
IMT-16-2015	Qin Zhang	Image Processing for Ice Parameter Identification in Ice Management, IMT
IMT-1-2016	Vincentius Rumawas	Human Factors in Ship Design and Operation: An Experiential Learning, IMT
IMT-2-2016	Martin Storheim	Structural response in ship-platform and ship-ice collisions, IMT
IMT-3-2016	Mia Abrahamsen Prsic	Numerical Simulations of the Flow around single and Tandem Circular Cylinders Close to a Plane Wall, IMT
IMT-4-2016	Tufan Arslan	Large-eddy simulations of cross-flow around ship sections, IMT

IMT-5-2016	Pierre Yves-Henry	Parametrisation of aquatic vegetation in hydraulic and coastal research,IMT
IMT-6-2016	Lin Li	Dynamic Analysis of the Instalation of Monopiles for Offshore Wind Turbines, CeSOS
IMT-7-2016	Øivind Kåre Kjerstad	Dynamic Positioning of Marine Vessels in Ice, IMT
IMT-8-2016	Xiaopeng Wu	Numerical Analysis of Anchor Handling and Fish Trawling Operations in a Safety Perspective, CeSOS
IMT-9-2016	Zhengshun Cheng	Integrated Dynamic Analysis of Floating Vertical Axis Wind Turbines, CeSOS
IMT-10-2016	Ling Wan	Experimental and Numerical Study of a Combined Offshore Wind and Wave Energy Converter Concept
IMT-11-2016	Wei Chai	Stochastic dynamic analysis and reliability evaluation of the roll motion for ships in random seas, CeSOS
IMT-12-2016	Øyvind Selnes Patricksson	Decision support for conceptual ship design with focus on a changing life cycle and future uncertainty, IMT
IMT-13-2016	Mats Jørgen Thorsen	Time domain analysis of vortex-induced vibrations, IMT
IMT-14-2016	Edgar McGuinness	Safety in the Norwegian Fishing Fleet – Analysis and measures for improvement, IMT
IMT-15-2016	Sepideh Jafarzadeh	Energy effiency and emission abatement in the fishing fleet, IMT
IMT-16-2016	Wilson Ivan Guachamin Acero	Assessment of marine operations for offshore wind turbine installation with emphasis on response-based operational limits, IMT
IMT-17-2016	Mauro Candeloro	Tools and Methods for Autonomous Operations on Seabed and Water Coumn using Underwater Vehicles, IMT
IMT-18-2016	Valentin Chabaud	Real-Time Hybrid Model Testing of Floating Wind Tubines, IMT
IMT-1-2017	Mohammad Saud Afzal	Three-dimensional streaming in a sea bed boundary layer
IMT-2-2017	Peng Li	A Theoretical and Experimental Study of Wave-induced Hydroelastic Response of a Circular Floating Collar
IMT-3-2017	Martin Bergström	A simulation-based design method for arctic maritime transport systems

IMT-4-2017	Bhushan Taskar	The effect of waves on marine propellers and propulsion
IMT-5-2017	Mohsen Bardestani	A two-dimensional numerical and experimental study of a floater with net and sinker tube in waves and current
IMT-6-2017	Fatemeh Hoseini Dadmarzi	Direct Numerical Simualtion of turbulent wakes behind different plate configurations
IMT-7-2017	Michel R. Miyazaki	Modeling and control of hybrid marine power plants
IMT-8-2017	Giri Rajasekhar Gunnu	Safety and effiency enhancement of anchor handling operations with particular emphasis on the stability of anchor handling vessels
IMT-9-2017	Kevin Koosup Yum	Transient Performance and Emissions of a Turbocharged Diesel Engine for Marine Power Plants
IMT-10-2017	Zhaolong Yu	Hydrodynamic and structural aspects of ship collisions
IMT-11-2017	Martin Hassel	Risk Analysis and Modelling of Allisions between Passing Vessels and Offshore Installations
IMT-12-2017	Astrid H. Brodtkorb	Hybrid Control of Marine Vessels – Dynamic Positioning in Varying Conditions
IMT-13-2017	Kjersti Bruserud	Simultaneous stochastic model of waves and current for prediction of structural design loads
IMT-14-2017	Finn-Idar Grøtta Giske	Long-Term Extreme Response Analysis of Marine Structures Using Inverse Reliability Methods
IMT-15-2017	Stian Skjong	Modeling and Simulation of Maritime Systems and Operations for Virtual Prototyping using co-Simulations
IMT-1-2018	Yingguang Chu	Virtual Prototyping for Marine Crane Design and Operations
IMT-2-2018	Sergey Gavrilin	Validation of ship manoeuvring simulation models
IMT-3-2018	Jeevith Hegde	Tools and methods to manage risk in autonomous subsea inspection,maintenance and repair operations
IMT-4-2018	Ida M. Strand	Sea Loads on Closed Flexible Fish Cages
IMT-5-2018	Erlend Kvinge Jørgensen	Navigation and Control of Underwater Robotic Vehicles

IMT-6-2018	Bård Stovner	Aided Intertial Navigation of Underwater Vehicles
IMT-7-2018	Erlend Liavåg Grotle	Thermodynamic Response Enhanced by Sloshing in Marine LNG Fuel Tanks
IMT-8-2018	Børge Rokseth	Safety and Verification of Advanced Maritime Vessels
IMT-9-2018	Jan Vidar Ulveseter	Advances in Semi-Empirical Time Domain Modelling of Vortex-Induced Vibrations
IMT-10-2018	Chenyu Luan	Design and analysis for a steel braceless semi-submersible hull for supporting a 5-MW horizontal axis wind turbine
IMT-11-2018	Carl Fredrik Rehn	Ship Design under Uncertainty
IMT-12-2018	Øyvind Ødegård	Towards Autonomous Operations and Systems in Marine Archaeology
IMT-13-2018	Stein Melvær Nornes	Guidance and Control of Marine Robotics for Ocean Mapping and Monitoring
IMT-14-2018	Petter Norgren	Autonomous Underwater Vehicles in Arctic Marine Operations: Arctic marine research and ice monitoring
IMT-15-2018	Minjoo Choi	Modular Adaptable Ship Design for Handling Uncertainty in the Future Operating Context
MT-16-2018	Ole Alexander Eidsvik	Dynamics of Remotely Operated Underwater Vehicle Systems
IMT-17-2018	Mahdi Ghane	Fault Diagnosis of Floating Wind Turbine Drivetrain- Methodologies and Applications
IMT-18-2018	Christoph Alexander Thieme	Risk Analysis and Modelling of Autonomous Marine Systems
IMT-19-2018	Yugao Shen	Operational limits for floating-collar fish farms in waves and current, without and with well-boat presence
IMT-20-2018	Tianjiao Dai	Investigations of Shear Interaction and Stresses in Flexible Pipes and Umbilicals
IMT-21-2018	Sigurd Solheim Pettersen	Resilience by Latent Capabilities in Marine Systems
IMT-22-2018	Thomas Sauder	Fidelity of Cyber-physical Empirical Methods. Application to the Active Truncation of Slender Marine Structures
IMT-23-2018	Jan-Tore Horn	Statistical and Modelling Uncertainties in the Design of Offshore Wind Turbines

IMT-24-2018	Anna Swider	Data Mining Methods for the Analysis of Power Systems of Vessels
IMT-1-2019	Zhao He	Hydrodynamic study of a moored fish farming cage with fish influence
IMT-2-2019	Isar Ghamari	Numerical and Experimental Study on the Ship Parametric Roll Resonance and the Effect of Anti-Roll Tank
IMT-3-2019	Håkon Strandenes	Turbulent Flow Simulations at Higher Reynolds Numbers
IMT-4-2019	Siri Mariane Holen	Safety in Norwegian Fish Farming – Concepts and Methods for Improvement
IMT-5-2019	Ping Fu	Reliability Analysis of Wake-Induced Riser Collision
IMT-6-2019	Vladimir Krivopolianskii	Experimental Investigation of Injection and Combustion Processes in Marine Gas Engines using Constant Volume Rig
IMT-7-2019	Anna Maria Kozlowska	Hydrodynamic Loads on Marine Propellers Subject to Ventilation and out of Water Condition.
IMT-8-2019	Hans-Martin Heyn	Motion Sensing on Vessels Operating in Sea Ice: A Local Ice Monitoring System for Transit and Stationkeeping Operations under the Influence of Sea Ice
IMT-9-2019|	Stefan Vilsen	Method for Real-Time Hybrid Model Testing of Ocean Structures – Case on Slender Marine Systems
IMT-10-2019	Finn-Christian W. Hanssen	Non-Linear Wave-Body Interaction in Severe Waves
IMT-11-2019	Trygve Olav Fossum	Adaptive Sampling for Marine Robotics
IMT-12-2019	Jørgen Bremnes Nielsen	Modeling and Simulation for Design Evaluation
IMT-13-2019	Yuna Zhao	Numerical modelling and dyncamic analysis of offshore wind turbine blade installation
IMT-14-2019	Daniela Myland	Experimental and Theoretical Investigations on the Ship Resistance in Level Ice
IMT-15-2019	Zhengru Ren	Advanced control algorithms to support automated offshore wind turbine installation
IMT-16-2019	Drazen Polic	Ice-propeller impact analysis using an inverse propulsion machinery simulation approach
IMT-17-2019	Endre Sandvik	Sea passage scenario simulation for ship system performance evaluation

IMT-18-2019	Loup Suja-Thauvin	Response of Monopile Wind Turbines to Higher Order Wave Loads
IMT-19-2019	Emil Smilden	Structural control of offshore wind turbines – Increasing the role of control design in offshore wind farm development
IMT-20-2019	Aleksandar-Sasa Milakovic	On equivalent ice thickness and machine learning in ship ice transit simulations
IMT-1-2020	Amrit Shankar Verma	Modelling, Analysis and Response-based Operability Assessment of Offshore Wind Turbine Blade Installation with Emphasis on Impact Damages
IMT-2-2020	Bent Oddvar Arnesen Haugaløkken	Autonomous Technology for Inspection, Maintenance and Repair Operations in the Norwegian Aquaculture
IMT-3-2020	Seongpil Cho	Model-based fault detection and diagnosis of a blade pitch system in floating wind turbines
IMT-4-2020	Jose Jorge Garcia Agis	Effectiveness in Decision-Making in Ship Design under Uncertainty
IMT-5-2020	Thomas H. Viuff	Uncertainty Assessment of Wave-and Current-induced Global Response of Floating Bridges
IMT-6-2020	Fredrik Mentzoni	Hydrodynamic Loads on Complex Structures in the Wave Zone
IMT-7-2020	Senthuran Ravinthrakumar	Numerical and Experimental Studies of Resonant Flow in Moonpools in Operational Conditions
IMT-8-2020	Stian Skaalvik Sandøy	Acoustic-based Probabilistic Localization and Mapping using Unmanned Underwater Vehicles for Aquaculture Operations
IMT-9-2020	Kun Xu	Design and Analysis of Mooring System for Semi-submersible Floating Wind Turbine in Shallow Water
IMT-10-2020	Jianxun Zhu	Cavity Flows and Wake Behind an Elliptic Cylinder Translating Above the Wall
IMT-11-2020	Sandra Hogenboom	Decision-making within Dynamic Positioning Operations in the Offshore Industry – A Human Factors based Approach
IMT-12-2020	Woongshik Nam	Structural Resistance of Ship and Offshore Structures Exposed to the Risk of Brittle Failure
IMT-13-2020	Svenn Are Tutturen Værnø	Transient Performance in Dynamic Positioning of Ships: Investigation of Residual Load Models and Control Methods for Effective Compensation
IMT-14-2020	Mohd Atif Siddiqui	Experimental and Numerical Hydrodynamic Analysis of a Damaged Ship in Waves
IMT-15-2020	John Marius Hegseth	Efficient Modelling and Design Optimization of Large Floating Wind Turbines

IMT-16-2020	Asle Natskår	Reliability-based Assessment of Marine Operations with Emphasis on Sea Transport on Barges
IMT-17-2020	Shi Deng	Experimental and Numerical Study of Hydrodynamic Responses of a Twin-Tube Submerged Floating Tunnel Considering Vortex-Induced Vibration
IMT-18-2020	Jone Torsvik	Dynamic Analysis in Design and Operation of Large Floating Offshore Wind Turbine Drivetrains
IMT-1-2021	Ali Ebrahimi	Handling Complexity to Improve Ship Design Competitiveness
IMT-2-2021	Davide Proserpio	Isogeometric Phase-Field Methods for Modeling Fracture in Shell Structures
IMT-3-2021	Cai Tian	Numerical Studies of Viscous Flow Around Step Cylinders
IMT-4-2021	Farid Khazaeli Moghadam	Vibration-based Condition Monitoring of Large Offshore Wind Turbines in a Digital Twin Perspective
IMT-5-2021	Shuaishuai Wang	Design and Dynamic Analysis of a 10-MW Medium-Speed Drivetrain in Offshore Wind Turbines
IMT-6-2021	Sadi Tavakoli	Ship Propulsion Dynamics and Emissions
IMT-7-2021	Haoran Li	Nonlinear wave loads, and resulting global response statistics of a semi-submersible wind turbine platform with heave plates
IMT-8-2021	Einar Skiftestad Ueland	Load Control for Real-Time Hybrid Model Testing using Cable-Driven Parallel Robots
IMT-9-2021	Mengning Wu	Uncertainty of machine learning-based methods for wave forecast and its effect on installation of offshore wind turbines
IMT-10-2021	Xu Han	Onboard Tuning and Uncertainty Estimation of Vessel Seakeeping Model Parameters
IMT-01-2022	Ingunn Marie Holmen	Safety in Exposed Aquacultrue Operations
IMT-02-2022	Prateek Gupta	Ship Performance Monitoring using In-service Measurements and Big Data Analysis Methods
IMT-03-2022	Sangwoo Kim	Non-linear time domain analysis of deepwater riser vortex-induced vibrations
IMT-04-2022	Jarle Vinje Kramer	Hydrodynamic Aspects of Sail-Assisted Merchant Vessels
IMT-05-2022	Øyvind Rabliås	Numerical and Expermental Studies of Maneuvering in Regular and Irregular Waves

IMT-06-2022	Pramod Ghimire	Simulation-Based Ship Hybrid Power System Conspet Studies and Performance Analyses
IMT-07-2022	Carlos Eduardo Silva de Souza	Structural modelling, coupled dynamics, and design of large floating wind turbines
IMT-08-2022	Lorenzo Balestra	Design of hybrid fuel cell & battery systems for maritime vessels
IMT-09-2022	Sharmin Sultana	Process safety and risk management using system perspectives – A contribution to the chemical process and petroleum industry
IMT-10-2022	Øystein Sture	Autonomous Exploration for Marine Minerals
IMT-11-2022	Tiantian Zhu	Information and Decision-making for Major Accident Prevention – A concept of information-based strategies for accident prevention
IMT-12-2022	Siamak Karimi	Shore-to-Ship Charging Systems for Battery-Electric Ships
IMT-01-2023	Huili Xu	Fish-inspired Propulsion Study: Numerical Hydrodynamics of Rigid/Flexible/Morphing Foils and Observations on Real Fish
IMT-02-2023	Chana Sinsabvarodom	Probabilistic Modelling of Ice-drift and Ice Loading on Fixed and Floating Offshore Structures
IMT-03-2023	Martin Skaldebø	Intelligent low-cost solutions for underwater intervention using computer vision and machine learning
IMT-04-2023	Hans Tobias Slette	Vessel operations in exposed aquaculture – Achieving safe and efficient operation of vessel fleets in fish farm systems experiencing challenging metocean conditions
IMT-05-2023	Ruochen Yang	Methods and models for analyzing and controlling the safety in operations of autonomous marine systems
IMT-06-2023	Tobias Rye Torben	Formal Approaches to Design and Verification of Safe Control Systems for Autonomous Vessels
IMT-07-2023	YoungRong Kim	Modeling Operational Performance for the Global Fleet & Application of an Energy Saving Measure
IMT-08-2023	Henrik Schmidt-Didlaukies	Modeling and Hybrid Feedback Control of Underwater Vehicles
IMT-09-2023	Ehsan Esmailian	Optimal Ship Design for Operating in Real Sea States
IMT-10-2023	Astrid Vamråk Solheim	Exploring the performance of conceptual offshore production systems for deep-sea mining
IMT-11-2023	Benjamin Lagemann	Conceptual design of low-emission ships

IMT-12-2023	Erling Neerland Lone	Fatigue reliability of offshore Mooring chains under influence of mean load and corrosion
IMT-13-2023	Kamyar Malekibagherabadi	Simulator Approach to Concept Analysis and Optimization of Marine Power Plants
IMT-14-2023	Håvard Snefjellås Løvås	Optical Techniques for Hyperspectral Imaging of the Seafloor